

**Final Technical Report on NASA Grant NAG3-1121**  
**Use of Rotation to Suppress Thermosolutal Convection in**  
**Directionally Solidified Binary Alloys**

FINAL  
1N-26-CR  
OCIT  
19563  
p. 238

Arne J. Pearlstein  
Department of Mechanical and Industrial Engineering  
University of Illinois at Urbana-Champaign  
1206 West Green Street  
Urbana, IL 61801

July 15, 1994

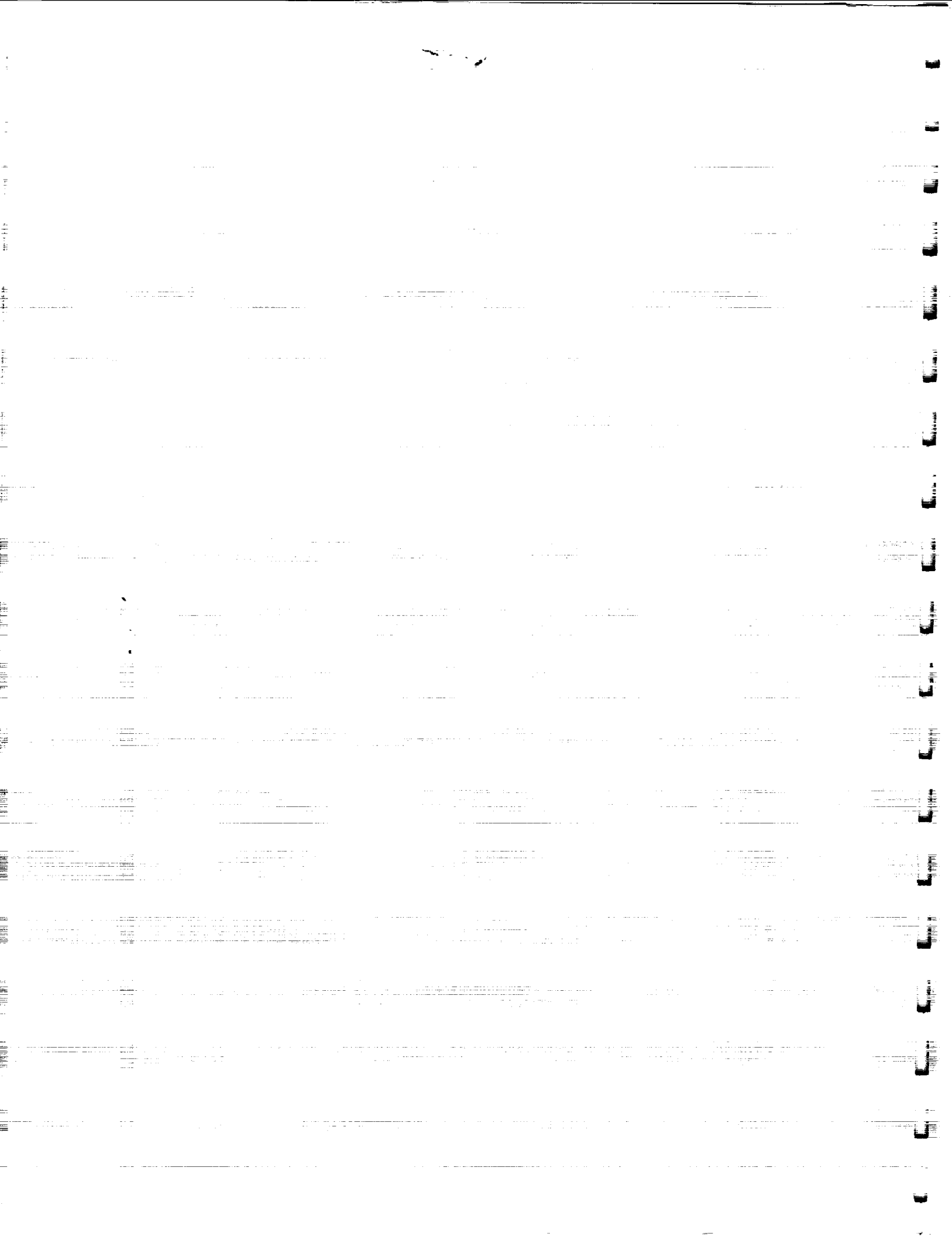
UILU-ENG 94-4008

(NASA-CR-196372) USE OF ROTATION  
TO SUPPRESS THERMOSOLUTAL  
CONVECTION IN DIRECTIONALLY  
SOLIDIFIED BINARY ALLOYS Final  
Technical Report (Illinois Univ.)  
238 p

N94-36811

Unclass

G3/26 0019563

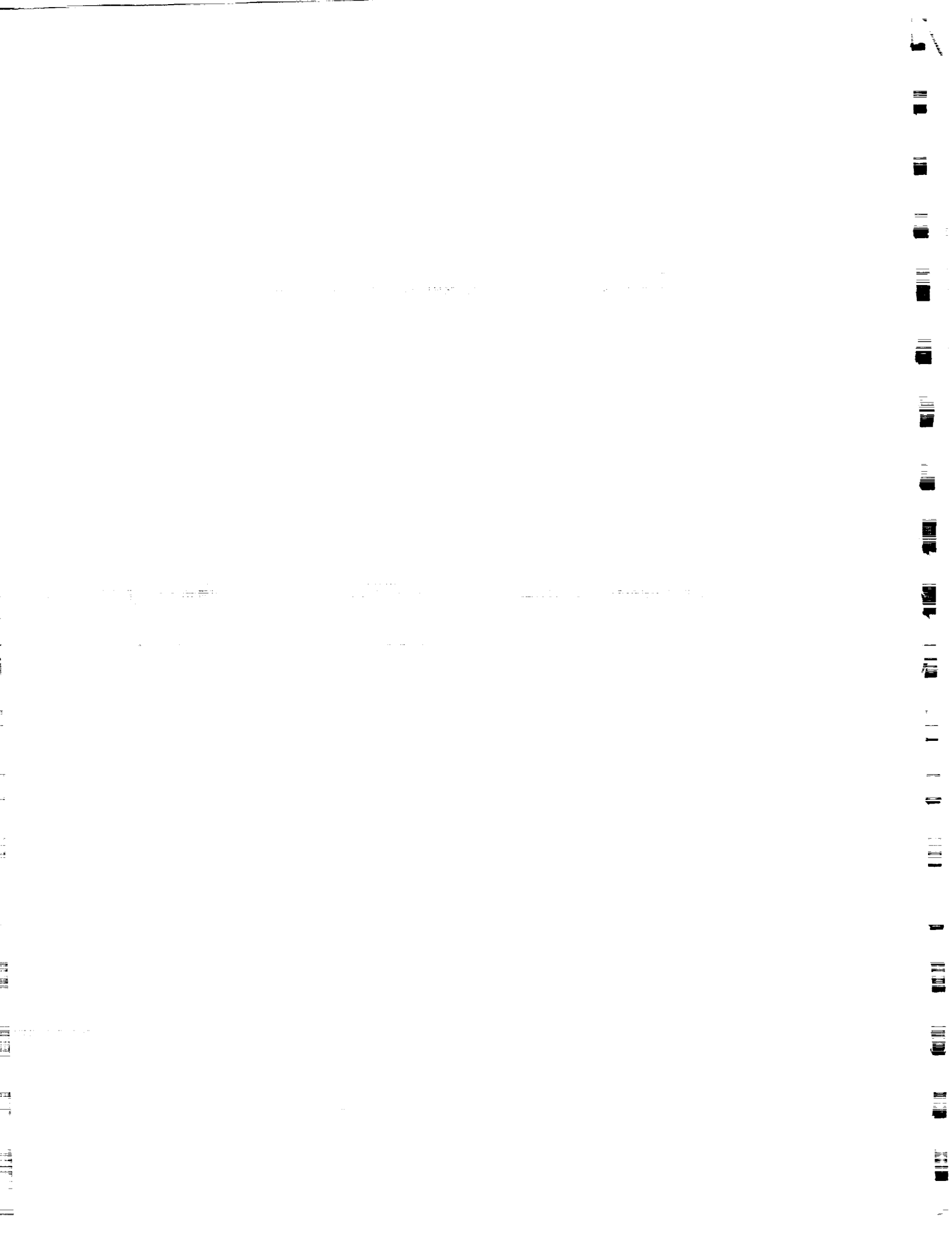


**Final Technical Report on NASA Grant NAG3-1121**

**Use of Rotation to Suppress Thermosolutal Convection in  
Directionally Solidified Binary Alloys**

**Arne J. Pearlstein**  
**Department of Mechanical and Industrial Engineering**  
**University of Illinois at Urbana-Champaign**  
**1206 West Green Street**  
**Urbana, IL 61801**

**July 15, 1994**





# Final Technical Report on NASA Grant NAG3-1121

## Use of Rotation to Suppress Thermosolutal Convection in Directionally Solidified Binary Alloys

July 15, 1994

Arne J. Pearlstein  
Department of Mechanical and Industrial Engineering  
University of Illinois at Urbana-Champaign  
1206 West Green Street  
Urbana, IL 61801

### Abstract

Effects of rotation on onset of convection during plane-front directional solidification of Pb-Sn and the pseudobinary system mercury cadmium telluride ( $\text{Hg}_{1-x}\text{Cd}_x\text{Te}$ ), and on dendritic solidification of Pb-Sn have been studied by means of linear stability analysis.

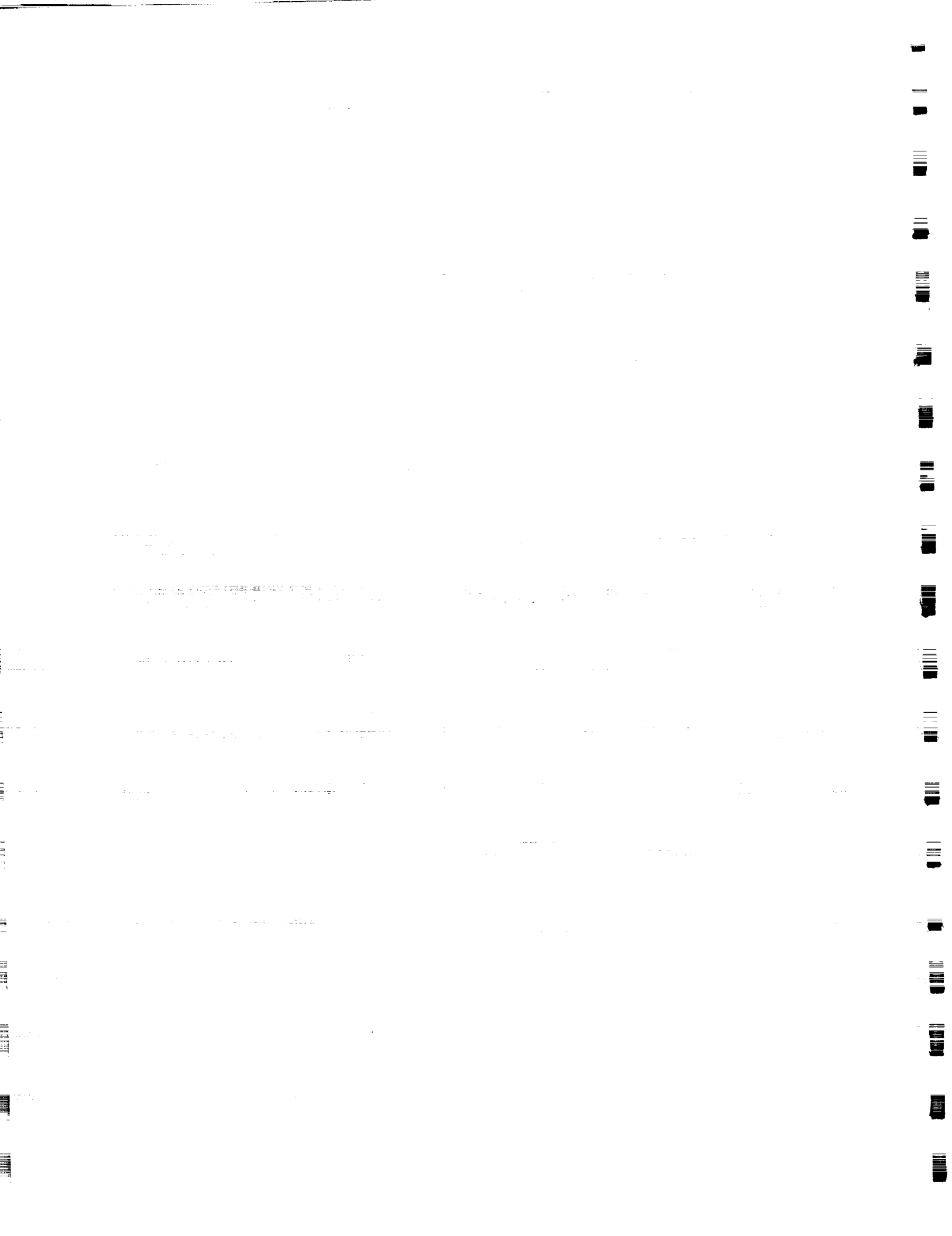
Incorporating Coriolis and centrifugal accelerations into the momentum equation of Coriell *et al.*, we find that under realistic processing conditions, a large degree of stabilization can be achieved using modest rotation rates for both Pb-Sn and mercury cadmium telluride ( $\text{Hg}_{1-x}\text{Cd}_x\text{Te}$ ).

At a growth velocity of  $5\text{ }\mu\text{/sec}$  and nominal liquid-side temperature gradient of  $200\text{ K/cm}$  in Pb-Sn, rotation at 500 rpm results in a hundredfold increase in the critical Sn concentration. Large increases in the maximum allowable growth velocity at fixed melt composition are also attainable with modest rotation rates. The effect is amplified under conditions of reduced gravitational acceleration.

For  $\text{Hg}_{1-x}\text{Cd}_x\text{Te}$ , we have also studied the nonrotating case. The key differences are due to the existence of a composition range for  $\text{Hg}_{1-x}\text{Cd}_x\text{Te}$  in which the melt density has a local maximum as a function of temperature. When the melt solidifies by cooling from below, the liquid density may initially increase with distance above the interface, before ultimately decreasing as the melt temperature increases above the value at which the local density maximum occurs. In contrast to the Pb-Sn case where density depends monotonically on temperature and composition, for  $\text{Hg}_{1-x}\text{Cd}_x\text{Te}$  there exists a critical value of the growth velocity above which plane-front solidification is unstable for all bulk CdTe mole fractions. Again, rotation leads to significant inhibition of onset.

We identify the predicted stabilization with the Taylor-Proudman mechanism by which rotation inhibits thermal convection in a single-component fluid heated from below. In a binary liquid undergoing solidification, rotation inhibits the onset of buoyancy-driven convection, and has no effect on the short-wavelength morphological instability.

At large growth velocities, the plane-front interface between liquid and solid becomes unstable with respect to a morphological instability and solidification occurs dendritically, with a mushy zone of dendrites and interdendritic fluid separating the solid from the melt. For the Pb-Sn system, rotation substantially suppresses the onset of convection in the mushy zone and in the overlying liquid, holding open the promise that rotation can suppress freckling and other macrosegregation defects.



## 1. Introduction

During directional solidification of alloys, it is frequently desired to produce large single crystals with very low densities of macrosegregation defects and other imperfections. In principle, this can sometimes be achieved by "plane-front" solidification, in which the melt-solid interface remains perfectly planar. In such a case, the solidification process would be steady in a reference frame moving with the interface, and the only spatial variation would be in a direction normal to the interface. However, in real systems, several instabilities can cause departures from the nominally steady and one-dimensional plane-front case.

First, the solid-liquid interface may be subject to the so-called morphological instability, which has been studied extensively since the early work of Mullins and Sekerka (1964). This instability causes deformation of the nominally planar interface, ultimately leading to formation of a two-phase "mushy zone" of dendrites and interdendritic liquid. Departures from one-dimensionality and steadiness in the mushy zone result in nonuniform distribution of solute in the solidified material.

Second, the density of a binary or multicomponent melt depends on both temperature and composition. When an alloy is solidified by cooling from below, rejection of solute(s) at the growing interface is potentially destabilizing if the solute-enriched liquid just above the interface is less dense than the warmer overlying bulk liquid. Under some conditions, this adverse solute gradient overcomes the stabilizing temperature gradient, leading to convection in the melt. This fluid motion provides another transport mechanism, besides molecular diffusion, for redistributing solute(s) into the bulk liquid from the relatively enriched region near the interface. Convection in the melt is often referred to as thermosolutal convection, or because the diffusivities of heat and solute are different, as doubly-diffusive convection.

Convective and morphological instabilities in a binary alloy undergoing directional solidification were first studied by Coriell *et al.* (1980) using a linear stability analysis. These authors showed that motion may occur due to either morphological or convective instabilities, and that the buoyancy force does not sensibly alter the criterion for onset of morphological instability, which occurs at higher wavenumbers than does the buoyancy-driven instability. Subsequent work was reviewed by Glicksman *et al.* (1986), and Sekerka and Coriell (1987). More general discussions of the effects of convection on plane-front and dendritic solidification have been given recently by Worster (1991), Davis (1990), Huppert (1990), Polezhaev (1988), and Müller (1988).

Buoyancy-driven convection in the melt has been shown to be the dominant factor in the formation of "freckles", a macrosegregation defect deleterious to the mechanical properties of directionally solidified alloys. The formation and characterization of freckles in nickel-based superalloys were first studied experimentally by Giamei and Kear (1970). Poirier *et al.* (1981) investigated macrosegregation in electrosag ingots, showed that convection in the melt results in freckling in the solidified material, and suggested that rotation might reduce freckling. Ridder *et al.* (1981) studied the effects of fluid flow on macrosegregation in nominally axisymmetric ingots and showed that melt convection results in macrosegregation in the mushy zone. In a theoretical study of a binary alloy solidifying radially inward, Maples and Poirier (1984) concluded that macrosegregation results from natural convection in the mushy zone driven by nonuniform temperature and solute distributions. A recent review of the effects of buoyancy-driven convection on macrosegregation in binary and quasi-binary nonmetallic systems has been given by Müller (1988).

One means by which the onset of convection can be inhibited in a density-stratified fluid layer is to subject the layer to a magnetic field aligned parallel or perpendicular to the stratification (Müller 1988). For horizontal Pb-Sn layers solidified from below at several growth velocities, Coriell *et al.* (1980) showed theoretically that the critical Sn concentration above which instability occurs can be increased an order of magnitude by applying a vertical magnetic field of the order of one tesla. This technique requires that the liquid be an electrical conductor, and so is applicable to metallic alloys, semiconductors, and aqueous solutions.

Macrosegregation might also be controlled by increasing or decreasing the magnitude of the gravitational acceleration or changing its direction. Alexander *et al.* (1989) and Heinrich *et al.*



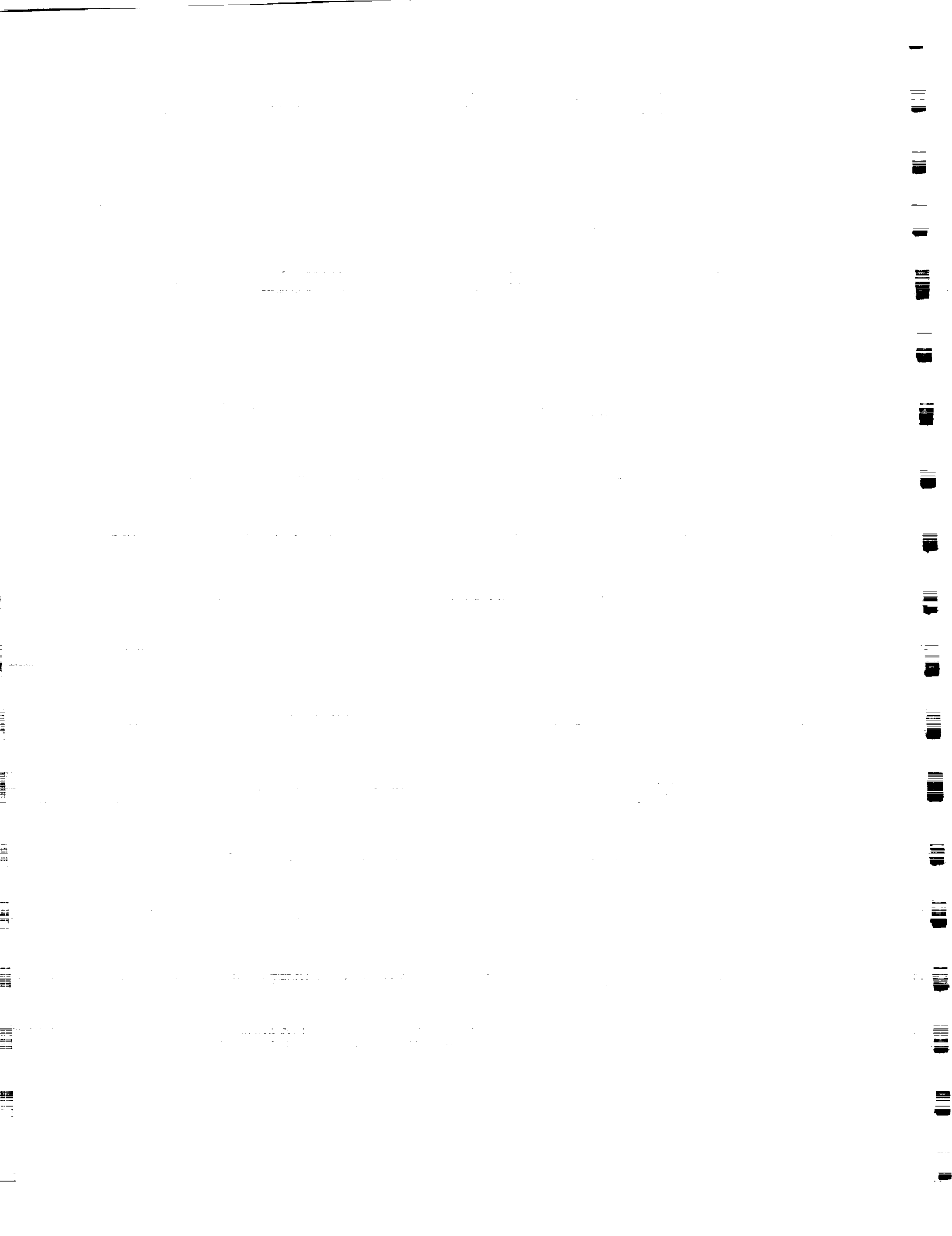
(1989a,b) theoretically studied the effect of reduced gravity on macrosegregation in directionally solidified alloys. These authors suggested that macrosegregation in alloys can be reduced by solidification in a low-gravity environment. Müller (1990) and Weber *et al.* (1990) have recently discussed solidification under conditions where the magnitude of the body force is greater or less than that of normal gravity.

Both gravity and an external magnetic field are body forces which act on the liquid. As opposed to contact forces such as pressure, viscous stress, and surface tension, which act on the surfaces of a fluid element, body forces act on the mass of a fluid element. Hence, their local strengths are proportional to the local fluid density. In addition to gravitational and magnetic body forces, there are other "pseudo-body forces" which manifest themselves as fictitious accelerations (centripetal and Coriolis) when the reference frame to which the fluid motion is referred undergoes steady rotation relative to an inertial frame. (An additional fictitious acceleration, with which we will not be concerned, manifests itself if the rotation of the noninertial frame relative to the inertial frame is unsteady.) Although these accelerations do not correspond directly to forces (as in the case of the gravitational acceleration), they have the same mathematical form as accelerations associated with body forces, and can have dynamical consequences equally as profound as the gravitational and magnetic forces discussed above (Greenspan 1968). In light of this, and the fact that modification of the gravitational field or imposition of an external magnetic field may not always be possible, the possibility of using rotation to suppress the onset of convection in a liquid undergoing directional solidification is of interest.

Several effects of rotation on solidification have been discussed by Schulz-DuBois (1972). The experiments of Kou (1978), Kou *et al.* (1978), Sample and Hellawell (1984), Müller (1990), and Weber *et al.* (1990) have shown that rotation can significantly reduce the degree of macrosegregation in binary alloys directionally solidified under plane-front or dendritic conditions. Kou and Kou *et al.* studied the effect of steady rotation about a vertical axis on freckle formation in Sn-Pb alloys. Sample and Hellawell considered solidification of the transparent alloy  $\text{NH}_4\text{Cl-H}_2\text{O}$  in a crucible rotating about an axis inclined between 0 and 30 degrees with respect to the vertical. Müller (1990) and Weber *et al.* have studied the effect of rotation on the growth of Te-doped InSb crystals, and have shown that striations can be suppressed at sufficiently high rotation rates. These studies show that the degree of macrosegregation (freckles and striations) can be significantly reduced by rotation.

There are two means by which steady rotation about a fixed axis can influence the motion of a fluid. In terms of a reference frame rotating with constant angular velocity  $\Omega$  about an axis, these correspond to the centripetal and Coriolis accelerations, for which the terms  $\rho_L \Omega \times \Omega \times \mathbf{r}$  and  $2\rho_L \Omega \times \mathbf{u}$ , respectively, are added to the momentum equation. Here,  $\mathbf{r}$  is the position vector measured from the axis of rotation,  $\mathbf{u}$  is the local fluid velocity relative to the noninertial reference frame, and  $\rho_L$  is the local density of the liquid.

Previous theoretical studies of the effects of rotation on the onset of buoyancy-driven convection have been restricted to cases where no solidification occurs. For a horizontally unbounded layer of a single-component fluid, Chandrasekhar (1961), Chandrasekhar and Elbert (1955), and Niiler and Bisshopp (1965) have shown that steady uniform rotation about a vertical axis can significantly inhibit the onset of convection, with the Coriolis-related Taylor-Proudman mechanism (1961) playing the dominant role. The effects of centripetal, Coriolis, and gravitational accelerations on convection in horizontally confined rotating fluids in cylindrical containers of various aspect ratios was considered in an early series of papers by Homsy and Hudson (1969, 1971a-c, 1972). More recently, for a single-component fluid Weber *et al.* (1990) have computed buoyancy-driven flows equivalent to those which can be driven by a temperature gradient maintained between the ends of an otherwise insulated right circular cylinder rotating at constant angular velocity about an axis perpendicular to and intersecting the cylinder axis but not passing through the cylinder. Three-dimensional computations, in which the variation of the magnitude of the centripetal acceleration  $\Omega \times \Omega \times \mathbf{r}$  along the cylinder axis was neglected (a good approximation when the cylinder length is small compared to the shortest distance between the axis of rotation and the cylinder), were performed with the term accounting for the Coriolis acceleration  $2\Omega \times \mathbf{u}$  either



included or omitted. Weber *et al.* found excellent agreement between experiment and computation when the Coriolis acceleration was included.

For a binary fluid, Pearlstein (1981) has shown that the Coriolis acceleration can either stabilize or destabilize a horizontally unbounded layer, depending on the values of the Prandtl and Schmidt numbers, the dimensionless rotation rate (expressed in terms of a Taylor number), and the dimensionless temperature or solute gradient (expressed in terms of thermal and solutal Rayleigh numbers). Other work concerning the effect of rotation on doubly-diffusive convection in binary fluids (with no phase change) has been reported by Sengupta and Gupta (1971), Masuda (1978), Antoranz and Velarde (1978, 1979), Schmitt and Lambert (1979), Riahi (1983), Worthem *et al.* (1983), and Bhattacharjee (1988a-c).

Even though our analysis is limited to horizontally unbounded layers, work for single-component fluids not undergoing phase change (Homsy and Hudson 1971a; Bühler and Oertel 1982) suggests that for fixed finite aspect ratios (ratio of mold radius to height) our predictions will be qualitatively correct if  $\Omega_0 R_0 / g$  (a Froude number, where  $R_0$  is the mold radius) is sufficiently small. For the onset of thermal convection in rotating water or mercury layers heated from below, the excellent qualitative agreement between linear stability theory for a horizontally unbounded layer (Chandrasekhar 1953; Chandrasekhar and Elbert 1955; Nakagawa and Frenzen 1955) and experimental work for finite aspect ratios (Nakagawa and Frenzen 1955; Fultz and Nakagawa 1955; Goroff 1960) clearly demonstrates the potential of the Coriolis acceleration to suppress buoyancy-driven convection in a rotating fluid.

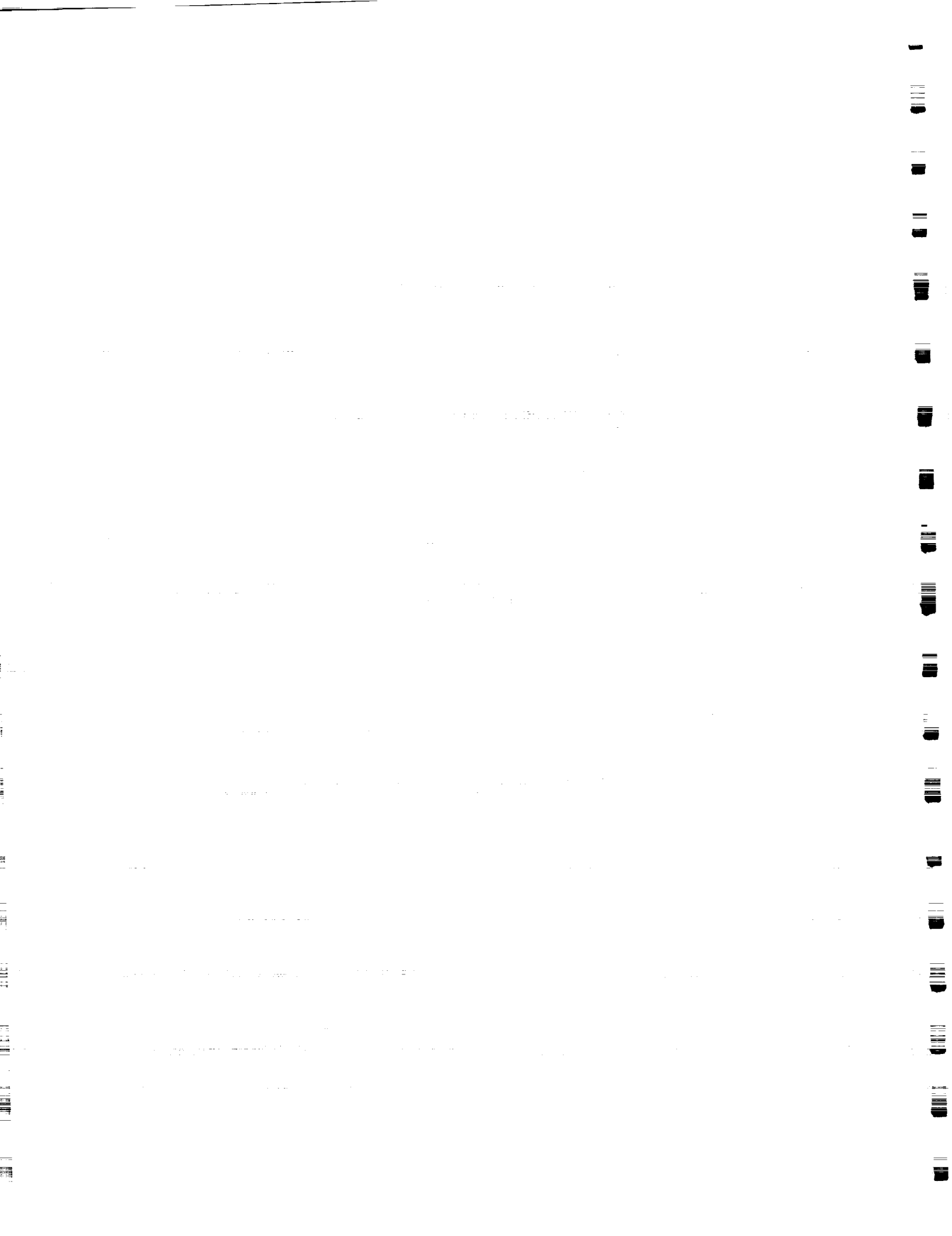
In this work, we use linear stability analysis to study the effect of the Coriolis acceleration on convective and morphological instability for alloys which solidify with a nominally planar interface. This work serves to identify the mechanism by which Coriolis effects affect the onset of convection in solidifying binary alloys. The analysis is illustrated by results for the Pb-Sn system undergoing both plane-front and dendritic solidification, as well as for mercury cadmium telluride undergoing plane-front solidification. The details of the analysis, and plots showing results are shown in the 1992 University of Illinois Ph.D. Dissertation of Alparslan Öztekin (currently at the MIT Department of Chemical Engineering), in a paper co-authored with Dr. Öztekin (*Metallurgical Transactions* 23B, 73-80, 1992), and in preprints of two papers submitted to *Journal of Crystal Growth*, copies of which are included in this report. Other papers are in preparation, and will be submitted in due course.

## 2. Effect of Rotation on Plane-front Solidification of Pb-Sn

Earlier work by Coriell *et al.* (1980) established that plane-front solidification of Pb-Sn alloys can become unstable with respect to either a buoyancy-driven convective mode or a morphological mode. We have considered the effect of rotation on the onset of instability in this system.

To test our code, we first considered the nonrotating case, and compared our results to those of Coriell *et al.* The neutral curves were generally similar to those shown by Coriell *et al.* The only qualitative difference was that, in our work, several new oscillatory neutral curves were found to branch from steady neutral curves found by Coriell *et al.* and in the present work. We believe that our detection of these additional oscillatory neutral curves (which in each case lie well above the critical value of  $c_\infty$  and are hence of no practical consequence) is due to use of a numerical technique which simultaneously computes a large number of temporal eigenvalues at each combination of  $c_\infty$  and  $V_1$ , as opposed to the shooting technique of Coriell *et al.*, which individually computes the temporal eigenvalues by a one-point iteration scheme.

Our results are described in a paper in *Metallurgical Transactions* (23B, 73-80, 1992). We present our principal results in terms of stability boundaries in the  $V_1$ - $c_\infty$  plane, where  $V_1$  is the growth rate and  $c_\infty$  is the bulk concentration of tin. The critical value of  $c_\infty$  (below which the plane-front solution is stable) on the convective branch is an increasing function of the rotation rate  $\Omega_0$  at any value of  $V_1$ , clearly indicating the inhibitory effect of rotation on the onset of buoyancy-driven convection. We note that for  $V_1 = 5 \mu \text{ sec}^{-1}$ , rotation at  $\Omega_0 = 500 \text{ rpm}$  increases by slightly more than two orders of magnitude relative to the nonrotating case the critical Sn concentration above which the plane-front solution becomes unstable. We further note that the morphological branch is





unaffected by rotation, whereas as  $\Omega_0$  increases, the value of  $V_I$  at which the onset of instability shifts from the convective branch to the morphological branch decreases from about  $40 \mu \text{ sec}^{-1}$  in the nonrotating case to about  $27 \mu \text{ sec}^{-1}$  for  $\Omega_0 = 500 \text{ rpm}$ .

For each value of  $\Omega_0$ , we see a local minimum near  $V_I = 1 \mu \text{ sec}^{-1}$ , with the minimum shifting to smaller growth velocities and becoming relatively more shallow as  $\Omega_0$  increases. We note that the maximum relative stabilization by rotation occurs near the local minimum, and that for  $\Omega_0 = 500 \text{ rpm}$ , the critical bulk concentration of Sn is increased more than a hundredfold. Although Coriell *et al.* (1980) noted a local minimum in the stability boundary near  $V_I = 1 \mu \text{ sec}^{-1}$  in the nonrotating case for the largest gravitational acceleration considered, they offered no explanation for its existence. This minimum is a consequence of the fact that as  $V_I \rightarrow 0$ , the concentration gradient  $G_C = (k-1)\rho_S c_\infty V_I / (k\rho_L D)$  vanishes. As the temperature gradient is independent of  $c_\infty$  and is stabilizing, the critical value of  $c_\infty$  must ultimately increase as  $V_I \rightarrow 0$ . (Of course, the weight percent of the solute,  $c_\infty$ , cannot exceed 100). As  $c_\infty^*$  must initially decrease with increasing  $V_I$ , there must be a local minimum on the convective branch before  $c_\infty^*$  can increase to join up with the morphological branch of the stability boundary. This nonmonotonic dependence of  $c_\infty^*$  on  $V_I$  can be interpreted in terms of the existence of four critical values of  $V_I$  for certain values of  $c_\infty$ . (We note that for sufficiently large  $V_I$ ,  $c_\infty^*$  ultimately increases on the morphological branch (Davis 1990).

The remarkable stabilization obtainable at low growth rates (more than a hundredfold increase in the critical value of  $c_\infty$  at  $V_I = 1 \mu \text{ sec}^{-1}$  can be achieved by rotating the layer at 500 rpm for the two values of  $G_L$  considered) is undoubtedly due to the well-known Taylor-Proudman mechanism, described by Chandrasekhar (1961). According to the Taylor-Proudman theorem, steady motion parallel to the axis of rotation in a uniformly rotating inviscid fluid is prohibited at any nonzero rotation rate. If this theorem were strictly applicable to a viscous fluid, the onset of steady convection would be prohibited, since the flow in convection cells must have a vertical component. Instead, in a viscous fluid, one sees an inhibition of the onset of steady convection, with the degree of inhibition (expressed here as an increase in  $c_\infty$ ) increasing with  $\Omega_0$ . That the onset of oscillatory convection is hardly affected is due to the fact that the Taylor-Proudman theorem applies only to steady flows. It is also not surprising that the morphological instability is unaffected by rotation. The morphological instability occurs at very short wavelengths, so the motion is almost perpendicular to the solidification front (i.e., aligned with the axis of rotation). Hence, the Coriolis acceleration does not sensibly affect the morphological instability.

The relatively modest rotation rates required to significantly inhibit the onset of convection in the Pb-Sn system make the proposed method an interesting candidate for a program of laboratory experiments. Experiments might be conducted using a completely filled cylindrical mold, thermally insulated on the vertical surface, and mounted axisymmetrically on a rotating horizontal turntable. If the liquid at the top of the rotating mold is in contact with a gas or vacuum, it will have a nearly paraboloidal free surface, on which the elevation above the point on the axis of rotation is  $\Delta z = \Omega_0^2 r^2 / (2g)$ . Although this configuration is consistent with rigid-body rotation, it also leads to a nearly paraboloidal solid-melt interface. For high rotation rates or large mold radius, this will in turn lead to significant radial variations in the solidified alloy. Also, cooling at the radial boundary leads to a radial temperature gradient, which in turn leads to significant centrifugal effects. Experiments of the type proposed above were initiated some time ago by Copley (private communication) for the crystallization of ammonium chloride from aqueous solution.

Finally, we note that for many binary systems, plane-front solidification does not occur at practical growth velocities, and that the morphological instability results in dendritic solidification. In this case, rotation might also suppress buoyancy-driven convection in the melt and interdendritic liquid; this is discussed in §6.



### 3. Combined Effects of Rotation and Reduced Gravity on Stability of Plane-Front Solidification of Pb-Sn

The combined effects of rotation and reduced gravity on the stability of plane-front solidification were studied for dilute Pb-Sn alloys. The onset of buoyancy-driven convection is suppressed to a far greater degree than would be expected on the basis of earlier work, in which suppression by the individual effects of reduced gravity (Coriell *et al.* 1980) and uniform rotation (Öztek and Pearlstein 1992) was demonstrated.

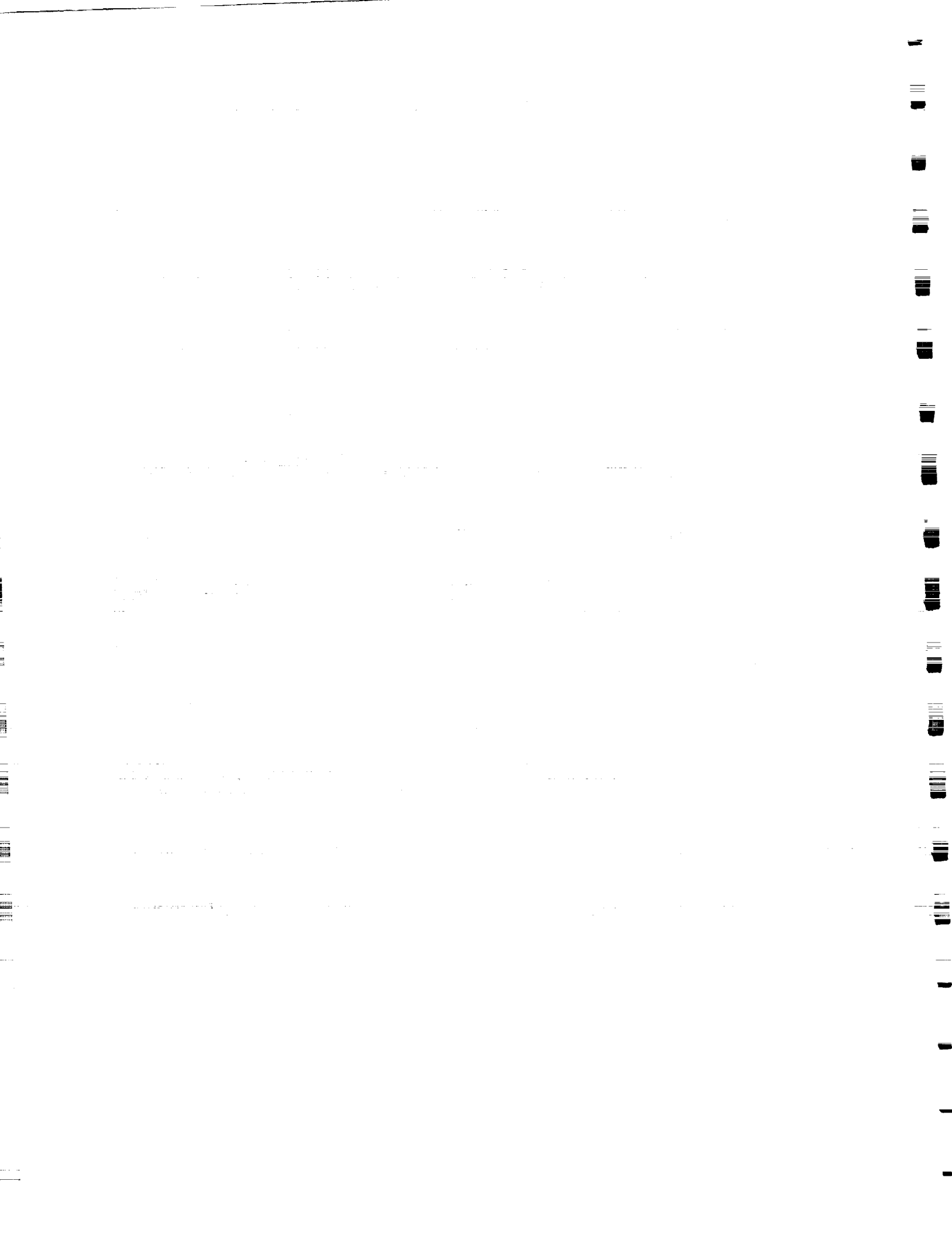
Our results are presented in terms of the effects of rotation and reduced gravity on the onset of convection in molten Pb-Sn undergoing solidification by cooling from below. The individual effects of reduced gravity have been considered by Coriell *et al.* (1980), who showed for several combinations of the liquid-side temperature gradient  $G_L$  and gravity level  $0 < \zeta = g/g_0 < 1$  that the stability boundary in the  $V_1$ - $c_\infty^*$  plane consists of morphological and convective branches, and that the convective branch is stabilized by reducing  $\zeta$  (i.e., at any  $V_1$ , the critical value of  $c_\infty$  on the convective branch increases as  $\zeta$  decreases). Öztek and Pearlstein (1992) showed for  $\zeta = 1$  (full gravity) with  $G_L = 200 \text{ K cm}^{-1}$  and  $\Omega_0 = 0, 100, 200, 300$ , and  $500 \text{ rpm}$  (their Figure 1) that rotation stabilizes the convective branch (i.e., for any  $V_1$ , the critical value of  $c_\infty$  on the convective branch increases with  $\Omega_0$ ). For example, with  $V_1 = 5 \mu \text{ sec}^{-1}$ , the critical Sn concentration above which plane-front solidification is unstable is more than two orders of magnitude higher at  $\Omega_0 = 500 \text{ rpm}$  than in the nonrotating case. They also showed that the morphological branch was unaffected by rotation, and that as  $\Omega_0$  increases, the value of  $V_1$  at which the onset of instability shifts from the convective branch to the morphological branch decreases from about  $40 \mu \text{ sec}^{-1}$  in the nonrotating case to about  $27 \mu \text{ sec}^{-1}$  for  $\Omega_0 = 500 \text{ rpm}$ .

For  $G_L = 200 \text{ K cm}^{-1}$  and  $\Omega_0 = 0$ , we find that stability boundaries for  $\zeta = 1, 10^{-2}, 10^{-4}$ , and  $10^{-6}$ , each consist of some portion of the morphological branch ( $c_\infty^*$  decreasing with increasing  $V_1$ ) joined to a convective branch. The critical value on the convective branch increases with decreasing  $\zeta$ , showing the inhibitory effects of reduced gravity on the onset of buoyancy-driven convection. Note that for  $V_1 = 1 \mu \text{ sec}^{-1}$ , reducing the gravity level to  $10^{-6}g_e$  increases the critical Sn concentration at which plane-front solidification becomes unstable by about four orders of magnitude relative to the full gravity case. We also note that the stabilizing effect of reduced gravity is relatively less at lower solidification rates than at higher solidification rate. As expected, the morphological instability branch is not affected by the gravity level, whereas as  $\zeta$  decreases, the value of  $V_1$  at which the onset of instability shifts from the convective to the morphological branch decreases from about  $40 \mu \text{ sec}^{-1}$  for  $\zeta = 1$  to about  $1.3 \mu \text{ sec}^{-1}$  for  $\zeta = 10^{-6}$ .

For the same liquid-side temperature gradient ( $G_L = 200 \text{ K cm}^{-1}$ ), we find that for small rotation rates ( $\Omega_0 = 5 \text{ rpm}$ ) the degree of stabilization achievable at each gravity level is considerably larger than the sum of the individual effects of rotation and reduced gravity. As in the full gravity case, the critical Sn concentration is increased more at lower solidification rates than at higher solidification rates. For  $\zeta = 10^{-2}$  and  $\Omega_0 = 5 \text{ rpm}$ , the critical concentration is increased by about an order of magnitude for  $V_1 = 0.5 \mu \text{ sec}^{-1}$ , however, the inhibition of convection for  $V_1 = 0.5 \mu \text{ sec}^{-1}$  is very small. In contrast to the rotating case, the inhibition of the onset of convection by reduced gravity is larger at higher rotation rate. Hence the decrease of the solidification rate at which the onset of instability shifts from convective branch to the morphological branch by reduced gravity is considerably more than the decrease by the rotation. For  $\zeta = 10^{-2}$  and  $\Omega_0 = 25 \text{ rpm}$ , the critical Sn concentration on the convective branch is more than three orders of magnitude higher than for the nonrotating normal-gravity case at all solidification rates.

For  $G_L = 200 \text{ K cm}^{-1}$ , stability boundaries for  $\zeta = 1$  and  $\Omega_0 = 0$ ,  $\zeta = 1$  and  $\Omega_0 = 5 \text{ rpm}$ ,  $\zeta = 10^{-4}$  and  $\Omega_0 = 0$ , and  $\zeta = 10^{-4}$  and  $\Omega_0 = 5 \text{ rpm}$  show that rotation more effectively inhibits the onset of convection in the reduced gravity case than in the full gravity case.

The remarkable stabilization obtainable at low growth rates (more than a hundredfold increase in the critical value of  $c_\infty$  at  $V_1 = 1 \mu \text{ sec}^{-1}$  can be achieved by rotating the layer at  $500 \text{ rpm}$  for the two values of  $G_L$  considered) is again undoubtedly due to the well-known Taylor-Proudman mechanism



#### 4. Stability of Plane-Front Solidification of $\text{Hg}_{1-x}\text{Cd}_x\text{Te}$

In a binary (i.e., two-component) liquid for which the density does not depend monotonically on temperature (e.g., has a local maximum) for some range of composition, we consider the stability of plane-front solidification when the liquid is cooled from below. In contrast to the normal case where the density depends monotonically on temperature and composition (e.g., the Pb-Sn alloys considered by Coriell *et al.* (1980)), for certain combinations of the operating parameters (solidification rate, nominal liquid-side vertical temperature gradient, and bulk solute concentration) there can exist a critical value of the bulk mole fraction ( $C_\infty$ ) below which plane-front solidification is unstable at all dimensionless solidification rates  $\gamma$ , whereas in the normal case plane-front solidification at any  $C_\infty$  is linearly stable for all sufficiently small solidification rates. Moreover, when the density varies nonmonotonically with temperature, there can exist a critical value of the dimensionless solidification rate  $\gamma_c$  such that for  $\gamma > \gamma_c$  plane-front solidification is unstable for all  $C_\infty$ . In this case, for  $\gamma < \gamma_c$  there is a finite range of  $C_\infty$  for which plane-front solidification is stable. This latter result differs from the normal case, for which at all dimensionless solidification rates, plane-front solidification is stable for all values of  $C_\infty$  lying below some critical value. The stability boundaries and neutral curves, differing qualitatively from those for the normal case, are discussed in terms of the existence adjacent to the liquid-solid interface of a sublayer in which the thermal stratification is destabilizing. Results are presented for solutions of CdTe in HgTe, of considerable importance due to the wide use of this pseudobinary system in the fabrication of electro-optic detectors.

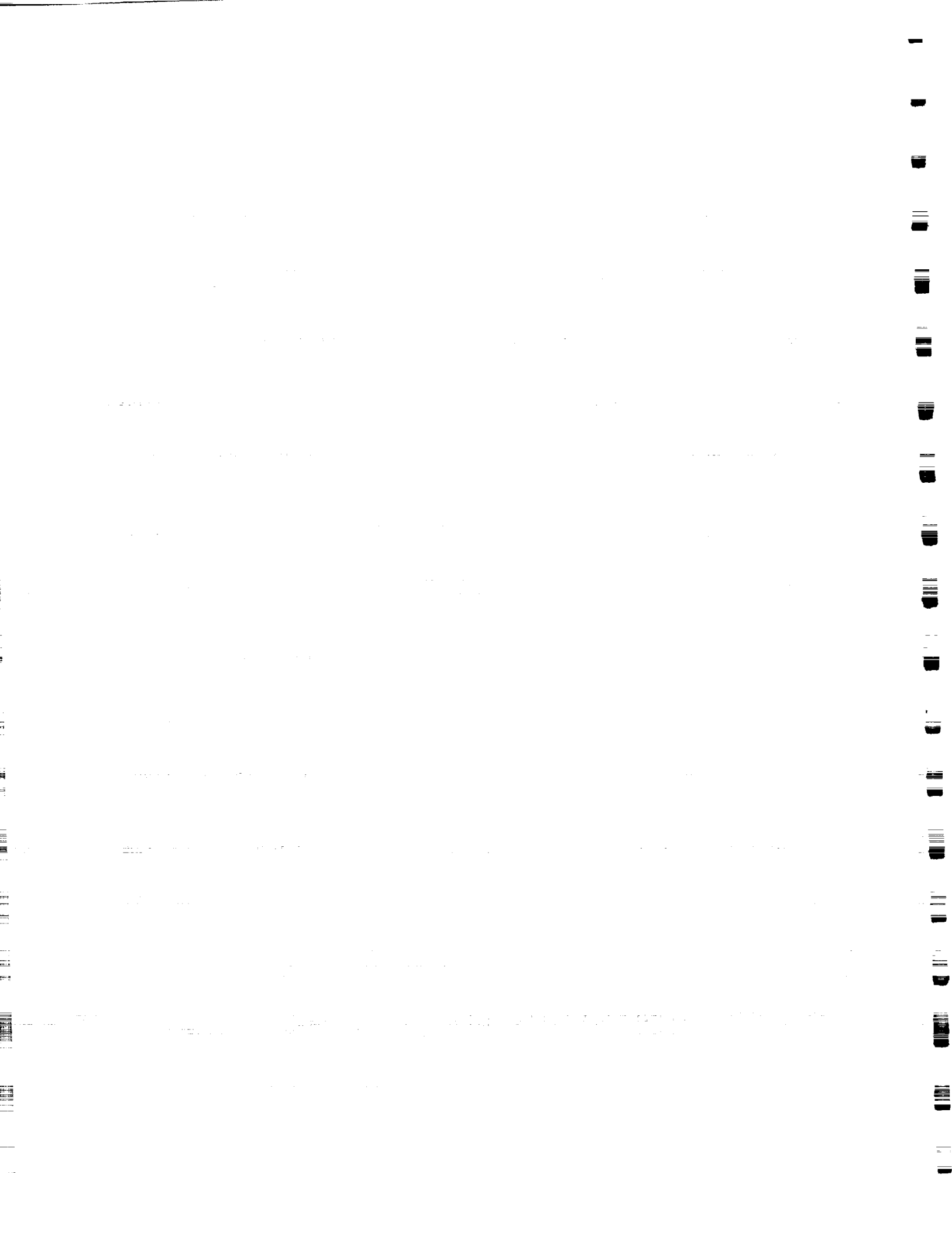
We have computed stability boundaries in the  $\gamma$ - $C_\infty$  plane for four values of the dimensionless liquid-side temperature gradient  $\Gamma = G_L k_{L0} / [L_0 (g D_L)^{1/3}]$ . The stability boundary consists of some portion of the morphological branch joined to a convective branch. For  $\Gamma = 8.2 \times 10^{-4}$ , above the morphological branch disturbances grow in some wavenumber range and the plane-front solution is unstable. Similarly, disturbances grow below the convective branch for some range of  $a$ . On the other hand, below the morphological branch and above the convective branch, disturbances of all wavenumbers decay and plane-front solidification is stable. Beyond the critical solidification rate  $\gamma_c = 2.70 \times 10^{-4}$  ( $V_1 = 1.02 \mu/\text{sec}$ ) at which the convective and morphological branches intersect, there is no stable range of bulk mole fraction  $C_\infty$ . For  $\Gamma = 1.64 \times 10^{-3}$ , the stable region in the  $\gamma$ - $C_\infty$  plane is analogous to that for  $\Gamma = 8.2 \times 10^{-4}$ . The morphological branch has shifted to the right and the convective branch has shifted slightly downward. Their intersection occurs at a higher  $\gamma$  ( $\gamma_c = 5.61 \times 10^{-4}$ ,  $V_1 = 2.12 \mu/\text{sec}$ ), and the stable region is larger. Increasing  $\Gamma$  still more leads to further enlargement of the stable region and larger values of  $\gamma_c$  for  $\Gamma = 3.28 \times 10^{-3}$  and  $6.56 \times 10^{-3}$  ( $G_L = 100$  and  $200 \text{ K/cm}$ ), respectively.

The qualitative differences between these neutral curves and stability boundaries and those characteristic of the normal case in which density varies linearly with temperature and composition (e.g., the Pb-Sn results of Coriell *et al.* 1980) lead us to consider how the equation of state affects or alters the mechanism by which the onset of motion occurs during directional solidification of a binary liquid cooled from below.

We note that the mechanism responsible for the morphological instability is insensitive to the net density stratification in the liquid, and is insensitive to variations of temperature and composition outside a relatively thin layer adjacent to the interface. This is evident from a comparison of the neutral curves and stability boundaries for the present case to those for Pb-Sn (Coriell *et al.* 1980; Öztekin and Pearlstein 1992).

On the other hand, the onset of buoyancy-driven convection depends strongly on the nature of the stabilizing or destabilizing temperature and solute gradients in the liquid, as well as on the diffusivities of the stratifying agencies (Stern 1960; Baines and Gill 1969). The density of a binary liquid solidified by cooling from below can depend nonmonotonically on the vertical coordinate even if the density depends monotonically on temperature and composition.

For binary liquids such as  $\text{Hg}_{1-x}\text{Cd}_x\text{Te}$  for which the dependence of density on temperature or solute mole fraction is not monotonic, solidification by cooling from below for some combinations of the bulk mole fraction, liquid-side temperature gradient, and solidification rate can lead to a configuration in which there exists adjacent to the interface a sublayer in which the positive



temperature and solute gradients are destabilizing and stabilizing, respectively. If a liquid parcel in this sublayer is displaced downward, it will lose its excess heat more rapidly than its excess CdTe mole fraction, again because the thermal diffusivity is much larger than the solute diffusivity. Its CdTe mole fraction will thus exceed that of the surroundings, and so the parcel will be less dense than the surrounding liquid. The resulting buoyancy force will tend to move the parcel vertically upward. Hence, the initial displacement engenders a restoring force, which can result in overshoot of the parcel's initial (equilibrium) position. Such a configuration is in the "diffusive" regime, and the motion is said to be "overstable", with the temporally growing oscillatory parcel displacements leading to the oscillatory onset of convection.

The difference between the mechanisms by which the onset of motion occurs in configurations in which the temperature gradient is everywhere stabilizing, and in those in which temperature is destabilizing in a sublayer adjacent to the interface, is manifested in qualitative differences between the neutral curves, and hence the stability boundaries, for the Pb-Sn and  $\text{Hg}_{1-x}\text{Cd}_x\text{Te}$  systems.

The most notable feature of the neutral curves in the present case is that the onset of buoyancy-driven convective instability is associated with an oscillatory mode, unlike the normal (e.g., Pb-Sn) case. Moreover, for each wavenumber for which it exists, the corresponding oscillatory neutral curve bounds the range of stable  $C_\infty$  from below, rather than from above as in the normal case. As the extremal values of  $C_\infty$  on the morphological and oscillatory convective neutral curves approach, the range of bulk mole fractions for which plane-front solidification is stable disappears. This contrasts to the normal case, in which plane-front solidification is always stable for sufficiently dilute solutions (i.e.,  $C_\infty$  lying below the minima of the morphological and steady convective neutral curves).

These features of the neutral curves have profound consequences for the stability boundaries in the  $\gamma$ - $C_\infty$  plane. For  $\text{Hg}_{1-x}\text{Cd}_x\text{Te}$ , plane-front solidification can be unstable at all solidification rates if the bulk mole fraction is chosen sufficiently low, as shown in §5. This is because the effect of a destabilizing temperature gradient in the sublayer adjacent to the interface becomes stronger as the bulk mole fraction decreases (due to a more prominent density maximum as the composition approaches pure HgTe), and the stabilizing effect of the solute gradient diminishes (because it is proportional to  $C_\infty$ ). On the other hand, in Pb-Sn directionally solidified by cooling from below, plane-front solidification is stable for any solidification rate and liquid-side temperature gradient if the solute bulk mole fraction is sufficiently low (Coriell *et al.* 1980; Öztekin and Pearlstein 1992).

For  $\text{Hg}_{1-x}\text{Cd}_x\text{Te}$ , plane-front solidification can be unstable at all values of the bulk mole fraction (less than  $C_\infty = 0.2$ ) if the solidification rate exceeds a critical value  $\gamma_c$ . For sufficiently small values of  $C_\infty$ , plane-front solidification is unstable with respect to the onset of overstable buoyancy-driven convection, because the stabilizing influence of the bottom-heavy solute stratification is insufficiently strong to overcome the destabilizing temperature gradient in the sublayer adjacent to the interface. For sufficiently large values of  $C_\infty$ , the configuration is unstable with respect to the morphological instability. As  $\gamma$  approaches  $\gamma_c$  from below, the stable region is "pinched" from below and above until at  $\gamma_c$  it finally disappears. This situation differs from that for Pb-Sn, for which plane-front solidification is stable in a region bounded above by the morphological and convective portions of the stability boundaries.

In a single-component fluid with an unstably stratified layer overlying or underlying a stably stratified region, convective motion is typically localized in the unstably stratified layer, but may penetrate into the adjacent stable region. In his early analysis of the onset of thermal convection in a water layer with the temperature maintained at  $0^\circ\text{C}$  at the bottom and in excess of  $4^\circ\text{C}$  at the top, Veronis (1963) showed that convection occurs in the unstably stratified region and penetrates into the stably stratified region as well. He determined the extent of penetration for different ratios of the stably stratified layer thickness to the total layer thickness. He also found that convection in the stably stratified region is viscously coupled to the more vigorous motion in the unstable layer. Walton (1982) and Zangrando and Bertram (1985) have considered a doubly-diffusive fluid layer with a uniform vertical temperature gradient and a nonuniform vertical solute gradient. Both of these studies show the disturbances to be localized about the neighborhood of the critical depth at which the salinity gradient reaches its minimum value. In our work, when the liquid-solid





interface is adjacent to a sublayer in which the temperature gradient is destabilizing, the disturbances associated with the oscillatory onset of buoyancy-driven convection are largely confined to that thermally unstably stratified sublayer.

As discussed above, the oscillatory onset of buoyancy-driven convection and the localization of the disturbances are associated with the occurrence of a sublayer in which the temperature gradient is destabilizing. Hence, the results should be expected to apply qualitatively to the solidification of other binary or multicomponent liquids in which  $(\partial\rho_L/\partial T)(\partial T_L/\partial z)$  changes sign within the layer.

Our results demonstrate that nonmonotonic variation of density with temperature can have dramatic qualitative effects on the onset of instability in an unbounded horizontal fluid layer undergoing plane-front solidification. The existence of a sublayer in which the thermal stratification is destabilizing should also have important consequences for the convection which occurs in vertical Bridgman growth in ampoules of finite radius, as well as in zone melting and other processes used to grow  $\text{Hg}_{1-x}\text{Cd}_x\text{Te}$  crystals from the melt. To date, however, these effects have not been observed in simulations of buoyancy-driven convection in  $\text{Hg}_{1-x}\text{Cd}_x\text{Te}$  for these geometries, which have used equations of state that do not properly account for the nonmonotonic dependence of density on temperature. The axisymmetric simulations of vertical Bridgman growth by Kim and Brown (1989) employ a linear equation of state of the form (1), even though the CdTe mole fraction in the liquid near the interface is about 0.075 in each computation and the density is known to depend nonmonotonically on temperature for CdTe mole fractions up to at least 0.1. The computations of Apanovich and Ljumkis (1991) for zone melting of  $\text{Hg}_{1-x}\text{Cd}_x\text{Te}$  use an equation of state in which the density of  $\text{Hg}_{1-x}\text{Cd}_x\text{Te}$  is independent of temperature for a CdTe mole fraction of 0.13.

## 5. Effects of Rotation on Stability of Plane-Front Solidification of $\text{Hg}_{1-x}\text{Cd}_x\text{Te}$

A linear stability analysis was used to assess the potential of steady uniform rotation about the vertical axis to suppress the onset of convection during directional solidification of mercury cadmium telluride cooled from below. Since for sufficiently small  $x$  the density of  $\text{Hg}_{1-x}\text{Cd}_x\text{Te}$  does not depend monotonically on temperature, there is a range of operating conditions (bulk CdTe mole fraction, nominal solidification rate, and liquid-side temperature gradient) for which, adjacent to the liquid-solid interface there is a sublayer in which the thermal stratification is destabilizing. This differs from the normal case (i.e., binary alloys characterized by a linear equation of state, such as Pb-Sn), in which the thermal stratification is stabilizing everywhere. Thus, in  $\text{Hg}_{1-x}\text{Cd}_x\text{Te}$  melts there can exist a critical bulk CdTe mole fraction  $x_\infty$  below which plane-front solidification is unstable at all solidification rates  $V_I$ , whereas in the normal case plane-front solidification at any  $x_\infty$  is linearly stable for sufficiently small  $V_I$ . Moreover, for  $\text{Hg}_{1-x}\text{Cd}_x\text{Te}$  there can exist a critical solidification rate  $V_I^{\text{cr}}$  such that for  $V_I < V_I^{\text{cr}}$  plane-front solidification is unstable for all  $x_\infty$ . Our results show that modest rates of uniform rotation can significantly suppress the onset of buoyancy-driven convection for the  $\text{Hg}_{1-x}\text{Cd}_x\text{Te}$  system, and that rotation can substantially increase the critical solidification rate  $V_I^{\text{cr}}$  beyond which plane-front solidification is unstable for all bulk CdTe mole fractions.

The stability boundaries consist of some portion of the morphological branch joined to an oscillatory convective branch. For  $G_L = 50 \text{ K cm}^{-1}$ , the stability boundaries for  $\Omega_0 = 0, 25, 50$ , and 100 rpm show that above the morphological branch, disturbances grow for some range of wavenumber  $a$  and plane-front solidification is unstable. Similarly, below the convective branch appropriate to each rotation rate shown, disturbances grow for some range of  $a$ . However, between the morphological branch and the convective branch associated with each rotation rate (i.e., for  $x_\infty^* < x_\infty < x_\infty^{**}$ ), disturbances decay for all wavenumbers and plane-front solidification is stable. Note that the morphological branch is unaffected by rotation, whereas as  $\Omega_0$  increases, the convective branch is shifted downward. The critical bulk CdTe mole fraction  $x_\infty^{**}$  on the convective branch is a decreasing function of  $\Omega_0$  at any solidification rate, clearly indicating the inhibitory effect of rotation on the onset of buoyancy-driven convection. Beyond the critical



solidification rate (denoted by  $V_I^{cr}$ ) at which the convective and morphological branches intersect, there is no stable range of bulk CdTe mole fraction  $x_\infty$ . Thus, plane-front solidification is unstable at all bulk CdTe mole fractions for sufficiently high solidification rates. The critical solidification rate  $V_I^{cr}$  at which the morphological and convective branches intersect occurs at higher  $x_\infty$  with increasing rotation rate  $\Omega_o$ . The critical value  $V_I^{cr}$  is increased by more than a factor of ten at  $\Omega_o = 100$  rpm relative to the nonrotating case. We also note that the convective branch has a relatively shallow local minimum near  $V_I = 1 \mu\text{sec}^{-1}$ , the location of which depends only weakly on  $\Omega_o$ . Thus, for a given rotation rate, operation at the solidification rate corresponding to this local minimum allows plane-front solidification to be conducted stably at the lowest value of  $x_\infty$ .

For  $G_L = 25 \text{ K cm}^{-1}$  and  $\Omega_o = 0$  and 100 rpm, the morphological branch is shifted to the left, reducing the range of solidification rates and bulk mole fractions for which plane-front solidification is stable, as expected on the basis of the results of Coriell *et al.* (1980) for Pb-Sn without rotation. On the other hand, the convective branch is shifted downwards relative to the  $G_L = 50 \text{ K cm}^{-1}$  case, corresponding to an increase in the range of stable operating conditions. We note that decreasing the temperature gradient has very little effect on the onset of convection in a nonrotating layer, but reduces the range of stable bulk CdTe mole fractions by more than twofold for a layer rotating at 100 rpm. The critical value of  $V_I$  is higher by more than a factor of five at  $\Omega_o = 100$  rpm relative to the nonrotating case, although the degree of stabilization is less than the factor of ten predicted for  $G_L = 25 \text{ K cm}^{-1}$ . Although the reduction in  $x_\infty$  has very little effect on the critical value of  $V_I$  at which the morphological and convective stability boundaries intersect in the nonrotating case, for  $\Omega_o = 100$  rpm the critical value of  $V_I$  decreases by a factor of three when the temperature gradient is reduced.

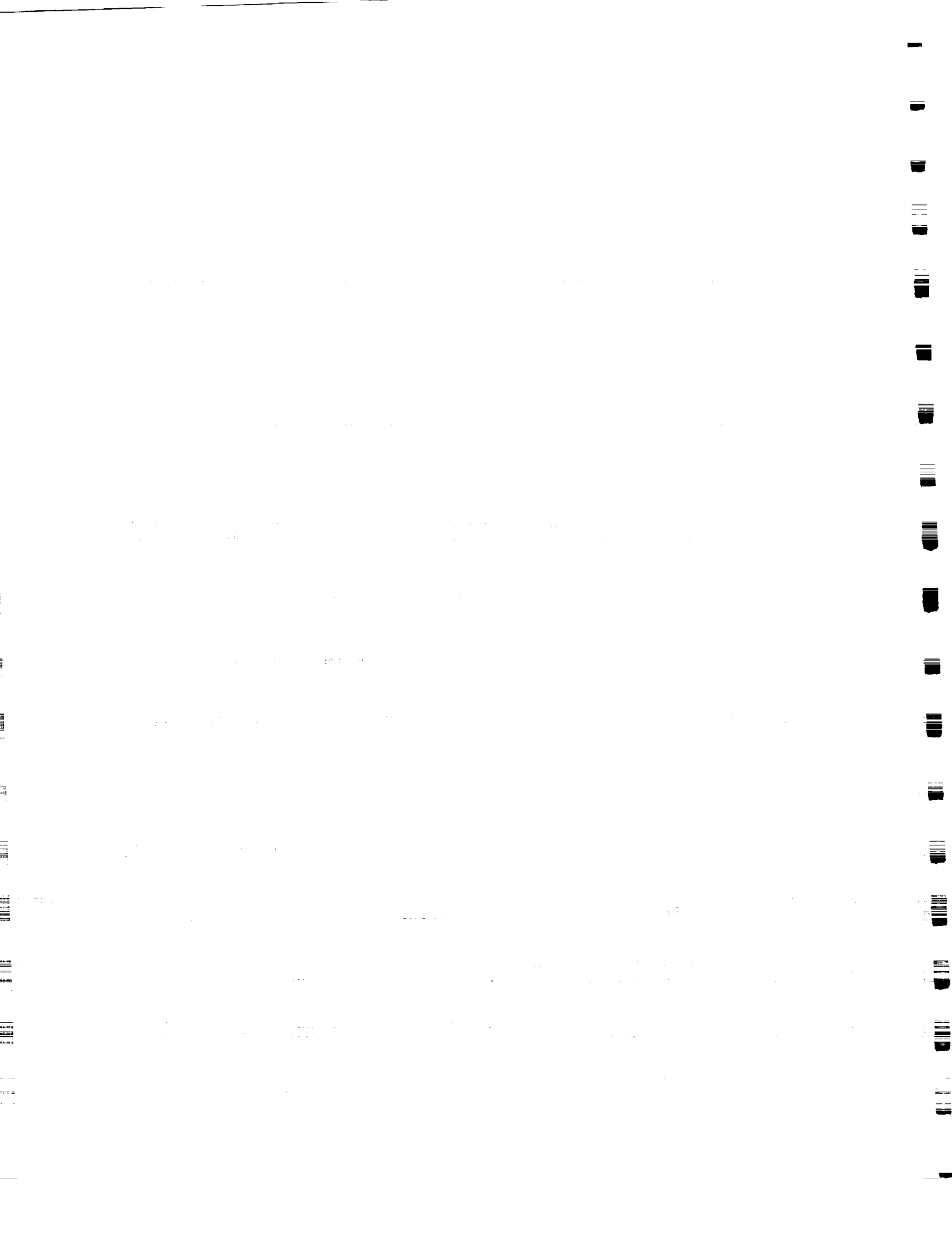
As discussed for the Pb-Sn case (Öztekin and Pearlstein 1992), at each value of  $\Omega_o$  the onset of morphological instability occurs via a short wavelength (large wavenumber) instability, while convection sets in via disturbances with relatively longer wavelengths. In the following section this point is discussed in the context of the mechanism by which rotation inhibits the onset of convection.

During directional solidification of binary alloys cooled from below and characterized by a linear equation of state, with rejection of a light solute at the liquid-solid interface (e.g., Pb-Sn), the vertical temperature and solute gradients are stabilizing and destabilizing, respectively, throughout the liquid layer. In the Pb-Sn system, the onset of buoyancy-driven convection occurs via monotonically growing disturbances, as shown by Coriell *et al.* (1980). However, for the pseudobinary  $\text{Hg}_{1-x}\text{Cd}_x\text{Te}$  system, the CdTe gradient is everywhere stabilizing, and adjacent to the liquid-solid interface there can exist a sublayer in which the thermal stratification is destabilizing. In this system, the onset of convection occurs via oscillatory disturbances. We note that the system is unstable at the indicated values of  $G_L$  for all  $V_I$  when  $x_\infty$  is sufficiently small, corresponding to the absence of a stably stratified thin liquid layer adjacent to the interface for small  $x_\infty$ .

For Pb-Sn alloys we have shown (Öztekin and Pearlstein 1992) that significant suppression of the onset of buoyancy-driven convection occurs at modest rotation rates, and is due to the well-known Taylor-Proudman mechanism. Again, the morphological instability is unaffected by rotation since it occurs at very short wavelengths, with the motion nearly perpendicular to the solidification front (i.e., aligned with the rotation axis).

## 6. Effect of Rotation on Stability of Dendritic Solidification of Pb-Sn

We have assessed the stability of the one-dimensional dendritic solution for Pb-Sn melts undergoing solidification by cooling from below. The two-phase mushy zone is modeled as a porous medium with anisotropic permeability. The local porosity, as well as the locations of the boundaries separating the solid from the mushy zone and the mushy zone from the liquid, are taken to be dynamical variables. The one-dimensional basic state, computed using a thermodynamically self-consistent nonlinear model of solidification, exists for only some combinations of the operating parameters (solidification rate, nominal liquid-side vertical temperature gradient, and bulk



solute concentration). A division of the parameter space according to the existence and stability of solutions corresponding to plane-front and dendritic solidification is presented and discussed for the Pb-Sn system. Under some conditions the dendritic solution exists when plane-front solidification is linearly stable with respect to morphological disturbances. This point is discussed in light of previous work on nonlinear morphological stability. For a given liquid-side temperature gradient, the dendritic solution is unstable below a critical solidification rate, nearly independent of composition. As the imposed temperature gradient decreases, the critical solidification rate decreases, and the dendritic solution is stabilized.

The thermophysical properties of the liquid and solid phases are as used by Coriell *et al.* (1980) at reference conditions corresponding to pure lead at its melting point. (The diffusivity of Sn in Pb used corresponds to an infinitely dilute solution.) The two-phase mushy zone is modeled as a porous medium with anisotropic permeability. The local porosity, as well as the locations of the boundaries separating the solid from the mushy zone and the mushy zone from the liquid, are taken to be dynamical variables. The one-dimensional basic state, computed using a thermodynamically self-consistent nonlinear model of solidification, exists for only some combinations of the operating parameters (solidification rate, nominal liquid-side vertical temperature gradient, and bulk solute concentration). A division of the parameter space according to the existence and stability of solutions corresponding to plane-front and dendritic solidification is presented and discussed for the Pb-Sn system. Under some conditions the dendritic solution exists when plane-front solidification is linearly stable with respect to morphological disturbances. This point is discussed in light of previous work on nonlinear morphological stability. For a given liquid-side temperature gradient, the dendritic solution is unstable below a critical solidification rate, nearly independent of composition. As the imposed temperature gradient decreases, the critical solidification rate decreases, and the dendritic solution is stabilized.

For  $C_\infty = 0.2$ ,  $\gamma = 2.59 \times 10^{-2}$ , and  $\Gamma = 7.12 \times 10^{-2}$  (corresponding to dimensionless solidification rate and liquid-side temperature gradient of  $V_1 = 80 \mu \text{ sec}^{-1}$  and  $G_L = 50 \text{ K cm}^{-1}$  for Pb-Sn), the solute profile varies almost linearly in the mushy zone, within which almost all of the solute variation is confined. On the liquid side of the liquid/mushy-zone interface, there is a solutal boundary layer, which is thin compared to the mushy-zone thickness. For the mushy zone the lengthscale is the thickness  $H_m$ , the dimensional value of which is 1.685 cm for this combination of  $G_L$ ,  $V_1$ , and  $C_\infty$ , and for the liquid the lengthscale is the diffusion length, which in this case is  $3.75 \times 10^{-3} \text{ cm}$ .) The volume fraction is largest ( $\phi = 1$ ) at the liquid/mushy-zone interface, and decreases monotonically to a nonzero value at the mushy-zone/solid interface. These results show that as  $C_\infty$  increases, the porosity distribution becomes more linear and its value at the mushy-zone/solid interface increases monotonically. The mushy-zone thickness ( $H_m = 0.527 \text{ cm}$ ) for  $C_\infty = 0.5$  is much smaller (so that the liquid in the porous medium is more mobile) than for  $C_\infty = 0.1$ , 0.2, or 0.35.

For  $\gamma = 3.24 \times 10^{-2}$  ( $V_1 = 100 \mu \text{ sec}^{-1}$ ),  $1.62 \times 10^{-2}$  ( $V_1 = 50 \mu \text{ sec}^{-1}$ ),  $9.72 \times 10^{-3}$  ( $V_1 = 30 \mu \text{ sec}^{-1}$ ), respectively,  $H_m$  is a strong function of  $\Gamma$  and  $C_\infty$ , depends relatively weakly on  $\gamma$ , and assumes a maximum near  $C_\infty = 0.2$  for each combination of solidification rate and temperature gradient. This maximum occurs because the composition difference  $\Delta C_m = C_m(1) - C_m(0)$  between the top and bottom of the mushy zone reaches a maximum near  $C_\infty = 0.2$ , and the mushy-zone composition varies almost linearly with  $z$ . As  $\Delta C_m$  decreases to zero as  $C_\infty$  approaches  $C_E$ ,  $H_m$  asymptotically decreases to zero. The decrease of  $H_m$  as  $C_\infty$  decreases to the left of the maximum  $H_m$  is again due to the fact that  $\Delta C_m$  decreases with decreasing  $C_\infty$ . For  $\Gamma = 7.12 \times 10^{-3}$  ( $G_L = 5 \text{ K cm}^{-1}$ ),  $H_m$  is a decreasing function of  $\gamma$ . For  $\Gamma = 7.12 \times 10^{-2}$  ( $G_L = 50 \text{ K cm}^{-1}$ ), the variation of  $H_m$  with  $\gamma$  is much weaker, and for  $\Gamma = 0.285$  ( $G_L = 200 \text{ K cm}^{-1}$ ) is nearly independent of  $\gamma$ . We also note that the mushy-zone thickness decreases strongly with increasing temperature gradient.

For  $\Gamma = 7.12 \times 10^{-2}$  ( $G_L = 50 \text{ K cm}^{-1}$ ) the neutral curves ( $\gamma$  versus  $a$ ) correspond to steady onset of buoyancy-driven convection; we have found no evidence for the oscillatory onset of instability in the dendritic solidification of Pb-Sn alloys. For given values of  $C_\infty$  and  $\Gamma$ , the critical solidification rate (denoted by  $\gamma^*$ ) is the maximum point on each neutral curve and determines one



point on the stability boundary. For  $\gamma > \gamma^*$ , the one-dimensional dendritic basic state solution is stable for all wavenumbers  $a$ , whereas for  $\gamma < \gamma^*$  it is unstable for some range of  $a$ .

For  $C_\infty = 0.1$ , the critical solidification rate (at the extremum) is  $\gamma = 2.20 \times 10^{-2}$  ( $V_1 = 68 \mu \text{ sec}^{-1}$ ) and the critical wavenumber is  $a = 0.32$ . For  $C_\infty = 0.2$  the critical solidification rate assumes a maximum [ $\gamma^* = 2.59 \times 10^{-2}$  ( $V_1 = 80 \mu \text{ sec}^{-1}$ )] before shifting slightly downward to smaller solidification rates [ $\gamma^* = 1.98 \times 10^{-2}$  ( $V_1 = 61 \mu \text{ sec}^{-1}$ )] for  $C_\infty = 0.55$ . We note that the stable range of solidification rates is smallest for  $C_\infty = 0.2$ , which will be discussed below in connection with the stability boundaries.

Examination of the vertical structure of the disturbance amplitudes of vertical velocity and temperature in the liquid and mushy zone, solute mass fraction in the liquid, and volume fraction in the mushy zone shows that the disturbances correspond to the least stable mode (i.e., that with least positive or most negative  $\text{Re}(\sigma)$ ).

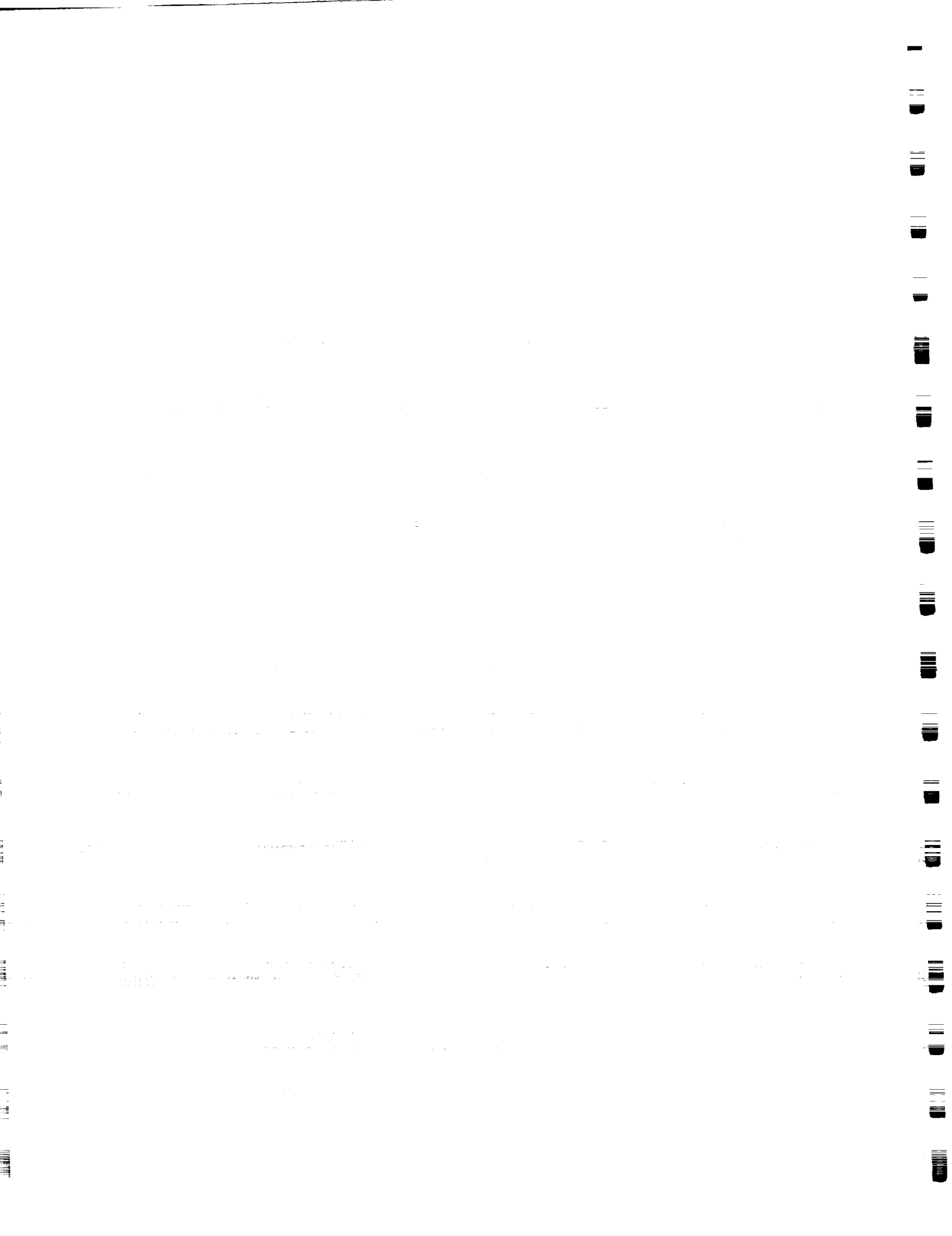
For  $C_\infty = 0.55$  and  $\Gamma = 7.12 \times 10^{-2}$ , inspection of the disturbance amplitudes at the critical conditions  $\gamma = 1.976 \times 10^{-2}$  ( $V_1 = 61 \mu \text{ sec}^{-1}$ ) and  $a = 0.32$  (as determined from the neutral curve) shows that the vertical velocity disturbance assumes a maximum just above the liquid/mushy-zone interface and decays strongly in both layers. We also note that the depth of penetration of the convective disturbance in each layer is of the same order. The structure of the temperature disturbance is similar, except near the mushy-zone/solid interface where the temperature disturbance does not approach zero. This is due to the fact that the boundary conditions require that on the deformed mushy-zone/solid interface the solute mass fraction in the interdendritic fluid be equal to the eutectic mass fraction. Thus, the relationship between the temperature and solute mass fraction disturbances in the mushy zone requires that the disturbance temperature be nonzero whenever that interface is deformed. Disturbances to the liquid composition and mushy-zone volume fraction are largely confined to very thin layers adjacent to the liquid/mushy-zone interface.

Our principal results are discussed in terms of a division of the  $\gamma$ - $C_\infty$  plane for four values of  $\Gamma$ . We have determined the regions in which the one-dimensional dendritic solution exists, along with information regarding its stability and the stability of the one-dimensional plane-front solution (which exists for all combinations of  $C_\infty$ ,  $\gamma$ , and  $\Gamma$ ). Each region is characterized according to whether the one-dimensional dendritic solution exists (and if so, whether it is stable), and whether the plane-front solution is stable with respect to morphological and convective disturbances (Coriell *et al.* 1980; Öztekin and Pearlstein 1992).

For  $\Gamma = 0.285$  ( $G_L = 200 \text{ K cm}^{-1}$ ), the one-dimensional dendritic solution exists in regions 1 and 2, and is stable at sufficiently high solidification rates (region 1) and unstable for lower values of  $\gamma$  (region 2). In regions 3-5, no one-dimensional steady solution of the governing equations exists. The plane-front solution exists in regions 1-5, but is unstable with respect to morphological instability in regions 1-3. The plane-front convective stability boundary (curve C) separates region 4, in which the plane-front solution is morphologically stable but convectively unstable, from region 5, in which the plane-front solution is stable with respect to both morphological and convective disturbances. In summary, the one-dimensional dendritic solution is stable in region 1 and the one-dimensional plane-front solution is stable in region 5; elsewhere the plane-front solution is unstable and the dendritic solution either does not exist or is unstable.

The topology of the division of the  $\gamma$ - $C_\infty$  plane becomes more complex as the temperature gradient decreases. For  $\Gamma = 7.12 \times 10^{-2}$  ( $G_L = 50 \text{ K cm}^{-1}$ ), a new region (6) exists in which both the plane-front and dendritic solutions are stable. For the plane-front solution, the morphological and convective stability boundaries have shifted downward, and stable plane-front solidification is confined to a smaller part of the  $\gamma$ - $C_\infty$  plane than for  $\Gamma = 0.285$ . However, for this smaller temperature gradient, dendritic solidification is stable for a larger range of  $\gamma$  and  $C_\infty$  relative to the  $\Gamma = 0.285$  case. For  $\Gamma = 7.12 \times 10^{-2}$ , the dendritic stability boundary intersects the dendritic existence curve just above the latter's intersection with the plane-front morphological stability boundary. Note also that the turning point on the dendritic stability boundary is more pronounced.

For  $\Gamma = 3.56 \times 10^{-2}$  ( $G_L = 25 \text{ K cm}^{-1}$ ), the dendritic stability boundary intersects the dendritic existence curve well below the plane-front morphological stability boundary, so that the part of the  $\gamma$ - $C_\infty$  plane in which the plane-front solution is stable and the dendritic solution exists has been divided according to the stability of the dendritic solution. In region 6, the dendritic and plane-





front solutions are both stable, as for  $\Gamma = 7.12 \times 10^{-2}$ , while in region 7, the dendritic solution is unstable. We note that the mushy-zone thickness predicted in the lower part of region 6 is exceedingly small; one can conceive of more sophisticated solidification models (e.g., specifically predicting cellular solidification and imposing a threshold criterion on mushy-zone thickness for dendritic solidification) that would not predict the existence of a dendritic solution in the lower part of region 6.

For  $\Gamma = 7.12 \times 10^{-3}$  ( $G_L = 5 \text{ K cm}^{-1}$ ), the dendritic solution exists in a part of the  $\gamma$ - $C_\infty$  plane (region 8) in which the plane-front solution is morphologically stable and convectively unstable. Here, as in region 2, both the dendritic and plane-front solutions exist, but neither is stable. The characteristics of the other regions are unchanged. Note that the region in which dendritic solidification is stable becomes larger with decreasing temperature gradient. For  $C_\infty < 1 \times 10^{-5}$  we have not determined the boundary separating regions 6 and 7 because, as discussed above, the basic state mushy-zone thickness predicted by our model becomes exceedingly small as the bulk mass fraction decreases further.

Our analysis of the conditions under which the governing equations admit a steady one-dimensional dendritic solution for Pb-Sn alloys, and the conditions under which that solution and the one-dimensional plane-front solution are stable, allows for a more complete discussion of the solidification regimes for binary alloys than has heretofore been possible.

That a one-dimensional steady dendritic solution exists for only some combinations of the temperature gradient, solidification rate, and bulk mass fraction is not surprising since this basic state is determined as the solution of a nonlinear system of ordinary differential equations, for which a solution need not exist. The boundary in the parameter space within which the dendritic solution exists is determined by two constraints. One is that the volume fraction at the liquid/mushy-zone interface is unity and cannot exceed that value within the mushy zone. Hence, the vertical derivative of the volume fraction at the liquid/mushy-zone interface should be nonnegative. This condition is satisfied in the region above the lower branch of the dendritic existence curve. The other constraint is that the solute mass fraction in the interdendritic fluid cannot exceed the eutectic composition,  $C_E$ . In the basic state, the interdendritic solute mass fraction depends monotonically on the vertical coordinate. Therefore, if the solute mass fraction at the liquid/mushy-zone interface is less than  $C_E$ , this constraint can be satisfied everywhere in the mushy zone. Below the upper branch of the dendritic existence curve, the latter constraint is satisfied, and the mushy-zone thickness asymptotically approaches zero as this branch of the curve is approached from below. Hence, a one-dimensional dendritic solution exists only in the region between the two branches of the dendritic existence curve.

When the plane-front morphological stability boundary is crossed, a cellular interface develops. As the solidification rate increases past the critical value, the cells become deformed and deepen. The formation and evolution of the cells have been studied theoretically by Ungar and Brown (1984) and Ungar *et al.* (1984). For still larger solidification rates, dendritic solidification occurs, with dendrites typically consisting of long vertical stems with secondary and tertiary branches. The development of the cellular interface and transition to dendritic solidification were observed experimentally by Trivedi (1984) and Venugopalan and Kirkaldy (1984). We thus conclude that the part of region 3 below the lower branch of the dendritic existence curve is a region of cellular solidification, in which the plane-front solution is morphologically unstable and the dendritic solution does not exist. The experimental evidence showing that dendritic solidification occurs when either the bulk mass fraction or solidification rate is increased for fixed temperature gradient is consistent with the location and character of the dendritic regions 1 and 2 in our results.

For a given solute bulk mass fraction, there exists a critical solidification rate above which the one-dimensional dendritic solution is stable with respect to infinitesimal disturbances. For all values of  $\Gamma$  dendritic solidification is least stable with respect to buoyancy-driven convection for solute mass fractions near 0.2 (the value at which the dendritic stability boundary has a turning point). This occurs because the mushy-zone thickness  $H_m$  and composition difference  $\Delta C_m$  attain their maxima for this  $C_\infty$ , independent of temperature gradient and solidification rate. If the Rayleigh number  $R_m$  we define for the mushy zone is proportional to  $\Delta C_m H_m$  (Worster 1992),



maximum destabilization for the Pb-Sn system occurs for  $C_\infty$  near 0.2. Fowler (1985) defined a Rayleigh number  $R = (\alpha_C - \alpha_T) m_L \rho_0 g \bar{K} / V_I$ , where  $\bar{K}$  is a monotonically increasing function of the permeability, and showed that there is a critical value  $R_c \propto 1/(C_E - C_\infty)$  such that if  $R < R_c$ , then dendritic solidification is stable with respect to small disturbances. Note that for Pb-Sn,  $R_c$  assumes a minimum near  $C_\infty = 0.2$ . Thus, there is a critical solidification rate above which the condition  $R < R_c$  is satisfied, and dendritic solidification is convectively stable. Our numerical results are thus consistent with the approximate analytical results of Fowler (1985) and Worster (1992).

We also note that the stable range of  $\gamma$  and  $C_\infty$  grows as  $\Gamma$  decreases. This is due to the fact that volume fraction (and hence permeability) decreases with decreasing temperature gradient, so that the permeability of the mushy zone decreases and the onset of convection is suppressed. That is also consistent with Fowler's result, since the Rayleigh number decreases as permeability decreases.

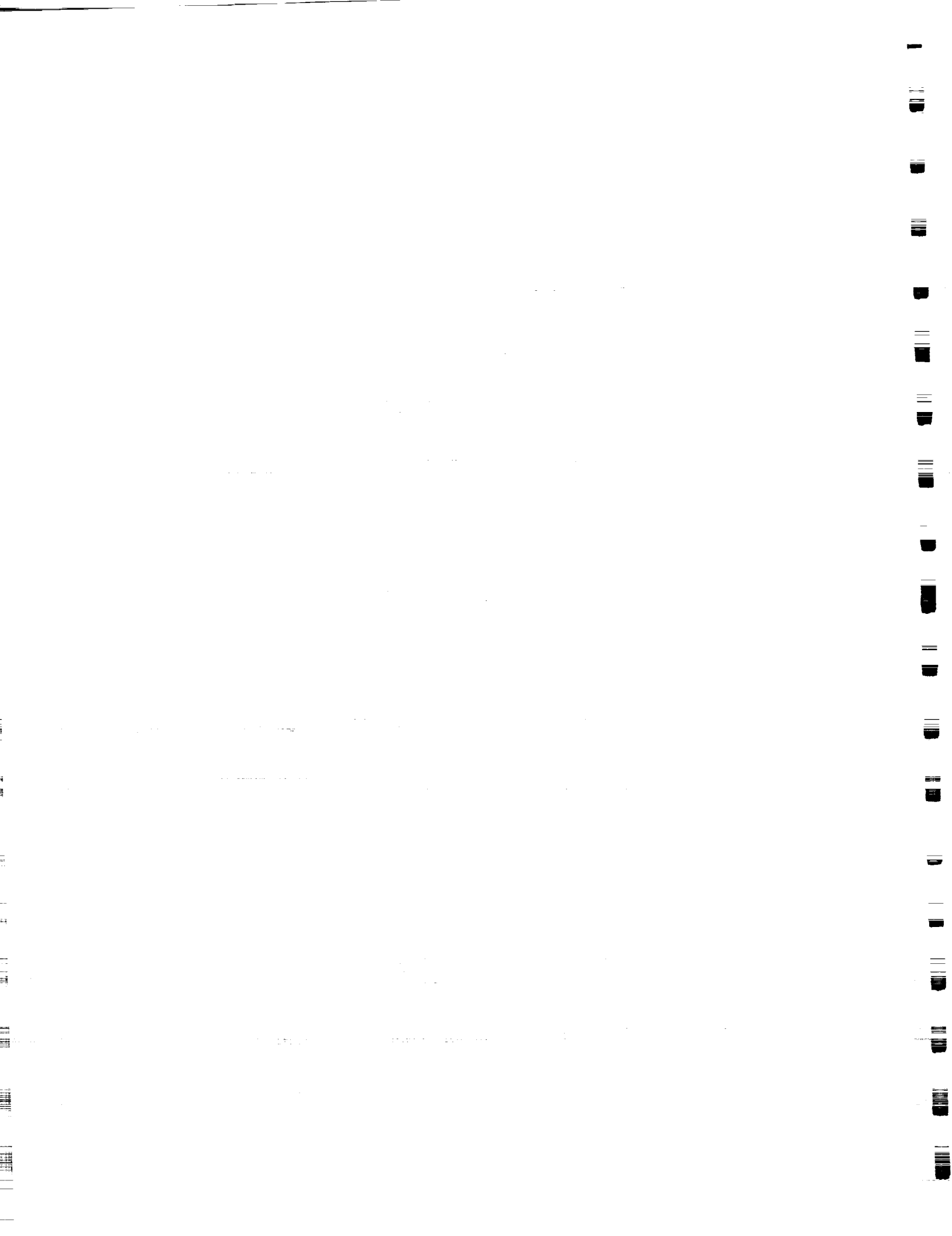
The amplitude of the disturbance to the vertical velocity assume a maximum on the liquid side of the liquid/mushy-zone interface, and decay strongly away from the interface. The onset of buoyancy-driven convection is largely localized in the liquid just above the interface and in the part of the mushy zone where the permeability is highest (near the liquid/mushy-zone interface). The interdendritic fluid farther from the liquid/mushy-zone interface is essentially stagnant. For  $\Gamma = 7.12 \times 10^{-2}$  ( $G_L = 50 \text{ K cm}^{-1}$ ), the critical wavenumber ranges from approximately 0.25 to 0.35, depending on  $C_\infty$ , so that the corresponding convective wavelength (0.06 cm) is small compared to the mushy-zone thickness ( $H_m = 0.311 \text{ cm}$  for  $C_\infty = 0.55$ ), but large compared to the diffusion length for a typical solidification rate ( $H_L = D_L/V_I = 4.92 \times 10^{-3} \text{ cm}$  for  $V_I = 61 \mu \text{ sec}^{-1}$  at the critical value of  $\gamma$ ). This type of onset corresponds to the mushy layer mode described by Worster (1992).

That a one-dimensional dendritic solution exists under conditions for which plane-front solidification is linearly stable with respect to morphological disturbances might at first seem inconsistent. However, upon closer examination this result is less surprising, since the plane-front stability analysis is restricted to infinitesimal disturbances (Coriell *et al.* 1980). In fact, in part of the parameter space where the plane-front solution is linearly stable, it is unstable with respect to subcritical ("finite amplitude") morphological disturbances (Wollkind and Segel 1970; Alexander *et al.* 1986; Ungar and Brown 1984). Thus, in the region in which the plane-front solution is linearly stable, it is not surprising that we also find a one-dimensional dendritic solution.



## References

- Alexander J.I.D. D.J. Wollkind, and R.F. Sekerka 1986 *J. Crystal Growth*, **79**, 849-865.
- Alexander J.I.D. J. Ouazzani, and F. Rosenberger 1989 *J. Crystal Growth*, **97**, 285-302.
- Antoranz, J.C. and M.G. Velarde 1978 *Phys. Lett. A*, **65**, 377-379.
- Antoranz, J.C. and M.G. Velarde 1979 *Phys. Fluids*, **22**, 1038-1043.
- Baines, P. G. and A.E. Gill 1969 *J. Fluid Mech.* **37**, 289-306.
- Bhattacharjee, J.K. 1988a *Phys. Fluids*, **31**, 2456-2461.
- Bhattacharjee, J.K. 1988b *Phys. Fluids*, **31**, 2462-2466.
- Bhattacharjee, J.K. 1988c *Phys. Rev. A*, **37**, 1368-1370.
- Bühler, K. and H. Oertel 1982 *J. Fluid Mech.* **114**, 261-282.
- Chandrasekhar, S. 1953 *Proc. Roy. Soc. London A*, **217**, 306-327.
- Chandrasekhar, S. and D.D. Elbert 1955 *Proc. Roy. Soc. London A*, **231**, 198-210.
- Chandrasekhar, S. 1961 *Hydrodynamic and Hydromagnetic Stability*, Clarendon, Oxford, pp. 76-85.
- Coriell, S.R., M.R. Cordes, W.J. Boettinger, and R.F. Sekerka 1980 *J. Crystal Growth*, **49**, 13-28.
- Davis, S.H. 1990 *J. Fluid Mech.* **212**, 241-262.
- Fowler, A.C. 1985 *IMA J. Appl. Maths.* **35**, 159-174.
- Fultz, D. and Y. Nakagawa 1955 *Proc. Roy. Soc. London A*, **231**, 211-225.
- Giamei, A.F. and B.H. Kear 1970 *Metall. Trans.* **1**, 2185-2192.
- Glicksman, M.E., S.R. Coriell, and G.B. McFadden 1986 *Ann. Rev. Fluid Mech.* **18**, 307-335.
- Goroff, I.R. 1960 *Proc. Roy. Soc. London A*, **254**, 537-541.
- Heinrich, J.C., S. Felicelli, P. Nandapurkar, and D.R. Poirier 1989a *Metall. Trans.*, **20B**, 883-891.
- Heinrich, J.C., S. Felicelli, P. Nandapurkar, and D.R. Poirier 1989b AIAA Paper 89-0626.
- Homsy, G.M. and J.L. Hudson 1969 *J. Fluid Mech.* **35**, 33-52.
- Homsy, G.M. and J.L. Hudson 1971a *J. Fluid Mech.* **45**, 353-373.
- Homsy, G.M. and J.L. Hudson 1971b *J. Fluid Mech.* **48**, 605-624.
- Homsy, G.M. and J.L. Hudson 1971c *Int. J. Heat Mass Transfer* **14**, 1149-1159.
- Homsy, G.M. and J.L. Hudson 1972 *Appl. Sci. Res.* **26**, 53-67.
- Huppert, H.E. 1990 *J. Fluid Mech.* **212**, 209-240.
- Kim, D. H. and R.A. Brown 1989 *J. Crystal Growth*, **96**, 609-627.
- Kou, S 1978 *Macrosegregation in Electroslag Remelted Ingots*, Ph.D. Thesis, Massachusetts Institute of Technology.
- Kou, S., D.R. Poirier, and M.C. Flemings 1978 *Metall. Trans.* **9B**, 711-719.
- Maples, A.L. and D.R. Poirier 1984 *Metall. Trans.* **15B**, 163-172.



- Masuda, A. 1978 *J. Oceanogr. Soc. Japan*, **34**, 8-16.
- Müller, G. 1990 *J. Crystal Growth*, **99**, 1242-1257.
- Müller, G. 1988 *Crystals*, **12**, Crystal Growth from the Melt, H.C. Freyhardt, ed., Springer-Verlag, Berlin.
- Mullins, W.W. and R.F. Sekerka 1964 *J. Appl. Phys.*, **35**, 444-451.
- Nakagawa, Y. and P. Frenzen 1955 *Tellus*, **7**, 1-21.
- Niiler, P.P. and F.E. Bisshopp 1965 *J. Fluid Mech.* **22**, 753-761.
- Öztekin, A. & Pearlstein, A. J. 1992 *Metall. Trans. B*, **23**, 73-80.
- Pearlstein, A.J. 1981 *J. Fluid Mech.* **103**, 389-412.
- Poirier, D.R., M.C. Flemings, R. Mehrabian, and H.J. Klein 1981 in *Advances in Metal Processing*, J.J. Burke, R. Mehrabian, and V. Weiss, eds., Plenum, New York, pp. 277-317.
- Polezhaev, V.I. 1988 in *Crystals*, **10**, Growth and Defect Structures, H.C. Freyhardt, ed., Springer-Verlag, Berlin, 87-141.
- Riahi, N. 1983 *J. Phys. Soc. Japan*, **52**, 2620-2621.
- Ridder, S.D., S. Kou, and R. Mehrabian 1981 *Metall. Trans.* **12B**, 435-447.
- Sample, A.K. and A. Hellawell 1984 *Metall. Trans.* **15A**, 2163-2173.
- Schmitt, R.W. and R.B. Lambert 1979 *J. Fluid Mech.* **90**, 449-463.
- Schulz-DuBois, E.O 1972 *J. Crystal Growth*, **12**, 81-87.
- Sekerka, R.F. and S.R. Coriell 1987 in *Proc. Sixth European Symp. on Material Sciences under Microgravity Conditions*, Bordeaux, December 2-5, 1986, ESA-SP-256, 3-11.
- Sengupta, S. and A.S. Gupta 1971 *Z. Angew. Math. Phys.* **22**, 906-914.
- Stern, M. E. 1960 *Tellus*, **12**, 172-175.
- Trivedi, R. 1984 *Metall. Trans. A*, **15**, 977-982.
- Ungar, L.H., M.J. Bennett, and R.A. Brown 1984 *Phys. Rev. B*, **31**, 5923-5930.
- Ungar, L.H. and R.A. Brown 1984 *Phys. Rev. B*, **29**, 1367-1380.
- Venugopalan, D. and J.S. Kirkaldy 1984 *Acta. Metall.* **32**, 893-906.
- Veronis, G. 1963 *Astrophys. J.* **137**, 641-663.
- Wollkind, D.J. and L.A. Segel 1970 *Phil. Trans. Roy. Soc. London, A* **268**, 351-380.
- Worster, M.G. 1991 *J. Fluid Mech.* **224**, 335-359.
- Wortherm, S., E. Mollo-Christensen, and F. Ostapoff 1983 *J. Fluid Mech.* **133**, 297-319.
- Walton, I. C. 1982 *J. Fluid Mech.* **125**, 123-135.
- Zangrando, F. and L.A. Bertram 1985 *J. Fluid Mech.* **151**, 55-79.





# Coriolis Effects on the Stability of Plane-Front Solidification of Dilute Pb-Sn Binary Alloys

ALPARSLAN OZTEKIN and ARNE J. PEARLSTEIN

The possibility of using steady uniform rotation about a vertical axis to suppress the onset of buoyancy-driven convection during solidification of a binary alloy is considered using a linear stability analysis. For Pb-Sn alloys, our results clearly show that the onset of convection in a horizontally unbounded layer can be suppressed significantly at modest rotation rates. Specifically, "plane-front" solidification is linearly stable at higher Sn concentrations in a rotating configuration than in a nonrotating one. The predicted inhibitory effects of rotation on convection are discussed in terms of previous experimental and theoretical studies of the effect of rotation on the onset of buoyancy-driven convection in single-component fluids heated from below and in binary fluids subject to thermal and solutal stratification.

## I. INTRODUCTION

DURING directional solidification of alloys, it is frequently desired to produce large single crystals with very low densities of macrosegregation defects and other imperfections. In principle, this can sometimes be achieved by "plane-front" solidification, in which the melt-solid interface remains perfectly planar. In such a case, the solidification process would be steady in a reference frame moving with the interface, and the only spatial variation would be in a direction normal to the interface. However, in real systems, several instabilities can cause departures from the nominally steady and one-dimensional plane-front case.

First, the solid-liquid interface may be subject to the so-called morphological instability, which has been studied extensively since the early work of Mullins and Sekerka.<sup>[1]</sup> This instability causes deformation of the nominally planar interface, ultimately leading to formation of a two-phase "mushy zone" of dendrites and interdendritic liquid. Departures from one-dimensionality and steadiness in the mushy zone result in nonuniform distribution of solute in the solidified material.

Second, the density of a binary or multicomponent melt depends on both temperature and composition. When an alloy is solidified by cooling from below, rejection of solute(s) at the growing interface is potentially destabilizing if the solute-enriched liquid just above the interface is less dense than the warmer overlying bulk liquid. Under some conditions, this adverse solute gradient overcomes the stabilizing temperature gradient, leading to convection in the melt. This fluid motion provides another transport mechanism, besides molecular diffusion, for redistributing solute(s) into the bulk liquid from the relatively enriched region near the interface. Convection in the melt is often referred to as thermosolutal convection or, because the diffusivities of heat and solute are different, as doubly diffusive convection.

Convective and morphological instabilities in a binary alloy undergoing directional solidification were first studied by Coriell *et al.*<sup>[2]</sup> using a linear stability analysis. These authors showed that motion may occur due to either morphological or convective instabilities and that the buoyancy force does not sensibly alter the criterion for onset of morphological instability, which occurs at higher wavenumbers than does the buoyancy-driven instability. Subsequent work was reviewed by Glicksman *et al.*<sup>[3]</sup> and Sekerka and Coriell.<sup>[4]</sup> More general discussions of the effects of convection on plane-front and dendritic solidification have been given recently by Worster,<sup>[5]</sup> Davis,<sup>[6]</sup> Huppert,<sup>[7]</sup> Polezhaev,<sup>[8]</sup> and Müller.<sup>[9]</sup>

Buoyancy-driven convection in the melt has been shown to be the dominant factor in the formation of "freckles," a macrosegregation defect deleterious to the mechanical properties of directionally solidified alloys. The formation and characterization of freckles in nickel-based superalloys were first studied experimentally by Giamei and Kear.<sup>[10]</sup> Poirier *et al.*<sup>[11]</sup> investigated macrosegregation in electroslag ingots, showed that convection in the melt results in freckling in the solidified material, and suggested that rotation might reduce freckling. Ridder *et al.*<sup>[12]</sup> studied the effects of fluid flow on macrosegregation in nominally axisymmetric ingots and showed that melt convection results in macrosegregation in the mushy zone. In a theoretical study of a binary alloy solidifying radially inward, Maples and Poirier<sup>[13]</sup> concluded that macrosegregation results from natural convection in the mushy zone driven by nonuniform temperature and solute distributions. A recent review of the effects of buoyancy-driven convection on macrosegregation in binary and pseudobinary nonmetallic systems have been given by Müller.<sup>[9]</sup>

One means by which the onset of convection can be inhibited in a density-stratified fluid layer is to subject the layer to a magnetic field aligned parallel or perpendicular to the stratification.<sup>[9]</sup> For horizontal Pb-Sn layers solidified from below at several growth velocities, Coriell *et al.*<sup>[2]</sup> showed theoretically that the critical Sn concentration above which instability occurs can be increased an order of magnitude by applying a vertical magnetic field of the order of one tesla. This technique requires

ALPARSLAN OZTEKIN, Research Assistant, and ARNE J. PEARLSTEIN, Associate Professor, are with the Department of Mechanical and Industrial Engineering, University of Illinois at Urbana-Champaign, Urbana, IL 61801.

Manuscript submitted April 15, 1991.

that the liquid be an electrical conductor and so is applicable to metallic alloys, semiconductors, and aqueous solutions.

Macrosegregation might also be controlled by increasing or decreasing the magnitude of the gravitational acceleration or changing its direction. Alexander *et al.*<sup>[14]</sup> and Heinrich *et al.*<sup>[15,16]</sup> theoretically studied the effect of reduced gravity on macrosegregation in directionally solidified alloys. These authors suggested that macrosegregation in alloys can be reduced by solidification in a low-gravity environment. Müller<sup>[17]</sup> and Weber *et al.*<sup>[18]</sup> have recently discussed solidification under conditions where the magnitude of the body force is greater or less than that of normal gravity.

Both gravity and an external magnetic field are body forces which act on the liquid. As opposed to contact forces such as pressure, viscous stress, and surface tension, which act on the surfaces of a fluid element, body forces act on the mass of a fluid element. Hence, their local strengths are proportional to the local fluid density. In addition to gravitational and magnetic body forces, there are other "pseudo-body forces" which manifest themselves as fictitious accelerations (centripetal and Coriolis) when the reference frame to which the fluid motion is referred undergoes steady rotation relative to an inertial frame. (An additional fictitious acceleration, with which we will not be concerned, manifests itself if the rotation of the noninertial frame relative to the inertial frame is unsteady.) Although these accelerations do not correspond directly to forces (as in the case of gravitational acceleration), they have the same mathematical form as accelerations associated with body forces and can have dynamical consequences equally as profound as the gravitational and magnetic forces discussed above.<sup>[19]</sup> In light of this, and the fact that modification of the gravitational field or imposition of an external magnetic field may not always be possible, the possibility of using rotation to suppress the onset of convection in a liquid undergoing directional solidification is of interest.

Several effects of rotation on solidification have been discussed by Schulz-DuBois.<sup>[20]</sup> The experiments of Kou,<sup>[21]</sup> Kou *et al.*,<sup>[22]</sup> Sample and Hellawell,<sup>[23]</sup> Müller,<sup>[17]</sup> and Weber *et al.*<sup>[18]</sup> have shown that rotation can significantly reduce the degree of macrosegregation in binary alloys directionally solidified under plane-front or dendritic conditions. Kou and Kou *et al.* studied the effect of steady rotation about a vertical axis on freckle formation in Sn-Pb alloys. Sample and Hellawell considered solidification of the transparent alloy  $\text{NH}_4\text{Cl-H}_2\text{O}$  in a crucible rotating about an axis inclined between 0 and 30 deg with respect to the vertical. Müller<sup>[17]</sup> and Weber *et al.* have studied the effect of rotation on the growth of Te-doped InSb crystals and have shown that striations can be suppressed at sufficiently high rotation rates. These studies show that the degree of macrosegregation (freckles and striations) can be significantly reduced by rotation.

There are two means by which steady rotation about a fixed axis can influence the motion of a fluid. In terms of a reference frame rotating with constant angular velocity  $\Omega$  about an axis, these correspond to the centripetal and Coriolis accelerations, for which the terms

$\rho_L \Omega \times \Omega \times \mathbf{r}$  and  $2\rho_L \Omega \times \mathbf{u}$ , respectively, are added to the momentum equation. Here,  $\mathbf{r}$  is the position vector measured from the axis of rotation,  $\mathbf{u}$  is the local fluid velocity relative to the noninertial reference frame, and  $\rho_L$  is the local density of the liquid.

Previous theoretical studies of the effects of rotation on the onset of buoyancy-driven convection have been restricted to cases where no solidification occurs. For a horizontally unbounded layer of a single-component fluid, Chandrasekhar,<sup>[24]</sup> Chandrasekhar and Elbert,<sup>[25]</sup> and Niiler and Bisshopp<sup>[26]</sup> have shown that steady uniform rotation about a vertical axis can significantly inhibit the onset of convection, with the Coriolis-related Taylor-Proudman mechanism<sup>[27]</sup> playing the dominant role. The effects of centripetal, Coriolis, and gravitational accelerations on convection in horizontally confined rotating fluids in cylindrical containers of various aspect ratios were considered in an early series of articles by Homsy and Hudson.<sup>[28-32]</sup> More recently, for a single-component fluid, Weber *et al.*<sup>[18]</sup> have computed buoyancy-driven flows equivalent to those which can be driven by a temperature gradient maintained between the ends of an otherwise insulated right circular cylinder rotating at constant angular velocity about an axis perpendicular to and intersecting the cylinder axis but not passing through the cylinder. Three-dimensional computations, in which the variation of the magnitude of the centripetal acceleration  $\Omega \times \Omega \times \mathbf{r}$  along the cylinder axis was neglected (a good approximation when the cylinder length is small compared to the shortest distance between the axis of rotation and the cylinder), were performed with the term accounting for the Coriolis acceleration  $2\Omega \times \mathbf{u}$  either included or omitted. Weber *et al.* found excellent agreement between experiment and computation when the Coriolis acceleration was included.

For a binary fluid, Pearlstein<sup>[33]</sup> has shown that the Coriolis acceleration can either stabilize or destabilize a horizontally unbounded layer, depending on the values of the Prandtl and Schmidt numbers, the dimensionless rotation rate (expressed in terms of a Taylor number), and the dimensionless temperature or solute gradient (expressed in terms of thermal and solutal Rayleigh numbers). Other work concerning the effect of rotation on doubly diffusive convection in binary fluids (with no phase change) has been reported by Sengupta and Gupta,<sup>[34]</sup> Masuda,<sup>[35]</sup> Antoranz and Velarde,<sup>[36,37]</sup> Schmitt and Lambert,<sup>[38]</sup> Riahi,<sup>[39]</sup> Worthem *et al.*,<sup>[40]</sup> and Bhattacharjee.<sup>[41,42,43]</sup>

In this work, we use linear stability analysis to study the effect of the Coriolis acceleration on convective and morphological instability for alloys which solidify with a nominally planar interface. This work serves to identify the mechanism by which Coriolis effects affect the onset of convection in solidifying binary alloys. The analysis is illustrated by results for the Pb-Sn system.

## II. BASIC STATE AND LINEAR DISTURBANCE EQUATIONS

We adopt the model of solidification used by Coriell *et al.*,<sup>[2]</sup> in which the Oberbeck-Boussinesq equations govern motion in the liquid. In a reference frame translating with the nominally steady velocity ( $V_f$ ) of the

moving interface and rotating with constant angular velocity  $\Omega$ , the basic state

$$\bar{\mathbf{u}} = (0, 0, -\varepsilon V_l) \quad [1]$$

$$\bar{T}_L = T_M + \frac{m_L c_\infty}{k} + \frac{\rho_{L0} \kappa_L G_L}{\rho_S V_l} \left[ 1 - \exp \left( -\frac{\rho_S V_l}{\rho_{L0} \kappa_L} z \right) \right] \quad [2]$$

$$\bar{c}_L = c_\infty \left[ 1 + \frac{1-k}{k} \exp \left( -\frac{\rho_S V_l}{\rho_{L0} D_L} z \right) \right] \quad [3]$$

$$\bar{T}_S = T_M + \frac{m_L c_\infty}{k} + \frac{\kappa_S G_S}{V_l} \left[ 1 - \exp \left( -\frac{V_l}{\kappa_S} z \right) \right] \quad [4]$$

is the same used by Coriell *et al.*, where  $\bar{\mathbf{u}}$ ,  $\bar{T}_L$ ,  $\bar{c}_L$ , and  $\bar{T}_S$  are, respectively, basic state values of velocity, temperature, and solute concentration in the liquid and temperature in the solid,  $\kappa_L$  and  $\kappa_S$  are the thermal diffusivities of the liquid and solid, respectively,  $D_L$  is the diffusion coefficient,  $\rho_S$  is the solid density,  $\rho_{L0}$  is the liquid density of pure lead at its melting point,  $c_\infty$  is the bulk concentration,  $G_L$  is the liquid-side temperature gradient at the planar interface,  $V_l$  is the nominal growth rate,  $k$  is the segregation coefficient,  $m_L$  is the slope of the liquidus,  $T_M$  is the melting temperature of Pb,  $\varepsilon = \rho_S/\rho_{L0} - 1$  is the fractional shrinkage,  $G_S = (LV_l + G_L k_l)/k_s$  is the solid-side temperature gradient at the planar interface,  $k_l$  and  $k_s$  are the thermal conductivities of the liquid and solid, respectively, and  $L$  is the latent heat of fusion per unit volume. (All concentrations used herein are weight percentages.) We note that the basic-state temperature distribution in the solid (Eq. [4]) is valid only near the interface.

As in stability analyses of other flows subject to uniform rotation,<sup>[24-26,33,44]</sup> the linear disturbance equations we use differ from those in the nonrotating case only by addition of the Coriolis acceleration to the disturbance momentum equation. (This approach neglects the consequences of density variation in the term corresponding to the centripetal acceleration.) The equations governing small disturbances in the liquid are

$$\nabla \cdot \mathbf{u} = 0 \quad [5]$$

$$\frac{\partial \mathbf{u}}{\partial t} - \frac{\rho_S}{\rho_{L0}} V_l \frac{\partial \mathbf{u}}{\partial z} + 2\Omega \times \mathbf{u} = -\frac{\nabla p}{\rho_{L0}} - \alpha_T g T_L \mathbf{i}_z - \alpha_C g c_L \mathbf{i}_z + \nu \nabla^2 \mathbf{u} \quad [6]$$

$$\frac{\partial T_L}{\partial t} - \frac{\rho_S}{\rho_{L0}} V_l \frac{\partial T_L}{\partial z} + G_L w \exp \left( -\frac{\rho_S V_l}{\rho_{L0} \kappa_L} z \right) = \kappa_L \nabla^2 T_L \quad [7]$$

$$\frac{\partial c_L}{\partial t} - \frac{\rho_S}{\rho_{L0}} V_l \frac{\partial c_L}{\partial z} + G_C w \exp \left( -\frac{\rho_S V_l}{\rho_{L0} D_L} z \right) = D_L \nabla^2 c_L \quad [8]$$

where the dependent variables  $\mathbf{u}$ ,  $w$ ,  $p$ ,  $T_L$ , and  $c_L$  are, respectively, the disturbance values of the velocity, its  $z$ -component, pressure, temperature, and concentration

in the liquid. Here,  $\mathbf{i}_z$  is the unit vector in the  $z$ -direction,  $g$  is the magnitude of the gravitational acceleration,  $\nu$  is the viscosity,  $\alpha_T$  and  $\alpha_C$  are the thermal and solutal expansion coefficients, respectively,  $G_C = (k-1)\rho_S c_\infty V_l / (k\rho_{L0} D_L)$  is the concentration gradient at the planar interface,  $\Omega = \Omega_0 \mathbf{i}_z$  is the angular velocity, and  $\Omega_0$  is a constant. The disturbance energy equation in the solid is

$$\frac{\partial T_S}{\partial t} - V_l \frac{\partial T_S}{\partial z} = \kappa_S \nabla^2 T_S \quad [9]$$

where  $T_S$  is the disturbance temperature in the solid.

Taking the curl of Eq. [6] and the dot product of the result with  $\mathbf{i}_z$ , we obtain an equation

$$\frac{\partial \omega_z}{\partial t} - \frac{\rho_S}{\rho_{L0}} V_l \frac{\partial \omega_z}{\partial z} - 2\Omega_0 \frac{\partial w}{\partial z} = \nu \nabla^2 \omega_z \quad [10]$$

for the  $z$ -component of the vorticity,  $\omega_z$ . After twice taking the curl of Eq. [6], the vertical component of the resulting equation is

$$\begin{aligned} \frac{\partial}{\partial t} \nabla^2 w - \frac{\rho_S}{\rho_{L0}} V_l \frac{\partial}{\partial z} \nabla^2 w + 2\Omega_0 \frac{\partial \omega_z}{\partial z} \\ = \alpha_T g \nabla_\perp^2 T_L + \alpha_C g \nabla_\perp^2 c_L + \nu \nabla^4 w \end{aligned} \quad [11]$$

The disturbance boundary conditions at the interface are

$$u(x, y, 0, t) = \varepsilon V_l \frac{\partial \eta(x, y, t)}{\partial x} \quad [12a]$$

$$v(x, y, 0, t) = \varepsilon V_l \frac{\partial \eta(x, y, t)}{\partial y} \quad [12b]$$

$$w(x, y, 0, t) = -\varepsilon \frac{\partial \eta(x, y, t)}{\partial t} \quad [12c]$$

$$\frac{\partial w(x, y, 0, t)}{\partial z} = -\varepsilon V_l \nabla_\perp^2 \eta(x, y, t) \quad [12d]$$

$$\begin{aligned} L \frac{\partial \eta(x, y, t)}{\partial t} = -k_L \frac{\partial T_L(x, y, 0, t)}{\partial z} + k_S \frac{\partial T_S(x, y, 0, t)}{\partial z} \\ + \left( \frac{\rho_S}{\rho_{L0}} \frac{G_L V_l k_L}{\kappa_L} - \frac{G_S V_l k_S}{\kappa_S} \right) \eta(x, y, t) \end{aligned} \quad [12e]$$

$$\begin{aligned} \frac{V_l^2 \rho_S c_\infty}{D_L \rho_{L0}} \eta(x, y, t) + V_l c_L(x, y, 0, t) + \frac{c_\infty}{k} \frac{\partial \eta(x, y, t)}{\partial t} \\ = -\frac{\rho_{L0} D_L}{\rho_S (1-k)} \frac{\partial c_L(x, y, 0, t)}{\partial z} \end{aligned} \quad [12f]$$

$$\begin{aligned} T_L(x, y, 0, t) + G_L \eta(x, y, t) = T_S(x, y, 0, t) \\ + G_S \eta(x, y, t) \end{aligned} \quad [12g]$$

$$\begin{aligned} T_L(x, y, 0, t) + G_L \eta(x, y, t) = m_L G_C \eta(x, y, t) \\ + m_L c_L(x, y, 0, t) + T_M \Psi \nabla_\perp^2 \eta(x, y, t) \end{aligned} \quad [12h]$$

where  $\eta$  is the interface position and  $\Psi$  is the capillary coefficient.

### III. NONDIMENSIONALIZATION AND FOURIER DECOMPOSITION

We scale the velocity, time, length, temperature, concentration, and vorticity with  $\kappa_L/H$ ,  $H^2/\nu$ ,  $H$ ,  $G_L H$ ,  $c_\infty$ , and  $\kappa_L/H^2$ , respectively, where  $H = D_L/V_i$  is the characteristic length (associated with the destabilizing gradient of rejected solute, see Eq. [3]), and write the horizontal and temporal dependence of the nondimensional disturbance quantities as  $\exp(\sigma\tau + ia_x X + ia_y Y)$ , where  $a_x$  and  $a_y$  are the  $x$ - and  $y$ -components of the wavevector and  $\sigma$  is the temporal eigenvalue. Substitution into Eqs. [7] through [11] yields

$$\sigma(D^2 - a^2)W - \frac{\rho}{Sc}D(D^2 - a^2)W = -Ra_T a^2 \Theta_L - Ra_S Le a^2 C_L + (D^2 - a^2)^2 W - \Omega_0^* D \Omega_Z \quad [13]$$

$$\sigma \Omega_Z - \frac{\rho}{Sc} D \Omega_Z = \Omega_0^* DW + (D^2 - a^2) \Omega_Z \quad [14]$$

$$Pr \sigma \Theta_L - \rho Le D \Theta_L = (D^2 - a^2) \Theta_L - W \exp(-\rho Le Z) \quad [15]$$

$$Sc \sigma C_L - \rho DC_L = (D^2 - a^2) C_L + \frac{\gamma \rho}{Le} W \exp(-\rho Z) \quad [16]$$

in the melt and

$$Pr \sigma \Theta_S - Le D \Theta_S = \kappa(D^2 - a^2) \Theta_S \quad [17]$$

in the solid. Here,  $Pr = \nu/\kappa_L$  is the Prandtl number,  $Sc = \nu/D_L$  is the Schmidt number,  $Le = D_L/\kappa_L$  is the Lewis number,  $Ra_T = \alpha_T G_L H^4/(\kappa_L \nu)$  and  $Ra_S = \alpha_S G_L H^4/(\kappa_L \nu)$  are the thermal and solutal Rayleigh numbers, respectively,  $\Omega_0^* = 2\Omega_0 H^2/\nu$  is the square root of the Taylor number,  $\rho = \rho_S/\rho_{L0}$  is the density ratio,  $\kappa = \kappa_S/\kappa_L$  is the thermal diffusivity ratio, and  $\gamma = (1 - k)/k$ . The boundary conditions (Eqs. [12a] through [12h]) at the interface become

$$W(0) = -\epsilon Pr \sigma \beta \quad [18a]$$

$$DW(0) = \epsilon Le a^2 \beta \quad [18b]$$

$$\Omega_Z(0) = 0 \quad [18c]$$

$$Sc \sigma \beta = -k_L^* D \Theta_L(0) + k_S^* D \Theta_S(0) + Le(k_L^* \rho - k_L^*/\kappa - 1/\kappa) \beta \quad [18d]$$

$$(1 - G) \beta = \Theta_S(0) - \Theta_L(0) \quad [18e]$$

$$(Sc \sigma + k \rho) \beta = -k C_L(0) - \frac{1}{\gamma \rho} DC_L(0) \quad [18f]$$

$$(-a^2 T_M^* + m^* - 1) \beta = \frac{m^*}{\rho \gamma} C_L(0) + \Theta_L(0) \quad [18g]$$

where  $W$ ,  $C_L$ ,  $\Omega_Z$ , and  $\Theta_L$  are, respectively, the amplitudes of the disturbances to the vertical velocity, concentration, vertical vorticity, and temperature in the melt,  $\Theta_S$  is the amplitude of the disturbance temperature in the solid, and  $\beta$  (a constant) is the amplitude of the disturbed interface position. Here, we define dimensionless parameters  $k_L^* = G_L k_L H/(LD_L)$ ,  $k_S^* = G_L k_S H/(LD_L)$ ,

$m^* = m_L G_C/G_L$ ,  $T_M^* = T_M \Psi/(G_L H^2)$ , and  $G = G_S/G_L$ . For the far-field boundary conditions, we follow Coriell *et al.*<sup>[2]</sup> and set all disturbances to zero

$$W = DW = \Omega_Z = C_L = \Theta_L = 0 \quad \text{as } Z \rightarrow \infty \quad [19a]$$

$$\Theta_S = 0 \quad \text{as } Z \rightarrow -\infty \quad [19b]$$

far from the interface.

### IV. NUMERICAL SOLUTION

Our objective is to find conditions under which infinitesimally small disturbances neither grow nor decay for a finite number of wavenumbers and decay for all other wavenumbers. Disturbances which neither grow nor decay are said to be neutral. The neutral disturbances can be of two types, depending on the imaginary part of  $\sigma$ . If the imaginary part of  $\sigma$  is zero for a neutral disturbance, the onset of instability will be *via* monotonically growing disturbances (steady onset). If the imaginary part of  $\sigma$  is not zero, the neutral disturbance will oscillate in time (oscillatory onset).

In the previous section, we formulated an eigenvalue problem for two systems of ordinary differential equations on two semi-infinite intervals (in the melt and in the solid), coupled by boundary conditions at the deformable interface. For convenience, we follow Coriell *et al.*<sup>[2]</sup> and solve the problem on a finite interval  $[-h, h]$ , where  $2h$  is the dimensionless height of the computational domain. With regard to the far-field boundary conditions at  $Z = \pm\infty$ , we set all disturbances to zero

$$W = DW = \Omega_Z = C_L = \Theta_L = 0 \quad \text{at } Z = h \quad [20a]$$

in the melt and

$$\Theta_S = 0 \quad \text{at } Z = -h \quad [20b]$$

in the solid. In this work, we have used  $h = 10$ . (For steady onset, we have checked a number of our results using more accurate asymptotic boundary conditions applied at  $Z = \pm h$  derived following Keller's<sup>[45]</sup> procedure and have found excellent agreement between the eigenvalues computed using the two sets of boundary conditions.) Since we use Chebyshev polynomials in our numerical solution, we scale the liquid and solid regions by  $z_2 = (2Z - h)/h$  and  $z_1 = (2Z + h)/h$ , respectively, so that each region lies between  $-1$  and  $+1$ . The resulting system is then solved using a spectral Galerkin technique developed by Zebib.<sup>[46]</sup> The problem thus is reduced to a matrix eigenvalue problem

$$\mathbf{A} \mathbf{x} + \sigma \mathbf{B} \mathbf{x} = \mathbf{0} \quad [21]$$

where  $\sigma$  is the temporal eigenvalue and the elements of the square matrices  $\mathbf{A}$  and  $\mathbf{B}$  depend on  $a^2 = a_x^2 + a_y^2$  (the square of the horizontal wavenumber), the bulk concentration  $c_\infty$ , and the other dimensionless parameters.

In what follows, we characterize the stability of the nominally plane-front solution in terms of the growth velocity  $V_i$  and bulk concentration  $c_\infty$ , with all other parameters taken as fixed. For each value of  $V_i$ , we seek one or more critical values of  $c_\infty$  (denoted by  $c_\infty^*$ ), such that for  $c_\infty < c_\infty^*$ , disturbances decay for all wavenumbers, while for  $c_\infty > c_\infty^*$ , disturbances grow for all wavenumbers in some range. In order to determine the

critical value(s) of  $c_\infty$ , we first determine the neutral curve ( $c_\infty$  vs the wavenumber  $a$ ), separating those combinations of  $c_\infty$  and  $a$  for which all temporal eigenvalues  $\sigma$  lie in the left half-plane (a stable basic state) from those for which at least one eigenvalue lies in the right half-plane (an unstable basic state). To determine the bulk concentration on the neutral curve for an arbitrarily chosen wavenumber  $a$ , we first guess a value of  $c_\infty$  and compute all eigenvalues  $\sigma$  using Eq. [21]. If all eigenvalues have negative real parts, the value of  $c_\infty$  is increased by doubling the previous value; otherwise, the new value of  $c_\infty$  is chosen as half the previous value. This process is continued until we determine two values of  $c_\infty$  between which at least one sign change is obtained in the real part of the least stable temporal eigenvalue. The concentration on the neutral curve is then determined using a bisection method.

To compute the critical concentration  $c_\infty^*$  at which instability first occurs (*i.e.*, the minimum on the neutral curve), we arbitrarily choose a wavenumber and compute the corresponding  $c_\infty$  on the neutral curve using the procedure described above. We then fix  $c_\infty$  at the value computed at the previous step and compute the eigenvalues  $\sigma$  for a discrete set of wavenumbers in a chosen range. From this set, we select the wavenumber corresponding to the  $\sigma$  with largest real part. If this wavenumber is at an endpoint of the chosen range, we extend the range to include the wavenumber corresponding to the largest  $\text{Re}(\sigma)$ . We then select this wavenumber and determine the corresponding  $c_\infty$  on the neutral curve. We continue this process until the relative change in  $c_\infty$  is less than  $10^{-6}$ .

## V. RESULTS

The solutions of Eqs. [13] through [19] depend on 15 nondimensional parameters, as defined in Sections II and III. To determine the stability of a basic state with a nominally planar interface, numerical values of these parameters need to be specified. (Solutions on a finite interval depend also on  $h$ .) Therefore, it is not possible to numerically explore the effects of more than a few combinations of these parameters on the onset of instability. In this work, we have thus restricted ourselves to the Pb-Sn system which, due to the low melting points of both components, has been the subject of several experimental studies. The parameter values (other than  $\Omega_0^*$ ) are as used by Coriell *et al.*<sup>[2]</sup> at reference conditions corresponding to pure lead at its melting point. (The diffusivity of Sn in Pb corresponds to an infinitely dilute solution.)

To test our code, we first considered the nonrotating case and compared our results to those of Coriell *et al.* Taking the liquid-side temperature gradient at the interface as  $G_L = 200 \text{ K cm}^{-1}$ , we computed neutral curves  $c_\infty$  vs  $a$  for various values of the solidification rate  $V_I$ . The neutral curves were generally similar to those shown by Coriell *et al.* The only qualitative difference was that in our work, several new oscillatory neutral curves were found to branch from steady neutral curves found by Coriell *et al.* and in the present work. We believe that our detection of these additional oscillatory neutral curves (which in each case lie well above the critical value of

$c_\infty$  and are hence of no practical consequence) is due to use of a numerical technique which simultaneously computes a large number of temporal eigenvalues at each combination of  $c_\infty$  and  $V_I$ , as opposed to the shooting technique of Coriell *et al.* which individually computes the temporal eigenvalues by a one-point iteration scheme.

We present our principal results in terms of stability boundaries in the  $V_I - c_\infty^*$  plane. For ease of comparison to the work of Coriell *et al.*,<sup>[2]</sup> results are presented in terms of dimensional variables. With  $G_L$  fixed at  $200 \text{ K cm}^{-1}$ , Figure 1 shows stability boundaries for  $\Omega_0 = 0, 100, 200, 300$ , and  $500 \text{ rpm}$ . For each value of  $\Omega_0$ , the stability boundary consists of some portion of the morphological branch ( $c_\infty^*$  decreasing with increasing  $V_I$ ) found by Coriell *et al.* (their Figure 1) joined to a convective branch. The critical value of  $c_\infty$  on the convective branch is an increasing function of  $\Omega_0$  at any value of  $V_I$ , clearly indicating the inhibitory effect of rotation on the onset of buoyancy-driven convection. We note that for  $V_I = 5 \mu \text{ s}^{-1}$ , rotation at  $\Omega_0 = 500 \text{ rpm}$  increases by slightly more than two orders of magnitude relative to the nonrotating case the critical Sn concentration above which the plane-front solution becomes unstable. We further note that the morphological branch is unaffected by rotation, whereas as  $\Omega_0$  increases, the value of  $V_I$  at which the onset of instability shifts from the convective branch to the morphological branch decreases from about  $40 \mu \text{ s}^{-1}$  in the nonrotating case to about  $27 \mu \text{ s}^{-1}$  for  $\Omega_0 = 500 \text{ rpm}$ .

For each value of  $\Omega_0$ , we see a local minimum near  $V_I = 1 \mu \text{ s}^{-1}$ , with the minimum shifting to smaller growth velocities and becoming relatively more shallow as  $\Omega_0$  increases. We note that the maximum relative stabilization by rotation occurs near the local minimum, and that for  $\Omega_0 = 500 \text{ rpm}$ , the critical bulk concentration of Sn is increased more than a hundredfold. Although Coriell *et al.*<sup>[2]</sup> noted a local minimum in the stability boundary near  $V_I = 1 \mu \text{ s}^{-1}$  in the nonrotating case for the largest gravitational acceleration considered, they offered no explanation for its existence. This minimum is

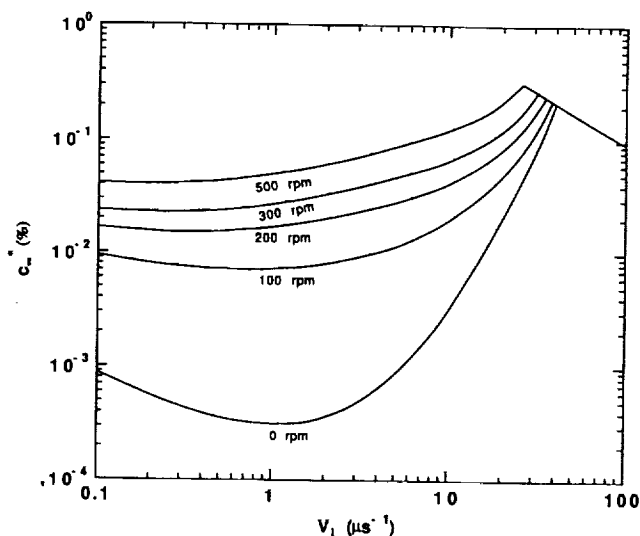


Fig. 1— $V_I - c_\infty^*$  stability boundaries for  $G_L = 200 \text{ K cm}^{-1}$ , with  $\Omega_0 = 0, 100, 200, 300$ , and  $500 \text{ rpm}$ .

a consequence of the fact that as  $V_l \rightarrow 0$ , the concentration gradient  $G_c = (k - 1)\rho_s c_\infty V_l / (k\rho_{L0}D_L)$  vanishes. As the temperature gradient is independent of  $c_\infty$  and is stabilizing, the critical value of  $c_\infty$  must ultimately increase as  $V_l \rightarrow 0$ . (Of course, the weight percent of the solute,  $c_\infty$ , cannot exceed 100.) As  $c_\infty^*$  must initially decrease with increasing  $V_l$ , there must be a local minimum on the convective branch before  $c_\infty^*$  can increase to join up with the morphological branch of the stability boundary. This nonmonotonic dependence of  $c_\infty^*$  on  $V_l$  can be interpreted in terms of the existence of four critical values of  $V_l$  for certain values of  $c_\infty$ . (In addition to the three critical values shown in Figures 1 and 2, we note that for sufficiently large  $V_l$ ,  $c_\infty^*$  ultimately increases on the morphological branch.<sup>[6]</sup>)

As discussed by Coriell *et al.*<sup>[2]</sup> for the nonrotating case, at each value of  $\Omega_0$ , the onset of morphological instability occurs *via* a short wavelength (large wavenumber) instability while convective instability sets in *via* disturbances with relatively longer wavelengths. In the following section, this point is discussed in the context of the mechanism by which rotation inhibits the onset of convection.

For  $G_L = 400 \text{ K cm}^{-1}$ , Figure 2 shows stability boundaries ( $c_\infty^*$  vs  $V_l$ ) analogous to those for  $G_L = 200 \text{ K cm}^{-1}$ . Aside from a slight shift of the stability boundaries to higher values of  $c_\infty^*$ , the results are qualitatively similar to those for  $G_L = 200 \text{ K cm}^{-1}$ . In particular, the onset of convection is suppressed but the morphological instability is not influenced by rotation, and the critical value of  $c_\infty$  passes through a minimum near  $V_l = 1 \mu \text{ s}^{-1}$ .

## VI. DISCUSSION

The remarkable stabilization obtainable at low growth rates (more than a hundredfold increase in the critical value of  $c_\infty$  at  $V_l = 1 \mu \text{ s}^{-1}$  can be achieved by rotating the layer at 500 rpm for the two values of  $G_L$  considered) is undoubtedly due to the well-known Taylor-Proudman mechanism described by Chandrasekhar.<sup>[27]</sup> According to the Taylor-Proudman theorem, steady motion parallel

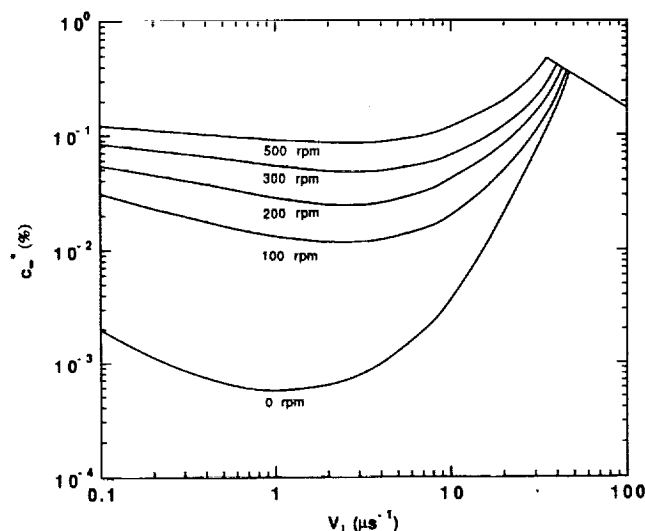


Fig. 2— $V_l$ - $c_\infty^*$  stability boundaries for  $G_L = 400 \text{ K cm}^{-1}$ , with  $\Omega_0 = 0, 100, 200, 300$ , and  $500 \text{ rpm}$ .

to the axis of rotation in a uniformly rotating inviscid fluid is prohibited at any nonzero rotation rate. If this theorem were strictly applicable to a viscous fluid, the onset of steady convection would be prohibited, since the flow in convection cells must have a vertical component. Instead, in a viscous fluid, one sees an inhibition of the onset of steady convection, with the degree of inhibition (expressed here as an increase in  $c_\infty$ ) increasing with  $\Omega_0$ . That the onset of oscillatory convection is hardly affected is due to the fact that the Taylor-Proudman theorem applies only to steady flows. It is also not surprising that the morphological instability is unaffected by rotation. The morphological instability occurs at very short wavelengths, so the motion is almost perpendicular to the solidification front (*i.e.*, aligned with the axis of rotation). Hence, the Coriolis acceleration does not sensibly affect the morphological instability.

For a horizontally unbounded binary fluid layer in which the density depends on temperature and one composition variable, Pearlstein's linear stability analysis<sup>[33]</sup> shows that Coriolis effects generally inhibit the onset of convection (by the Taylor-Proudman mechanism). Under some conditions, however, rotation can destabilize the layer, depending on the values of  $Pr$ ,  $Sc$ , the dimensionless rotation rate (characterized by a Taylor number), and the dimensionless temperature or solute gradients (characterized by thermal and solutal Rayleigh numbers). For conditions under which destabilization (on a linear basis) occurs relative to the nonrotating case, instability sets in *via* an oscillatory mode, in which the natural frequency of oscillation of a buoyant fluid element is tuned (by rotation) in such a way that there is a local minimum in the critical value of  $Ra_T$  as a function of the dimensionless rotation rate. This behavior was found<sup>[33]</sup> for  $Pr$  and  $Sc$  both less than unity, although there is no apparent reason why such destabilization cannot occur under other conditions when onset is *via* an oscillatory mode.

Although Pearlstein<sup>[33]</sup> found in the rotating doubly diffusive case that for  $Pr < 1 < Sc$  (a condition satisfied in the present case, in which  $Pr = 0.023$  and  $Sc = 81$ ) there can exist as many as three critical values of the solute Rayleigh number for certain values of the Taylor, Prandtl, Schmidt, and thermal Rayleigh numbers, we have found no evidence of such multivalued stability boundaries in the present calculations. As in the case investigated earlier,<sup>[33]</sup> it is possible that such behavior occurs in relatively small regions of the parameter space ( $G_L$ ,  $V_l$ , *etc.*) and has gone undetected so far. As discussed in Section V, however, Figures 1 and 2 imply that for certain values of  $c_\infty$ , there exist four critical values of  $V_l$  (including the unshown portion of the morphological branch).

Even though the foregoing analysis is restricted to a horizontally unbounded fluid layer, the work of Homsy and Hudson<sup>[29]</sup> and Bühler and Oertel<sup>[47]</sup> suggests that its predictions will be qualitatively correct for finite aspect ratios (ratio of mold radius to height) if the parameter  $\Omega_0^2 R_0 / g$  (a Froude number, where  $R_0$  is the mold radius) is sufficiently small. For the onset of thermal convection in rotating water or mercury layers heated from below, the excellent quantitative agreement between classical linear stability analysis for a horizontally unbounded layer<sup>[24,25,44]</sup> and experimental work for finite aspect

ratios<sup>[44,48,49]</sup> provides a clear demonstration of the potential of the Coriolis acceleration to suppress buoyancy-driven convection in a rotating fluid.

Interpretation of the results of a stability analysis restricted to infinitesimal disturbances is obviously subject to the caveat that larger disturbances might grow, even though sufficiently small disturbances are predicted to decay. Indeed, it is known that for rotating fluid layers heated from below, the onset of thermal convection sometimes does occur<sup>[50,51,52]</sup> at lower Rayleigh numbers than predicted by linear theory. However, in that case, accounting for finite (*i.e.*, noninfinitesimal) amplitude disturbances modifies the quantitative predictions of the theory; the basic qualitative prediction of stabilization by rotation remains unchanged.

The relatively modest rotation rates required to significantly inhibit the onset of convection in the Pb-Sn system make the proposed method an interesting candidate for a program of laboratory experiments. (We note here that the experimental work of Müller<sup>[17]</sup> and Weber *et al.*<sup>[18]</sup> focuses on the effect of rotation on the time-dependence of the supercritical flow, with no information given on the effect of rotation on the suppression of motion. Furthermore, although these authors have concluded that the Coriolis acceleration is key to the elimination of striations at high rotation rates, their experimental design complicates the separation of effects of the Coriolis acceleration from the increased "pseudo-gravitational" effects associated with the centripetal acceleration.) Experiments might be conducted using a completely filled cylindrical mold, thermally insulated on the vertical surface and mounted axisymmetrically on a rotating horizontal turntable. If the liquid at the top of the rotating mold is in contact with a gas or vacuum, it will have a nearly paraboloidal free surface, on which the elevation above the point on the axis of rotation is  $\Delta z = \Omega_0^2 r^2 / (2g)$ . Although this configuration is consistent with rigid-body rotation, it also leads to a nearly paraboloidal solid-melt interface. For high rotation rates or large mold radius, this will in turn lead to significant radial variations in the solidified alloy. Also, cooling at the radial boundary leads to a radial temperature gradient, which in turn leads to significant centrifugal effects. For these reasons, the results of the present analysis cannot be compared to the experimental work of Kou,<sup>[21]</sup> Kou *et al.*,<sup>[22]</sup> or Sample and Hellawell,<sup>[23]</sup> in which strong radial variations in macrosegregation are observed in the solid. Experiments of the type proposed above were initiated some time ago by Copley<sup>[53]</sup> for the crystallization of ammonium chloride from aqueous solution.

Finally, we note that for many binary systems, plane-front solidification does not occur at practical growth velocities, and that the morphological instability results in dendritic solidification. In this case, rotation might also suppress buoyancy-driven convection in the melt and interdendritic liquid; this possibility is currently being investigated by us for the Pb-Sn system.

## LIST OF SYMBOLS

$a$  magnitude of wavevector  
 $a_x$  x-component of wavevector

$a_y$  y-component of wavevector  
 $c_L$  disturbance concentration  
 $\bar{c}_L$  basic state concentration distribution  
 $C_L$  amplitude of disturbance concentration  
 $c_\infty$  bulk concentration  
 $c_\infty^*$  critical bulk concentration  
 $D_L$  diffusion coefficient  
 $g$  magnitude of gravitational acceleration  
 $G$   $G_S/G_L$   
 $G_C$   $(k-1)\rho_S c_\infty V_I / (k\rho_{L0} D_L)$  (nominal concentration gradient at interface)  
 $G_L$  nominal liquid-side temperature gradient at interface  
 $G_S$   $(LV_I + G_L k_L) / k_S$  (nominal solid-side temperature gradient at interface)  
 $h$  dimensionless height of computational domain in liquid and solid  
 $H$   $D_L / V_I$   
 $\mathbf{i}_z$  unit vector in z-direction  
 $k$  segregation coefficient  
 $k_L$  thermal conductivity of liquid  
 $k_L^*$   $G_L k_L H / (LD_L)$   
 $k_S$  thermal conductivity of solid  
 $k_S^*$   $G_L k_S H / (LD_L)$   
 $L$  latent heat of fusion per unit volume  
 $Le$   $D_L / \kappa_L$  (Lewis number)  
 $m^*$   $m_L G_C / G_L$   
 $m_L$  slope of liquidus  
 $p$  disturbance pressure  
 $Pr$   $\nu / \kappa_L$  (Prandtl number)  
 $\mathbf{r}$  position vector  
 $R_0$  mold radius  
 $Ra_T$   $\alpha_T g G_L H^4 / (\kappa_L \nu)$  (thermal Rayleigh number)  
 $Ra_S$   $\alpha_C g c_\infty H^3 / (D_L \nu)$  (solutal Rayleigh number)  
 $Sc$   $\nu / D_L$  (Schmidt number)  
 $t$  time  
 $T_L$  disturbance temperature in melt  
 $\bar{T}_L$  basic state temperature distribution in melt  
 $T_M$  melting temperature of Pb  
 $T_M^*$   $T_M \Psi / (G_L H^2)$   
 $T_S$  disturbance temperature in solid  
 $\bar{T}_S$  basic state temperature distribution in solid  
 $\mathbf{u}$  disturbance velocity  
 $\bar{\mathbf{u}}$  basic state velocity  
 $V_I$  nominal growth rate  
 $w$  z-component of disturbance velocity  
 $W$  amplitude of z-component of disturbance velocity  
 $x, y, z$  cartesian coordinates  
 $X, Y, Z$  dimensionless cartesian coordinates  
 $z_1$   $(2Z + h) / h$  (vertical coordinate in solid)  
 $z_2$   $(2Z - h) / h$  (vertical coordinate in liquid)  
 $\alpha_C$  solutal expansion coefficient  
 $\alpha_T$  thermal expansion coefficient  
 $\beta$  amplitude of disturbed interface position  
 $\gamma$   $(1 - k) / k$   
 $\varepsilon$   $\rho_S / \rho_{L0} - 1$  (fractional shrinkage)  
 $\eta$  interface deflection relative to nominally planar condition  
 $\Theta_L$  amplitude of disturbance temperature in melt  
 $\Theta_S$  amplitude of disturbance temperature in solid  
 $\kappa$   $\kappa_S / \kappa_L$   
 $\kappa_L$  thermal diffusivity of liquid

$\kappa_S$	thermal diffusivity of solid
$\nu$	kinematic viscosity
$\rho$	$\rho_S/\rho_{L0}$
$\rho_L$	local density of liquid
$\rho_{L0}$	density of liquid at reference temperature and composition
$\rho_S$	density of solid
$\sigma$	temporal eigenvalue
$\tau$	dimensionless time
$\Psi$	capillary coefficient
$\Omega$	angular velocity
$\Omega_0$	magnitude of $\Omega$
$\Omega_0^*$	$2\Omega_0 H^2/\nu$ (square root of the Taylor number $Ta = 4\Omega_0^2 H^4/\nu^2$ )
$\Omega_z$	amplitude of z-component of disturbance vorticity
$\omega_z$	z-component of disturbance vorticity

## ACKNOWLEDGMENTS

The authors acknowledge several helpful discussions with Professor David R. Poirier of the University of Arizona. We also thank an anonymous reviewer for his perceptive comments. This work was supported by the Microgravity Science and Applications Division of the National Aeronautics and Space Administration through Grant No. NAG3-1121. Partial support from NSF Grant CTS-9017181 is also acknowledged.

## REFERENCES

- W.W. Mullins and R.F. Sekerka: *J. Appl. Phys.*, 1964, vol. 35, pp. 444-51.
- S.R. Coriell, M.R. Cordes, W.J. Boettinger, and R.F. Sekerka: *J. Cryst. Growth*, 1980, vol. 49, pp. 13-28.
- M.E. Glicksman, S.R. Coriell, and G.B. McFadden: *Ann. Rev. Fluid Mech.*, 1986, vol. 18, pp. 307-35.
- R.F. Sekerka and S.R. Coriell: in *Proc. 6th Europ. Symp. on Material Sciences under Microgravity Conditions*, Bordeaux, December 2-5, 1986, ESA-SP-256, pp. 3-11, 1987.
- M.G. Worster: *J. Fluid Mech.*, 1991, vol. 224, pp. 335-59.
- S.H. Davis: *J. Fluid Mech.*, 1990, vol. 212, pp. 241-62.
- H.E. Huppert: *J. Fluid Mech.*, 1990, vol. 212, pp. 209-40.
- V.I. Polezhaev: in *Crystals, Vol. 10, Growth and Defect Structures*, H.C. Freyhardt, ed., Springer-Verlag, Berlin, 1988, pp. 87-141.
- G. Müller: in *Crystals, Vol. 12, Crystal Growth from the Melt*, H.C. Freyhardt, ed., Springer-Verlag, Berlin, 1988.
- A.F. Giamei and B.H. Kear: *Metall. Trans.*, 1970, vol. 1, pp. 2185-92.
- D.R. Poirier, M.C. Flemings, R. Mehrabian, and H.J. Klein: in *Advances in Metal Processing*, J.J. Burke, R. Mehrabian, and V. Weiss, eds., Plenum, New York, NY, 1981, pp. 277-317.
- S.D. Ridder, S. Kou, and R. Mehrabian: *Metall. Trans. B*, 1981, vol. 12B, pp. 435-47.
- A.L. Maples and D.R. Poirier: *Metall. Trans. B*, 1984, vol. 15B, pp. 163-72.
- J.I.D. Alexander, J. Ouazzani, and F. Rosenberger: *J. Cryst. Growth*, 1989, vol. 97, pp. 285-302.
- J.C. Heinrich, S. Felicelli, P. Nandapurkar, and D.R. Poirier: *Metall. Trans. B*, 1989, vol. 20B, pp. 883-91.
- J.C. Heinrich, S. Felicelli, P. Nandapurkar, and D.R. Poirier: AIAA Paper No. 89-0626, 1989.
- G. Müller: *J. Cryst. Growth*, 1990, vol. 99, pp. 1242-57.
- W. Weber, G. Neumann, and G. Müller: *J. Cryst. Growth*, 1990, vol. 100, pp. 145-58.
- H.P. Greenspan: *The Theory of Rotating Fluids*, Cambridge University Press, Cambridge, UK, 1968.
- E.O. Schulz-DuBois: *J. Cryst. Growth*, 1972, vol. 12, pp. 81-87.
- S. Kou: Ph.D. Thesis, Massachusetts Institute of Technology, Cambridge, MA, 1978.
- S. Kou, D.R. Poirier, and M.C. Flemings: *Metall. Trans. B*, 1978, vol. 9B, pp. 711-19.
- A.K. Sample and A. Hellawell: *Metall. Trans. A*, 1984, vol. 15A, pp. 2163-73.
- S. Chandrasekhar: *Proc. R. Soc. London A*, 1953, vol. 217, pp. 306-27.
- S. Chandrasekhar and D.D. Elbert: *Proc. R. Soc. London A*, 1955, vol. 231, pp. 198-210.
- P.P. Niiler and F.E. Bisschopp: *J. Fluid Mech.*, 1965, vol. 22, pp. 753-61.
- S. Chandrasekhar: *Hydrodynamic and Hydromagnetic Stability*, Clarendon, Oxford, UK, 1961, pp. 76-85.
- G.M. Homsy and J.L. Hudson: *J. Fluid Mech.*, 1969, vol. 35, pp. 33-52.
- G.M. Homsy and J.L. Hudson: *J. Fluid Mech.*, 1971, vol. 45, pp. 353-73.
- G.M. Homsy and J.L. Hudson: *J. Fluid Mech.*, 1971, vol. 48, pp. 605-24.
- G.M. Homsy and J.L. Hudson: *Int. J. Heat Mass Transfer*, 1971, vol. 14, pp. 1149-59.
- G.M. Homsy and J.L. Hudson: *Appl. Sci. Res.*, 1972, vol. 26, pp. 53-67.
- A.J. Pearlstein: *J. Fluid Mech.*, 1981, vol. 103, pp. 389-412.
- S. Sengupta and A.S. Gupta: *Z. Angew. Math. Phys.*, 1971, vol. 22, pp. 906-14.
- A. Masuda: *J. Oceanogr. Soc. Jpn.*, 1978, vol. 34, pp. 8-16.
- J.C. Antoranz and M.G. Velarde: *Phys. Lett. A*, 1978, vol. 65, pp. 377-79.
- J.C. Antoranz and M.G. Velarde: *Phys. Fluids*, 1979, vol. 22, pp. 1038-43.
- R.W. Schmitt and R.B. Lambert: *J. Fluid Mech.*, 1979, vol. 90, pp. 449-63.
- N. Riahi: *J. Phys. Soc. Jpn.*, 1983, vol. 52, pp. 2620-21.
- S. Worthem, E. Mollo-Christensen, and F. Ostapoff: *J. Fluid Mech.*, 1983, vol. 133, pp. 297-319.
- J.K. Bhattacharjee: *Phys. Fluids*, 1988, vol. 31, pp. 2456-61.
- J.K. Bhattacharjee: *Phys. Fluids*, 1988, vol. 31, pp. 2462-66.
- J.K. Bhattacharjee: *Phys. Rev. A*, 1988, vol. 37, pp. 1368-70.
- Y. Nakagawa and P. Frenzen: *Tellus*, 1955, vol. 7, pp. 1-21.
- H.B. Keller: *Numerical Solution of Two Point Boundary Value Problems*, SIAM, Philadelphia, PA, 1976, pp. 49-58.
- A. Zebib: *J. Comput. Phys.*, 1987, vol. 70, pp. 521-25.
- K. Bühler and H. Oertel: *J. Fluid Mech.*, 1982, vol. 114, pp. 261-82.
- D. Fultz and Y. Nakagawa: *Proc. R. Soc. London A*, 1955, vol. 231, pp. 211-25.
- I.R. Goroff: *Proc. R. Soc. London A*, 1960, vol. 254, pp. 537-41.
- G. Veronis: *J. Fluid Mech.*, 1959, vol. 5, pp. 401-35.
- G. Veronis: *J. Fluid Mech.*, 1966, vol. 24, pp. 545-54.
- G. Veronis: *J. Fluid Mech.*, 1968, vol. 31, pp. 113-39.
- S.M. Copley: University of Southern California, Los Angeles, CA, private communication, 1976.



**Coriolis Effects on the Stability of  
Plane-Front Solidification of  $\text{Hg}_{1-x}\text{Cd}_x\text{Te}$**

by

**Alparslan Öztekin\***

and

**Arne J. Pearlstein**

**Department of Mechanical and Industrial Engineering  
University of Illinois at Urbana-Champaign  
1206 West Green Street  
Urbana, IL 61801**

---

\* Present address: Department of Chemical Engineering  
Massachusetts Institute of Technology  
Cambridge, MA 02139



## Abstract

A linear stability analysis is used to assess the potential of steady uniform rotation about the vertical axis to suppress the onset of convection during directional solidification of mercury cadmium telluride cooled from below. Since for sufficiently small  $x$  the density of  $\text{Hg}_{1-x}\text{Cd}_x\text{Te}$  does not depend monotonically on temperature, there is a range of operating conditions (bulk CdTe mole fraction, nominal solidification rate, and liquid-side temperature gradient) for which, adjacent to the liquid-solid interface there is a sublayer in which the thermal stratification is destabilizing. This differs from the normal case (i.e., binary alloys characterized by a linear equation of state, such as Pb-Sn), in which the thermal stratification is stabilizing everywhere. Thus, in  $\text{Hg}_{1-x}\text{Cd}_x\text{Te}$  melts there can exist a critical bulk CdTe mole fraction  $x_\infty$  below which plane-front solidification is unstable at all solidification rates  $V_I$ , whereas in the normal case plane-front solidification at any  $x_\infty$  is linearly stable for sufficiently small  $V_I$ . Moreover, for  $\text{Hg}_{1-x}\text{Cd}_x\text{Te}$  there can exist a critical solidification rate  $V_I^{\text{cr}}$  such that for  $V_I < V_I^{\text{cr}}$  plane-front solidification is unstable for all  $x_\infty$ . Our results show that modest rates of uniform rotation can significantly suppress the onset of buoyancy-driven convection for the  $\text{Hg}_{1-x}\text{Cd}_x\text{Te}$  system, and that rotation can substantially increase the critical solidification rate  $V_I^{\text{cr}}$  beyond which plane-front solidification is unstable for all bulk CdTe mole fractions.



# 1. Introduction

The crystal growth of mercury cadmium telluride ( $\text{Hg}_{1-x}\text{Cd}_x\text{Te}$ ) is of considerable interest due to its extensive use in the fabrication of infrared detectors and other electro-optical devices. This has led to a number of experimental [1,2] and theoretical [3-5] studies of the solidification of  $\text{Hg}_{1-x}\text{Cd}_x\text{Te}$  from the melt. For a more extensive discussion, the reader is referred to the reviews by Micklethwaite [6] and Capper [7]. In those applications in which crystal size and defect density are critical, with the goal being to produce large, nearly perfect single crystals, it is frequently desired to achieve "plane-front" solidification in order to reduce segregation. If this could be accomplished, the process would be steady in a reference frame moving with the interface, and the only spatial variation would be in a direction normal to the interface. However, in real systems, several instabilities can cause departures from the nominally steady one-dimensional plane-front case.

First, the liquid-solid interface may be subject to a so-called morphological instability, studied extensively since the early work of Mullins and Sekerka [8]. This instability deforms the nominally planar interface, ultimately leading to formation of a two-phase "mushy zone" of dendrites and interdendritic liquid. Departures from one-dimensionality and steadiness in the mushy zone can result in solute segregation in the solidified material. Second, depending on how the liquid density varies with temperature and composition, and according to whether the segregation coefficient is greater or less than unity (i.e., whether solute is rejected or preferentially incorporated at the interface), the melt may be subject to a buoyancy-driven convective instability. The resulting flow can contribute significantly to the redistribution of solute, and hence to segregation [9-12].

Convective and morphological instabilities in a binary liquid undergoing directional solidification were first studied by Coriell et al. [13] for Pb-Sn alloys. These authors showed that motion may occur due to either morphological or convective instabilities, and that the buoyancy force does not sensibly alter the criterion for onset of the former, which occurs at higher wavenumbers than the latter. Subsequent work has been reviewed by Glicksman et al. [14], and Sekerka and Coriell [15]. More general discussions of the effects of convection on plane-front and dendritic solidification have been given recently by Müller [12], Worster [16], Davis [17], Huppert [18], and Polezhaev [19].

One means by which the onset of buoyancy-driven convection in a density-stratified fluid layer can be inhibited is to subject the layer to a magnetic field aligned perpendicular or



parallel to the stratification [12]. For horizontal Pb-Sn layers solidified from below at several growth velocities, Coriell et al. [13] showed theoretically that the critical bulk Sn concentration above which instability occurs can be increased an order of magnitude by a vertical magnetic field of the order of one tesla. This technique requires the liquid to be an electrical conductor, and is applicable to metallic alloys, semiconductors, and aqueous solutions.

Segregation might also be controlled by increasing or decreasing the magnitude of the gravitational acceleration or changing its direction. The theoretical studies of Coriell et al. [13], Alexander et al. [20], and Heinrich et al. [21,22] suggested that macrosegregation during directional solidification of binary alloys can be reduced by operating in a low-gravity environment. Müller [23] and Weber et al. [24] have recently discussed solidification under conditions where the magnitude of the body force is greater or less than that of normal gravity.

Both gravity and an external magnetic field are body forces which act on the fluid. As opposed to contact forces such as pressure, viscous stress, and surface tension, which act on the surfaces of a fluid element, body forces act on the mass of a fluid element. Hence, their local strengths are proportional to the local fluid density. In addition to gravitational and magnetic body forces, there are other "pseudo-body forces" which manifest themselves as fictitious accelerations (centrifugal and Coriolis) when the reference frame to which the fluid motion is referred undergoes steady rotation relative to an inertial frame. (An additional fictitious acceleration associated with unsteady rotation relative to the inertial frame will not concern us here.) Although these accelerations do not correspond directly to forces (unlike the gravitational acceleration), they have the same mathematical form as accelerations associated with body forces, and can have dynamical consequences equally as profound as the gravitational and magnetic forces discussed above [25]. In light of this, and the fact that imposition of an external magnetic field or modification of the gravitational field is not always feasible, the possibility of using rotation to suppress the onset of convection in a liquid undergoing directional solidification is of interest.

The idea of using rotation to affect fluid motion and solute distribution in the melt, and ultimately segregation in the solid, is not a new one. Beginning with the seminal work of Czochralski [26] on the use of differential rotation of a growing crystal relative to the crucible, there have been many attempts to use rotation to reduce compositional variations in crystal growth. Among these are the accelerated crucible rotation technique (ACRT) developed by Scheel and Schulz-DuBois [27] and Schulz-DuBois [28], in which axisymmetric azimuthal or





more complicated shear flows are generated by unsteady rotation of the crucible relative to the fluid. At about the same time, Copley [29] conducted preliminary experiments in which the solidification of aqueous ammonium chloride was conducted on a rotating turntable. Later, Kou [30], Kou et al. [31], and Poirier et al. [10] experimentally investigated the effects of rotation on macrosegregation in the solidification of Pb-Sn and Al-Cu alloys under conditions such that centrifugal effects were thought to be dominant. Sample and Hellawell [32,33] experimentally investigated the effects of mold precession on the solidification of Pb-Sn alloys and aqueous ammonium chloride solutions. More recently, Müller [23], Weber et al. [24], Rodot et al. [34], and Chen and Chen [35] have considered crystal growth in or on a centrifuge.

Rotation can manifest its effects in a number of ways. The rotation of one or more solid boundaries can generate a shear flow (as in the ACRT technique) which directly affects the redistribution of solute through the advection term ( $\mathbf{u} \cdot \nabla \mathbf{x}$ , where  $\mathbf{u}$  is the velocity vector and  $\mathbf{x}$  is the mole fraction) in the solute transport equation. Alternatively, if all solid boundaries rotate at the same steady angular velocity, then the fluid may be in solid-body rotation. In a rotating frame, the fluid is then motionless ( $\mathbf{u} = 0$ ) and there is no advective contribution to solute transport. However, the resulting fictitious accelerations can have important consequences for the stability of the solid-body rotation [25,36], either enhancing or suppressing the secondary flows responsible for solute redistribution.

As discussed above, steady rotation at constant angular velocity  $\Omega$  about a fixed axis can influence the motion of a fluid by means of two "pseudo-body" forces. These correspond to the centripetal and Coriolis accelerations, for which the terms  $\rho_L \Omega \times \Omega \times \mathbf{r}$  and  $2\rho_L \Omega \times \mathbf{u}$ , respectively, are added to the momentum equation. Here,  $\mathbf{r}$  is the position vector measured from the axis of rotation,  $\mathbf{u}$  is the local fluid velocity relative to the rotating frame, and  $\rho_L$  is the local density of the liquid. If the density variation is neglected, the centrifugal acceleration has no dynamical consequences. If the density variation cannot be neglected, then for a given geometry, the ratio of the magnitudes of these accelerations is  $2u_{\perp}/(\Omega_o r_o)$ , where  $\Omega_o$ ,  $r_o$ , and  $u_{\perp}$  are the rotation rate, characteristic length (e.g., mold radius), and component of fluid velocity relative to the moving frame and perpendicular to the axis of rotation, respectively. Thus, if  $u_{\perp}$  is independent of or increases sublinearly with  $\Omega_o$ , the importance of the Coriolis acceleration relative to the centrifugal acceleration will increase with decreasing  $\Omega_o$ .

Öztekin and Pearlstein [37] have recently considered the effect of Coriolis acceleration on the stability of plane-front solidification of dilute Pb-Sn binary alloys, for which a linear



dependence of density on temperature and mass fraction is an excellent approximation to the equation of state. Their theoretical work shows that relatively modest rotation rates can significantly suppress the onset of buoyancy-driven convection in horizontally unbounded layers of that alloy undergoing directional solidification.

The question naturally arises as to what effects rotation has on the onset of convection in the  $\text{Hg}_{1-x}\text{Cd}_x\text{Te}$  system, in which the nonmonotonic dependence of liquid density on temperature [38] can give rise to, adjacent to the solid/liquid interface, a sublayer in which the thermal stratification is destabilizing. It is the purpose of the present work to investigate this question.

We follow the approach of Öztekin and Pearlstein [37] and use a linear stability analysis to study the effects of the Coriolis acceleration on the onset of instability during solidification of  $\text{Hg}_{1-x}\text{Cd}_x\text{Te}$ . The paper is organized as follows. In §2, we present the governing equations. The one-dimensional basic state and linear disturbance equations are given in §3. The latter are nondimensionalized and Fourier-decomposed in §4. The numerical solution technique is described in §5. Results for  $\text{Hg}_{1-x}\text{Cd}_x\text{Te}$  are presented in §6, followed by a discussion in §7.

## 2. Governing Equations and Formulation

We adopt the solidification model used by Coriell et al. [13] and Öztekin and Pearlstein [37], in which the fluid properties, except density, are taken to be constant throughout the liquid. The variation of density with temperature and CdTe mole fraction will be accounted for in the buoyancy term and neglected everywhere else. The equations governing the fluid motion are the Oberbeck-Boussinesq equations in a reference frame translating with the nominally steady velocity ( $i_z V_1$ ) of the moving interface and rotating at a constant angular velocity  $\Omega$  about the vertical axis

$$\nabla \cdot \mathbf{u} = 0, \quad (1a)$$

$$\frac{\partial \mathbf{u}}{\partial t} + \mathbf{u} \cdot \nabla \mathbf{u} + 2\Omega \times \mathbf{u} + \Omega \times \Omega \times \mathbf{r} = -\frac{1}{\rho_{Lo}} \nabla p - \frac{\rho_L(x_L, T_L)}{\rho_{Lo}} i_z + \nu \nabla^2 \mathbf{u}, \quad (1b)$$

$$\frac{\partial T_L}{\partial t} + \mathbf{u} \cdot \nabla T_L = \kappa_L \nabla^2 T_L, \quad (1c)$$

$$\frac{\partial x_L}{\partial t} + \mathbf{u} \cdot \nabla x_L = D_L \nabla^2 x_L, \quad (1d)$$

where the dependent variables  $\mathbf{u}$ ,  $p$ ,  $x_L$ , and  $T_L$  are respectively, velocity, pressure, CdTe mole



fraction, and temperature in the liquid,  $i_z$  is the unit vector in the Z-direction,  $V_l$  is the nominal solidification rate (with dimensions of velocity),  $\kappa_L$  is the thermal diffusivity of the liquid,  $D_L$  is the diffusivity of CdTe in the liquid,  $\nu$  is the kinematic viscosity,  $\rho_{L0}$  is the liquid density at a particular reference temperature and CdTe mole fraction,  $\Omega = \Omega_0 i_z$  is the constant angular velocity, and  $g$  is the magnitude of the earth's gravitational acceleration. We note that the fluid velocity  $u$  and interface velocity  $V_s$  (*vide infra*) are referred to the moving frame, unlike the velocities employed in reference 13. Finally, we note that (1d) assumes that mass transport in the system can be accounted for using a binary model, in which CdTe diffuses through HgTe, and that the trace quantities of atomic Hg, Cd, and Te present in the liquid are negligible.

We have used an equation of state based on the experimental data of Chandra and Holland [38] and Mokrovskii and Regel [39]. The variation of liquid density with temperature and CdTe mole fraction is represented by bivariate polynomials

$$\rho_L(x, T) = \sum_{i=0}^3 \sum_{j=0}^{4-i} b_{ij} x^i (T - 1030 \text{ K})^j \quad \text{for } T < T_{\max}(x) \quad (2a)$$

and

$$\rho_L(x, T) = \sum_{i=0}^3 \sum_{j=0}^1 d_{ij} x^i (T - 1030 \text{ K})^j \quad \text{for } T > T_{\max}(x) \quad (2b)$$

where

$$T_{\max}(x) = \sum_{i=0}^3 r_i x^i \quad (3)$$

is a polynomial fit to the largest temperature for which liquid density data are available in the literature. The linear dependence of density on temperature (2b) for  $T > T_{\max}(x)$  is chosen to match  $\rho_L$  and  $\partial \rho_L / \partial T$  at  $T_{\max}$ . Details are given in Öztekin and Pearlstein [40].

The energy equation in the solid is

$$\frac{\partial T_s}{\partial t} - V_l \frac{\partial T_s}{\partial z} = \kappa_s \nabla^2 T_s, \quad (4)$$

where  $T_s$  is the temperature in the solid, and  $\kappa_s$  is the thermal diffusivity of the solid.

The boundary conditions at the liquid-solid interface are



$$-(\epsilon V_S + \rho^* i_z V_I) \cdot n = u \cdot n, \quad (5a)$$

$$(u + i_z V_I) \cdot t = 0 \quad (5b)$$

where  $n$  and  $t$  are unit vectors normal and tangential to the interface, respectively,  $V_S$  is the local interface velocity,  $\rho^* = \rho_S / \rho_{Lo}$  is the density ratio,  $\rho_S$  is the (constant) solid density, and  $\epsilon = \rho^* - 1$  is the fractional shrinkage. The energy balance at the liquid-solid interface is

$$L(V_S + i_z V_I) \cdot n = (-k_L \nabla T_L + k_S \nabla T_S) \cdot n, \quad (5c)$$

where the right-hand side represents the difference between the normal components of the heat flux vectors in the liquid and solid, and the left-hand side represents the product of the latent heat  $L(x_\infty)$  and the normal component of the solidification velocity. Here  $k_L(x_\infty)$  and  $k_S(x_\infty)$  are the thermal conductivities of the liquid and solid, respectively. The solute balance at the interface is

$$\rho_S(x_L - x_S)(V_S + i_z V_I) \cdot n = -\rho_{Lo} D_L \nabla x_L \cdot n, \quad (5d)$$

where  $x_S$  is the CdTe mole fraction in the solid, and solid-state diffusion has been neglected. We also require the temperature to be continuous

$$T_L = T_S, \quad (5e)$$

across the interface, the liquid and solid concentrations of CdTe at the interface to be related according to the binary phase diagram

$$x_S = k x_L, \quad (5f)$$

where  $k$  is the segregation coefficient, and the temperature and CdTe mole fraction at the interface to be related by

$$T_L = T_M + m_L x_L - T_M \Psi \left( \frac{1}{R_1} + \frac{1}{R_2} \right), \quad (5g)$$

where  $T_M$  is the melting temperature of HgTe,  $m_L$  is the slope of the liquidus,  $R_1$  and  $R_2$  are the principal radii of curvature of the interface, and  $\Psi$  is the capillary coefficient. The temperature- and composition-dependence of most of the thermophysical properties (other than  $\rho$ ) is given in Appendix A. For the remaining properties, values measured at selected temperatures and compositions are taken as constant over the entire range.





### 3. Basic State and Linear Disturbance Equations

In the reference frame described in §2, the steady one-dimensional basic state specified by

$$\bar{V}_S = 0, \quad (6a)$$

with

$$\bar{u} = -\rho^* V_I i_z, \quad (6b)$$

$$\bar{T}_L = T_M + \frac{m_L x_\infty}{k} + \frac{\kappa_L G_L}{\rho^* V_I} [1 - \exp(-\rho^* V_I Z / \kappa_L)], \quad (6c)$$

$$\bar{x}_L = x_\infty \left[ 1 + \frac{1-k}{k} \exp(-\rho^* V_I Z / D_L) \right], \quad (6d)$$

in the liquid, and

$$\bar{T}_S = T_M + \frac{m_L x_\infty}{k} + \frac{\kappa_S G_S}{V_I} [1 - \exp(-V_I Z / \kappa_S)], \quad (6e)$$

in the solid is, aside from the velocities, which we refer to a translating and rotating frame, the same as that used by Coriell et al. [13]. Here,  $\bar{V}_S$ ,  $\bar{u}$ ,  $\bar{T}_L$ ,  $\bar{x}_L$ , and  $\bar{T}_S$  are, respectively, the basic state interface velocity, velocity, temperature and CdTe distributions in the liquid, and temperature distribution in the solid, and  $G_L$  and  $G_S$  are the liquid-side and solid-side temperature gradients, respectively. Our basic state differs from that of Coriell et al. in that  $\bar{V}_S = 0$  and  $\bar{u}$  is not proportional to the shrinkage  $\epsilon$ , because in our formulation the interface and fluid velocities are referred to the same (moving) inertial reference frame.

As in stability analyses of other flows subject to uniform rotation [41-45], the linear disturbance equations we use differ from those in the nonrotating case only by addition of the Coriolis acceleration to the disturbance momentum equation. (This approximation, discussed by Homsy and Hudson [48], neglects the consequences of density variation in the term corresponding to the centrifugal acceleration.) The equations governing small disturbances in the liquid are

$$\nabla \cdot \mathbf{u}' = 0, \quad (7a)$$

$$\frac{\partial \mathbf{u}'}{\partial t} - \rho^* V_I \frac{\partial \mathbf{u}'}{\partial Z} + 2\Omega \times \mathbf{u}' = -\frac{1}{\rho_{L0}} \nabla p' - f_T T'_L i_z + f_x x'_L i_z + \nu \nabla^2 \mathbf{u}', \quad (7b)$$

$$\frac{\partial T'_L}{\partial t} - \rho^* V_I \frac{\partial T'_L}{\partial Z} + G_L w' \exp(-\rho^* V_I Z / \kappa_L) = \kappa_L \nabla^2 T'_L, \quad (7c)$$



$$\frac{\partial x'_L}{\partial t} - \rho^* V_I \frac{\partial x'_L}{\partial Z} + G_x w' \exp(-\rho^* V_I Z/D_L) = D_L \nabla^2 x'_L, \quad (7d)$$

where  $u'$ ,  $w'$ ,  $T'_L$ ,  $x'_L$ , and  $p'$  are, respectively, the disturbances to the liquid velocity, its Z-component, temperature, CdTe mole fraction, and pressure. Here, we define

$$f_T = \left. \frac{\partial \rho_L(x, T)}{\partial T} \right|_{\bar{x}_L, \bar{T}_L} \quad f_x = \left. \frac{\partial \rho_L(x, T)}{\partial x} \right|_{\bar{x}_L, \bar{T}_L} \quad (8)$$

and  $G_x = (k-1)\rho^* V_I x_\infty / (kD_L)$  is the CdTe gradient at the nominally planar interface. The disturbance energy equation in the solid is

$$\frac{\partial T'_S}{\partial t} - V_I \frac{\partial T'_S}{\partial Z} = \kappa_S \nabla^2 T'_S, \quad (9)$$

where  $T'_S$  is the temperature disturbance in the solid.

Taking the curl of (7b) and the dot product of the result with  $i_z$ , we obtain an equation

$$\frac{\partial \omega'_Z}{\partial t} - \rho^* V_I \frac{\partial \omega'_Z}{\partial Z} - 2\Omega_o \frac{\partial w'}{\partial Z} = \nu \nabla^2 \omega'_Z \quad (10)$$

for the Z-component of the vorticity,  $\omega'_Z$ . After twice taking the curl of (7b), the vertical component of the resulting equation is

$$\frac{\partial}{\partial t} \nabla^2 w' - \rho^* V_I \frac{\partial}{\partial Z} \nabla^2 w' + 2\Omega_o \frac{\partial \omega'_Z}{\partial Z} = f_T g \nabla^2 T'_L + f_x g \nabla^2 x'_L + \nu \nabla^4 w'. \quad (11)$$

The disturbance boundary conditions linearized about the nominal interface position ( $Z = 0$ ) are

$$u'(X, Y, 0, t) = \varepsilon V_I \frac{\partial \eta(X, Y, t)}{\partial X}, \quad (12a)$$

$$v'(X, Y, 0, t) = \varepsilon V_I \frac{\partial \eta(X, Y, t)}{\partial Y}, \quad (12b)$$

$$w'(X, Y, 0, t) = -\varepsilon \frac{\partial \eta(X, Y, t)}{\partial t}, \quad (12c)$$

$$\frac{\partial w'(X, Y, 0, t)}{\partial Z} = -\varepsilon V_I \nabla_\perp^2 \eta(X, Y, t), \quad (12d)$$

$$L \frac{\partial \eta(X, Y, t)}{\partial t} = -k_L \frac{\partial T'_L(X, Y, 0, t)}{\partial Z} + k_S \frac{\partial T'_S(X, Y, 0, t)}{\partial Z} + \left( \frac{\rho^* G_L k_L}{\kappa_L} - \frac{G_S k_S}{\kappa_S} \right) V_I \eta(X, Y, t), \quad (12e)$$



$$\frac{\rho^* V_1^2}{x_\infty} \eta(X, Y, t) + V_1 x'_L(X, Y, 0, t) + \frac{x_\infty}{k} \frac{\partial \eta(X, Y, t)}{\partial t} = - \frac{D_L}{\rho^* (1-k)} \frac{\partial x'_L(X, Y, 0, t)}{\partial Z}, \quad (12f)$$

$$T'_L(X, Y, 0, t) + G_L \eta(X, Y, t) = T'_S(X, Y, 0, t) + G_S \eta(X, Y, t), \quad (12g)$$

$$T'_L(X, Y, 0, t) + G_L \eta(X, Y, t) = m_L G_x \eta(X, Y, t) + m_L x'_L(X, Y, 0, t) + T_M \Psi \nabla_\perp^2 \eta(X, Y, t), \quad (12h)$$

where  $\eta$  is the interface deflection,  $V'_S(X, Y, t) = i_z \partial \eta / \partial t$  is the linearization of the disturbance interface velocity, and  $X$  and  $Y$  are horizontal coordinates.

#### 4. Nondimensionalization and Fourier Decomposition

We scale the velocity, time, length, temperature, CdTe mole fraction, and vorticity with  $\kappa_L/H$ ,  $H^2/\nu$ ,  $H$ ,  $G_L H$ ,  $x_\infty$ , and  $\kappa_L/H^2$ , respectively, where  $H = D_L/V_1$  is the characteristic length [associated with the stabilizing gradient of preferentially incorporated CdTe, see (6d)], and write the horizontal and temporal dependence of the dimensionless disturbance quantities as  $\exp(\sigma t + i a_x X^* + i a_y Y^*)$ , where  $a_x$  and  $a_y$  are the  $X$ - and  $Y$ -components of the wavevector,  $X^*$  and  $Y^*$  are the dimensionless horizontal coordinates, and  $\sigma$  is the temporal eigenvalue. Substitution into (7) and (9-12) yields

$$\sigma(D^2 - a^2)W - \frac{\rho^*}{Sc} D(D^2 - a^2)W = -F_T a^2 \Theta_L - F_x a^2 \chi_L + (D^2 - a^2)^2 W - \Omega_o^* DQ, \quad (13a)$$

$$\sigma Q - \frac{\rho^*}{Sc} DQ = \Omega_o^* DW + (D^2 - a^2)Q, \quad (13b)$$

$$\sigma Pr \Theta_L - \rho^* Le D \Theta_L = (D^2 - a^2) \Theta_L - W \exp(-\rho^* Le Z^*), \quad (13c)$$

$$\sigma Sc \chi_L - \rho^* D \chi_L = (D^2 - a^2) \chi_L + \frac{\gamma \rho^*}{Le} W \exp(-\rho^* Z^*) \quad (13d)$$

in the liquid, and

$$\sigma Pr \Theta_S - Le D \Theta_S = \kappa(D^2 - a^2) \Theta_S \quad (14)$$

in the solid. Here,  $Pr = \nu/\kappa_L$  is the Prandtl number,  $Sc = \nu/D_L$  is the Schmidt number,  $Le = D_L/\kappa_L$  is the Lewis number,  $F_T = f_T g G_L H^4/(\kappa_L \nu)$ ,  $F_x = f_x g x_\infty H^3/(\kappa_L \nu)$ ,  $\Omega_o^* = 2\Omega_o H^2/\nu$  is the square root of the Taylor number,  $\kappa = \kappa_S/\kappa_L$  is the thermal diffusivity ratio,  $Z^*$  is the dimensionless vertical coordinate, and  $\gamma = (1-k)/k$ . The boundary conditions (12a-h) at the



interface become

$$W(0) = -\varepsilon\sigma\beta Pr, \quad (15a)$$

$$DW(0) = \varepsilon a^2 \beta Le, \quad (15b)$$

$$Q(0) = 0, \quad (15c)$$

$$\sigma Sc \beta = -k_L^* D\Theta_L(0) + k_S^* D\Theta_S(0) + Le(k_L^* \rho^* - k_L^* / \kappa - 1/\kappa)\beta, \quad (15d)$$

$$(1-G)\beta = \Theta_S(0) - \Theta_L(0), \quad (15e)$$

$$(\sigma Sc + k\rho^*)\beta = -k\chi_L(0) - \frac{1}{\gamma\rho^*} D\chi_L(0), \quad (15f)$$

$$(-a^2 T_M^* + m^* - 1)\beta = \frac{m^*}{\gamma\rho^*} \chi_L(0) + \Theta_L(0), \quad (15g)$$

where  $W$ ,  $\chi_L$ ,  $Q$  and  $\Theta_L$  are, respectively, the amplitudes of the disturbances to the vertical velocity, concentration, vertical vorticity, and temperature in the liquid,  $\Theta_S$  is the amplitude of the disturbance temperature in the solid, and  $\beta$  (a constant) is the amplitude of the disturbed interface position. Here we define dimensionless parameters  $k_L^* = G_L k_L H / (LD_L)$ ,  $k_S^* = G_L k_S H / (LD_L)$ ,  $m^* = m_L G_x / G_L$ ,  $T_M^* = T_M \Psi / (G_L H^2)$ , and  $G = G_S / G_L$ . For the far-field boundary conditions, we follow Coriell et al. [13] and set all disturbances to zero

$$W = DW = Q = \chi_L = \Theta_L = 0 \quad \text{as } Z^* \rightarrow \infty, \quad (16a-e)$$

$$\Theta_S = 0 \quad \text{as } Z^* \rightarrow -\infty, \quad (16f)$$

far from the interface.

## 5. Numerical Solution

Our objective is to find conditions under which infinitesimally small disturbances neither grow nor decay for a finite number of wavenumbers, and decay for all other wavenumbers. Disturbances which neither grow nor decay are said to be neutral. The neutral disturbances can be of two types, depending on the imaginary part of  $\sigma$ . If the imaginary part of  $\sigma$  is zero for a





neutral disturbance, the onset of instability will be *via* monotonically growing disturbances (steady onset). If the imaginary part of  $\sigma$  is not zero, the neutral disturbance will oscillate in time (oscillatory onset).

In the previous section, we formulated an eigenvalue problem for two systems of ordinary differential equations on two semi-infinite intervals (in the liquid and solid), coupled by boundary conditions at the deformable interface. For convenience, we follow Coriell et al. [13] and solve the problem on a finite interval  $[-h, h]$ , where  $2h$  is the dimensionless height of the computational domain. With regard to the far-field boundary conditions at  $Z^* = \pm\infty$ , we set all disturbances to zero

$$W = DW = Q = \chi_L = \Theta_L = 0 \quad \text{at } Z^* = h \quad (17a-e)$$

in the liquid and

$$\Theta_S = 0 \quad \text{at } Z^* = -h \quad (17f)$$

in the solid. In this work, we have taken  $h$  to be at least 10, depending on the vertical structure of the basic state temperature and solute fields (6c,d). (For steady onset, we have checked a number of our results using more accurate asymptotic boundary conditions applied at  $Z^* = \pm h$  derived following Keller's [46] procedure, and have found excellent agreement between the eigenvalues computed using the two sets of boundary conditions.) Since we use Chebyshev polynomials in our numerical solution, we scale the liquid and solid regions by  $z_2 = (2Z^* - h) / h$  and  $z_1 = (2Z^* + h) / h$ , respectively, so that each region lies between  $-1$  and  $+1$ . The resulting system is then solved using a spectral Galerkin technique developed by Zebib [47]. The problem is thus reduced to a matrix eigenvalue problem

$$A s + \sigma B s = 0, \quad (18)$$

where  $\sigma$  is the temporal eigenvalue, and the elements of the square matrices  $A$  and  $B$  depend on the square of the horizontal wavenumber  $a^2 = a_x^2 + a_y^2$ , the bulk CdTe mole fraction  $x_\infty$ , and the other dimensionless parameters.

In §6, we characterize the stability of the nominally plane-front solution in terms of the bulk CdTe mole fraction  $x_\infty$  and solidification rate  $V_I$ , with all other parameters taken as fixed. As shown schematically in figure 1, there is a critical value of  $V_I$  (denoted by  $V_I^{cr}$ ) such that for  $V_I > V_I^{cr}$ , some disturbances (i.e., for some wavenumbers) grow for all values of  $x_\infty$ , while for  $V_I < V_I^{cr}$ , disturbances of every wavenumber decay for some range of bulk CdTe mole



fractions. The upper and lower limits of that range are denoted by  $x_{\infty}^*$  and  $x_{\infty}^{**}$ , respectively. To determine the critical values of  $x_{\infty}$  ( $x_{\infty}^*$  and  $x_{\infty}^{**}$ ) we first find the morphological and convective neutral curves ( $x_{\infty}$  versus  $a$ ) separating those combinations of  $x_{\infty}$  and  $a$  for which all temporal eigenvalues  $\sigma$  lie in the left half-plane (LHP) from those for which at least one eigenvalue lies in the right half-plane (RHP), corresponding to stable and unstable basic states, respectively.

In order to determine the bulk CdTe mole fraction on the morphological and convective neutral curves for an arbitrarily chosen wavenumber  $a$ , we first compute all eigenvalues  $\sigma$  of (18) at each of  $N$  values of  $x_{\infty}$  ( $x_{\infty}^{(n)}$ ,  $1 \leq n \leq N$ ) in the range  $[x_{\infty}^{\min}, 0.2]$ , where the lower bound is typically  $10^{-4}$  and the upper bound is determined by the largest CdTe mole fraction for which we have data for the equation of state. We then attempt to determine a range of  $x_{\infty}$  for which all temporal eigenvalues are in the LHP. If one of the original  $N$  values of  $x_{\infty}$  selected is stable (i.e., all temporal eigenvalues lie in the LHP), we then determine two intervals such that as  $x_{\infty}$  increases, within one a transition from instability to stability occurs, and within the other a transition from stability to instability occurs. Through these two intervals pass the convective and morphological neutral curves, respectively. If none of the original  $N$  values of  $x_{\infty}$  is stable, we choose the value (say,  $x_{\infty}^{(j)}$ ) for which the most unstable temporal eigenvalue has the smallest real part, and subdivide the interval  $[x_{\infty}^{(j-1)}, x_{\infty}^{(j+1)}]$  until we either find a stable value of  $x_{\infty}$  (at which juncture we proceed to isolate the two intervals described above), or abandon the search when the real part of the least stable temporal eigenvalue and the difference between consecutive values of  $x_{\infty}$  supports the expectation that all intermediate values of  $x_{\infty}$  are unstable. Having found the intervals of  $x_{\infty}$  in which the transitions occur, we then compute the bulk CdTe mole fractions on the convective and morphological neutral curves using a bisection method.

To compute the critical bulk CdTe mole fraction  $x_{\infty}^*$  (i.e., the minimum on the morphological neutral curve), we arbitrarily choose a wavenumber and compute the corresponding  $x_{\infty}$  on the morphological neutral curve using the procedure described above. We then fix  $x_{\infty}$  at the value computed in the previous step, and compute the eigenvalues  $\sigma$  for a discrete set of wavenumbers in a chosen range. We next select the wavenumber from among this set at which the  $\sigma$  with largest real part was obtained. If this wavenumber is at an endpoint of the chosen range, we extend the range until the wavenumber corresponding to the largest  $\text{Re}(\sigma)$  is inside the range. We then select this wavenumber and determine the corresponding  $x_{\infty}$  on the neutral curve. We continue this process until the relative change in  $x_{\infty}$  is less than  $10^{-6}$ . We



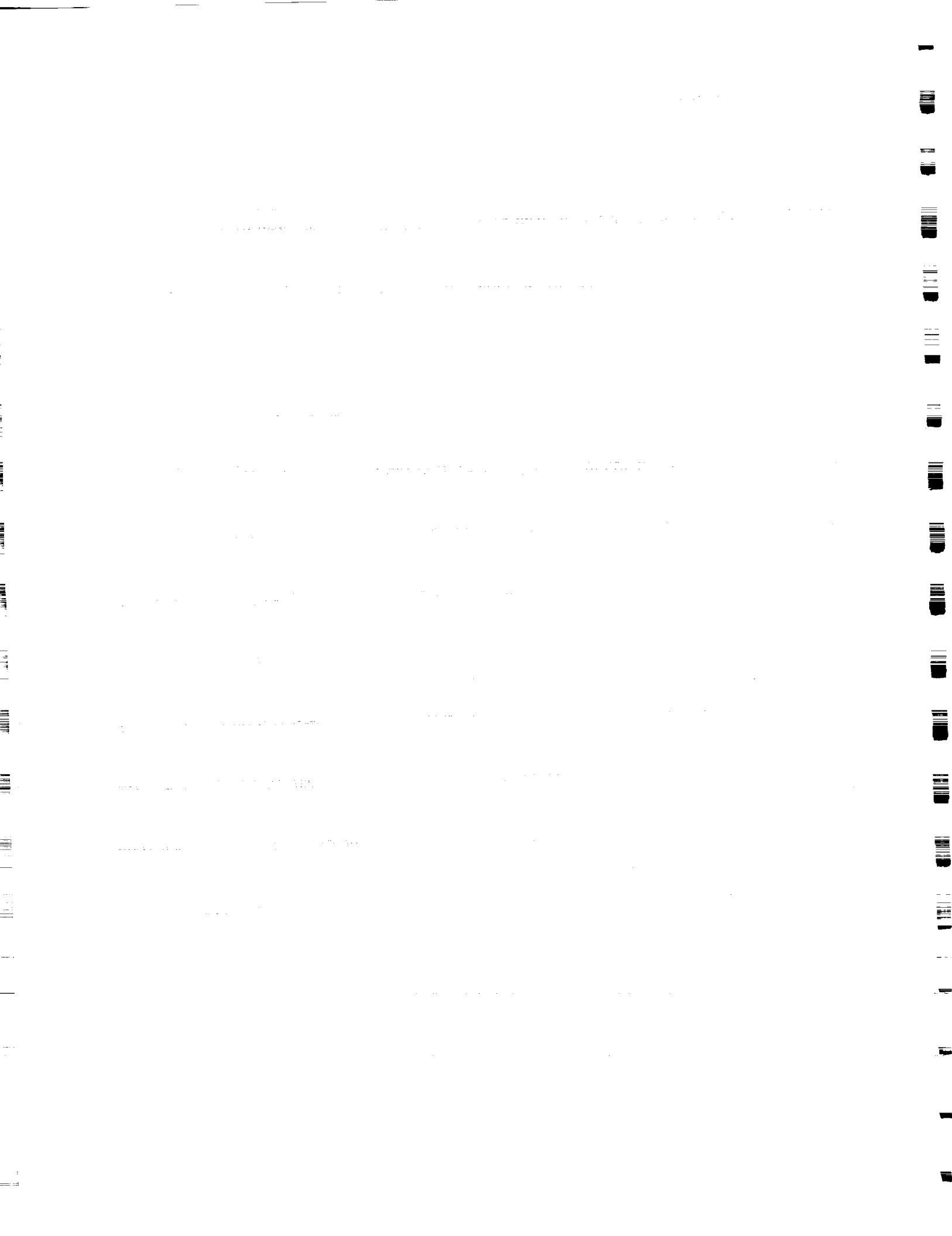
compute  $x_{\infty}^{**}$  following the same procedure.

## 6. Results

The solutions of (13-16) depend on a number of parameters, as defined in §2-4. (Solutions on a finite interval depend also on  $h$ .) Restriction of the analysis to the pseudobinary system  $\text{Hg}_{1-x}\text{Cd}_x\text{Te}$  reduces the parameters to the solidification rate  $V_I$ , liquid-side temperature gradient  $G_L$ , bulk CdTe mole fraction  $x_{\infty}$ , and rotation rate  $\Omega_0$ . The thermophysical properties of the liquid and solid (other than liquid density) are taken as constants and evaluated using the functional forms given in Appendix A at the bulk CdTe mole fraction and corresponding liquidus or solidus temperatures.

We present our results in figures 2 and 3 in terms of stability boundaries in the  $V_I$ - $x_{\infty}$  plane for  $G_L = 25$  and  $50 \text{ K cm}^{-1}$  and several rotation rates  $\Omega_0$ . The stability boundaries consist of some portion of the morphological branch joined to an oscillatory convective branch. The solid curve in each figure represents the minimum on the neutral curve corresponding to morphological instability ( $x_{\infty}^*$ ). The dashed curve denotes the maximum on the neutral curve associated with the onset of buoyancy-driven convection ( $x_{\infty}^{**}$ ).

For  $G_L = 50 \text{ K cm}^{-1}$ , figure 2 shows the stability boundaries for  $\Omega_0 = 0, 25, 50$ , and  $100$  rpm. Above the morphological branch, disturbances grow for some range of wavenumber  $a$  and plane-front solidification is unstable. Similarly, below the convective branch appropriate to each rotation rate shown, disturbances grow for some range of  $a$ . However, between the morphological branch and the convective branch associated with each rotation rate (i.e., for  $x_{\infty}^{**} < x_{\infty} < x_{\infty}^*$ ), disturbances decay for all wavenumbers and plane-front solidification is stable. Note that the morphological branch is unaffected by rotation, whereas as  $\Omega_0$  increases, the convective branch is shifted downward. The critical bulk CdTe mole fraction  $x_{\infty}^{**}$  on the convective branch is a decreasing function of  $\Omega_0$  at any solidification rate, clearly indicating the inhibitory effect of rotation on the onset of buoyancy-driven convection. Beyond the critical solidification rate (denoted by  $V_I^{\text{cr}}$ ) at which the convective and morphological branches intersect, there is no stable range of bulk CdTe mole fraction  $x_{\infty}$ . Thus, plane-front solidification is unstable at all bulk CdTe mole fractions for sufficiently high solidification rates. The critical solidification rate  $V_I^{\text{cr}}$  at which the morphological and convective branches intersect occurs at higher  $x_{\infty}$  with increasing rotation rate  $\Omega_0$ . The critical value  $V_I^{\text{cr}}$  is increased by more than a factor of ten at  $\Omega_0 = 100$  rpm relative to the nonrotating case. We also



note that the convective branch has a relatively shallow local minimum near  $V_I = 1 \mu \text{ sec}^{-1}$ , the location of which depends only weakly on  $\Omega_o$ . Thus, for a given rotation rate, operation at the solidification rate corresponding to this local minimum allows plane-front solidification to be conducted stably at the lowest value of  $x_\infty$ .

For  $G_L = 25 \text{ K cm}^{-1}$  and  $\Omega_o = 0$  and 100 rpm, figure 3 shows stability boundaries in the  $V_I - x_\infty$  plane analogous to those for  $G_L = 50 \text{ K cm}^{-1}$ . As expected on the basis of the results of Coriell et al. [13] for Pb-Sn without rotation, the morphological branch is shifted to the left, reducing the range of solidification rates and bulk mole fractions for which plane-front solidification is stable. On the other hand, the convective branch is shifted downwards relative to the  $G_L = 50 \text{ K cm}^{-1}$  case, corresponding to an increase in the range of stable operating conditions. We note that decreasing the temperature gradient has very little effect on the onset of convection in a nonrotating layer, but reduces the range of stable bulk CdTe mole fractions by more than twofold for a layer rotating at 100 rpm. The critical value of  $V_I$  is higher by more than a factor of five at  $\Omega_o = 100 \text{ rpm}$  relative to the nonrotating case, although the degree of stabilization is less than the factor of ten predicted for  $G_L = 25 \text{ K cm}^{-1}$ . Although the reduction in  $x_\infty$  has very little effect on the critical value of  $V_I$  at which the morphological and convective stability boundaries intersect in the nonrotating case, for  $\Omega_o = 100 \text{ rpm}$  the critical value of  $V_I$  decreases by a factor of three when the temperature gradient is reduced.

As discussed for the Pb-Sn case [37], at each value of  $\Omega_o$  the onset of morphological instability occurs *via* a short wavelength (large wavenumber) instability, while convection sets in *via* disturbances with relatively longer wavelengths. In the following section this point is discussed in the context of the mechanism by which rotation inhibits the onset of convection.

## 7. Discussion

During directional solidification of binary alloys cooled from below and characterized by a linear equation of state, with rejection of a light solute at the liquid-solid interface (e.g., Pb-Sn), the vertical temperature and solute gradients are stabilizing and destabilizing, respectively, throughout the liquid layer. In the Pb-Sn system, the onset of buoyancy-driven convection occurs *via* monotonically growing disturbances, as shown by Coriell et al. [13]. However, for the pseudobinary  $\text{Hg}_{1-x}\text{Cd}_x\text{Te}$  system, the CdTe gradient is everywhere stabilizing, and adjacent to the liquid-solid interface there can exist a sublayer in which the thermal stratification is destabilizing. In this system, the onset of convection occurs *via*



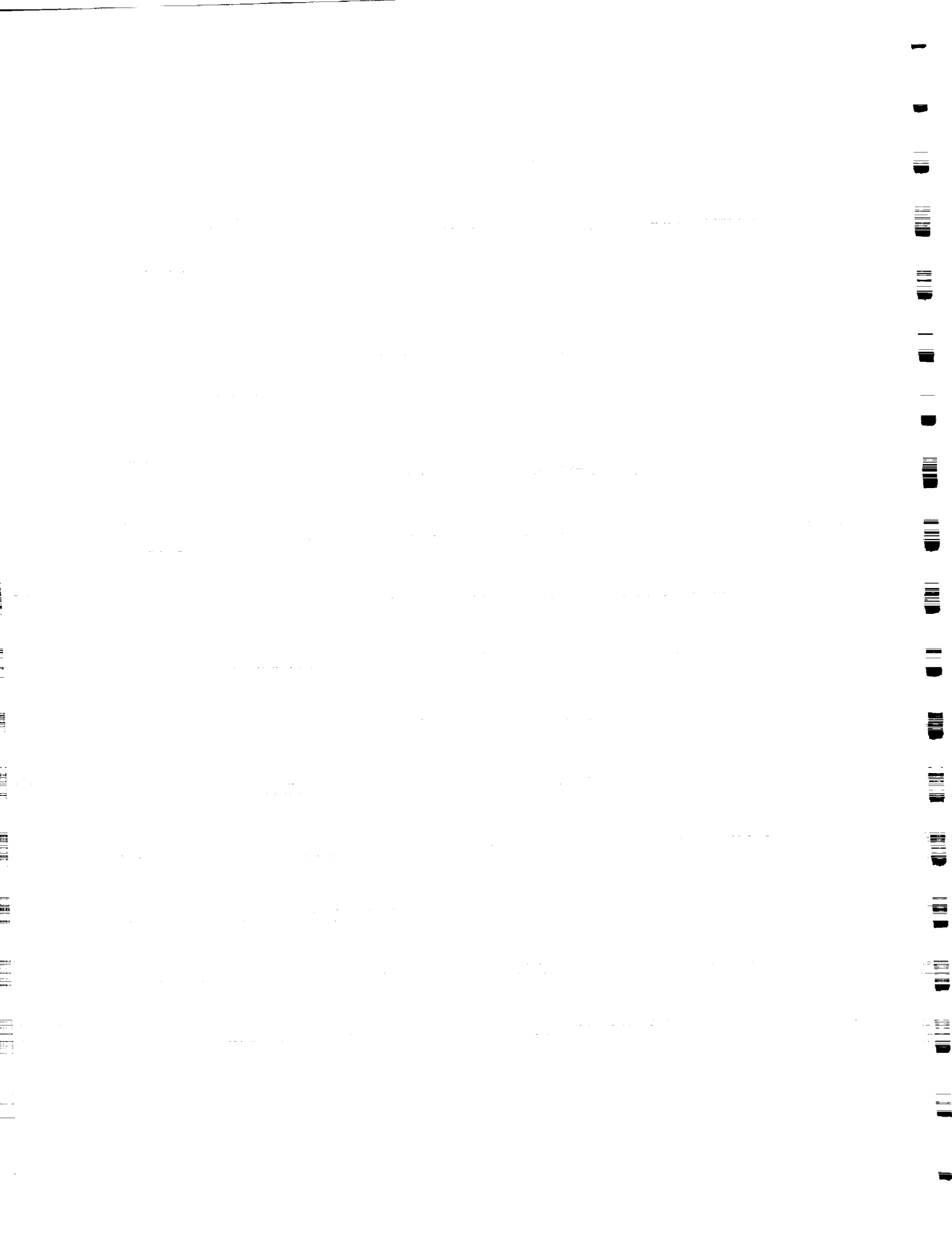


oscillatory disturbances. We note that, as shown in Figures 2 and 3, the system is unstable at the indicated values of  $G_L$  for all  $V_I$  when  $x_\infty$  is sufficiently small, corresponding to the absence of a stably stratified thin liquid layer adjacent to the interface for small  $x_\infty$ .

For Pb-Sn alloys we have shown [37] that significant suppression of the onset of buoyancy-driven convection occurs at modest rotation rates, and is due to the well-known Taylor-Proudman mechanism. According to the Taylor-Proudman theorem [36], steady motion parallel to the axis of rotation in a uniformly rotating inviscid fluid is prohibited. If this theorem applied to viscous fluids, steady convection would be prohibited, since cellular convective flow must have a vertical component. Instead, in viscous fluids the onset of steady convection is inhibited, with the degree of inhibition (expressed as an increase in  $x_\infty$ ) increasing with rotation rate. Although the Taylor-Proudman theorem strictly applies only to steady flow, the Coriolis acceleration also suppresses the oscillatory onset of buoyancy-driven convection during directional solidification of  $Hg_{1-x}Cd_xTe$  as shown in §6. It is not surprising that the morphological instability is unaffected by rotation since it occurs at very short wavelengths, with the motion nearly perpendicular to the solidification front (i.e., aligned with the rotation axis).

For a horizontally unbounded fluid layer in which density depends linearly on temperature and composition and no phase change occurs, a linear analysis [45] shows that Coriolis effects generally inhibit the onset of convection (by the Taylor-Proudman mechanism). However, for some combinations of  $Pr$ ,  $Sc$ , and the dimensionless rotation rate (characterized by a Taylor number  $Ta$ ) and solute and temperature gradients (characterized by solutal and thermal Rayleigh numbers  $Ra_S$  and  $Ra_T$ ), rotation destabilizes the layer (on a linear basis) relative to the nonrotating case. This occurs only when convection sets in *via* oscillations and the natural frequency of a buoyant fluid element is tuned (by rotation) so that the critical  $Ra_T$  has a local minimum as a function of  $Ta$ . With linear gradients and no phase change, this destabilization is found for  $Pr$  and  $Sc$  both less than unity [45], although there is no apparent reason why it cannot occur under other conditions when onset is *via* an oscillatory mode. We have found no such destabilization by rotation for the solidification of  $Hg_{1-x}Cd_xTe$ .

Even though our analysis is limited to horizontally unbounded layers, work for single-component fluids not undergoing phase change [48,49] suggests that for fixed finite aspect ratios (ratio of mold radius to height) our predictions will be qualitatively correct if  $\Omega_o^2 R_o / g$  (a Froude number, where  $R_o$  is the mold radius) is sufficiently small. For the onset of thermal



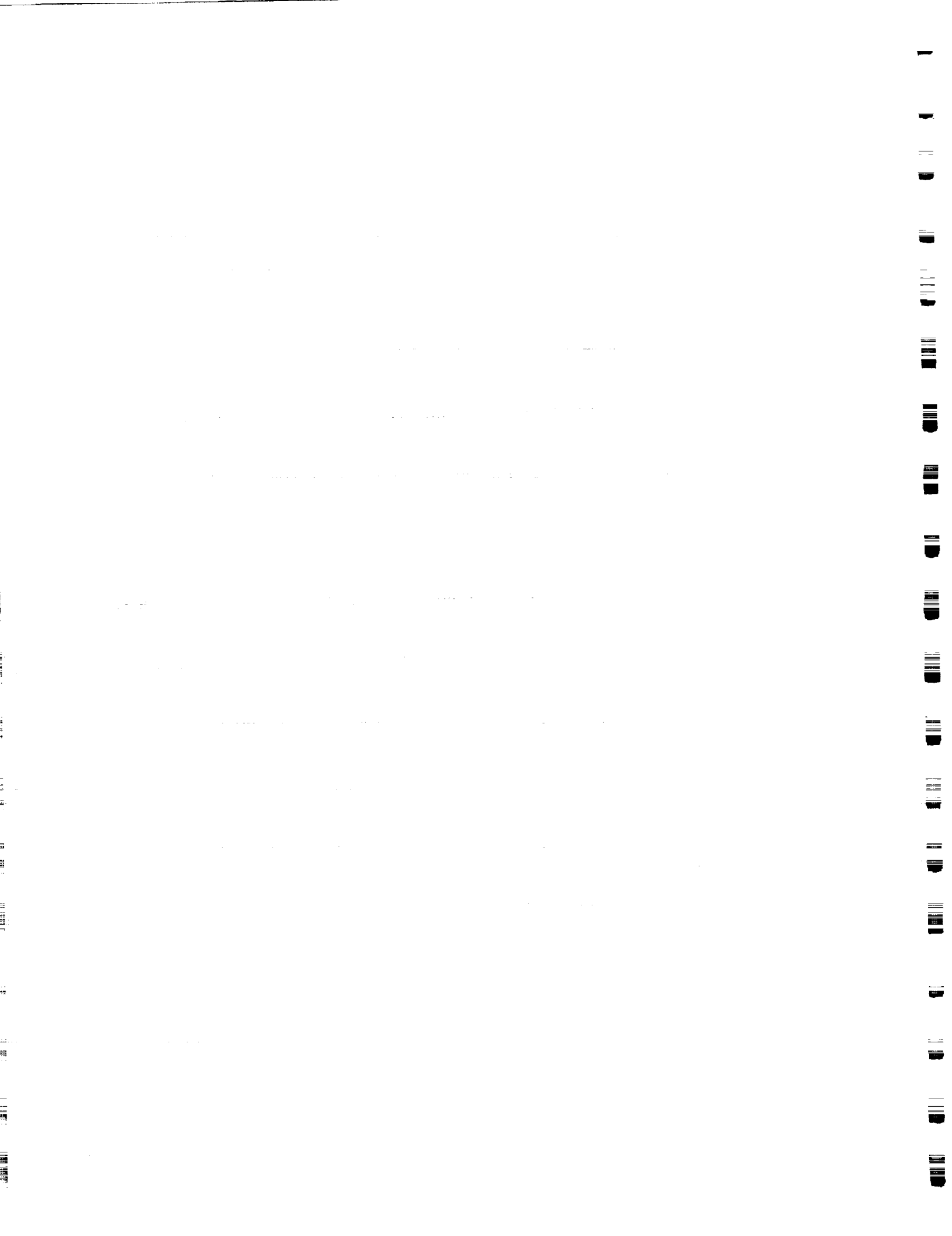
convection in rotating water or mercury layers heated from below, the excellent quantitative agreement between linear stability theory for a horizontally unbounded layer [41-43] and experimental work for finite aspect ratios [43,50,51] clearly demonstrates the potential of the Coriolis acceleration to suppress buoyancy-driven convection in a rotating fluid.

The results of a linear stability analysis are subject to the caveat that even when infinitesimal disturbances are predicted to decay, larger disturbances might grow. Indeed, for rotating fluid layers heated from below, the onset of thermal convection can occur at lower Rayleigh numbers than predicted by linear theory [52-54]. However, in that case accounting for disturbances of noninfinitesimal amplitude modifies only the degree of stabilization predicted.

The modest rotation rates that can significantly inhibit the onset of convection in the  $\text{Hg}_{1-x}\text{Cd}_x\text{Te}$  and Pb-Sn systems make uniform rotation about the vertical a good candidate for experimental verification. Experiments should be conducted with completely filled cylindrical molds, insulated on the vertical surface, and mounted on the axis of a rotating horizontal turntable. If these precautions are not taken, the Coriolis-related stabilization may be overwhelmed by other effects. For example, if the liquid's top surface is in contact with a gas or vacuum, it and the liquid-solid interface will be nearly paraboloidal, which may lead to radial segregation in the solid for high rotation rates or large mold radii. Cooling the vertical surface leads to a radial temperature gradient and centrifugal effects. For these reasons, our results cannot be compared to earlier experimental work [30-33].

We note that the experimental work of Müller [23] and Weber et al. [24] focuses on the effect of rotation on the time-dependence of the supercritical flow, with no information given on suppression of the onset of motion. Furthermore, although these authors concluded that the Coriolis acceleration is key to eliminating striations at high rotation rates, their experimental design complicates the separation of Coriolis effects from the "pseudo-gravitational" effects associated with high centrifugal accelerations.

Finally, Antar [55] has recently presented a linear analysis of the onset of convection in a fluid layer cooled from below, using an approximate equation of state for  $\text{Hg}_{1-x}\text{Cd}_x\text{Te}$ . Although this work purports to consider "convective instabilities in the melt for solidifying mercury cadmium telluride", it differs from ours in that it includes no phenomena associated with solidification (existence of a moving or deformable interface where phase change occurs, nonlinear basic state solute stratification due to rejection or preferential incorporation at the



interface, latent heat effects, etc.) Comparison to its results is further precluded since the linear basic state thermal stratification and the definition of the temperature difference  $\Delta T$  across the fluid layer are inconsistent. Specifically, the bottom temperature (see Antar's eqn. (1)) is  $T_o - \Delta T$ , which is inconsistent with the definitions of  $T_o$  (temperature where  $\partial\rho/\partial T$  is zero, determined by the equation of state) and  $\Delta T$ . Put differently, Antar defines  $\Delta T$  as the temperature difference across the layer, (e.g.,  $\Delta T = |T_{\text{top}} - T_{\text{bottom}}| = |T(d) - T(0)|$ ). His temperature profile, however, yields  $T(d) = T_o - (d_o - d)\Delta T / d_o$  and  $T(0) = T_o - \Delta T$ , from which it follows that  $|T(d) - T(0)| = d \Delta T / d_o$ , which is inconsistent with the definition of  $\Delta T$ . This error vitiates the analysis, which uses a thermal Rayleigh number based on a temperature difference inconsistent with the basic state. That this inconsistency is not simply an apparent one due to a typographical error is confirmed by reference to an earlier paper [56] which uses the same basic state and disturbance equations. A different (and very unusual) definition of  $\Delta T$  (related to the overall temperature difference by a constant dependent on the top or bottom temperature; see figure 1 of [56]) was used to maintain consistency. That definition of  $\Delta T$  was the only one compatible with the basic state, and hence with the analysis and results. Unfortunately, in reference 55,  $\Delta T$  is defined as the overall temperature difference, which is wrong.

## Acknowledgments

The authors acknowledge several helpful discussions with Professor David R. Poirier of the University of Arizona. This work was supported by the Microgravity Science and Applications Division of the National Aeronautics and Space Administration through Grant NAG3-1121. Partial support was also provided by NSF Grant CTS-9017181.



## Appendix A

The thermophysical properties of the liquid and solid (other than the density of the liquid) are taken as constants evaluated using the functional forms shown below at the bulk mole fraction and corresponding liquidus or solidus temperatures  $T_{\text{liq}}$  and  $T_{\text{sol}}$ ).

We have taken the density of solid  $\text{Hg}_{1-x}\text{Cd}_x\text{Te}$  as

$$\frac{1}{\rho_s} = \frac{\zeta}{\rho_{\text{CdTe}}} + \frac{1-\zeta}{\rho_{\text{HgTe}}}, \quad (\text{A1})$$

where  $\zeta = xM_{\text{CdTe}}/M$  is the CdTe mass fraction, the molecular weights of CdTe and HgTe are  $M_{\text{CdTe}} = 240 \text{ g/mol}$  and  $M_{\text{HgTe}} = 328.2 \text{ g/mol}$ ,  $M = xM_{\text{CdTe}} + (1-x)M_{\text{HgTe}}$ , and  $\rho_{\text{CdTe}}$  and  $\rho_{\text{HgTe}}$  are the solid densities of pure CdTe and HgTe, respectively, represented by

$$\rho_{\text{CdTe}} = \lambda_0 + \lambda_1 T \quad (\text{A2a})$$

and

$$\rho_{\text{HgTe}} = \phi_0 + \phi_1 T, \quad (\text{A2b})$$

where the coefficients  $\lambda_i$  and  $\phi_i$  are determined by least-squares fits to the experimental data of Glazov et al. [57] and Mokrovskii and Regel [39], respectively. The values of  $\lambda_i$  and  $\phi_i$  are

$$\begin{aligned} \lambda_0 &= 5.820 \text{ g cm}^{-3} & \lambda_1 &= -8.095 \times 10^{-5} \text{ g cm}^{-3} \text{K}^{-1} \\ \phi_0 &= 8.201 \text{ g cm}^{-3} & \phi_1 &= -1.230 \times 10^{-4} \text{ g cm}^{-3} \text{K}^{-1} \end{aligned}$$

The viscosity is represented over the entire range by

$$\nu = 1 \times 10^{-2} \exp(\Phi_0 + \Phi_1/T) \text{ cm}^2 \text{sec}^{-1}, \quad (\text{A3})$$

where  $\Phi_0 = -3.401$  and  $\Phi_1 = 3445 \text{ K}$  are computed by least-squares fit to the experimental data of Glazov et al. [58] for pure CdTe. Due to the lack of experimental viscosity data for HgTe, we use (A3) for the viscosity of  $\text{Hg}_{1-x}\text{Cd}_x\text{Te}$ , independent of composition.

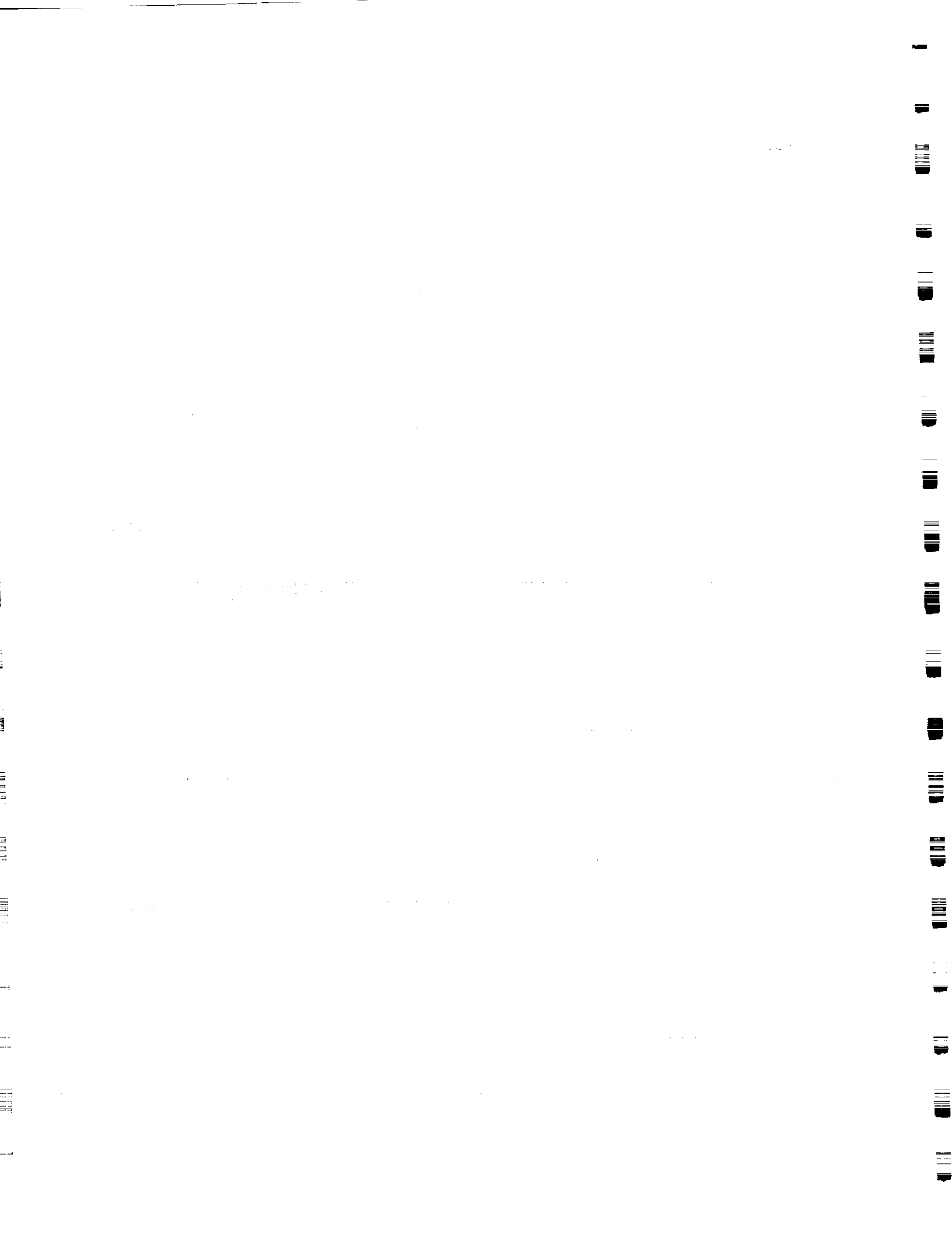
The thermal diffusivity of liquid and solid  $\text{Hg}_{1-x}\text{Cd}_x\text{Te}$  are approximated by

$$\kappa_L = (E_0 + E_1 x^{1/2} + E_2 x) \ln(T/K) - (U_0 + U_1 x^{1/2} + U_2 x), \quad (\text{A4a})$$

$$\kappa_S = \sum_{j=0}^2 T^j (S_{0j} + S_{1j} x^{1/2} + S_{2j} x) \quad (\text{A4b})$$

where the coefficients

$$E_0 = 0.104 \text{ cm}^2 \text{sec}^{-1} \quad E_1 = -0.146 \text{ cm}^2 \text{sec}^{-1}$$





$$E_2 = 0.118 \text{ cm}^2 \text{sec}^{-1}$$

$$U_1 = -0.941 \text{ cm}^2 \text{sec}^{-1}$$

$$S_{00} = -5.945 \times 10^{-3} \text{ cm}^2 \text{sec}^{-1}$$

$$S_{20} = -0.114 \text{ cm}^2 \text{sec}^{-1}$$

$$S_{11} = 1.646 \times 10^{-4} \text{ cm}^2 \text{sec}^{-1}$$

$$S_{02} = -7.829 \times 10^{-8} \text{ cm}^2 \text{sec}^{-1} \text{K}^{-2}$$

$$S_{22} = -4.120 \times 10^{-7} \text{ cm}^2 \text{sec}^{-1} \text{K}^{-2}$$

$$U_0 = 0.668 \text{ cm}^2 \text{sec}^{-1}$$

$$U_2 = 0.783 \text{ cm}^2 \text{sec}^{-1}$$

$$S_{10} = 1.698 \times 10^{-2} \text{ cm}^2 \text{sec}^{-1}$$

$$S_{01} = -7.148 \times 10^{-3} \text{ cm}^2 \text{sec}^{-1} \text{K}^{-1}$$

$$S_{21} = 4.475 \times 10^{-4} \text{ cm}^2 \text{sec}^{-1} \text{K}^{-1}$$

$$S_{12} = 1.969 \times 10^{-7} \text{ cm}^2 \text{sec}^{-1} \text{K}^{-2}$$

are determined by least-squares fit to the experimental data of Holland and Taylor [57].

The specific heat of liquid  $\text{Hg}_{1-x}\text{Cd}_x\text{Te}$  is represented by

$$c_{p,L}(T, x) = \sum_{i=0}^2 \sum_{j=0}^{2-i} q_{ij} x^i (T - 943 \text{ K})^j. \quad (\text{A5})$$

The coefficients  $q_{ij}$  found by least-squares fit to the calculated specific heat of Su [60] are

$$q_{00} = 65.08 \text{ J K}^{-1} \text{ mol}^{-1}$$

$$q_{01} = -0.101 \text{ J K}^{-2} \text{ mol}^{-1}$$

$$q_{02} = 3.961 \times 10^{-4} \text{ J K}^{-3} \text{ mol}^{-1}$$

$$q_{10} = 1.648 \text{ J K}^{-1} \text{ mol}^{-1}$$

$$q_{11} = 7.004 \times 10^{-3} \text{ J K}^{-2} \text{ mol}^{-1}$$

$$q_{20} = -5.044 \times 10^{-3} \text{ J K}^{-1} \text{ mol}^{-1},$$

where we have used the relation  $1 \text{ mol} = 2 \text{ g-atom}$  for the pseudobinary system  $\text{Hg}_{1-x}\text{Cd}_x\text{Te}$  to convert Su's data (in  $\text{cal K}^{-1} \text{ g-atom}^{-1}$ ) to  $\text{J K}^{-1} \text{ mol}^{-1}$ .

The specific heat of solid  $\text{Hg}_{1-x}\text{Cd}_x\text{Te}$  is taken as

$$c_{p,S} = (1-x)c_{p,S,\text{HgTe}} + xc_{p,S,\text{CdTe}}, \quad (\text{A6})$$

where the specific heats of pure HgTe and CdTe vary with temperature [61] according to

$$c_{p,S,\text{HgTe}} = [52.09 + 9.08 \times 10^{-3} (T/\text{K})] \text{ J K}^{-1} \text{ mol}^{-1} \quad (\text{A7a})$$

and

$$c_{p,S,\text{CdTe}} = [40.0 + 3.3 \times 10^{-2} (T/\text{K})] \text{ J K}^{-1} \text{ mol}^{-1}. \quad (\text{A7b})$$

The latent heat of fusion is approximated by

$$L(x) = (1-x)L_{\text{HgTe}} + xL_{\text{CdTe}}, \quad (\text{A8})$$

where  $L_{\text{HgTe}} = 3.6 \times 10^4 \text{ J/mol}$  and  $L_{\text{CdTe}} = 4 \times 10^4 \text{ J/mol}$  are used for the pure components



[61]. The interfacial energy is estimated by comparing  $\text{Hg}_{1-x}\text{Cd}_x\text{Te}$  and  $\text{InSb}$  (in reference 62 Ge and  $\text{InSb}$  are compared to estimate the interfacial energy of  $\text{InSb}$ )

$$\sigma_{\text{Hg}_{1-x}\text{Cd}_x\text{Te}} = \left( \frac{L}{a_o^2} \right)_{\text{Hg}_{1-x}\text{Cd}_x\text{Te}} \left( \frac{a_o^2}{L} \right)_{\text{InSb}} \sigma_{\text{InSb}}, \quad (\text{A9})$$

where the latent heat of fusion per unit volume for  $\text{Hg}_{1-x}\text{Cd}_x\text{Te}$  is taken to vary linearly with  $\text{CdTe}$  mole fraction (A8),  $a_o = 6.4797 \text{ \AA}$  for  $\text{InSb}$ , and  $a_o = 6.465 \text{ \AA}$  is used for  $\text{Hg}_{1-x}\text{Cd}_x\text{Te}$  independent of  $x$  [58]. Here the surface tension is taken as  $\sigma_{\text{InSb}} = 8.5 \times 10^{-6} \text{ J cm}^{-2}$ , and the latent heat of fusion per unit volume of  $\text{InSb}$  is  $L = 1.20 \times 10^3 \text{ J cm}^{-3}$ . The capillary coefficient is then computed from

$$\Psi = \sigma_{\text{Hg}_{1-x}\text{Cd}_x\text{Te}} \frac{T_{\text{liq}}}{L}, \quad (\text{A10})$$

where  $T_{\text{liq}}$  is the liquidus temperature for a given bulk mole fraction of  $\text{CdTe}$  in the liquid.

We determine the liquidus and solidus temperatures

$$T_{\text{liq}} = (943 + 681x - 372x^2) \text{ K}, \quad (\text{A11a})$$

$$T_{\text{sol}} = (943 + 202x - 150x^2 + 324x^3) \text{ K}, \quad (\text{A11b})$$

the liquidus slope

$$m_L = (681 - 745x) \text{ K}, \quad (\text{A12})$$

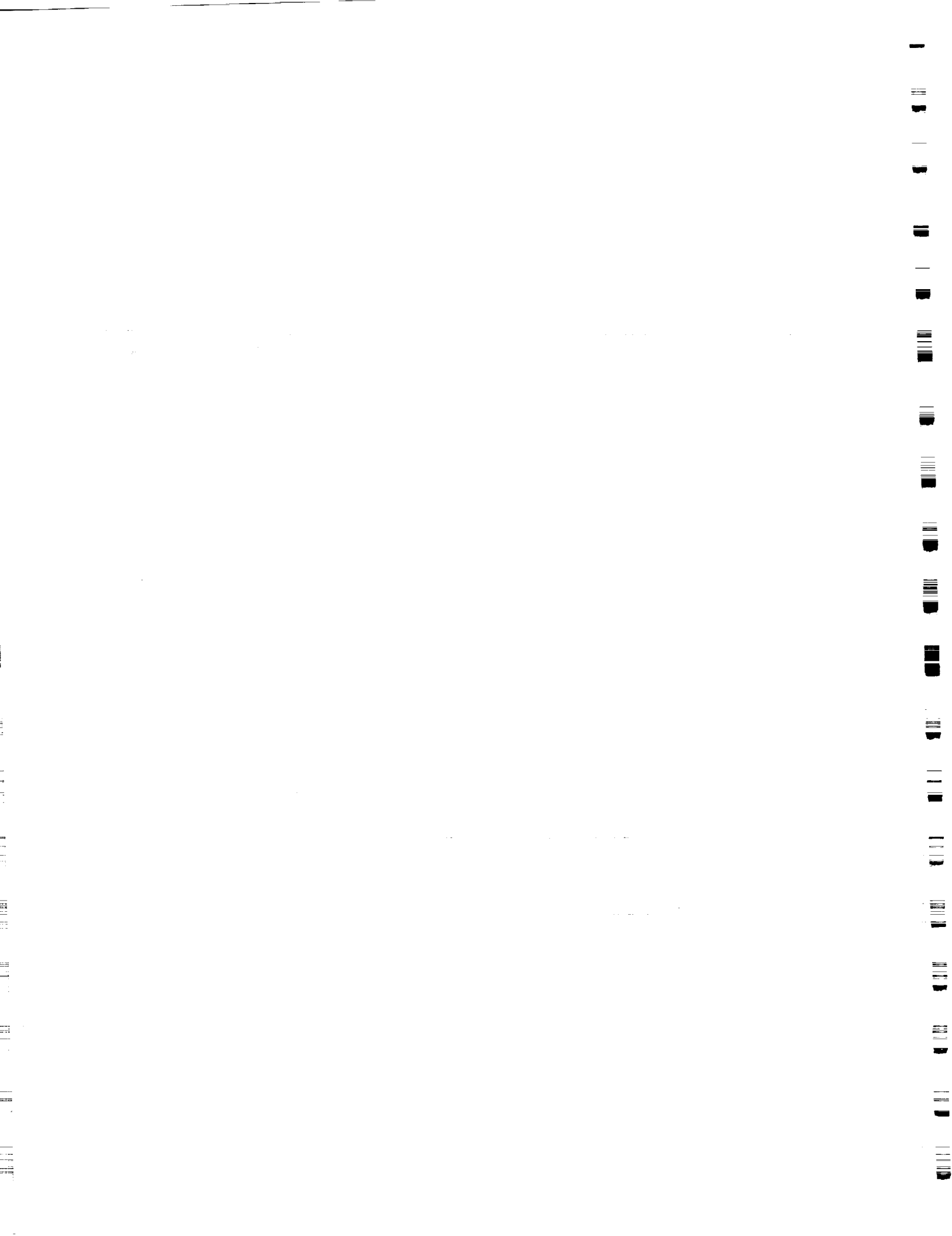
and the segregation coefficient

$$k = x(0.30 - 2.24 \times 10^{-3} \text{ K}^{-1} T_{\text{sol}} + 2.67 \times 10^{-6} \text{ K}^{-2} T_{\text{sol}}^2) \quad \text{for } x > 0.1, \quad (\text{A13a})$$

$$k = 3.74 \quad \text{for } x < 0.1, \quad (\text{A13b})$$

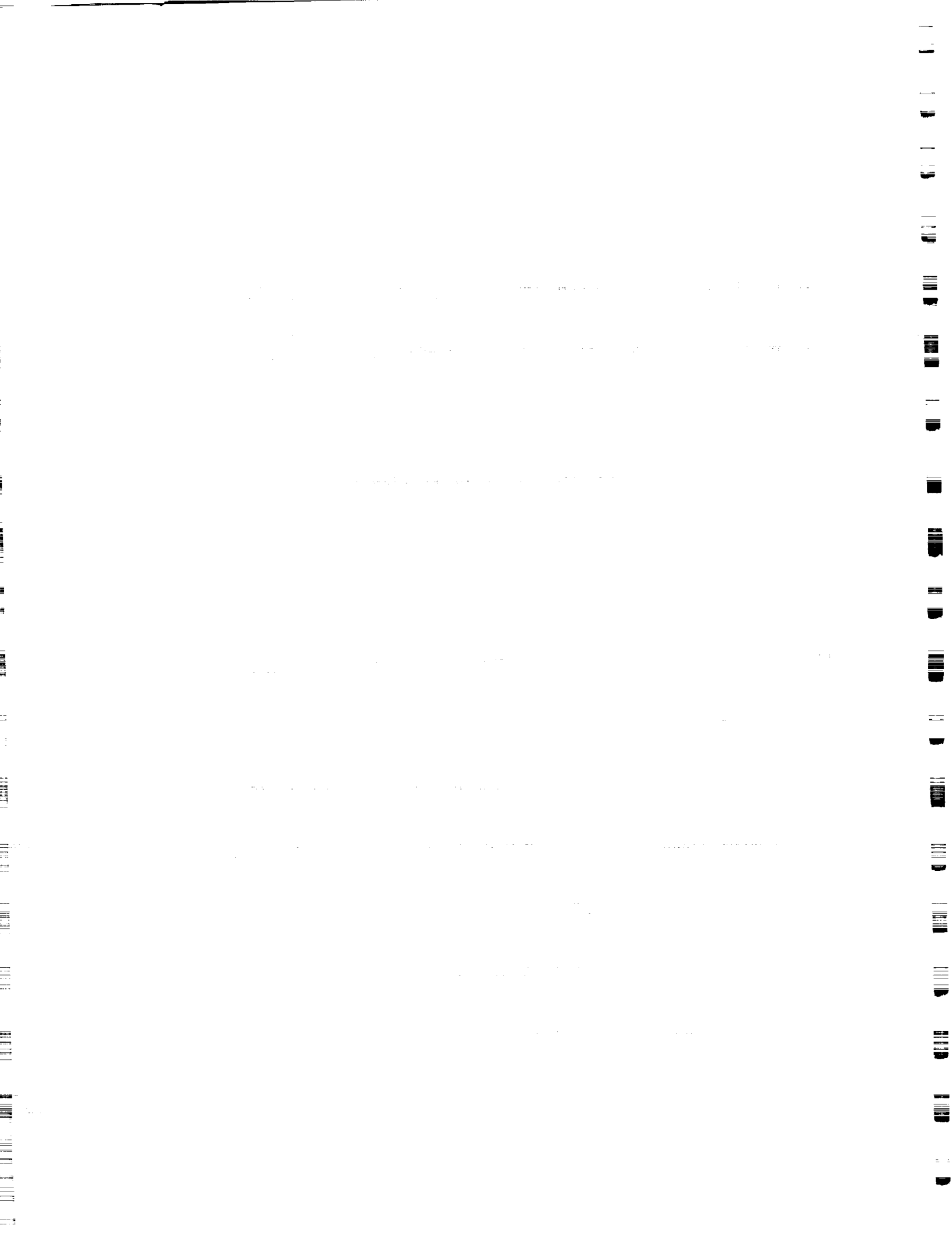
as functions of  $\text{CdTe}$  mole fraction by least-squares fits to data of Szofran and Lehoczky [63].

Finally, the solute diffusion coefficient is taken as  $D_L = 5.5 \times 10^{-5} \text{ cm}^2/\text{sec}$ , the value most commonly used in the literature [3].



## References

- [1] R.R. Galazka, T. Warminski, J. Bak, J. Auleytner, T. Dietl, A.S. Okhotin, R.P. Borovikova and I.A. Zubritskij, *J. Crystal Growth* 53 (1981) 397.
- [2] P. Capper, J.J. Gosney, C.L. Jones and I. Kenworthy, *J. Electron. Mater.* 15 (1986) 371.
- [3] D.H. Kim and R.A. Brown, *J. Crystal Growth* 96 (1989) 609.
- [4] E.D. Bourret, J.J. Derby and R.A. Brown, *J. Crystal Growth* 71 (1985) 587.
- [5] Yu.V. Apanovich and E.D. Ljumkis, *J. Crystal Growth* 110 (1991) 839.
- [6] W.F.H. Micklethwaite, in: *Mercury Cadmium Telluride*, Eds. R.K. Willardson and A.C. Beer, Vol. 18 in: *Semiconductors and Semimetals* (Academic Press, New York, 1981) p. 47.
- [7] P. Capper, *Prog. Crystal Growth Charact.* 19 (1989) 259.
- [8] W.W. Mullins and R.F. Sekerka, *J. Appl. Phys.* 35 (1964) 444.
- [9] A.F. Giamei and B.H. Kear, *Metall. Trans.* 1 (1970) 2185.
- [10] D.R. Poirier, M.C. Flemings, R. Mehrabian and H.J. Klein, in: *Advances in Metal Processing*, Eds. J.J. Burke, R. Mehrabian and V. Weiss (Plenum, New York, 1981) p. 277.
- [11] S.D. Ridder, S. Kou and R. Mehrabian, *Metall. Trans. B* 12 (1981) 435.
- [12] G. Müller, in: *Crystal Growth from the Melt*, Ed. H.C. Freyhardt, Vol. 12 in: *Crystals* (Springer-Verlag, Berlin, 1988).
- [13] S.R. Coriell, M.R. Cordes, W.J. Boettinger and R.F. Sekerka, *J. Crystal Growth* 49 (1980) 13.
- [14] M.E. Glicksman, S.R. Coriell and G.B. McFadden, *Ann. Rev. Fluid Mech.* 18 (1986) 307.
- [15] R.F. Sekerka and S.R. Coriell, in: *Proc. Sixth European Symp. on Material Sciences under Microgravity Conditions*, Comp. W.R. Burke, Bordeaux, December 2-5, 1986, ESA-SP-256 (1987), p. 3.
- [16] M.G. Worster, *J. Fluid Mech.* 224 (1991) 335.
- [17] S.H. Davis, *J. Fluid Mech.* 212 (1990) 241.
- [18] H.E. Huppert, *J. Fluid Mech.* 212 (1990) 209.
- [19] V.I. Polezhaev, in: *Growth and Defect Structures*, Ed. H.C. Freyhardt, Vol. 10 in: *Crystals* (Springer-Verlag, Berlin, 1988) p. 87.
- [20] J.I.D. Alexander, J. Ouazzani and F. Rosenberger, *J. Crystal Growth* 97 (1989) 285.



- [21] J.C. Heinrich, S. Felicelli, P. Nandapurkar and D.R. Poirier, *Metall. Trans. B* 20 (1989) 883.
- [22] J.C. Heinrich, S. Felicelli, P. Nandapurkar and D.R. Poirier, *AIAA Paper* 89-0626, 1989.
- [23] G. Müller, *J. Crystal Growth* 99 (1990) 1242.
- [24] W. Weber, G. Neumann and G. Müller, *J. Crystal Growth* 100 (1990) 145.
- [25] H.P. Greenspan, *The Theory of Rotating Fluids* (Cambridge University Press, Cambridge, 1968).
- [26] J. Czochralski, *Z. Phys. Chem.* 92 (1918) 219.
- [27] H.J. Scheel and E.O. Schulz-DuBois *J. Crystal Growth* 8 (1971) 304.
- [28] E.O. Schulz-DuBois, *J. Crystal Growth* 12 (1972) 81.
- [29] S.M. Copley, private communication, 1976.
- [30] S. Kou, *Macrosegregation in Electroslag Remelted Ingots*, Ph.D. Thesis, Massachusetts Institute of Technology, 1978.
- [31] S. Kou, D.R. Poirier and M.C. Flemings, *Metall. Trans. B* 9 (1978) 711.
- [32] A.K. Sample and A. Hellawell, *Metall. Trans. A* 15 (1984) 2163.
- [33] A. Sample and A. Hellawell, *Metall. Trans. B.* 13 (1982) 495.
- [34] H. Rodot, L.L. Regel, and A.M. Turtchaninov, *J. Crystal Growth* 104 (1990) 280.
- [35] C.F. Chen and F. Chen, *Phys. Fluids A* 4 (1992) 451
- [36] S. Chandrasekhar, *Hydrodynamic and Hydromagnetic Stability* (Clarendon, Oxford, 1961).
- [37] A. Öztekin and A. J. Pearlstein, *Metall. Trans. B* 23 (1992) 73.
- [38] D. Chandra and L.R. Holland, *J. Vac. Sci. Tech. A* 1 (1983) 1620.
- [39] N.P. Mokrovskii and A.R. Regel, *Zh. Tekh. Fiz.* 22 (1952) 1281.
- [40] A. Öztekin and A.J. Pearlstein, *J. Crystal Growth*, submitted for publication.
- [41] S. Chandrasekhar, *Proc. Roy. Soc. London A* 217 (1953) 306.
- [42] S. Chandrasekhar and D.D. Elbert, *Proc. Roy. Soc. London A* 231 (1953) 198.
- [43] Y. Nakagawa and P. Frenzen, *Tellus* 7 (1955) 1.
- [44] P.P. Niiler and F.E. Bisshopp, *J. Fluid Mech.* 22 (1965) 753.
- [45] A.J. Pearlstein, *J. Fluid Mech.* 103 (1981) 389.
- [46] H.B. Keller, *Numerical Solution of Two Point Boundary Value Problems* (SIAM, Philadelphia, 1976) p. 49.



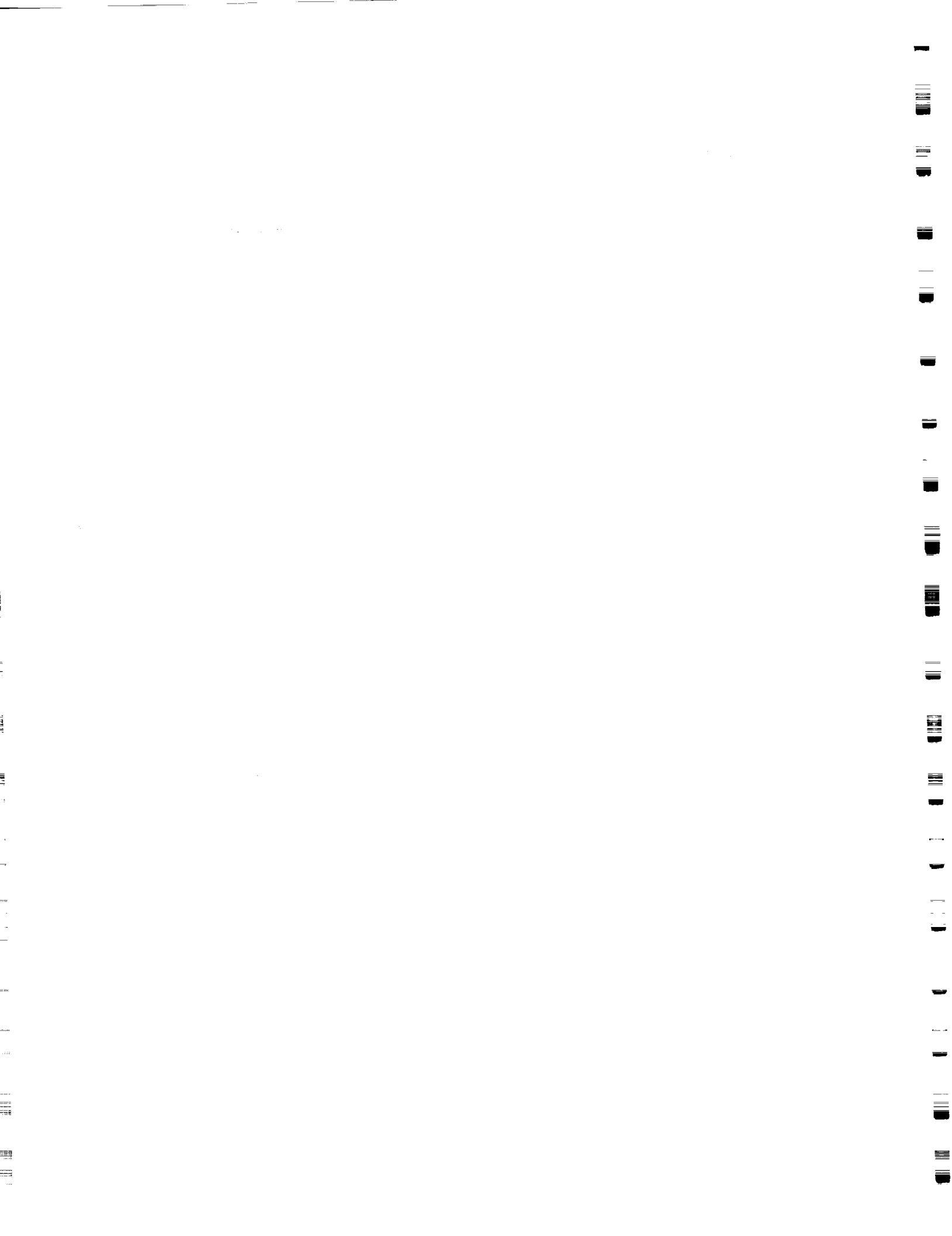


- [47] A. Zebib, J. Comput. Phys. 70 (1987) 521.
- [48] G.M. Homsy and J.L. Hudson, J. Fluid Mech. 45 (1971) 353.
- [49] K. Bühler and H. Oertel, J. Fluid Mech. 114 (1982) 261.
- [50] D. Fultz and Y. Nakagawa, Proc. Roy. Soc. London A 231 (1955) 211.
- [51] I.R. Goroff, Proc. Roy. Soc. London A 254 (1960) 537.
- [52] G. Veronis, J. Fluid Mech. 5 (1959) 401.
- [53] G. Veronis, J. Fluid Mech. 24 (1966) 545.
- [54] G. Veronis, J. Fluid Mech. 31 (1968) 113.
- [55] B.N. Antar, J. Crystal Growth 113 (1991) 92.
- [56] B.N. Antar, Phys. Fluids 30 (1987) 322.
- [57] V.M. Glazov, S.N. Chizhevskaya and S. B. Evgen'ev, Russ. J. Phys. Chem. 43 (1969) 201.
- [58] V.M. Glazov, S.N. Chizhevskaya and N.N. Glagoleva, Liquid Semiconductors (Plenum, New York, 1969).
- [59] L. R. Holland and R. E. Taylor, J. Vac. Sci. Tech. A 1 (1983) 1615.
- [60] C.-H. Su, J. Crystal Growth 78 (1986) 51.
- [61] K.C. Mills, Thermodynamic Data for Inorganic Sulphides, Selenides, and Tellurides (Butterworths, London, 1974).
- [62] R.G. Seidensticker and D.R. Hamilton, J. Phys. Chem. Solids 24 (1963) 1585.
- [63] F.R. Szofran and S.L. Lehoczky, J. Electron. Mater. 10 (1981) 1131.



## Figure Captions

- Figure 1. Schematic depiction of the stability boundary.
- Figure 2.  $V_I$ - $x_\infty$  stability boundaries for  $G_L = 50 \text{ K cm}^{-1}$  with  $\Omega_0 = 0, 25, 50,$  and  $100 \text{ rpm}$ .
- Figure 3.  $V_I$ - $x_\infty$  stability boundaries for  $G_L = 25 \text{ K cm}^{-1}$  with  $\Omega_0 = 0$  and  $100 \text{ rpm}$ .



**STABILITY OF PLANE-FRONT AND DENDRITIC SOLIDIFICATION OF  
BINARY LIQUIDS: THE EFFECTS OF ROTATION**

**BY**

**ALPARSLAN OZTEKIN**

**B.S., Technical University of Istanbul, 1982  
M.S., University of Arizona, 1987**

**THESIS**

**Submitted in partial fulfillment of the requirements  
for the degree of Doctor of Philosophy in Mechanical Engineering  
in the Graduate College of the  
University of Illinois at Urbana-Champaign, 1992**

**Urbana, Illinois**



**STABILITY OF PLANE-FRONT AND DENDRITIC SOLIDIFICATION OF  
BINARY LIQUIDS: THE EFFECTS OF ROTATION**

**BY**

**ALPARSLAN OZTEKIN**

**B.S., Technical University of Istanbul, 1982  
M.S., University of Arizona, 1987**

**THESIS**

**Submitted in partial fulfillment of the requirements  
for the degree of Doctor of Philosophy in Mechanical Engineering  
in the Graduate College of the  
University of Illinois at Urbana-Champaign, 1992**

**Urbana, Illinois**





## Abstract

The convective and morphological instabilities in a horizontally unbounded binary liquid undergoing directional solidification by cooling from below are studied by means of linear stability analysis. The possibility of using steady uniform rotation about a vertical axis to suppress the onset of buoyancy-driven convection is considered for both plane-front and dendritic solidification.

For dilute Pb-Sn alloys, our results clearly show that the onset of convection in a horizontally unbounded layer undergoing plane-front solidification can be suppressed significantly at modest rotation rates. Specifically, plane-front solidification is linearly stable at higher Sn concentrations in a rotating configuration than in a nonrotating one. The predicted inhibitory effects of rotation on convection are discussed in terms of previous experimental and theoretical studies of the effect of rotation on the onset of buoyancy-driven convection in single-component fluids heated from below and in binary fluids subject to thermal and solutal stratification.

We also consider the stability of one-dimensional plane-front solidification of the pseudobinary  $\text{Hg}_{1-x}\text{Cd}_x\text{Te}$  system (of considerable importance due to its wide application in the fabrication of electro-optic detectors) in which the liquid density does not depend monotonically on temperature (e.g., has a local maximum) for some range of the bulk solute composition. In contrast to the normal case where the density depends monotonically on temperature and composition (e.g., the Pb-Sn alloys considered by Coriell *et al.* (1980)), for certain combinations of the operating parameters (solidification rate, nominal liquid-side vertical temperature gradient, and bulk solute concentration) there can exist a critical value of the bulk mole fraction ( $C_\infty$ ) below which plane-front solidification is unstable at all dimensionless solidification rates  $\gamma$ , whereas in the normal case plane-front solidification at any  $C_\infty$  is linearly stable for all sufficiently small dimensionless solidification rates. Moreover, when the density varies nonmonotonically with temperature, there can exist a critical value of the dimensionless solidification rate  $\gamma_c$  such that for  $\gamma > \gamma_c$  plane-front

solidification is unstable for all  $C_{\infty}$ . In this case, for  $\gamma < \gamma_c$  there is a finite range of  $C_{\infty}$  for which plane-front solidification is stable. This latter result differs from the normal case, for which at all dimensionless solidification rates, plane-front solidification is stable for all values of  $C_{\infty}$  lying below some critical value. The stability boundaries and neutral curves, differing qualitatively from those for the normal case, are discussed in terms of the existence adjacent to the liquid-solid interface of a sublayer in which the thermal stratification is destabilizing. For  $\text{Hg}_{1-x}\text{Cd}_x\text{Te}$ , our results show that uniform rotation at modest rotation rates can significantly suppress the onset of buoyancy-driven convection.

For a binary liquid undergoing solidification by cooling from below, we assess the stability of the one-dimensional dendritic solution. The mushy zone, consisting of liquid and solid phases, is modeled as a porous medium with anisotropic permeability. The local porosity, as well as the location of the boundaries separating the solid from the mushy zone and the mushy zone from the liquid, are taken to be dynamical variables. The basic state, computed using a thermodynamically self-consistent nonlinear model of solidification, exists for only some combinations of the operating parameters (solidification rate, nominal vertical temperature gradient, and bulk solute concentration). The dendritic solution also exists under conditions for which plane-front solidification is linearly stable with respect to morphological disturbances. This point is discussed in the light of previous work on nonlinear morphological instability. A division of the parameter space according to the existence and stability of solutions corresponding to plane-front and dendritic solidification is presented and discussed for the Pb-Sn system. Uniform rotation is shown to be less stabilizing than in the plane-front case.

## Acknowledgments

I would like to acknowledge my appreciation to my dissertation advisor Professor Arne J. Pearlstein for his great encouragement and guidance throughout this work. Without his support and counsel, this dissertation could not have been finished.

I would like to express my appreciation to Professor Jonathan A. Dantzig, Professor Michael M. Chen, and Professor John D. Buckmaster for serving as members of my committee. Several helpful discussions with Professor David R. Poirier and Professor C. F. Chen are also appreciated.

I am very grateful to my wife, Hulya for her endless support and patience.

Finally, I would like to gratefully acknowledge the support of the Microgravity Science and Applications Division of the National Aeronautics and Space Administration through Grant NAG3-1121. Additional support was provided by the National Science Foundation through Grants MSM-8451157 and CTS-9017181.

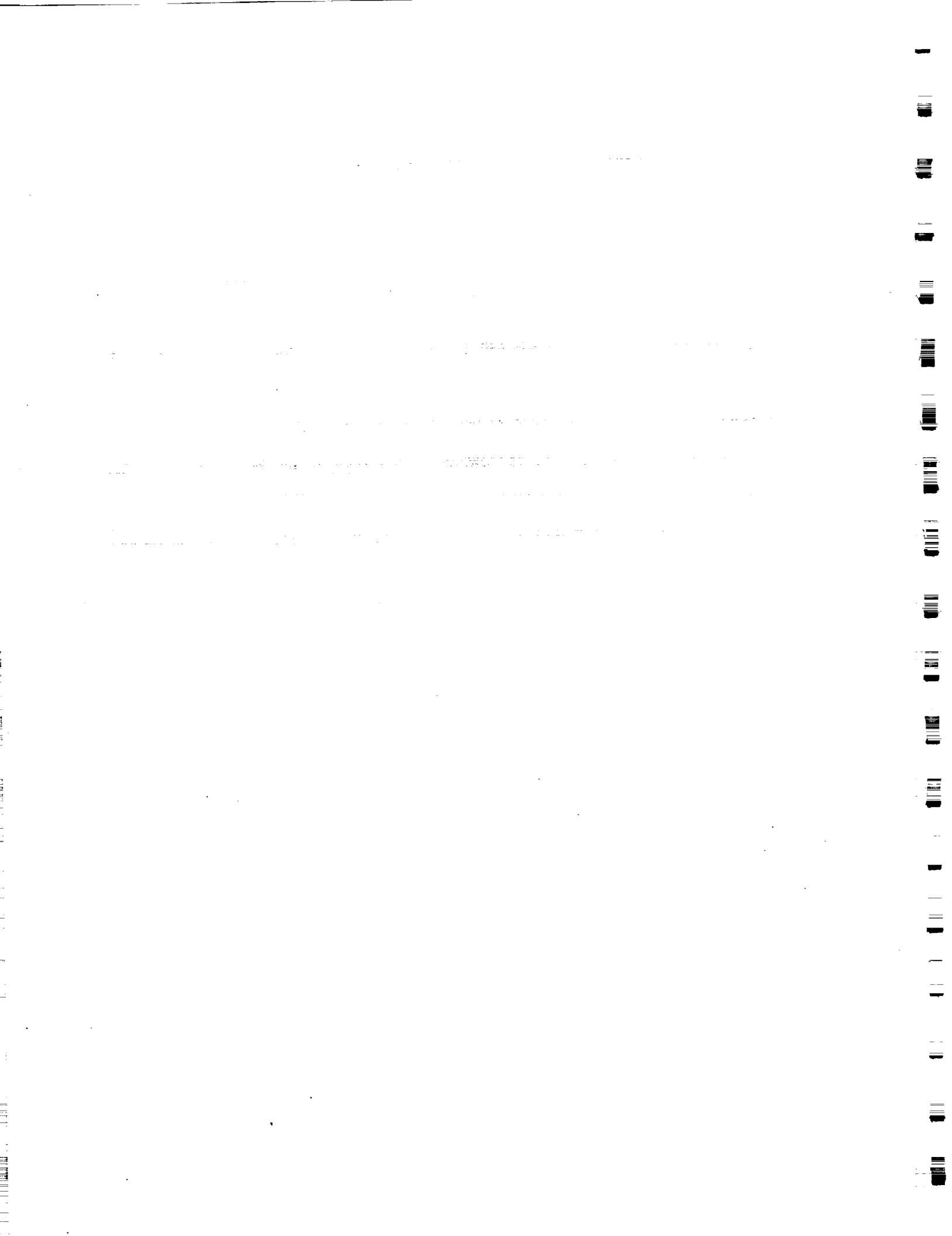


# Table of Contents

	Page
1. Introduction.....	1
1.1. Motivation and Previous Work.....	1
1.2. Overview of the Dissertation.....	6
2. Coriolis Effects on the Stability of Plane-Front Solidification of Dilute Pb-Sn Binary Alloys.....	8
2.1. Introduction.....	8
2.2. Basic State and Linear Disturbance Equations.....	9
2.3. Nondimensionalization and Fourier Decomposition.....	12
2.4. Numerical Solution.....	13
2.5. Results.....	15
2.6. Discussion.....	19
3. Stability of Plane-Front Solidification of a Binary Liquid for which the Density Depends Nonmonotonically on Temperature, including Coriolis Effects.....	23
3.1. Introduction.....	23
3.2. Governing Equations and Formulation.....	26
3.2.1. Equation of State.....	26
3.2.2. Dimensionless Governing Equations.....	27
3.3. Basic State and Linear Disturbance Equations.....	30
3.4. Numerical Solution.....	34
3.5. Results.....	38
3.5.1. Nonrotating Case.....	38
3.5.2. Rotating Case.....	43
3.6. Discussion.....	44
4. Stability of Dendritic Solidification of a Binary Liquid, including Coriolis Effects.....	51
4.1. Introduction.....	51
4.2. Formulation.....	54
4.2.1. Governing Equations.....	54
4.2.2. Boundary Conditions.....	58
4.3. Nondimensionalization.....	60
4.3.1. Dimensionless Governing Equations.....	60

4.3.2. Dimensionless Boundary Conditions.....	62
4.4. Basic State and Linear Disturbance Equations.....	63
4.4.1. Basic State.....	63
4.4.2. Disturbance Equations and Boundary Conditions.....	65
4.4.3. Fourier Decomposition .....	71
4.5. Numerical Solution .....	74
4.6. Results.....	77
4.7. Discussion .....	84
5. Conclusions.....	88
Appendix A .....	92
Appendix B .....	95
Appendix C .....	98
Appendix D .....	102
References .....	104
Tables .....	113
Figures .....	116
Vita .....	179

## CHAPTER 1

### Introduction

#### 1.1. Motivation and Previous Work

Many solid materials of practical interest are prepared by directional solidification of binary and multicomponent liquids. Examples include high-strength, high-temperature alloys for use in turbine blades, electronic and photonic materials, and protein crystals for use in x-ray crystallography.

In those applications in which the goal is to produce large, nearly perfect single crystals, it is frequently desired to achieve "plane-front" solidification. In such a situation, the liquid-solid interface remains planar, the temperature, concentration, and pressure fields are one-dimensional with their gradients normal to the interface, and the fluid motion (due solely to shrinkage) is in the direction of the interface motion and independent of position. The process is steady in a reference frame moving with the interface. It is easily shown that a necessary condition for the existence of this steady one-dimensional state is that the density gradient be parallel or anti-parallel to the gravitational acceleration. Even when this necessary condition is satisfied (e.g., by cooling the liquid from above or below, rather than from the side), however, several instabilities can cause departures from the nominally steady one-dimensional plane-front case.

First, the liquid-solid interface is subject to a morphological instability (Mullins & Sekerka 1964) deforming the planar interface and ultimately leading to formation of a two-phase "mushy zone" of dendrites and interdendritic liquid. In turn, departures from one-dimensionality and steadiness in the mushy zone result in nonuniform solute distribution in the solidified material. Second, the density of a binary liquid depends on both temperature and composition. When a liquid is solidified by cooling from below, preferential rejection or incorporation of solute at the interface is potentially destabilizing if the solute-enriched (or

depleted) liquid at the interface is less dense than the warmer overlying bulk liquid. This solute gradient can overcome the stabilizing temperature gradient, leading to buoyancy-driven convection in the liquid, thus providing another mechanism, besides molecular diffusion, for redistributing solute from the interface into the bulk liquid.

Convective and morphological instabilities in a binary liquid undergoing directional solidification were first studied by Coriell *et al.* (1980). They showed that the buoyancy force does not sensibly alter the criterion for onset of the morphological instability, which occurs at shorter wavelengths than does the convective mode. Subsequent work has been reviewed by Glicksman *et al.* (1986) and Sekerka & Coriell (1987); recent work includes papers by Polezhaev (1988), Müller (1988), Young & Davis (1989), Huppert (1990), Davis (1990), and Worster (1991).

Buoyancy-driven convection during directional solidification of binary alloys has been shown to be the dominant factor in the formation of "freckles", "channel segregates", and other macrosegregation defects deleterious to the mechanical properties of directionally solidified alloys. The formation and characterization of freckles in nickel-based superalloys were first studied experimentally by Giamei & Kear (1970). Following their work, Poirier *et al.* (1981) investigated macrosegregation in electroslag ingots, showed that convection in the melt results in freckling in the solidified material, and suggested that rotation might reduce freckling. Sarazin & Hellawell (1988) have experimentally demonstrated the formation of freckles in Pb-Sn, Pb-Sb, and Pb-Sn-Sb ingots. Specifically, compositional convection, in the form of discrete plumes emanating from chimneys in a mushy zone of dendritic crystals, has been observed by Copley *et al.* (1970) and Chen & Chen (1988) in laboratory experiments using transparent aqueous ammonium chloride solutions. The resulting convection leads to freckles strikingly similar to those found in ingots cast of metallic alloys. Ridder *et al.* (1981) studied the effects of fluid flow on macrosegregation in nominally axisymmetric ingots and showed that melt convection results in macrosegregation in the solidified materials. In a theoretical study of a binary alloy solidifying radially



inward, Maples & Poirier (1984) concluded that macrosegregation results from mushy-zone convection driven by nonuniform temperature and solute distributions. A recent review of the effects of buoyancy-driven convection on macrosegregation in binary and pseudobinary systems has been given by Müller (1988). In particular, much attention is currently focused on the questions of when and how the freckles and channel segregates and other macrosegregation defects are formed, with the main goal being to grow materials that are free of such macrosegregation defects resulting from convection during solidification.

One means by which the onset of convection can be inhibited in a density-stratified fluid layer is to subject the layer to a magnetic field aligned parallel or perpendicular to the stratification (Müller 1988). For horizontal Pb-Sn layers solidified from below at several growth velocities, Coriell *et al.* (1980) showed theoretically that the critical Sn concentration above which instability occurs can be increased an order of magnitude by applying a vertical magnetic field of the order of one tesla. This technique requires that the liquid be an electrical conductor, and so is applicable to metallic alloys, semiconductors, and aqueous solutions.

Macrosegregation might also be controlled by increasing or decreasing the magnitude of the gravitational acceleration or changing its direction. Alexander *et al.* (1989) and Heinrich *et al.* (1989a-b) theoretically studied the effect of reduced gravity on macrosegregation in directionally solidified alloys. These authors suggested that macrosegregation in alloys can be reduced by solidification in a low-gravity environment. Müller (1990) and Weber *et al.* (1990) have recently discussed solidification under conditions where the magnitude of the body force is greater or less than that of normal gravity.

Both gravity and an external magnetic field are body forces which act on the liquid. As opposed to contact forces such as pressure, viscous stress, and surface tension, which act on the surfaces of a fluid element, body forces act on the mass of a fluid element. Hence, their local strengths are proportional to the local fluid density. In addition to gravitational and magnetic body forces, there are other "pseudo-body forces" which manifest themselves as

fictitious accelerations (centripetal and Coriolis) when the reference frame to which the fluid motion is referred undergoes steady rotation relative to an inertial frame. (An additional fictitious acceleration, with which we will not be concerned, manifests itself if the rotation of the noninertial frame relative to the inertial frame is unsteady.) Although these accelerations do not correspond directly to forces (as in the case of the gravitational acceleration), they have the same mathematical form as accelerations associated with body forces, and can have dynamical consequences equally as profound as the gravitational and magnetic forces discussed above (Greenspan 1968). In light of this, and the fact that modification of the gravitational field or imposition of an external magnetic field may not always be feasible, the possibility of using rotation to suppress the onset of convection in a liquid undergoing directional solidification is of interest.

Several effects of rotation on solidification have been discussed by Schulz-DuBois (1972). The experiments of Kou (1978), Kou *et al.* (1978), Sample & Hellawell (1984), Müller (1990), and Weber *et al.* (1990) have shown that rotation can significantly reduce the degree of macrosegregation in binary alloys directionally solidified under plane-front or dendritic conditions. Kou and Kou *et al.* studied the effect of steady rotation about a vertical axis on freckle formation in Sn-Pb alloys. Sample & Hellawell considered solidification of the transparent alloy  $\text{NH}_4\text{Cl-H}_2\text{O}$  in a crucible rotating about an axis inclined between 0 and 30 degrees with respect to the vertical. Müller (1990) and Weber *et al.* have studied the effect of rotation on the growth of Te-doped InSb crystals, and have shown that striations can be suppressed at sufficiently high rotation rates. These studies show that the degree of macrosegregation (freckles and striations) can be significantly reduced by rotation.

There are two means by which steady rotation about a fixed axis can influence the motion of a fluid. In terms of a reference frame rotating with constant angular velocity  $\Omega$  about an axis, these correspond to the centripetal and Coriolis accelerations, for which the terms  $\rho_L \Omega \times \Omega \times \mathbf{r}$  and  $2\rho_L \Omega \times \mathbf{u}$ , respectively, are added to the momentum equation. Here,  $\mathbf{r}$  is the

position vector measured from the axis of rotation,  $u$  is the local fluid velocity relative to the noninertial reference frame, and  $\rho_L$  is the local density of the liquid.

Previous theoretical studies of the effects of rotation on the onset of buoyancy-driven convection have been restricted to cases where no solidification occurs. For a horizontally unbounded layer of a single-component fluid, Chandrasekhar (1953), Chandrasekhar & Elbert (1955), and Niiler & Bisshopp (1965) have shown that steady uniform rotation about a vertical axis can significantly inhibit the onset of convection, with the Coriolis-related Taylor-Proudman mechanism (Chandrasekhar 1961) playing the dominant role. The effects of centripetal, Coriolis, and gravitational accelerations on convection in horizontally confined rotating fluids in cylindrical containers of various aspect ratios were considered in an early series of papers by Homsy & Hudson (1969, 1971a-b, 1972). More recently, for a single-component fluid Weber *et al.* (1990) have computed buoyancy-driven flows equivalent to those that can be driven by a temperature gradient maintained between the ends of an otherwise insulated right circular cylinder rotating at constant angular velocity about an axis perpendicular to and intersecting the cylinder axis but not passing through the cylinder. Three-dimensional computations, in which the variation of the magnitude of the centripetal acceleration  $\Omega \times \Omega \times r$  along the cylinder axis was neglected (a good approximation when the cylinder length is small compared to the shortest distance between the axis of rotation and the cylinder), were performed with the term accounting for the Coriolis acceleration  $2\Omega \times u$  either included or omitted. Weber *et al.* found excellent agreement between experiment and computation when the Coriolis acceleration was included.

For a binary fluid, Pearlstein (1981) has shown that the Coriolis acceleration can either stabilize or destabilize a horizontally unbounded layer, depending on the values of the Prandtl and Schmidt numbers, the dimensionless rotation rate (expressed in terms of a Taylor number), and the dimensionless temperature or solute gradient (expressed in terms of thermal and solutal Rayleigh numbers). Other work concerning the effect of rotation on doubly-diffusive convection in binary fluids (with no phase change) has been reported by

Sengupta & Gupta (1971), Masuda (1978), Antoranz & Velarde (1978, 1979), Schmitt & Lambert (1979), Riahi (1983), Worthem *et al.* (1983), and Bhattacharjee (1988a-c).

## 1.2. Overview of the Dissertation

The purpose of the present work is to investigate the onset of morphological and buoyancy-driven convective instability in a binary liquid undergoing directional solidification and to identify the mechanism by which Coriolis effects affect the onset of buoyancy-driven convection. We consider the stability of plane-front solidification of a binary alloy (Pb-Sn) and the pseudobinary mercury cadmium telluride system, and the dendritic solidification of Pb-Sn.

The dissertation is organized as follows. In Chapter 2, the convective and morphological instabilities in a binary liquid undergoing plane-front solidification by cooling from below are studied. The effects of rotation on the onset of buoyancy-driven convective and morphological instabilities are considered using a linear stability analysis. Results for dilute Pb-Sn alloys are presented and discussed.

In Chapter 3, we use a linear stability analysis to study the onset of instability in binary liquids which exhibit a density maximum in the interior, and solidify with a nominally planar interface. We consider the stability of plane-front solidification of the pseudobinary mercury cadmium telluride system ( $\text{Hg}_{1-x}\text{Cd}_x\text{Te}$ , where  $x$  is the bulk mole fraction of CdTe) from the melt. The effect of a steady uniform rotation about a vertical axis has also been investigated, as for the Pb-Sn system.

In Chapter 4, we use a linear stability analysis to study the buoyancy-driven convection in the liquid and mushy zone and to investigate the effects of rotation on convective instability for alloys solidified dendritically by cooling from below. The mushy zone, consisting of dendrites saturated by interdendritic liquid, is modelled as a porous medium with anisotropic permeability. The local porosity, as well as the locations of the mushy-zone/solid and

liquid/mushy-zone interfaces are taken as dynamical variables, and so are determined as part of the solution. The analysis is illustrated by results for the Pb-Sn system.

The notation is generally consistent throughout the dissertation excepting the usage of  $C$  and its subscripted variants as composition variables, which are defined when first used in each Chapter. The numerical techniques employed in each Chapter are generally similar, but differ in important details, and hence are explained in full in each case.

## CHAPTER 2

# Coriolis Effects on the Stability of Plane-front Solidification of Dilute Pb-Sn Binary Alloys

### 2.1. Introduction

During directional solidification of alloys, it is frequently desired to produce large single crystals with very low densities of macrosegregation defects and other imperfections. In principle, this can sometimes be achieved by "plane-front" solidification, in which the melt-solid interface remains perfectly planar. In such a case, the solidification process would be steady in a reference frame moving with the interface, and the only spatial variation would be in a direction normal to the interface. However, in real systems, several instabilities can cause departures from the nominally steady and one-dimensional plane-front case.

Buoyancy-driven convection occurring during directional solidification of binary alloys leads to the formation of freckles and other macrosegregation defects deleterious to the mechanical properties of directionally solidified alloys. In particular, much attention is currently focused on the questions of when and how the freckles, channel segregates, and other macrosegregation defects are formed, with the main goal being to grow materials that are free of such macrosegregation defects resulting from convection during solidification.

The possibility of using steady uniform rotation about a vertical axis to suppress the onset of buoyancy-driven convection during solidification of a binary alloy is considered using a linear stability analysis. The predicted inhibitory effects of rotation on convection are discussed in terms of previous experimental and theoretical studies of the effect of rotation on the onset of buoyancy-driven convection in single-component fluids heated from below. The plane-front solidification of Pb-Sn binary melts, for which the density depends monotonically on temperature and composition, is considered.

In this Chapter, we use linear stability analysis to study the effect of the Coriolis acceleration on convective and morphological instability for Pb-Sn alloys which solidify with a nominally planar interface. This work serves to identify the mechanism by which Coriolis effects affect the onset of convection in solidifying binary alloys. The analysis is illustrated by results for the Pb-Sn system.

## 2.2. Basic State and Linear Disturbance Equations

We adopt the model of solidification used by Coriell *et al.* (1980), in which the Oberbeck-Boussinesq equations govern motion in the liquid. In a reference frame translating with the nominally steady velocity ( $V_I$ ) of the moving interface and rotating with constant angular velocity  $\Omega$ , as shown in figure 2.1, the basic state

$$\bar{\mathbf{u}} = (0, 0, -\frac{\rho_S}{\rho_{LO}} V_I), \quad (2.1)$$

$$\bar{T}_L = T_M + \frac{m_L C_\infty}{k} + \frac{\rho_{LO} \kappa_L G_L}{\rho_S V_I} \left[ 1 - \exp\left(-\frac{\rho_S V_I}{\rho_{LO} \kappa_L} z\right) \right], \quad (2.2)$$

$$\bar{C}_L = C_\infty \left[ 1 + \frac{1-k}{k} \exp\left(-\frac{\rho_S V_I}{\rho_{LO} D_L} z\right) \right], \quad (2.3)$$

$$\bar{T}_S = T_M + \frac{m_L C_\infty}{k} + \frac{\kappa_S G_S}{V_I} \left[ 1 - \exp\left(-\frac{V_I}{\kappa_S} z\right) \right], \quad (2.4)$$

is the same used by Coriell *et al.*, where  $\bar{\mathbf{u}}$ ,  $\bar{T}_L$ ,  $\bar{C}_L$ , and  $\bar{T}_S$  are, respectively, the basic state velocity (referred to the moving frame), temperature and solute concentration in the liquid, and temperature in the solid,  $\kappa_L$  and  $\kappa_S$  are the thermal diffusivities of the liquid and solid, respectively,  $D_L$  is the diffusion coefficient,  $\rho_S$  is the solid density,  $\rho_{LO}$  is the liquid density of pure lead at its melting point,  $C_\infty$  is the bulk concentration,  $G_L$  is the liquid-side temperature gradient at the planar interface,  $V_I$  is the nominal growth rate,  $k$  is the segregation coefficient,  $m_L$  is the slope of the liquidus,  $T_M$  is the melting temperature of Pb,  $\epsilon = \rho_S/\rho_{LO} - 1$  is the fractional shrinkage,  $G_S = (LV_I + G_L \kappa_L)/\kappa_S$  is the solid-side temperature gradient at the

planar interface,  $k_L$  and  $k_S$  are the thermal conductivities of the liquid and solid, respectively, and  $L$  is the latent heat of fusion per unit volume. (All concentrations used in this Chapter are weight percentages.) We note that the basic-state temperature distribution in the solid (2.4) is valid only near the interface.

As in stability analyses of other flows subject to uniform rotation (Chandrasekhar 1953; Chandrasekhar & Elbert 1955; Niller & Bisshopp 1965; Pearlstein 1981; Nakagawa & Frenzen 1955), the linear disturbance equations we use differ from those for the nonrotating case only by addition of the Coriolis acceleration to the disturbance momentum equation. (This approach neglects the consequences of density variation in the term corresponding to the centripetal acceleration, and is discussed in §2.6.) The equations governing small disturbances in the liquid are

$$\nabla \cdot \mathbf{u} = 0, \quad (2.5)$$

$$\frac{\partial \mathbf{u}}{\partial t} - \frac{\rho_S}{\rho_{L0}} V_I \frac{\partial \mathbf{u}}{\partial z} + 2 \boldsymbol{\Omega} \times \mathbf{u} = - \frac{\nabla p}{\rho_{L0}} - \alpha_T g T_L \mathbf{i}_z - \alpha_C g C_L \mathbf{i}_z + \nu \nabla^2 \mathbf{u}, \quad (2.6)$$

$$\frac{\partial T_L}{\partial t} - \frac{\rho_S}{\rho_{L0}} V_I \frac{\partial T_L}{\partial z} + G_L w \exp\left(-\frac{\rho_S V_I}{\rho_{L0} \kappa_L} z\right) = \kappa_L \nabla^2 T_L, \quad (2.7)$$

$$\frac{\partial C_L}{\partial t} - \frac{\rho_S}{\rho_{L0}} V_I \frac{\partial C_L}{\partial z} + G_C w \exp\left(-\frac{\rho_S V_I}{\rho_{L0} D_L} z\right) = D_L \nabla^2 C_L, \quad (2.8)$$

where the dependent variables  $\mathbf{u}$ ,  $w$ ,  $p$ ,  $T_L$ , and  $C_L$  are, respectively, the disturbance values of the velocity, its  $z$ -component, pressure, temperature, and concentration in the liquid. Here,  $\mathbf{i}_z$  is the unit vector in the  $z$ -direction,  $g$  is the magnitude of the earth's gravitational acceleration,  $\nu$  is the viscosity,  $\alpha_T$  and  $\alpha_C$  are the thermal and solutal expansion coefficients, respectively,  $G_C = (k-1)\rho_S C_\infty V_I / (k\rho_{L0} D_L)$  is the concentration gradient at the planar interface,  $\boldsymbol{\Omega} = \Omega_0 \mathbf{i}_z$  is the angular velocity, and  $\Omega_0$  is a constant. The disturbance energy equation in the solid is

$$\frac{\partial T_S}{\partial t} - V_I \frac{\partial T_S}{\partial z} = \kappa_S \nabla^2 T_S, \quad (2.9)$$



where  $T_S$  is the disturbance temperature in the solid.

Taking the curl of (2.6) and the dot product of the result with  $I_z$ , we obtain an equation

$$\frac{\partial \omega_z}{\partial t} - \frac{\rho_S}{\rho_{L0}} V_I \frac{\partial \omega_z}{\partial z} - 2 \Omega_0 \frac{\partial w}{\partial z} = \nu \nabla^2 \omega_z \quad (2.10)$$

for the z-component of the vorticity,  $\omega_z$ . After twice taking the curl of (2.6), the vertical component of the resulting equation is

$$\frac{\partial}{\partial t} \nabla^2 w - \frac{\rho_S}{\rho_{L0}} V_I \frac{\partial}{\partial z} \nabla^2 w + 2 \Omega_0 \frac{\partial \omega_z}{\partial z} = \alpha_T g \nabla_{\perp}^2 T_L + \alpha_{CG} \nabla_{\perp}^2 C_L + \nu \nabla^4 w. \quad (2.11)$$

The disturbance boundary conditions at the interface are

$$u(x, y, 0, t) = \epsilon V_I \frac{\partial \eta(x, y, t)}{\partial x}, \quad (2.12a)$$

$$v(x, y, 0, t) = \epsilon V_I \frac{\partial \eta(x, y, t)}{\partial y}, \quad (2.12b)$$

$$w(x, y, 0, t) = -\epsilon \frac{\partial \eta(x, y, t)}{\partial t}, \quad (2.12c)$$

$$\frac{\partial w(x, y, 0, t)}{\partial z} = -\epsilon V_I \nabla_{\perp}^2 \eta(x, y, t). \quad (2.12d)$$

$$L \frac{\partial \eta(x, y, t)}{\partial t} = -k_L \frac{\partial T_L(x, y, 0, t)}{\partial z} + k_S \frac{\partial T_S(x, y, 0, t)}{\partial z} + \left( \frac{\rho_S}{\rho_{L0}} \frac{G_L V_I k_L}{\kappa_L} - \frac{G_S V_I k_S}{\kappa_S} \right) \eta(x, y, t), \quad (2.12e)$$

$$\frac{V_I^2 \rho_S C_{\infty}}{D_L \rho_{L0}} \eta(x, y, t) + V_I C_L(x, y, 0, t) + \frac{C_{\infty}}{k} \frac{\partial \eta(x, y, t)}{\partial t} = -\frac{\rho_{L0} D_L}{\rho_S (1-k)} \frac{\partial C_L(x, y, 0, t)}{\partial z}, \quad (2.12f)$$

$$T_L(x, y, 0, t) + G_L \eta(x, y, t) = T_S(x, y, 0, t) + G_S \eta(x, y, t), \quad (2.12g)$$

$$T_L(x, y, 0, t) + G_L \eta(x, y, t) = m_L G_C \eta(x, y, t) + m_L C_L(x, y, 0, t) + T_M \Psi \nabla_{\perp}^2 \eta(x, y, t), \quad (2.12h)$$

where  $\eta$  is the interface position and  $\Psi$  is the capillary coefficient.

### 2.3. Nondimensionalization and Fourier Decomposition

We scale the velocity, time, length, temperature, concentration, and vorticity with  $\kappa_L/H$ ,  $H^2/\nu$ ,  $H$ ,  $G_L H$ ,  $C_\infty$ , and  $\kappa_L/H^2$ , respectively, where  $H = D_L/V_T$  is the characteristic length (associated with the destabilizing gradient of rejected solute, see (2.3)), and write the horizontal and temporal dependence of the dimensionless disturbance quantities as  $\exp(\sigma + ia_x X + ia_y Y)$ , where  $a_x$  and  $a_y$  are the x- and y-components of the wavevector, and  $\sigma$  is the temporal eigenvalue. Substitution into (2.7)-(2.11) yields

$$\sigma(D^2 - a^2)W - \frac{\rho}{Sc} D(D^2 - a^2)W = -Ra_T a^2 \Theta_L - Ra_S Le a^2 C_L + (D^2 - a^2)^2 W - \Omega_0^* D\Omega_Z, \quad (2.13)$$

$$\sigma \Omega_Z - \frac{\rho}{Sc} D\Omega_Z = \Omega_0^* DW + (D^2 - a^2) \Omega_Z, \quad (2.14)$$

$$Pr \sigma \Theta_L - \rho Le D\Theta_L = (D^2 - a^2) \Theta_L - W \exp(-\rho Le Z), \quad (2.15)$$

$$Sc \sigma \chi_L - \rho D\chi_L = (D^2 - a^2) \chi_L + \frac{\Xi \rho}{Le} W \exp(-\rho Z) \quad (2.16)$$

In the melt, and

$$Pr \sigma \Theta_S - Le D\Theta_S = \kappa (D^2 - a^2) \Theta_S \quad (2.17)$$

in the solid. Here,  $Pr = \nu/\kappa_L$  is the Prandtl number,  $Sc = \nu/D_L$  is the Schmidt number,  $Le = D_L/\kappa_L$  is the Lewis number,  $Ra_T = \alpha_T g G_L H^4/(\kappa_L \nu)$  and  $Ra_S = \alpha_C g C_\infty H^3/(D_L \nu)$  are the thermal and solutal Rayleigh numbers, respectively,  $\Omega_0^* = 2\Omega_0 H^2/\nu$  is the square root of the Taylor number,  $\rho = \rho_S/\rho_{L0}$  is the density ratio,  $\kappa = \kappa_S/\kappa_L$  is the thermal diffusivity ratio, and  $\Xi = (1-k)/k$ . The boundary conditions (2.12a-h) at the interface become

$$W(0) = -\epsilon Pr \sigma \beta, \quad (2.18a)$$

$$DW(0) = \epsilon Le a^2 \beta, \quad (2.18b)$$

$$\Omega_Z(0) = 0, \quad (2.18c)$$

$$Sc \sigma \beta = -k_L^* D\theta_L(0) + k_S^* D\theta_S(0) + Le (k_L^* \rho - k_L^*/\kappa - 1/\kappa) \beta, \quad (2.18d)$$

$$(1 - G) \beta = \theta_S(0) - \theta_L(0), \quad (2.18e)$$

$$(Sc \sigma + k \rho) \beta = -k \chi_L(0) - \frac{1}{\Xi \rho} D\chi_L(0), \quad (2.18f)$$

$$(-a^2 T_M^* + m^* - 1) \beta = \frac{m^*}{\rho \Xi} \chi_L(0) + \theta_L(0), \quad (2.18g)$$

where  $W$ ,  $\chi_L$ ,  $\Omega_Z$ , and  $\theta_L$  are, respectively, the amplitudes of the disturbances to the vertical velocity, concentration, vertical vorticity, and temperature in the melt,  $\theta_S$  is the amplitude of the disturbance temperature in the solid, and  $\beta$  (a constant) is the amplitude of the disturbed interface position. Here we define dimensionless parameters  $k_L^* = G_L k_L H / LD_L$ ,  $k_S^* = G_L k_S H / LD_L$ ,  $m^* = m_L G_C / G_L$ ,  $T_M^* = T_M \Psi / G_L H^2$ , and  $G = G_S / G_L$ . For the far-field boundary conditions, we follow Coriell *et al.* (1980) and set all disturbances to zero

$$W = DW = \Omega_Z = \chi_L = \theta_L = 0 \quad \text{as } Z \rightarrow \infty, \quad (2.19a)$$

$$\theta_S = 0 \quad \text{as } Z \rightarrow -\infty, \quad (2.19b)$$

far from the interface.

## 2.4. Numerical Solution

Our objective is to find conditions under which infinitesimally small disturbances neither grow nor decay for a finite number of wavenumbers, and decay for all other wavenumbers. Disturbances which neither grow nor decay are said to be neutral. The neutral disturbances can be of two types, depending on the imaginary part of  $\sigma$ . If the imaginary part of  $\sigma$  is zero for a neutral disturbance, the onset of instability will be *via* monotonically growing disturbances (steady onset). If the imaginary part of  $\sigma$  is not zero, the neutral disturbance will oscillate in time (oscillatory onset).

In the previous section, we formulated an eigenvalue problem for two systems of ordinary differential equations on two semi-infinite intervals (in the melt and in the solid), coupled by boundary conditions at the deformable interface. For convenience, we follow Coriell *et al.* (1980) and solve the problem on a finite interval  $[-h, h]$ , where  $2h$  is the dimensionless height of the computational domain. With regard to the far-field boundary conditions at  $Z = \pm \infty$ , we set all disturbances to zero

$$W = DW = \Omega_Z = \chi_L = \Theta_L = 0 \quad \text{at } Z = h \quad (2.20a)$$

in the melt and

$$\Theta_S = 0 \quad \text{at } Z = -h \quad (2.20b)$$

in the solid. We have used  $h = 10$ . (For steady onset, we have checked a number of our results using more accurate asymptotic boundary conditions applied at  $Z = \pm h$  derived following Keller's (1976) procedure, and have found excellent agreement between the eigenvalues computed using the two sets of boundary conditions.) Since we use Chebyshev polynomials in our numerical solution, we scale the vertical coordinates in the liquid and solid regions by  $z_2 = (2Z - h)/h$  and  $z_1 = (2Z + h)/h$ , respectively, so that each region lies between  $-1$  and  $+1$ . The resulting system is then solved using a spectral Galerkin technique developed by Zebib (1987). The problem is thus reduced to a matrix eigenvalue problem

$$\mathbf{A} \mathbf{s} + \sigma \mathbf{B} \mathbf{s} = 0, \quad (2.21)$$

where  $\sigma$  is the temporal eigenvalue, and the elements of the square matrices  $\mathbf{A}$  and  $\mathbf{B}$  depend on  $a^2 = a_x^2 + a_y^2$ , the square of the horizontal wavenumber, the bulk concentration  $C_\infty$ , and the other dimensionless parameters. The details are given in Appendix A.

In what follows, we characterize the stability of the nominally plane-front solution in terms of the growth velocity  $V_I$  and bulk concentration  $C_\infty$ , with all other parameters taken as fixed. For each value of  $V_I$ , we seek one or more critical values of  $C_\infty$  (denoted by  $C_\infty^*$ ) such

that for  $C_\infty < C_\infty^*$ , disturbances decay for all wavenumbers, while for  $C_\infty > C_\infty^*$ , disturbances grow for all wavenumbers in some range. In order to determine the critical value(s) of  $C_\infty$ , we first determine the neutral curve ( $C_\infty$  versus the wavenumber  $a$ ) separating those combinations of  $C_\infty$  and  $a$  for which all temporal eigenvalues  $\sigma$  lie in the left half-plane (a stable basic state) from those for which at least one eigenvalue lies in the right half-plane (an unstable basic state). To determine the bulk concentration on the neutral curve for an arbitrarily chosen wavenumber  $a$ , we first guess a value of  $C_\infty$  and compute all eigenvalues  $\sigma$  using (2.21). If all eigenvalues have negative real parts, the value of  $C_\infty$  is increased by doubling the previous value; otherwise the new value of  $C_\infty$  is chosen as half the previous value. This process is continued until we determine two values of  $C_\infty$  between which at least one sign change is obtained in the real part of the least stable temporal eigenvalue. The concentration on the neutral curve is then determined using a bisection method.

To compute the critical concentration  $C_\infty^*$  at which instability first occurs (i.e., the minimum on the neutral curve), we arbitrarily choose a wavenumber and compute the corresponding  $C_\infty$  on the neutral curve using the procedure described above. We then fix  $C_\infty$  at the value computed at the previous step and compute the eigenvalues  $\sigma$  for a discrete set of wavenumbers in a chosen range. From this set we select the wavenumber corresponding to the  $\sigma$  with largest real part. If this wavenumber is at an endpoint of the chosen range, we extend the range to include the wavenumber corresponding to the largest  $\text{Re}(\sigma)$ . We then select this wavenumber and determine the corresponding  $C_\infty$  on the neutral curve. We continue this process until the relative change in  $C_\infty$  is less than  $10^{-6}$ .

## 2.5. Results

The solutions of (2.13)-(2.19) depend on fifteen dimensionless parameters, as defined in §§2.2 and 2.3. To determine the stability of a basic state with a nominally planar interface, numerical values of these parameters need to be specified. (Solutions on a finite interval depend also on  $h$ .) It is therefore not possible to numerically explore the effects of

more than a few combinations of these parameters on the onset of instability. In this work, we have thus restricted ourselves to the Pb-Sn system which, due to the low melting points of both components, has been the subject of several experimental studies. The parameter values (other than  $\Omega_0^*$ ) are as used by Coriell *et al.* (1980) at reference conditions corresponding to pure lead at its melting point. (The diffusivity of Sn in Pb corresponds to an infinitely dilute solution.)

To test our code, we first considered the nonrotating case, and compared our results to those of Coriell *et al.* Taking the liquid-side temperature gradient at the interface as  $G_L = 200 \text{ K cm}^{-1}$ , we computed neutral curves ( $C_\infty$  versus  $a$ ) for various values of the solidification rate  $V_I$ . The neutral curves were generally similar to those shown by Coriell *et al.* The only qualitative difference was that, in our work, several new oscillatory neutral curves were found to branch from steady neutral curves found by Coriell *et al.* and in the present work. We believe that our detection of these additional oscillatory neutral curves (which in each case lie well above the critical value of  $C_\infty$  and are hence of no practical consequence) is due to use of a numerical technique which simultaneously computes a large number of temporal eigenvalues at each combination of  $C_\infty$  and  $V_I$ , as opposed to the shooting technique of Coriell *et al.*, which individually computes the temporal eigenvalues by a one-point iteration scheme. The solid and dashed curves represent the steady and oscillatory onset of convection in each of the neutral curves.

For  $G_L = 200 \text{ K cm}^{-1}$ ,  $\Omega_0 = 0 \text{ rpm}$ , and  $V_I = 5$  and  $80 \mu \text{ sec}^{-1}$ , figure 2.2 shows neutral curves similar to those obtained by Coriell *et al.* For  $V_I = 5 \mu \text{ sec}^{-1}$ , steady onset of buoyancy-driven convective instability is found, and the critical concentration below which the plane-front solidification is stable for all wavenumbers occurs on the convective branch, as shown in figure 2.2(a). However, for  $V_I = 80 \mu \text{ sec}^{-1}$ , morphological and oscillatory convective neutral curves are obtained, and the critical concentration occurs on the morphological instability curve, as shown in figure 2.2(b). Note that the critical

wavenumber for the morphological instability mode is larger than that for the buoyancy-driven convective mode.

For this temperature gradient, a transition between these two extreme cases is observed for intermediate values of the solidification rate. Figure 2.3 shows a sequence of neutral curves for increasing  $V_I$ , beginning with figure 2.3(a) for  $V_I = 5 \mu \text{ sec}^{-1}$  (figure 2.2a). When the solidification rate is increased to  $V_I = 12.5 \mu \text{ sec}^{-1}$ , the morphological neutral curve appears at much higher wavenumbers. For  $V_I = 15 \mu \text{ sec}^{-1}$ , one of the buoyancy-driven convective branches pinches off and disappears (figure 2.3c). Another branch pinches off by  $V_I = 20 \mu \text{ sec}^{-1}$  (figure 2.3d). As the solidification rate is further increased to  $V_I = 30 \mu \text{ sec}^{-1}$ , only one steady buoyancy-driven convective branch is left, and the critical concentration has shifted to larger values (figure 2.3e). The steady convective branch pinches off and becomes smaller with increasing solidification rate as shown in figure 2.3(f-h) for  $V_I = 35, 37.5$ , and  $39.375 \mu \text{ sec}^{-1}$ , respectively. Finally, for  $V_I = 40 \mu \text{ sec}^{-1}$  (figure 2.3i) the steady convective branch disappears and the minimum value of  $C_{\infty}$  (corresponding to the critical condition) occurs on the morphological instability branch. For comparison, the extreme case  $V_I = 80 \mu \text{ sec}^{-1}$  (figure 2.2b) is shown again in figure 2.3(j).

For  $G_L = 200 \text{ K cm}^{-1}$  and  $V_I = 30 \mu \text{ sec}^{-1}$ , figure 2.4 shows the neutral curves ( $C_{\infty}$ -a) for different rotation rates. Figure 2.4(a) shows the neutral curve for the nonrotating case (identical to figure 2.3e). If the system is rotated at  $\Omega_0 = 90 \text{ rpm}$ , the critical concentration increases to higher values, as shown in figure 2.4(b). As the rotation rate is increased further to  $\Omega_0 = 180 \text{ rpm}$ , the steady convective branch pinches off, and becomes smaller for  $\Omega_0 = 270 \text{ rpm}$  as illustrated in figure 2.4(c-d). Finally, the steady convective branch disappears, and the critical concentration occurs on the morphological branch for  $\Omega_0 = 360 \text{ rpm}$ . The transition is similar to that shown in figure 2.3.

We present our principal results in terms of stability boundaries in the  $V_I$ - $C_{\infty}^*$  plane. For ease of comparison to the work of Coriell *et al.* (1980), results are presented in terms of dimensional variables. With  $G_L$  fixed at  $200 \text{ K cm}^{-1}$ , figure 2.5 shows stability boundaries

for  $\Omega_0 = 0, 100, 200, 300,$  and  $500$  rpm. For each value of  $\Omega_0$ , the stability boundary consists of some portion of the morphological branch ( $C_{\infty}^*$  decreasing with increasing  $V_I$ ) found by Coriell *et al.* (their figure 1), joined to a convective branch. The critical value of  $C_{\infty}$  on the convective branch is an increasing function of  $\Omega_0$  at any value of  $V_I$ , clearly indicating the inhibitory effect of rotation on the onset of buoyancy-driven convection. We note that for  $V_I = 5 \mu \text{ sec}^{-1}$ , rotation at  $\Omega_0 = 500$  rpm increases by slightly more than two orders of magnitude relative to the nonrotating case the critical Sn concentration above which the plane-front solution becomes unstable. We further note that the morphological branch is unaffected by rotation, whereas as  $\Omega_0$  increases, the value of  $V_I$  at which the onset of instability shifts from the convective branch to the morphological branch decreases from about  $40 \mu \text{ sec}^{-1}$  in the nonrotating case to about  $27 \mu \text{ sec}^{-1}$  for  $\Omega_0 = 500$  rpm.

For each value of  $\Omega_0$ , we see a local minimum near  $V_I = 1 \mu \text{ sec}^{-1}$ , with the minimum shifting to smaller growth velocities and becoming relatively more shallow as  $\Omega_0$  increases. We note that the maximum relative stabilization by rotation occurs near the local minimum, and that for  $\Omega_0 = 500$  rpm, the critical bulk concentration of Sn is increased more than a hundredfold. Although Coriell *et al.* (1980) noted a local minimum in the stability boundary near  $V_I = 1 \mu \text{ sec}^{-1}$  in the nonrotating case for the largest gravitational acceleration considered, they offered no explanation for its existence. This minimum is a consequence of the fact that as  $V_I \rightarrow 0$ , the concentration gradient  $G_C = (k-1)\rho_S C_{\infty} V_I / (k\rho_L D)$  vanishes. As the temperature gradient is independent of  $C_{\infty}$  and is stabilizing, the critical value of  $C_{\infty}$  must ultimately increase as  $V_I \rightarrow 0$ . (Of course, the weight percentage of the solute,  $C_{\infty}$ , cannot exceed 100). As  $C_{\infty}^*$  must initially decrease with increasing  $V_I$ , there must be a local minimum on the convective branch before  $C_{\infty}^*$  can increase to join up with the morphological branch of the stability boundary. This nonmonotonic dependence of  $C_{\infty}^*$  on  $V_I$  can be interpreted in terms of the existence of four critical values of  $V_I$  for certain values of  $C_{\infty}$ . (In addition to the three shown in figures 2.5 and 2.6, we note that for sufficiently large  $V_I$ ,  $C_{\infty}^*$  ultimately increases on the morphological branch (Davis 1990).)



As discussed for the nonrotating case by Coriell *et al.* (1980), at each value of  $\Omega_0$  the onset of morphological instability occurs *via* a short wavelength (large wavenumber) instability, while convective instability sets in *via* disturbances with relatively longer wavelengths. In the following section this point is discussed in the context of the mechanism by which rotation inhibits the onset of convection.

For  $G_L = 400 \text{ K cm}^{-1}$ , figure 2.6 shows stability boundaries ( $C_{\infty}^*$  versus  $V_I$ ), analogous to those for  $G_L = 200 \text{ K cm}^{-1}$ . Aside from a slight shift of the stability boundaries to higher values of  $C_{\infty}^*$ , the results are qualitatively similar to those for  $G_L = 200 \text{ K cm}^{-1}$ . In particular, the onset of buoyancy-driven convection is suppressed but the morphological instability is not influenced by rotation, and the critical value of  $C_{\infty}$  passes through a minimum near  $V_I = 1 \mu \text{ sec}^{-1}$ .

## 2.6. Discussion

The remarkable stabilization obtainable at low growth rates (more than a hundredfold increase in the critical value of  $C_{\infty}$  at  $V_I = 1 \mu \text{ sec}^{-1}$  can be achieved by rotating the layer at 500 rpm for the two values of  $G_L$  considered) is undoubtedly due to the well-known Taylor-Proudman mechanism, described by Chandrasekhar (1961). According to the Taylor-Proudman theorem, steady motion parallel to the axis of rotation in a uniformly rotating inviscid fluid is prohibited at any nonzero rotation rate. If this theorem were strictly applicable to a viscous fluid, the onset of steady convection would be prohibited, since the flow in convection cells must have a vertical component. Instead, in a viscous fluid, one sees an inhibition of the onset of steady convection, with the degree of inhibition (expressed here as an increase in  $C_{\infty}$ ) increasing with  $\Omega_0$ . That the onset of oscillatory convection is hardly affected is due to the fact that the Taylor-Proudman theorem applies only to steady flows. It is also not surprising that the morphological instability is unaffected by rotation. The morphological instability occurs at very short wavelengths, so the motion is almost perpendicular to the

solidification front (i.e., aligned with the axis of rotation). Hence, the Coriolis acceleration does not sensibly affect the morphological instability.

For a horizontally unbounded binary fluid layer in which the density depends on temperature and one composition variable, Pearlstein's linear stability analysis (Pearlstein 1981) shows that Coriolis effects generally inhibit the onset of convection (by the Taylor-Proudman mechanism). Under some conditions, however, rotation can destabilize the layer, depending on the values of  $Pr$ ,  $Sc$ , the dimensionless rotation rate (characterized by a Taylor number), and the dimensionless temperature or solute gradients (characterized by thermal and solutal Rayleigh numbers). For conditions under which destabilization (on a linear basis) occurs relative to the nonrotating case, instability sets in *via* an oscillatory mode, in which the natural frequency of oscillation of a buoyant fluid element is tuned (by rotation) in such a way that there is a local minimum in the critical value of  $Ra_T$  as a function of the dimensionless rotation rate. This behavior was found (Pearlstein 1981) for  $Pr$  and  $Sc$  both less than unity, although there is no apparent reason why such destabilization cannot occur under other conditions when onset is *via* an oscillatory mode.

Although Pearlstein (1981) found in the rotating doubly-diffusive case that for  $Pr < 1 < Sc$  (a condition satisfied in the present case, in which  $Pr = 0.023$  and  $Sc = 81$ ) there can exist as many as three critical values of the solute Rayleigh number for certain values of the Taylor, Prandtl, Schmidt, and thermal Rayleigh numbers, we have found no evidence of such multivalued stability boundaries in the present calculations. As in the case investigated earlier (Pearlstein 1981), it is possible that such behavior occurs in relatively small regions of the parameter space ( $G_L$ ,  $V_1$ , etc.) and has gone undetected so far. As discussed in § 2.5, however, figures 2.5 and 2.6 imply that for certain values of  $C_\infty$  there exist four critical values of  $V_1$  (including the unshown portion of the morphological branch).

Even though the foregoing analysis is restricted to a horizontally unbounded fluid layer, the work of Homsy & Hudson (1971a) and Bühler & Oertel (1982) suggests that its predictions will be qualitatively correct for finite aspect ratios (ratio of mold radius to

height) if the parameter  $\Omega_0^2 R_0/g$  (a Froude number, where  $R_0$  is the mold radius) is sufficiently small. For the onset of thermal convection in rotating water or mercury layers heated from below, the excellent quantitative agreement between classical linear stability analysis for a horizontally unbounded layer (Chandrasekhar 1953; Chandrasekhar & Elbert 1955; Nakagawa & Frenzen 1955) and experimental work for finite aspect ratios (Nakagawa & Frenzen 1955; Fultz & Nakagawa 1955; Goroff 1960) provides a clear demonstration of the potential of the Coriolis acceleration to suppress buoyancy-driven convection in a rotating fluid.

Interpretation of the results of a stability analysis restricted to infinitesimal disturbances is obviously subject to the caveat that larger disturbances might grow, even though sufficiently small disturbances are predicted to decay. Indeed, it is known that for rotating fluid layers heated from below, the onset of thermal convection sometimes does occur (Veronis 1959, 1966, 1968) at lower Rayleigh numbers than predicted by linear theory. However, in that case, accounting for finite (i.e., non-infinitesimal) amplitude disturbances modifies the quantitative predictions of the theory; the basic qualitative prediction of stabilization by rotation remains unchanged.

The relatively modest rotation rates required to significantly inhibit the onset of convection in the Pb-Sn system make the proposed method an interesting candidate for a program of laboratory experiments. (We note here that the experimental work of Müller (1990) and Weber *et al.* (1990) focuses on the effect of rotation on the time-dependence of the supercritical flow, with no information given on the effect of rotation on the suppression of motion. Furthermore, although these authors have concluded that the Coriolis acceleration is key to the elimination of striations at high rotation rates, their experimental design complicates the separation of effects of the Coriolis acceleration from the increased "pseudo-gravitational" effects associated with the centripetal acceleration.) Experiments might be conducted using a completely filled cylindrical mold, thermally insulated on the vertical surface, and mounted axisymmetrically on a rotating horizontal turntable. If the liquid at the

top of the rotating mold is in contact with a gas or vacuum, it will have a nearly paraboloidal free surface, on which the elevation above the point on the axis of rotation is  $\Delta z = \Omega_0^2 r^2 / (2g)$ . Although this configuration is consistent with rigid-body rotation, it also leads to a nearly paraboloidal solid-melt interface. For high rotation rates or large mold radius, this will in turn lead to significant radial variations in the solidified alloy. Also, cooling at the radial boundary leads to a radial temperature gradient, which in turn leads to significant centrifugal effects. For these reasons, the results of the present analysis cannot be compared to the experimental work of Kou (1978), Kou *et al.* (1978), or Sample & Hellawell (1984), in which strong radial variations in macrosegregation are observed in the solid. Experiments of the type proposed above were initiated some time ago by Copley (1976) for the crystallization of ammonium chloride from aqueous solution.

Finally, we note that for many binary systems, plane-front solidification does not occur at practical growth velocities, and that the morphological instability results in dendritic solidification. In this case, rotation might also suppress buoyancy-driven convection in the melt and interdendritic liquid; this possibility is considered for the Pb-Sn system in Chapter 4.

## CHAPTER 3

### Stability of Plane-Front Solidification of a Binary Liquid for which the Density Depends Nonmonotonically on Temperature, including Coriolls Effects

#### 3.1. Introduction

In the previous work on binary liquids (e.g., the study of lead-tin alloys by Coriell *et al.* 1980) solidified by cooling from below (as in Bridgman growth), consideration was restricted to the case in which the liquid density ( $\rho$ ) depended linearly on temperature ( $T$ ) and solute mole fraction ( $C$ ), i.e.,

$$\rho(T, C) = \rho_0 [1 - \alpha(T - T_0) - \beta(C - C_0)] \quad (3.1)$$

where  $T_0$  and  $C_0$  are reference values. In general, the vertical variation of density is given by

$$\frac{\partial \rho}{\partial \hat{z}} = \frac{\partial \rho}{\partial T} \frac{\partial T}{\partial \hat{z}} + \frac{\partial \rho}{\partial C} \frac{\partial C}{\partial \hat{z}} \quad (3.2)$$

so that a local density extremum can occur even if the density depends monotonically on each of the stratifying agencies (as in (3.1)), and the profiles of the stratifying agencies vary monotonically with the vertical coordinate  $\hat{z}$ . For example, when  $T$  increases linearly with increasing elevation above the liquid-solid interface (an excellent approximation for many systems; cf. §3.3) and solute is rejected from or preferentially incorporated into the solid, the steady one-dimensional temperature and solute profiles near the interface can be approximated by

$$T(\hat{z}) = T_0 + G_L \hat{z} \quad (3.3a)$$

and

$$C(\hat{z}) = C_\infty \left[ 1 + \frac{1-k}{k} e^{-V_L \hat{z}/D_L} \right] \quad (3.3b)$$

where  $G_L > 0$  is the liquid-side temperature gradient at the interface,  $V_I$  is the solidification rate,  $D_L$  is the solute diffusion coefficient, and  $k$  is the segregation coefficient. We see that  $dC/d\hat{z} < 0$  for  $k < 1$  (rejection of solute) and  $dC/d\hat{z} > 0$  for  $k > 1$  (preferential incorporation of solute). From (3.2) and (3.3), we have

$$\frac{1}{\rho_0} \frac{\partial \rho}{\partial \hat{z}} = -\alpha G_L + \frac{\beta V_I C_\infty}{D_L} \frac{1-k}{k} e^{-V_I \hat{z}/D_L}, \quad (3.4)$$

so that if the inequality

$$\frac{\beta V_I C_\infty}{\alpha G_L D_L} \frac{1-k}{k} > 1 \quad (3.5)$$

is satisfied, the density will assume a maximum value at

$$\hat{z}^* = -\frac{D_L}{V_I} \ln \left[ \frac{\alpha G_L D_L k}{\beta V_I C_\infty (1-k)} \right] \quad (3.6)$$

in the liquid, notwithstanding the monotonic dependence of  $\rho$  on  $T$  and  $C$ , and of  $T$  and  $C$  on  $\hat{z}$ .

The density can also depend nonmonotonically on  $\hat{z}$  if  $\rho(T, C)$  varies nonmonotonically with one of the stratifying agencies, say  $T$ . Among the binary systems in which density does not depend monotonically on temperature are many dilute aqueous solutions, for which the local density maximum is associated with the 3.98°C density maximum of pure water (at one atmosphere), and dilute solutions of cadmium telluride in mercury telluride. As noted in §§3.5 and 3.6, the density can also have more than one local extremum, even though the temperature and solute distributions depend monotonically on  $\hat{z}$ .

Although fluid layers having local density maxima have been the subjects of previous studies of the onset of buoyancy-driven convection in water (Veronis 1963; Merker *et al.* 1979; Normand & Azouni 1992), directional solidification of a binary liquid differs in several important ways. First, one must account for the deformable moving interface. Second, in a fluid layer with a linear vertical temperature gradient, nonmonotonic dependence of density on temperature corresponds to a local density maximum in a single-component fluid, whereas (3.2) shows that in the binary case with density depending on temperature and

composition, the elevation where  $\partial\rho/\partial T = 0$  generally does not correspond to a local density maximum. Moreover, it is well-known that in a binary fluid, onset of buoyancy-driven convection depends on the individual stratifying agencies (temperature and solute in the present case), rather than on the density gradient. (Turner 1973, Chapter 8). Although this point has been recognized in analyses of convection in dilute aqueous solutions of NaCl (Foster 1972; Gebhart & Mollendorf 1978; Qureshi & Gebhart 1986), the stability of plane-front solidification of a liquid with a nonmonotonic dependence of density on temperature has not been previously considered.

The effects of rotation on convective and morphological instabilities have been reviewed by Öztekin & Pearlstein (1992) and in Chapter 2 herein. In the linear stability analysis for Pb-Sn alloys, the results of Chapter 2 show that the Coriolis acceleration suppresses buoyancy-driven convection in the melt, and plane-front solidification becomes stable in a larger range of solidification rate and concentration for any given temperature gradient. Here, we investigate the effect of rotation on the onset of instability for  $\text{Hg}_{1-x}\text{Cd}_x\text{Te}$  pseudobinary alloys.

We use a linear stability analysis to study the onset of instability in binary liquids which exhibit a density maximum in the interior, and solidify with a nominally planar interface. We also assess the potential of uniform rotation to suppress the onset of buoyancy-driven convection. We consider the stability of plane-front solidification of the pseudobinary alloy mercury cadmium telluride ( $\text{Hg}_{1-x}\text{Cd}_x\text{Te}$ , where  $x$  is the bulk mole fraction of CdTe, herein denoted by  $C_\infty$ ) from the melt. The growth of  $\text{Hg}_{1-x}\text{Cd}_x\text{Te}$  crystals is of considerable practical interest because of the uses this material finds in the fabrication of infrared detectors and other electro-optical devices. For these applications, crystal size and defect density are critical, with the goal being to produce large single crystals with very high degrees of uniformity and very low densities of macrosegregation defects and other imperfections. This has led to a number of experimental (Galazka *et al.* 1981; Capper *et al.* 1986) and theoretical (Bourret *et al.* 1985; Kim & Brown 1989; Apanovich & Ljumkis 1991) studies of

solidification of  $\text{Hg}_{1-x}\text{Cd}_x\text{Te}$  from the melt. For a more detailed discussion, the reader is referred to the reviews by Micklethwaite (1981) and Capper (1989).

This Chapter is organized as follows. In §3.2, we present the governing equations and an appropriate nondimensionalization. The one-dimensional basic state and linear disturbance equations are given in §3.3. The numerical solution technique is described in §3.4. Results for the  $\text{Hg}_{1-x}\text{Cd}_x\text{Te}$  pseudobinary system are presented in §3.5a and §3.5b for the nonrotating and rotating cases, respectively, followed in §3.6 by a general discussion of the solidification of binary liquids in which the density depends nonmonotonically on temperature.

## 3.2. Governing Equations and Formulation

### 3.2.1. Equation of State

For the solidification of mercury cadmium telluride, we have used an equation of state based on the experimental data of Chandra & Holland (1983) and Mokrovskii & Regel (1952). Since the density of pure  $\text{HgTe}$  liquid does not depend monotonically on temperature, the density of  $\text{Hg}_{1-x}\text{Cd}_x\text{Te}$  will also depend nonmonotonically on temperature for sufficiently small  $\text{CdTe}$  mole fractions. The variation of liquid density with temperature and composition is represented by bivariate polynomials of the form

$$\rho_L(T, C) = \sum_{i=0}^3 \sum_{j=0}^{4-i} b_{ij} C^j (T - 1030 \text{ K})^i \quad \text{for } T < T_{\max}(C) \quad (3.7a)$$

and

$$\rho_L(T, C) = \sum_{i=0}^3 \sum_{j=0}^1 d_{ij} C^j (T - 1030 \text{ K})^i \quad \text{for } T > T_{\max}(C) \quad (3.7b)$$

where

$$T_{\max}(C) = \sum_{i=0}^3 r_i C^i \quad (3.8)$$



is a polynomial fit to the largest temperature (as a function of  $C$ ) for which density data are available in the literature. The linear dependence of density on temperature (3.7b) for  $T > T_{\max}(C)$  is chosen to match  $\rho_L$  and  $\partial\rho_L/\partial T$  at  $T_{\max}$ . Details are given in Appendix B.

### 3.2.2. Dimensionless Governing Equations

We adopt the model of directional solidification used by Coriell *et al.* (1980), in which the thermophysical properties in the liquid are taken to be constant, except for the density. The spatial and temporal variation of liquid density according to (3.7a,b) will be accounted for in the buoyancy term and neglected everywhere else.

We scale the velocity, time, length, pressure, solute mole fraction, and the difference between the local and interface temperatures with  $V_I$ ,  $H/V_I$ ,  $H$ ,  $\rho_{L0}vV_I/H$ ,  $C_\infty$ , and  $G_L H$ , respectively, where  $H = D_L/V_I$  is the characteristic length associated with the solute gradient at the interface,  $V_I$  is the nominal solidification rate (with dimensions of velocity),  $\kappa_L$  is the thermal diffusivity of the liquid,  $D_L$  is the binary diffusivity of CdTe in the liquid,  $\nu$  is the kinematic viscosity,  $C_\infty$  is the bulk value of the solute mole fraction,  $\rho_{L0}$  is the liquid density at the bulk value of the solute mole fraction and the corresponding liquidus temperature, and  $G_L$  is the nominal liquid-side temperature gradient at the interface. The dimensionless equations governing the fluid motion are the Oberbeck-Boussinesq equations in a reference frame translating with the nominally steady velocity ( $I_2 V_I$ ) of the moving interface

$$\nabla \cdot \mathbf{u} = 0, \quad (3.9a)$$

$$\frac{1}{Sc} \left( \frac{\partial \mathbf{u}}{\partial \tau} + \mathbf{u} \cdot \nabla \mathbf{u} + 2\boldsymbol{\Omega}^* \times \mathbf{u}_L + \boldsymbol{\Omega}^* \times (\boldsymbol{\Omega}^* \times \mathbf{r}) \right) = -\nabla p - \frac{\rho_L(T_L, C_L)}{\rho_{L0}\gamma^3 Sc} I_2 + \nabla^2 \mathbf{u}, \quad (3.9b)$$

$$Le \left( \frac{\partial T_L}{\partial \tau} + \mathbf{u} \cdot \nabla T_L \right) = \nabla^2 T_L, \quad (3.9c)$$

$$\frac{\partial C_L}{\partial \tau} + \mathbf{u} \cdot \nabla C_L = \nabla^2 C_L, \quad (3.9d)$$

where the dimensionless variables  $u$ ,  $p$ ,  $T_L$ , and  $C_L$  are, respectively, velocity, pressure, temperature, and solute mole fraction in the liquid,  $Sc = \nu/D_L$  is the Schmidt number,  $Le = D_L/\kappa_L$  is the Lewis number,  $\gamma = V_I/(gD_L)^{1/3}$  is the dimensionless solidification rate,  $g$  is the magnitude of the gravitational acceleration, and  $\Omega^* = \Omega H/V_I = \Omega (D_L/g^2)^{1/3}/\gamma^2$  is the dimensionless angular velocity. We note that in (3.9a-d), the velocity is referred to the moving frame, unlike the mixed formulations employed by Coriell *et al.* (1980) and subsequent authors in which the velocity in the laboratory frame appears in equations written in the moving frame.

The energy equation in the solid is

$$Le \left( \frac{\partial T_S}{\partial \tau} - \frac{\partial T_S}{\partial z} \right) = \kappa^* \nabla^2 T_S, \quad (3.10)$$

where  $T_S$  is the dimensionless temperature in the solid,  $\kappa^* = \kappa_S/\kappa_L$  is the thermal diffusivity ratio, and  $\kappa_S$  is the thermal diffusivity of the solid.

Dimensionless boundary conditions at the interface are derived from conservation of mass

$$-\epsilon V_S \cdot \mathbf{n} - \rho^* l_z \cdot \mathbf{n} = \mathbf{u} \cdot \mathbf{n}, \quad (3.11a)$$

and the no-slip assumption

$$(\mathbf{u} + l_z) \cdot \mathbf{t} = 0, \quad (3.11b)$$

where  $\mathbf{n}$  and  $\mathbf{t}$  are unit vectors normal and tangential to the interface, respectively,  $V_S$  is the local interface velocity scaled by  $V_I$ ,  $\rho^* = \rho_S/\rho_{L0}$  is the density ratio,  $\rho_S$  is the (constant) solid density, and  $\epsilon = \rho^* - 1$  is the fractional shrinkage. The dimensionless energy balance at the interface is

$$\frac{\gamma}{\Gamma} L^* (V_S + l_z) \cdot \mathbf{n} = -k_L^* \nabla T_L \cdot \mathbf{n} + \Lambda \nabla T_S \cdot \mathbf{n}, \quad (3.11c)$$

where the right-hand side corresponds to the difference between the normal components of the heat flux vectors in the liquid and solid, and the left-hand side corresponds to the product of the latent heat ( $L^* = L(C_\infty)/L_0$ , where  $L(C_\infty)$  is the latent heat per unit volume and  $L_0 = L(0)$ ) and the normal component of the solidification velocity. Here  $\Gamma = G_L k_{L0} / [L_0 (g D_L)^{1/3}]$  is the dimensionless liquid-side temperature gradient at the interface,  $\Lambda = k_S(C_\infty) / k_{L0}$  is the thermal conductivity ratio,  $k_L^* = k_L(C_\infty) / k_{L0}$ ,  $k_{L0}$  is the thermal conductivity of pure HgTe liquid at its melting temperature, and  $k_L(C_\infty)$  and  $k_S(C_\infty)$  are the thermal conductivities of the liquid and solid, respectively. The dimensionless solute balance at the interface is

$$\rho^* (C_L - C_S) (V_S + I_2) \cdot \mathbf{n} = -\nabla C_L \cdot \mathbf{n}, \quad (3.11d)$$

where  $C_S$  is the solute mole fraction in the solid. We also require the temperature to be continuous

$$T_L = T_S, \quad (3.11e)$$

across the interface, the liquid and solid solute mole fractions at the interface to be related according to the binary phase diagram

$$C_S = k C_L, \quad (3.11f)$$

where  $k$  is the segregation coefficient, and the temperature and solute mole fraction on the liquid side of the interface to be related by

$$\frac{\Gamma}{\gamma} T_L = m_L^* \left( C_L - \frac{1}{k} \right) - \Psi^* \gamma \left( \frac{1}{R_1} + \frac{1}{R_2} \right), \quad (3.11g)$$

where  $m_L^* = m_L C_\infty k_{L0} / (D_L L_0)$ ,  $\Psi^* = T_M k_{L0} \Psi g^{1/3} / (D_L^{5/3} L_0)$ ,  $T_M$  is the melting temperature of HgTe,  $m_L$  is the slope of the liquidus,  $R_1$  and  $R_2$  are the principal radii of curvature of the interface, and  $\Psi$  is the capillary coefficient. The temperature- and composition-dependence

of most of the thermophysical properties (other than  $\rho_L$ ) is given for  $\text{Hg}_{1-x}\text{Cd}_x\text{Te}$  in Appendix C. For the remaining properties, values measured at selected temperatures and compositions are taken as constant over the entire range.

### 3.3. Basic State and Linear Disturbance Equations

In the reference frame described in §3.2.2, the steady one-dimensional basic state specified by

$$\bar{V}_S = 0, \quad (3.12a)$$

with

$$\bar{u} = -\rho^* l_z, \quad (3.12b)$$

$$\bar{T}_L = \frac{1}{\rho^* Le} [1 - \exp(-\rho^* Le z)], \quad (3.12c)$$

$$\bar{C}_L = 1 + \Xi \exp(-\rho^* z), \quad (3.12d)$$

in the liquid, and

$$\bar{T}_S = \frac{\kappa^*(k_L^* + L^*\gamma/\Gamma)}{\Lambda Le} [1 - \exp(-\frac{Le}{\kappa^*} z)], \quad (3.12e)$$

in the solid is, with one exception, the same as that used by Coriell *et al.* (1980). Here  $\bar{V}_S$ ,  $\bar{u}$ ,  $\bar{T}_L$ ,  $\bar{C}_L$ , and  $\bar{T}_S$  are, respectively, the dimensionless basic state interface velocity, velocity, temperature, and solute distributions in the liquid, and temperature distribution in the solid, and  $\Xi = (1-k)/k$ . Our basic state differs from that of Coriell *et al.* in that  $V_S = 0$  and  $u$  is not proportional to the shrinkage  $\epsilon$ , because in our formulation the interface and fluid velocities are referred to the same (moving) inertial reference frame. Note that for  $\rho^* \approx 1$  and  $Le = O(10^{-3})$ , (3.12c) can be approximated by a linear function of  $z$  (e.g., (3.3a)) from the interface out to fairly large values of  $z$ .

To determine the conditions under which a disturbance grows, we write the interface velocity, liquid velocity, temperature, solute mole fraction, and pressure as

$$\mathbf{V}_S(x, y, \tau) = \mathbf{0} + \mathbf{V}'_S(x, y, \tau) , \quad (3.13a)$$

$$\mathbf{u}(x, y, z, \tau) = \bar{\mathbf{u}} + \mathbf{u}'(x, y, z, \tau) , \quad (3.13b)$$

$$T_L(x, y, z, \tau) = \bar{T}_L(z) + T'_L(x, y, z, \tau) , \quad (3.13c)$$

$$C_L(x, y, z, \tau) = \bar{C}_L(z) + C'_L(x, y, z, \tau) , \quad (3.13d)$$

$$p(x, y, z, \tau) = \bar{p}(z) + p'(x, y, z, \tau) , \quad (3.13e)$$

and the solid temperature as

$$T_S(x, y, z, \tau) = \bar{T}_S(z) + T'_S(x, y, z, \tau) , \quad (3.13f)$$

where  $\mathbf{V}'_S$ ,  $\mathbf{u}'$ ,  $T'_L$ ,  $C'_L$ , and  $p'$  are, respectively, disturbances to the dimensionless interface velocity, liquid velocity, temperature, solute distribution, and pressure,  $T'_S$  is the dimensionless temperature disturbance in the solid, and  $\bar{p}$  is the dimensionless basic state pressure distribution. Substituting (3.13a-f) into the governing equations and boundary conditions, subtracting the basic state equations, and retaining only linear terms, we obtain dimensionless disturbance equations and boundary conditions. The equations governing small disturbances in the liquid are

$$\nabla \cdot \mathbf{u}' = 0 , \quad (3.14a)$$

$$\frac{1}{Sc} \left( \frac{\partial \mathbf{u}'}{\partial \tau} - \rho^* \frac{\partial \mathbf{u}'}{\partial z} + 2 \Omega^* \times \mathbf{u}' \right) = -\nabla p' - \frac{\Gamma F_T}{\gamma^4 Sc} T'_L \mathbf{l}_z - \frac{F_C}{\gamma^3 Sc} C'_L \mathbf{l}_z + \nabla^2 \mathbf{u}' , \quad (3.14b)$$

$$Le \left[ \frac{\partial T'_L}{\partial \tau} - \rho^* \frac{\partial T'_L}{\partial z} + w' \exp(-\rho^* Le z) \right] = \nabla^2 T'_L , \quad (3.14c)$$

$$\frac{\partial C'_L}{\partial \tau} - \rho^* \frac{\partial C'_L}{\partial z} - \Xi \rho^* w' \exp(-\rho^* z) = \nabla^2 C'_L , \quad (3.14d)$$

where  $w'$  is the dimensionless  $z$ -component of the disturbance velocity. Here, we define  $F_T = f_T L_0 D_L / (\rho_{L0} k_{L0})$ ,  $F_C = C_\infty f_C / \rho_{L0}$ ,  $f_T = \partial \rho_L(\bar{T}_L, \bar{C}_L) / \partial T$ ,  $f_C = \partial \rho_L(\bar{T}_L, \bar{C}_L) / \partial C$ ,  $\Omega^* = \Omega_0^* \mathbf{l}_z$ ,

and  $\Omega_0^* = \Omega_0 (D_L/g^2)^{1/3}/\gamma^2$  is the dimensionless rotation rate. We note that although the left-hand sides of the disturbance equations are similar to the corresponding left-hand sides of the disturbance equations of Coriell *et al.* and others, the second term in each of (3.14b-d) arises from a convective term of the type  $\mathbf{u} \cdot \nabla(\ )$ , whereas in previous work these terms arose from the mixed nature of the formulation.

The disturbance energy equation in the solid is

$$Le \left( \frac{\partial T'_S}{\partial \tau} - \frac{\partial T'_S}{\partial z} \right) = \kappa^* \nabla^2 T'_S. \quad (3.15)$$

Taking the curl of (3.14b) and the dot product of the result with  $\mathbf{I}_z$ , we obtain an equation

$$\frac{1}{Sc} \left( \frac{\partial \omega'}{\partial \tau} - \rho^* \frac{\partial \omega'}{\partial z} - 2\Omega_0^* \frac{\partial \omega'}{\partial z} \right) = \nabla^2 \omega' \quad (3.16a)$$

for the z-component of the vorticity,  $\omega'_L$ . Taking the curl of (3.14b) twice and the dot product of the result with  $\mathbf{I}_z$ , we obtain an equation

$$\frac{1}{Sc} \left( \frac{\partial}{\partial \tau} \nabla^2 w' - \rho^* \frac{\partial}{\partial z} \nabla^2 w' + 2\Omega_0^* \frac{\partial w'}{\partial z} \right) = \frac{\Gamma F_T}{\gamma^4 Sc} \nabla_{\perp}^2 T'_L + \frac{F_C}{\gamma^3 Sc} \nabla_{\perp}^2 C'_L + \nabla^4 w'. \quad (3.16b)$$

for the z-component of the velocity, where  $\nabla_{\perp}^2 = \partial^2/\partial x^2 + \partial^2/\partial y^2$  is the horizontal portion of the Laplacian operator.

The disturbance boundary conditions linearized about the nominal interface position ( $z = 0$ ) are

$$u'(x, y, 0, \tau) = \varepsilon \frac{\partial \eta(x, y, \tau)}{\partial x}, \quad (3.17a)$$

$$v'(x, y, 0, \tau) = \varepsilon \frac{\partial \eta(x, y, \tau)}{\partial y}, \quad (3.17b)$$

$$w'(x, y, 0, \tau) = -\varepsilon \frac{\partial \eta(x, y, \tau)}{\partial \tau}, \quad (3.17c)$$

$$\frac{\partial w'(x, y, 0, \tau)}{\partial z} = -\varepsilon \nabla_{\perp}^2 \eta(x, y, \tau), \quad (3.17d)$$

$$\frac{\gamma}{\Gamma} L^* \frac{\partial \eta(x, y, \tau)}{\partial \tau} = -k_L^* \frac{\partial T_L'(x, y, 0, \tau)}{\partial z} +$$

$$\Lambda \frac{\partial T_S'(x, y, 0, \tau)}{\partial z} + \text{Le} \left( k_L^* \rho^* - \frac{k_L^*}{\kappa^*} - \frac{L^* \gamma}{\kappa^* \Gamma} \right) \eta(x, y, \tau), \quad (3.17e)$$

$$k \rho^* \eta(x, y, \tau) + k C_L'(x, y, 0, \tau) + \frac{\partial \eta(x, y, \tau)}{\partial \tau} = -\frac{1}{\Xi \rho^*} \frac{\partial C_L'(x, y, 0, \tau)}{\partial z}, \quad (3.17f)$$

$$T_L'(x, y, 0, \tau) + \eta(x, y, \tau) = T_S'(x, y, 0, \tau) + \frac{1}{\Lambda} \left( k_L^* + L^* \frac{\gamma}{\Gamma} \right) \eta(x, y, \tau), \quad (3.17g)$$

$$\frac{\Gamma}{\gamma} \left[ T_L'(x, y, 0, \tau) + \eta(x, y, \tau) \right] = m_L^* \left[ C_L'(x, y, 0, \tau) - \rho^* \Xi \eta(x, y, \tau) \right] + \Psi^* \gamma \nabla_{\perp}^2 \eta(x, y, \tau), \quad (3.17h)$$

where  $V_S'(x, y, \tau) = I_z \partial \eta / \partial \tau$  is the linearization of the disturbance interface velocity, and  $\eta$  is the local dimensionless interface deflection.

We write the horizontal and temporal dependence of the dimensionless disturbance quantities as  $\exp(\sigma \tau + i a_x x + i a_y y)$ , where  $a_x$  and  $a_y$  are the  $x$ - and  $y$ -components of the horizontal wavevector, and  $\sigma$  is the temporal eigenvalue. Substitution into (3.14c,d), (3.15), and (3.16) yields

$$\begin{aligned} \frac{1}{Sc} \left[ \sigma(D^2 - a^2)W - \rho^* D(D^2 - a^2)W + 2\Omega_0^* D\omega \right] = \\ - \frac{\Gamma F_T}{\gamma^4 Sc} a^2 \Theta_L - \frac{F_C}{\gamma^3 Sc} a^2 \chi_L + (D^2 - a^2)^2 W, \end{aligned} \quad (3.18a)$$

$$\frac{1}{Sc} \left( \sigma \omega - \rho^* D\omega + 2\Omega_0^* DW \right) = (D^2 - a^2)\omega, \quad (3.18b)$$

$$\text{Le} \left( \sigma \Theta_L - \rho^* D\Theta_L \right) = (D^2 - a^2)\Theta_L - \text{Le} W \exp(-\rho^* \text{Le} z), \quad (3.18c)$$

$$\sigma \chi_L - \rho^* D\chi_L = (D^2 - a^2)\chi_L + \Xi \rho^* W \exp(-\rho^* z) \quad (3.18d)$$

in the liquid, and

$$\text{Le} \left( \sigma \Theta_S - D\Theta_S \right) = \kappa^* (D^2 - a^2)\Theta_S \quad (3.19)$$

In the solid; the boundary conditions (3.17a-h) at the interface become

$$W(0) = -\epsilon \sigma \beta, \quad (3.20a)$$

$$DW(0) = \epsilon a^2 \beta, \quad (3.20b)$$

$$\omega(0) = 0, \quad (3.20c)$$

$$\frac{\gamma}{\Gamma} L^* \sigma \beta = -k_L^* D\Theta_L(0) + \Lambda D\Theta_S(0) + Le \left( k_L^* \rho^* - \frac{k_L^*}{\kappa^*} - \frac{L^* \gamma}{\kappa^* \Gamma} \right) \beta, \quad (3.20d)$$

$$(\sigma + k \rho^*) \beta = -k \chi_L(0) - \frac{1}{\Xi \rho^*} D\chi_L(0), \quad (3.20e)$$

$$\Theta_L(0) + \beta = \Theta_S(0) + \frac{1}{\Lambda} \left( k_L^* + L^* \frac{\gamma}{\Gamma} \right) \beta, \quad (3.20f)$$

$$\frac{\Gamma}{\gamma} [\Theta_L(0) + \beta] = m_L^* [\chi_L(0) - \rho^* \Xi \beta] - \Psi^* \gamma a^2 \beta, \quad (3.20g)$$

where  $W$ ,  $\omega$ ,  $\chi_L$ , and  $\Theta_L$  are, respectively, the amplitudes of the disturbances to the vertical velocity, vertical vorticity, solute distribution, and temperature in the liquid,  $\Theta_S$  is the amplitude of the disturbance temperature in the solid, and  $\beta$  (a constant) is the amplitude of the disturbed interface position. For the boundary conditions far from the interface, we have followed Coriell *et al.* (1980) and set all disturbances to zero

$$W = DW = \omega = \chi_L = \Theta_L = 0 \quad \text{as } z \rightarrow \infty, \quad (3.21a-e)$$

$$\Theta_S = 0 \quad \text{as } z \rightarrow -\infty. \quad (3.21f)$$

### 3.4. Numerical Solution

Our objective is to find conditions for which infinitesimally small disturbances decay ( $\text{Re}(\sigma) < 0$ ) for all but a finite number of critical wavenumbers (typically one), and are neutral ( $\text{Re}(\sigma) = 0$ ) for the critical wavenumber(s). These conditions separate basic states that are linearly stable from those that are not.



In the previous section, we formulated an eigenvalue problem for systems of ordinary differential equations on two semi-infinite intervals (in the liquid and solid), coupled by boundary conditions at the deformable interface. For convenience, we follow Coriell *et al.* (1980) and solve the problem on a finite computational domain  $[-h, h]$ . With regard to the far-field boundary conditions at  $z = \pm \infty$ , we set all disturbances to zero at  $z = h$

$$W = DW = \omega = \chi_L = \Theta_L = 0 \quad \text{at } z = h, \quad (3.22a-e)$$

In the liquid and at  $z = -h$

$$\Theta_S = 0 \quad \text{at } z = -h. \quad (3.22f)$$

in the solid, where we have taken  $h$  to be at least 10, depending on the vertical structure of the basic state temperature and solute fields given by (3.12c,d). (For steady onset, we have checked a number of our results using more accurate asymptotic boundary conditions applied at  $z = \pm h$  derived following Keller's (1976) procedure, and have found excellent agreement between eigenvalues computed using the two sets of boundary conditions.) Since we use Chebyshev polynomials in our numerical solution, we scale the vertical coordinate in the liquid and solid regions by  $z_2 = (2z - h)/h$  and  $z_1 = (2z + h)/h$ , respectively, so that each region lies between  $-1$  and  $+1$ . The resulting system is solved using a spectral Galerkin technique developed by Zebib (1987).

We approximate the highest derivatives of the amplitude of the disturbance velocity, solute distribution, and temperature in the liquid, and temperature in the solid, by truncated sums of Chebyshev polynomials of the form

$$W^{(4)}(z_2) = \sum_{j=0}^J K_j T_j(z_2), \quad (3.23a)$$

$$\omega^{(2)}(z_2) = \sum_{j=0}^J M_j T_j(z_2), \quad (3.23b)$$

$$\chi_L^{(2)}(z_2) = \sum_{j=0}^J P_j T_j(z_2), \quad (3.23c)$$

$$\Theta_L^{(2)}(z_2) = \sum_{j=0}^J Q_j T_j(z_2), \quad (3.23d)$$

$$\Theta_S^{(2)}(z_1) = \sum_{j=0}^J Z_j T_j(z_1), \quad (3.23e)$$

where  $T_j$  is the  $j$ -th Chebyshev polynomial and the coefficients  $K_j$ ,  $M_j$ ,  $P_j$ ,  $Q_j$ , and  $Z_j$  are to be found. Representations of lower order derivatives can be found by integrating (3.23a-e) and using standard properties of Chebyshev polynomials. The procedure described by Zebib (1987) reduces the problem to a matrix eigenvalue problem

$$\mathbf{A} \mathbf{s} + \sigma \mathbf{B} \mathbf{s} = 0, \quad (3.24)$$

where  $\sigma$  is the temporal eigenvalue, and the elements of the square matrices  $\mathbf{A}$  and  $\mathbf{B}$  depend on the square of the horizontal wavenumber  $a^2 = a_x^2 + a_y^2$ , the bulk mole fraction  $C_\infty$ , and the other dimensionless parameters. A more detailed description is given in Appendix A.

In what follows, we characterize the stability of the nominally plane-front solution in terms of the bulk mole fraction  $C_\infty$  and dimensionless solidification rate  $\gamma$ , with all other parameters taken as fixed. As shown in §3.5, there is a critical value  $\gamma_c$  such that for  $\gamma > \gamma_c$ , there is no range of stable  $C_\infty$  (i.e., for any  $C_\infty$  a disturbance at some wavenumber will grow), while for  $\gamma < \gamma_c$ , disturbances of every wavenumber decay for some range of the bulk mole fraction. (See figure 3.1 for a schematic representation.) The upper and lower limits of this range are denoted by  $C_\infty^*$  and  $C_\infty^{**}$ , respectively, and depend on  $\gamma$ . These critical values of  $C_\infty$  correspond to the extrema on the morphological and convective neutral curves ( $C_\infty$  versus  $a$ ) separating those combinations of  $C_\infty$  and  $a$  for which all temporal eigenvalues  $\sigma$  lie in the left half-plane (LHP) from those for which at least one eigenvalue lies in the right half-plane, in turn corresponding to stable and unstable basic states, respectively.

In order to determine the bulk mole fractions on the morphological and convective neutral curves separating stable and unstable basic states for an arbitrarily chosen wavenumber  $a$ , we first compute all eigenvalues  $\sigma$  of (3.24) at each of  $N$  values of  $C_\infty$  ( $C_\infty^{(n)}$ ,  $1 \leq n \leq N$ ) in the range  $[C_\infty^{\min}, 0.2]$ , where the lower bound is typically  $10^{-4}$  and the upper bound is determined by the largest bulk mole fraction of CdTe for which we have data for the equation of state. We then attempt to determine a range of  $C_\infty$  for which all temporal eigenvalues are in the LHP. If one of the original values of  $C_\infty$  selected is stable (i.e., all temporal eigenvalues lie in the LHP), we then determine two intervals such that as  $C_\infty$  increases, in one a transition from instability to stability occurs, and in the other a transition from stability to instability occurs. Through these two intervals pass the convective and morphological neutral curves, respectively, as discussed in §5. If none of the original  $N$  values of  $C_\infty$  is stable, we choose the value (say,  $C_\infty^{(j)}$ ) for which the most unstable temporal eigenvalue has the smallest real part, and subdivide the interval  $[C_\infty^{(j-1)}, C_\infty^{(j+1)}]$  until we either find a stable value of  $C_\infty$  (at which juncture we proceed to isolate the two intervals described above), or abandon the search when the real part of the least stable temporal eigenvalue and the difference between consecutive values of  $C_\infty$  supports the expectation that all intermediate values of  $C_\infty$  are unstable. Having found the intervals of  $C_\infty$  in which the transitions occur, we then compute the bulk mole fractions on the convective and morphological neutral curves using a bisection method.

To compute the critical bulk mole fraction  $C_\infty^*$  (i.e., the minimum on the morphological neutral curve), we arbitrarily choose a wavenumber and compute the corresponding  $C_\infty$  on the morphological neutral curve using the procedure described above. We then fix  $C_\infty$  at the value computed in the previous step, and compute the eigenvalues  $\sigma$  for a discrete set of wavenumbers in a chosen range. We next select the wavenumber from among this set at which the  $\sigma$  with largest real part was obtained. If this wavenumber is at an endpoint of the chosen range, we extend the range until the wavenumber corresponding to the largest  $\text{Re}(\sigma)$  is inside the range. We then select this wavenumber and determine the corresponding  $C_\infty$  on the

neutral curve. We continue this process until the relative change in  $C_{\infty}$  is less than  $10^{-6}$ . We compute  $C_{\infty}^*$  following the same procedure. Spectral and domain convergence results are shown in Tables 1 and 2.

### 3.5. Results

#### 3.5.1. Nonrotating case

We begin by considering the basic state profiles of temperature, solute distribution, and density in the liquid. Equation (3.12c) shows that (for  $\rho^* \approx 1$ ) the dimensionless basic state temperature distribution decays exponentially away from the interface on a lengthscale  $1/Le$ , where  $4 \times 10^{-3} < Le < 10^{-2}$  for  $Hg_{1-x}Cd_xTe$ , and so is essentially linear on the scale of the basic state concentration profile (3.12d). As discussed in §3.1, the liquid density of  $Hg_{1-x}Cd_xTe$  does not depend monotonically on temperature for sufficiently small  $C$ . Hence, qualitatively different vertical density stratifications are obtained for fixed values of  $\gamma$  and  $\Gamma$ , depending on  $C_{\infty}$ . The nature of the density stratification and the thermal and solutal contributions thereto have profound consequences for the onset of convection.

For  $\gamma = 1.32 \times 10^{-4}$  and  $\Gamma = 8.2 \times 10^{-4}$  (corresponding to the dimensional solidification rate and temperature gradient  $V_I = 0.5 \mu/\text{sec}$  and  $G_L = 25 \text{ K/cm}$ , respectively), figure 3.2(a) shows basic state density profiles for different values of  $C_{\infty}$ . For  $C_{\infty} = 0.1$ , the density varies monotonically with elevation in the liquid. For  $C_{\infty} = 0.045$ , the density variation is still monotonic, but there is a considerable reduction in the magnitude of the density gradient near the interface. For smaller values of  $C_{\infty}$  (0.025 and 0.01), the density assumes a local maximum in the liquid. Figure 3.2(b) shows the vertical density stratifications for different values of  $C_{\infty}$  for  $\gamma = 2.64 \times 10^{-4}$  and  $\Gamma = 8.2 \times 10^{-4}$ . The basic state density profiles are generally similar to those for  $\gamma = 1.32 \times 10^{-4}$  and  $\Gamma = 8.2 \times 10^{-4}$ , being monotonic for larger values of  $C_{\infty}$ , and nonmonotonic for smaller values. We note, however, that for  $C_{\infty} = 0.025$ , the basic state density stratification has both a local minimum and a local maximum. (In figure 3.2, the approximate coincidence of the  $\rho_L/\rho_{L0}$  curves is only apparent, as can be seen

from figure 3.3, in which for  $\gamma = 2.64 \times 10^{-4}$  and  $\Gamma = 8.2 \times 10^{-4}$ , the derivative of  $\rho_L/\rho_{Lo}$  with respect to  $C_\infty$  vanishes at a slightly different  $z$  near 1.7 for each value of  $C_\infty$  shown.)

The solutions of (3.18)-(3.22) depend on sixteen dimensionless parameters, as defined in §§3.2 and 3.3. To determine the stability of a basic state with a nominally planar interface, numerical values of these parameters need to be specified. (The approximate solutions on the finite interval also depend on  $h$ .) It is therefore not feasible to numerically explore the effects of more than a few combinations of these parameters on the onset of instability. In this work, we present neutral curves ( $C_\infty$  versus  $a$ ) for fixed values of  $\gamma$  and  $\Gamma$ , amplitudes of the disturbances as a function of the vertical coordinate for selected values of  $C_\infty$ ,  $\gamma$ , and  $\Gamma$ , and stability boundaries (critical values of the bulk mole fraction  $C_\infty$  as a function of  $\gamma$ ) for selected values of  $\Gamma$ . The thermophysical properties are taken as constants, with most being evaluated at  $C_\infty$  using the functional forms shown in Appendices B and C at the melting temperature for liquid properties, and at the freezing temperature for solid properties. We have used  $g = 9.80 \text{ m/sec}^2$ .

Figure 3.4(a-c) shows neutral curves for  $\Gamma = 1.64 \times 10^{-3}$  ( $G_L = 50 \text{ K/cm}$ ) and three values of  $\gamma$ . The solid neutral curve at the top of each figure corresponds to morphological instability. The minimum on that curve (denoted by  $C_\infty^*$ ) determines one point on the stability boundary. The dashed neutral curve in each figure corresponds to an oscillatory buoyancy-driven convective instability mode. Just above that curve, all disturbance decay, whereas just below, oscillatory disturbances grow. The maximum on that curve determines another point ( $C_\infty^{**}$ ) on the stability boundary. In the unstable region below the oscillatory convective neutral curve, solid neutral curves correspond to steady convective modes. Since we have found no liquid density data for  $C_\infty > 0.2$ , computations were not performed for bulk mole fractions in excess of 0.2 (above the dashed-dot line in each of figures 3.4(a-c)).

Figure 3.4(a) shows the neutral curves for  $\gamma = 2.64 \times 10^{-4}$ . The buoyancy-driven instability modes occur in a wavenumber range of approximately 0.01 to 10. The extrema of the morphological and oscillatory convective neutral curves occur at  $C_\infty^* = 0.0989$  and

$C_{\infty}^{**} = 0.0369$ , respectively. For  $C_{\infty}^{**} < C_{\infty} < C_{\infty}^*$ , infinitesimal disturbances decay for all wavenumbers. Note that the critical bulk mole fraction  $C_{\infty}^*$  (below which there is no morphological instability) occurs at a larger wavenumber than  $C_{\infty}^{**}$  (above which there is no convective instability). When  $\gamma$  is increased to  $5.28 \times 10^{-4}$  ( $V_1 = 2 \mu/\text{sec}$ ),  $C_{\infty}^*$  decreases to 0.0464 and  $C_{\infty}^{**}$  increases to 0.042, so that the range of  $C_{\infty}$  in which disturbances decay for all wavenumbers is smaller, as shown in figure 3.4(b). The wavenumber range in which buoyancy-driven convection occurs is shifted slightly to the left. For  $\gamma = 7.92 \times 10^{-4}$  ( $V_1 = 3 \mu/\text{sec}$ ), the extremum on the morphological curve lies below the extremum on the convective curve, as shown in figure 3.4(c), and there is no range of  $C_{\infty}$  for which disturbances decay for all wavenumbers. For  $\Gamma = 1.64 \times 10^{-3}$ , we find a critical value of the dimensionless solidification rate  $\gamma_c = 5.61 \times 10^{-4}$  ( $V_1 = 2.12 \mu/\text{sec}$ ) above which plane-front solidification is unstable for all values of  $C_{\infty}$ .

The basic state density, its gradient and the thermal and solutal contributions thereto, and the amplitudes of disturbances to temperature, solute distribution, and vertical velocity, are shown as functions of  $z$  in figure 3.5(a-d) for  $\gamma = 2.64 \times 10^{-4}$ ,  $\Gamma = 1.64 \times 10^{-3}$ , and four values of  $C_{\infty}$  at  $a = 2.85$ . Figures 3.5a(i), 3.5b(i), 3.5c(i), and 3.5d(i) show the basic state density profiles for increasing values of  $C_{\infty}$ . We note that below  $C_{\infty} = 0.035$ , the density depends nonmonotonically on  $z$ . We point out that for the linear equation of state (3.1), the stabilizing or destabilizing character of the thermal and solutal stratifications can be determined by inspection of the basic state temperature and concentration profiles. For more complicated equations of state, it is necessary to individually examine the two terms on the right-hand side of (3.2). Thus, in figures 3.5a(ii), 3.5b(ii), 3.5c(ii), and 3.5d(ii), the solid, dashed, and dotted curves are the dimensionless basic state density gradient, and contributions to it from the solute and temperature gradients, respectively. Note that the solute gradient is stabilizing  $[(\partial \rho_L / \partial C)(\partial C_L / \partial z) < 0]$  throughout the liquid layer for all values of the bulk mole fraction  $C_{\infty}$ . However, the temperature gradient is destabilizing  $[(\partial \rho_L / \partial T)(\partial T_L / \partial z) > 0]$  in a sublayer adjacent to the liquid-solid interface, and stabilizing

$[(\partial\rho_L/\partial T)(\partial T_L/\partial z) < 0]$  above this sublayer, as shown in figures 3.5a(ii), 3.5b(ii), 3.5c(ii), and 3.5d(ii). As  $C_\infty$  increases, the height of this sublayer decreases, the magnitude of the destabilizing thermal contribution  $(\partial\rho_L/\partial T)(\partial T_L/\partial z)$  to the density gradient decreases, and the magnitude of the stabilizing solute contribution  $(\partial\rho_L/\partial C)(\partial C_L/\partial z)$  increases.

Figures 3.5a(iii-v), 3.5b(iii-v), 3.5c(iii-v), and 3.5d(iii-v) show the  $z$ -dependence of the real and imaginary parts (denoted by solid and dotted curves respectively) of the disturbances to the temperature, solute distribution, and vertical velocity associated with the most unstable oscillatory convective instability mode for different values of  $C_\infty$ . For  $C_\infty = 0.01$  (a value that for  $a = 2.85$  lies well below the oscillatory neutral curve in figure 3.4a), figure 3.5a(i) shows that the basic state density profile density assumes a maximum near  $z = 2.7$ , and that between the liquid-solid interface and this maximum, the liquid layer is hydrostatically unstable. Also, in this lower part of the liquid the temperature and solute gradients are destabilizing and stabilizing, respectively. As is clearly seen in figure 3.5a(iii-v), the disturbances are confined largely within the sublayer where the temperature gradient is destabilizing, although they penetrate weakly into the liquid above the density maximum, in which both the temperature and solute gradients are stabilizing.

For  $C_\infty = 0.035$  and  $0.0369$  figures 3.5b(i) and 3.5c(i) show that although there is no region in which the overall density gradient is hydrostatically unstable, there is a sublayer adjacent to the interface in which the temperature gradient is destabilizing. The disturbances associated with the oscillatory mode of convection are confined to this sublayer, as shown in figures 3.5b(iii-v) and 3.5c(iii-v). In this sublayer the temperature gradient is destabilizing and the solute gradient is stabilizing. As discussed in §3.6, these conditions in the sublayer thus correspond to the diffusive regime of doubly-diffusive convection, with oscillatory onset of buoyancy-driven convection. The vertical structure of the disturbances is very similar to that shown in figure 3.5a(iii-v). In both cases, the disturbances are confined largely within a sublayer in which the thermal stratification is destabilizing, and penetrate weakly into the liquid above the sublayer. The disturbances for  $C_\infty = 0.01$ ,

however, show more structure in the sublayer than those for  $C_\infty = 0.035$  or  $0.0369$ . This is because the effect of the destabilizing temperature gradient is stronger than for  $C_\infty = 0.035$  and  $0.0369$ , as discussed above. For  $C_\infty = 0.07$ , however, the structure of the eigenfunctions is completely different, as shown in figure 3.5d(iii-v). In this case, the eigenfunctions are associated with the least stable morphological instability mode. Although there still exists a small sublayer in which the temperature gradient is destabilizing, the disturbances are not confined to that region. The disturbances decay strongly with increasing  $z$ .

We present our principal results in terms of stability boundaries in the  $\gamma$ - $C_\infty$  plane for four values of  $\Gamma$  in figure 3.6(a-d). The stability boundary consists of some portion of the morphological branch joined to a convective branch. The dashed and solid curves in each figure correspond to minima on the morphological neutral curve ( $C_\infty^*$ ) and maxima on the neutral curve associated with buoyancy-driven convection ( $C_\infty^{**}$ ), respectively. Figure 3.6(a) shows the stability boundary for  $\Gamma = 8.2 \times 10^{-4}$ . Above the morphological branch, disturbances grow in some wavenumber range and the plane-front solution is unstable. Similarly, disturbances grow below the convective branch for some range of  $a$ . On the other hand, below the morphological branch and above the convective branch, disturbances of all wavenumbers decay and plane-front solidification is stable. Beyond the critical solidification rate  $\gamma_c = 2.70 \times 10^{-4}$  ( $V_1 = 1.02 \mu/\text{sec}$ ) at which the convective and morphological branches intersect, there is no stable range of bulk mole fraction  $C_\infty$ . For  $\Gamma = 1.64 \times 10^{-3}$ , figure 3.6(b) shows the stable region in the  $\gamma$ - $C_\infty$  plane analogous to that for  $\Gamma = 8.2 \times 10^{-4}$ . The morphological branch has shifted to the right and the convective branch has shifted slightly downward. Their intersection occurs at a higher  $\gamma$  ( $\gamma_c = 5.61 \times 10^{-4}$ ,  $V_1 = 2.12 \mu/\text{sec}$ ), and the stable region is larger. Increasing  $\Gamma$  still more leads to further enlargement of the stable region and larger values of  $\gamma_c$ , as shown in figures 3.6(c) and 3.6(d) for  $\Gamma = 3.28 \times 10^{-3}$  and  $6.56 \times 10^{-3}$  ( $G_L = 100$  and  $200 \text{ K/cm}$ ), respectively.



### 3.5.2. Rotating case

For  $\Gamma = 1.64 \times 10^{-3}$  ( $G_L = 50$  K/cm), figure 3.7 shows stability boundaries for  $\Omega_0 = 0, 25, 50,$  and  $100$  rpm. Above the morphological branch, disturbances grow for some range of wavenumber  $a$  and plane-front solidification is unstable. Similarly, below the convective branch appropriate to each rotation rate shown, disturbances grow for some range of  $a$ . However, between the morphological branch and the convective branch associated with each rotation rate (i.e., for  $C_{\infty}^{**} < C_{\infty} < C_{\infty}^*$ ), disturbances decay for all wavenumbers and plane-front solidification is stable. Note that the morphological branch is unaffected by rotation, whereas as  $\Omega_0$  increases, the convective branch is shifted downward. The critical CdTe bulk mole fraction  $C_{\infty}^{**}$  on the convective branch is a decreasing function of  $\Omega_0$  at any dimensionless solidification rate, clearly indicating the inhibitory effect of rotation on the onset of buoyancy-driven convection. Beyond the critical solidification rate (denoted by  $\gamma_c$ ) at which the convective and morphological branches intersect, there is no stable range of CdTe bulk mole fraction  $C_{\infty}$ . Thus, plane-front solidification is unstable at all CdTe bulk mole fractions for sufficiently high solidification rates. The critical solidification rate  $\gamma_c$  at which the morphological and convective branches intersect occurs at higher  $\gamma$  with increasing rotation rate. The critical value of  $\gamma_c$  is increased by more than a factor of ten at  $\Omega_0 = 100$  rpm relative to the nonrotating case. We also note that the convective branch has a relatively shallow local minimum near  $\gamma = 2.64 \times 10^{-4}$ , the location of which is only weakly dependent on  $\Omega_0$ . Thus, for a given rotation rate, operation at the solidification rate corresponding to this local minimum allows plane-front solidification to be stably conducted at the lowest value of  $C_{\infty}$ .

For  $\Gamma = 8.2 \times 10^{-4}$  ( $G_L = 25$  K/cm) and  $\Omega_0 = 0$  and  $100$  rpm, figure 3.8 shows stability boundaries in the  $\gamma$ - $C_{\infty}$  plane analogous to those for  $\Gamma = 1.64 \times 10^{-3}$ . As expected on the basis of the results of Coriell *et al.* (1980) for Pb-Sn without rotation, the morphological branch is shifted to the left, reducing the range of solidification rates and bulk mole fractions for

which plane-front solidification is stable. On the other hand, the convective branch is shifted downwards relative to the  $\Gamma = 1.64 \times 10^{-3}$  case, corresponding to an increase in the range of stable operating conditions. We note that decreasing the temperature gradient has very little effect on the onset of convection in a nonrotating layer, but reduces the range of stable CdTe bulk mole fractions by more than twofold for a layer rotating at 100 rpm. The critical solidification rate  $\gamma_c$  is more than a factor of five higher at  $\Omega_0 = 100$  rpm than in the nonrotating case, although the stabilization is less than the factor of ten predicted at  $\Gamma = 1.64 \times 10^{-3}$ . Although the reduction in  $\Gamma$  has very little effect on the critical value of  $\gamma$  at which the morphological and convective stability boundaries intersect in the nonrotating case, for  $\Omega_0 = 100$  rpm the critical value of  $\gamma$  decreases by a factor of three when the temperature gradient is reduced.

As discussed for the Pb-Sn case (Chapter 2), at each value of  $\Omega_0$  the onset of morphological instability occurs *via* a short wavelength (large wavenumber) instability, while convective instability sets in *via* disturbances with relatively longer wavelengths. In the following section this point is discussed in the context of the mechanism by which rotation inhibits the onset of convection.

### 3.6. Discussion

The qualitative differences between the neutral curves and stability boundaries presented in §3.5 and those characteristic of the normal case in which density varies linearly with temperature and solute mole fraction (e.g., the Pb-Sn results of Chapter 2; cf. Coriell *et al.* 1980, Öztekin & Pearlstein 1992) lead us to consider how the equation of state affects or alters the mechanism by which the onset of motion occurs during directional solidification of a binary liquid cooled from below.

We begin by noting that the mechanism responsible for the morphological instability is insensitive to the net density stratification in the liquid, and is insensitive to variations of temperature and composition outside a relatively thin layer adjacent to the interface. This is

evident from a comparison of the neutral curves and stability boundaries for the present case to those for Pb-Sn.

On the other hand, the onset of buoyancy-driven convection depends strongly on the nature of the stabilizing or destabilizing temperature and solute gradients in the liquid, as well as on the diffusivities of the stratifying agencies (Stern 1960; Baines & Gill 1969). As discussed in §3.1, the density of a binary liquid solidified by cooling from below can depend nonmonotonically on the vertical coordinate even if the density depends monotonically on temperature and composition. For example, if the equation of state is of the form (3.1) and  $\alpha > 0$ ,  $\beta > 0$ , and  $k < 1$  (as for Pb-Sn), then (3.5) provides a necessary criterion for the one-dimensional basic state to have a density maximum (3.6) within the liquid. However, for any system (e.g., Pb-Sn) characterized by the linear equation of state (3.1), even if the density has a maximum in the liquid, the temperature and composition distributions (3.3a) and (3.3b) will be stabilizing and destabilizing, respectively. Following the standard "parcel" argument for a linearly stratified doubly-diffusive fluid (Turner 1973, page 251), we note that if a fluid element is displaced downward, it will lose its excess heat more rapidly than its composition will adjust to the relatively solute-enriched surroundings, because the thermal diffusivity is much larger than the solute diffusivity. Hence, the displaced parcel will be dilute relative to the surroundings, and if  $\beta > 0$  and the resulting buoyancy force is sufficient to maintain the downward motion, the one-dimensional basic state will be unstable. In the context of doubly-diffusive flows, this configuration is in the "fingering" regime, and the onset of convection is said to be "steady" or "monotonic".

For binary liquids such as  $\text{Hg}_{1-x}\text{Cd}_x\text{Te}$ , for which the dependence of density on temperature or solute mole fraction is not monotonic, solidification by cooling from below for some combinations of the bulk mole fraction, liquid-side temperature gradient, and solidification rate can lead to, as discussed in §3.1, a configuration in which there exists adjacent to the interface a sublayer in which the positive temperature and solute gradients are destabilizing and stabilizing, respectively. If a liquid parcel in this sublayer is displaced

downward, it will lose its excess heat more rapidly than its excess CdTe mole fraction, again because the thermal diffusivity is much larger than the solute diffusivity. Its CdTe mole fraction will thus exceed that of the surroundings, and so the parcel will be less dense than the surrounding liquid. The resulting buoyancy force will tend to move the fluid parcel vertically upward. Hence, the initial displacement engenders a restoring force, which can result in overshoot of the parcel's initial (equilibrium) position. Such a configuration is in the "diffusive" regime, and the motion is said to be "overstable", with the temporally growing oscillatory parcel displacements leading to the oscillatory onset of convection.

The difference between the mechanisms by which the onset of motion occurs in configurations in which the temperature gradient is everywhere stabilizing, and in those in which temperature is destabilizing in a sublayer adjacent to the interface, is manifested in qualitative differences between the neutral curves, and hence the stability boundaries, for the Pb-Sn and  $\text{Hg}_{1-x}\text{Cd}_x\text{Te}$  systems.

The most notable feature of the neutral curves in the present case is that the onset of buoyancy-driven convective instability is associated with an oscillatory mode, unlike the normal (e.g., Pb-Sn) case. Moreover, for each wavenumber for which it exists, the corresponding oscillatory neutral curve bounds the range of stable  $C_\infty$  from below, rather than from above as in the normal case. As the extremal values of  $C_\infty$  on the morphological and oscillatory convective neutral curves approach, the range of bulk mole fractions for which plane-front solidification is stable disappears. This contrasts to the normal case, in which plane-front solidification is always stable for sufficiently dilute solutions (i.e.,  $C_\infty$  lying below the minima of the morphological and steady convective neutral curves).

These features of the neutral curves have profound consequences for the stability boundaries in the  $\gamma$ - $C_\infty$  plane. For  $\text{Hg}_{1-x}\text{Cd}_x\text{Te}$ , plane-front solidification can be unstable at all solidification rates if the bulk mole fraction is chosen sufficiently low, as shown in §3.5. This is because the effect of a destabilizing temperature gradient in the sublayer adjacent to the interface becomes stronger as the bulk mole fraction decreases (due to a more prominent

density maximum as the composition approaches pure HgTe), and the stabilizing effect of the solute gradient diminishes (because it is proportional to  $C_{\infty}$ ). On the other hand, in Pb-Sn directionally solidified by cooling from below, plane-front solidification is stable for any solidification rate and liquid-side temperature gradient if the solute bulk mole fraction is sufficiently low (Coriell *et al.* 1980; Öztekin & Pearlstein 1992).

For  $\text{Hg}_{1-x}\text{Cd}_x\text{Te}$ , plane-front solidification can be unstable at all values of the bulk mole fraction (less than  $C_{\infty} = 0.2$ ) if the solidification rate exceeds a critical value  $\gamma_c$ . The explanation for this result is made clear by reference to figure 3.6(a-d). For values of  $C_{\infty}$  below the dashed curves, plane-front solidification is unstable with respect to the onset of overstable buoyancy-driven convection, because the stabilizing influence of the bottom-heavy solute stratification is insufficiently strong to overcome the destabilizing temperature gradient in the sublayer adjacent to the interface. Above the solid curve, the configuration is unstable with respect to the morphological instability. As  $\gamma$  approaches  $\gamma_c$  from below, the stable region is "pinched" from below and above until at  $\gamma_c$  it finally disappears. This situation differs from that for Pb-Sn, for which plane-front solidification is stable in a region bounded above by the morphological and convective portions of the stability boundaries.

In a single-component fluid with an unstably stratified layer overlying or underlying a stably stratified region, convective motion is typically localized in the unstably stratified layer, but may penetrate into the adjacent stable region. In his early analysis of the onset of thermal convection in a water layer with the temperature maintained at  $0^{\circ}\text{C}$  at the bottom and in excess of  $4^{\circ}\text{C}$  at the top, Veronis (1963) showed that convection occurs in the unstably stratified region and penetrates into the stably stratified region as well. He determined the extent of penetration for different ratios of the stably stratified layer thickness to the total layer thickness. He also found that convection in the stably stratified region is viscously coupled to the more vigorous motion in the unstable layer. Walton (1982) and Zangrando & Bertram (1985) have considered a doubly-diffusive fluid layer with a uniform vertical

temperature gradient and a nonuniform vertical solute gradient. Both of these studies show the disturbances to be localized about the neighborhood of the critical depth at which the salinity gradient reaches its minimum value. In our work, when the liquid-solid interface is adjacent to a sublayer in which the temperature gradient is destabilizing, the disturbances associated with the oscillatory onset of buoyancy-driven convection are largely confined to that thermally unstably stratified sublayer.

As discussed above, the oscillatory onset of buoyancy-driven convection and the localization of the disturbances are associated with the occurrence of a sublayer in which the temperature gradient is destabilizing. Hence, the results should be expected to apply qualitatively to the solidification of other binary or multicomponent liquids in which  $(\partial \rho_L / \partial T)(\partial T_L / \partial z)$  changes sign within the layer.

We recall from §3.5 (see figure 3.2b for  $C_\infty = 0.025$ ) that for  $\text{Hg}_{1-x}\text{Cd}_x\text{Te}$ , basic state density profiles more complicated than monotonic and unimodal can occur. For several cases (both unstable and neutrally stable) in which the basic state density profile exhibits both a local maximum and a local minimum, examination of the eigenfunctions of the disturbances to the temperature, solute, and vertical velocity shows that the disturbances are localized within the sublayer in which the thermal stratification is destabilizing. The eigenfunctions are qualitatively similar to those for the case in which a single extremum (a maximum) occurs, which is not surprising since in each case disturbance localization is a consequence of confinement of the destabilizing temperature gradient to a sublayer adjacent to the liquid-solid interface, and even when the basic state density profile has two local extrema, the thermal contribution to the right-hand side of (3.2) has only one sign change.

Our results demonstrate that nonmonotonic variation of density with temperature can have dramatic qualitative effects on the onset of instability in an unbounded horizontal fluid layer undergoing plane-front solidification. The existence of a sublayer in which the thermal stratification is destabilizing should also have important consequences for the convection which occurs in vertical Bridgman growth in ampoules of finite radius, as well as in zone

melting and other processes used to grow  $\text{Hg}_{1-x}\text{Cd}_x\text{Te}$  crystals from the melt. To date, however, these effects have not been observed in simulations of buoyancy-driven convection in  $\text{Hg}_{1-x}\text{Cd}_x\text{Te}$  for these geometries, which have used equations of state that do not properly account for the nonmonotonic dependence of density on temperature. The axisymmetric simulations of vertical Bridgman growth by Kim & Brown (1989) employ a linear equation of state of the form (3.1), even though the CdTe mole fraction in the liquid near the interface is about 0.075 in each computation and the density is known to depend nonmonotonically on temperature for CdTe mole fractions up to at least 0.1. The computations of Apanovich & Ljumkis (1991) for zone melting of  $\text{Hg}_{1-x}\text{Cd}_x\text{Te}$  use an unusual equation of state in which the density of  $\text{Hg}_{1-x}\text{Cd}_x\text{Te}$  depends quadratically on temperature for  $x \neq 0.13$ , and is independent of temperature for  $x = 0.13$ .

For Pb-Sn alloys, we have shown in Chapter 2 (cf. Öztekin and Pearlstein 1992) that the onset of convection can be suppressed significantly at modest rotation rates. This is undoubtedly due to the well-known Taylor-Proudman mechanism, described by Chandrasekhar (1961). According to the Taylor-Proudman theorem, steady motion parallel to the axis of rotation in a uniformly rotating inviscid fluid is prohibited at any nonzero rotation rate. If this theorem were strictly applicable to a viscous fluid, the onset of steady convection would be prohibited, since the flow in convection cells must have a vertical component. Instead, in a viscous fluid, one sees an inhibition of the onset of steady convection, with the degree of inhibition (expressed here as an increase in  $C_{\infty}$ ) increasing with  $\Omega_0$ . Although, the Taylor-Proudman theorem applies only to steady flows, we find that the rotation still suppress the oscillatory onset of buoyancy-driven convection during directional solidification of  $\text{Hg}_{1-x}\text{Cd}_x\text{Te}$ , as presented in §3.6. It is not surprising that the morphological instability is unaffected by rotation. The morphological instability occurs at very short wavelengths, so the motion is almost perpendicular to the solidification front (i.e., aligned with the axis of rotation). Hence, the Coriolis acceleration does not sensibly affect the morphological instability.

Finally, Antar (1991) has presented a linear analysis of the onset of convection in a horizontal fluid layer cooled from below, using an approximate equation of state for  $\text{Hg}_{1-x}\text{Cd}_x\text{Te}$ . Although he purports to consider "convective instabilities in the melt for solidifying mercury cadmium telluride" his analysis differs from ours in that no phenomena associated with solidification (existence of a moving or deformable interface at which phase change occurs, nonlinear basic state solute stratification due to rejection or preferential incorporation at the interface, latent heat effects at the interface, etc.) are included. Moreover, comparison to Antar's results is precluded because his linear vertical basic state thermal stratification is inconsistent with his definition of the temperature difference across the fluid layer. Specifically, the basic state temperature distribution (Antar's equation (1)) requires the bottom temperature to be  $T_0 - \Delta T$ , which is inconsistent with his definitions of  $T_0$  (temperature where  $\partial\rho/\partial T$  is zero, determined by Antar's equation of state) and  $\Delta T$  (temperature difference between top and bottom of the layer). This error vitiates his analysis, which uses a thermal Rayleigh number defined in terms of a temperature difference inconsistent with the basic state. That this inconsistency is not simply an apparent one due to a typographical error is confirmed by reference to an earlier paper (Antar 1987) employing the same basic state and disturbance equations, in which a different (and highly unusual) definition of  $\Delta T$  (related to the actual overall temperature difference by a constant dependent on the temperature at the top or bottom wall; see figure 1 of Antar 1987) was used to achieve consistency. That definition of  $\Delta T$  was the only one consistent with the basic state, and hence with the analysis and results. Unfortunately, Antar's 1991 paper defines  $\Delta T$  as the overall temperature difference, and so is wrong.



## CHAPTER 4

### Stability of Dendritic Solidification of a Binary Liquid, Including Coriolis Effects

#### 4.1. Introduction

Although plane-front solidification (in which the liquid and solid are separated by a well-defined interface that remains planar and translates at a constant velocity) is desirable in many applications, solidification of many binary alloys under conditions of practical interest occurs dendritically. Dendritic solidification occurs in a so-called "mushy" zone between the solid and melt in which dendrites, consisting of long vertical stems with secondary and tertiary branches, are immersed in interdendritic fluid. This phenomenon is illustrated in photographs by Huppert & Worster (1985) and Chen & Chen (1991) of the mushy zone in a dendritically solidifying aqueous ammonium chloride solution. In such a case, the dendritic region might be modeled as a single domain, in which the macroscopic structure (i.e., features that scale with the mushy-zone thickness) are considered to be more important than the microscopic morphology (i.e., features dependent on a detailed stochastic description of dendrite location and shape). Thus, in many previous theoretical investigations of its evolution and behavior, the mushy zone has been considered as a porous medium with anisotropic permeability. A review of plane-front and dendritic solidification has been given by Glicksman *et al.* (1986).

The gradients of temperature and solute which necessarily occur in a solidifying binary or multicomponent liquid can destabilize the nominally motionless basic state, leading to the onset of buoyancy-driven convection. Analysis of the convective motion in solidifying alloys is complicated by the fact that temperature and composition in the mushy zone are related by the phase diagram, and by the fact that phase change leads to motion and deformation of the boundaries between the melt, mushy zone, and solid. We will refer to these boundaries as the

liquid/mushy-zone and mushy-zone/solid interfaces. Characteristic of a moving boundary problem, their locations are not known in advance, and must be computed as part of the solution.

For binary liquids with  $k < 1$  (e.g., Pb-Sn alloys) for which the equation of state is adequately represented by the linear relation

$$\rho = \rho_0 [1 - \alpha_T(T - T_0) - \alpha_C(C - C_0)] , \quad (4.1)$$

cooling from below leads to dendritic solidification with a stabilizing temperature gradient and a destabilizing composition gradient in both the mushy zone and liquid. The vertical composition gradient in the mushy zone is almost constant, while in the liquid there is a thin compositional boundary layer adjacent to the liquid/mushy-zone interface. These stratifications can lead to two different convective modes, as discussed by Worster (1992) in his analysis of the stability of dendritically solidified binary alloys. One mode, referred to as the boundary layer mode, associated with the thin compositional boundary layer in the liquid adjacent to the liquid/mushy-zone interface, is largely confined within this layer, and has a relatively small critical wavelength (on the order of its thickness). The boundary layer mode penetrates only weakly into the mushy zone, which is thus essentially stagnant. On the other hand, the mushy layer mode is driven by the adverse compositional stratification in the mushy zone and has a larger critical wavelength that scales with the mushy-zone thickness. These two convective mode types are analogous to those found by Chen & Chen (1988) in superposed porous and liquid layers heated from below.

The onset of buoyancy-driven convection in dendritically solidified binary liquids has been investigated by Fowler (1985), Nandapurkar *et al.* (1989), and Worster (1992) by means of linear stability analysis. In all three studies, the mushy zone was modeled as a porous medium, in which the kinetics of the phase change are sufficiently fast so that nucleation and other nonequilibrium effects can be neglected. Thus, the temperature and composition of the mushy zone were taken to be related by the liquidus of the phase diagram.

Fowler (1985) considered solid volume fraction of solid in the porous layer to be a dynamical variable, but did not admit perturbations to the liquid/mushy-zone or mushy-zone/solid boundaries. He used Darcy's law as an approximate description of the conservation of momentum in the porous layer, and considered the case in which the solute diffusivity vanishes, so that the thickness of the solutal boundary layer adjacent to the liquid/mushy-zone interface is zero. Thus, the onset of convection must occur *via* the mushy layer mode. Although Fowler's general formulation allowed for the solid volume fraction to be treated as a dynamical variable, his analysis was restricted to a case in which that quantity was asymptotically zero. Thus, no interaction was allowed between buoyancy-driven convection and solidification.

Nandapurkar *et al.* (1989) used the momentum equation developed by Ganesan & Poirier (1990) from systematic averaging of the Navier-Stokes equation over a "representative volume" large compared to the microscopic scale (primary dendrite arm spacing) and small compared to the characteristic length scale (i.e., thickness) of the mushy zone. In their analysis of the one-dimensional basic state, the volume fraction of liquid was computed from a thermodynamically self-consistent formulation. However, the volume fraction of liquid was not allowed to be disturbed in the stability analysis, which is thermodynamically inconsistent. Moreover, the stability analysis of these authors did not allow the mushy-zone/liquid interface to move (relative to an inertial frame) or deform. These assumptions significantly suppressed potential interactions between convection and solidification.

Like Fowler, Worster (1992) uses Darcy's law in the porous medium and takes the porosity to be a dynamical variable, but admits disturbances to the location and shape of the liquid/mushy-zone boundary, although not to the mushy-zone/solid interface. He concluded that onset *via* the boundary layer mode is relatively independent of the structure of the mushy zone, while onset *via* the mushy layer mode is strongly dependent on the structure of the porous medium, and in particular on the porosity profile in the mushy zone.

We use a linear stability analysis to study the onset of buoyancy-driven convection in the horizontally unbounded liquid and underlying mushy zone of a binary alloy undergoing dendritic solidification. The mushy zone is modeled as a porous medium with anisotropic permeability. The local porosity, as well as the locations of the boundaries between the solid and mushy zone and between the mushy zone and liquid, are taken as dynamical variables, to be determined as part of the solution. This work serves to identify the mechanism by which Coriolis effects affect the onset of buoyancy-driven convection in dendritically solidifying binary alloys. The analysis is illustrated by results for the Pb-Sn system.

This Chapter is organized as follows. We present the governing equations in §4.2 and an appropriate nondimensionalization in §4.3. The one-dimensional basic state and linear disturbance equations, both derived from the dimensionless equations, are given in §4.4. The numerical solution technique is described in §4.5. Results for Pb-Sn binary alloys are presented in §4.6 and discussed in §4.7.

## 4.2. Formulation

### 4.2.1. Governing Equations

A schematic of the solidifying system is shown in figure 4.1. A binary liquid of infinite horizontal extent in which the bulk mass fraction of solute is  $C_\infty$  solidifies at a constant nominal rate  $V_1$  due to cooling from below, and is rotated at a constant angular velocity  $\Omega$  about a vertical axis parallel to the gravity vector  $\mathbf{g} = -g\mathbf{l}_z$ . A mushy zone of nominal height  $H_m$  (to be determined as part of the solution) lies between the melt and solid. For convenience, we adopt the practice of previous investigators (e.g., Coriell et al. 1980; Fowler 1985; Worster 1992) and write the governing equations in a reference frame translating with the nominally steady velocity ( $\mathbf{l}_z V_1$ ) of the moving interface and rotating at a constant angular velocity  $\Omega$  about  $\mathbf{l}_z$ , but refer the velocities to the laboratory frame.

The fluid density,  $\rho_f$ , is taken as a constant ( $\rho_0$ , the liquid density at its melting point for  $C_\infty = 0$ ) except in the buoyancy terms in the liquid and mushy-zone momentum equations,

where it is approximated by (4.1). The density of the solid is also taken as  $\rho_0$ , so that the effects of solidification shrinkage are neglected.

In the liquid, the motion is governed by the Oberbeck-Boussinesq equations

$$\nabla \cdot \mathbf{u}_L = 0, \quad (4.2a)$$

$$\frac{\partial \mathbf{u}_L}{\partial t} - V_I \frac{\partial \mathbf{u}_L}{\partial z} + \mathbf{u}_L \cdot \nabla \mathbf{u}_L + 2 \boldsymbol{\Omega} \times \mathbf{u}_L + \boldsymbol{\Omega} \times (\boldsymbol{\Omega} \times \mathbf{r}) = - \frac{\nabla p_L}{\rho_0} - \frac{\rho_L g}{\rho_0} \mathbf{i}_z + \nu \nabla^2 \mathbf{u}_L, \quad (4.2b)$$

In a reference frame translating with the nominally steady velocity ( $\mathbf{i}_z V_I$ ) of the moving interface and rotating at a constant angular velocity  $\boldsymbol{\Omega}$  about  $\mathbf{i}_z$ , where  $\mathbf{u}_L$  and  $p_L$  are the velocity and pressure in the liquid, and  $\nu$  is the kinematic viscosity. The equations for conservation of energy and species in the liquid are

$$\frac{\partial T_L}{\partial t} - V_I \frac{\partial T_L}{\partial z} + \mathbf{u}_L \cdot \nabla T_L = \kappa_L \nabla^2 T_L, \quad (4.2c)$$

$$\frac{\partial C_L}{\partial t} - V_I \frac{\partial C_L}{\partial z} + \mathbf{u}_L \cdot \nabla C_L = D_L \nabla^2 C_L, \quad (4.2d)$$

where  $T_L$ ,  $C_L$ ,  $\kappa_L$ , and  $D_L$  are the temperature, solute concentration, thermal diffusivity, and the solute diffusivity in the liquid, respectively. Since the reference state corresponds to the pure solvent at its melting point, the equation of state in the liquid can be written as

$$\rho_f = \rho_0 \left[ 1 - \alpha_T (T_L - T_M) - \alpha_C C_L \right], \quad (4.2e)$$

where  $\alpha_T$  and  $\alpha_C$  are the thermal and solutal expansion coefficients, respectively, and  $T_M$  is the melting temperature of pure solvent.

The mushy zone is modelled as a porous medium saturated by interdendritic fluid. Its permeability is taken to be orthotropic, with horizontal isotropy. For conservation of mass and momentum, we adopt the model of Ganesan & Poirier (1990) developed by systematic

averaging of the Navier-Stokes equations over a "representative volume" large compared to the microscopic scale (primary dendrite arm spacing) and small compared to the thickness of the mushy zone. In a reference frame translating with the nominally steady velocity ( $l_z V_l$ ) of the moving interface and rotating at constant angular velocity  $\Omega$  about  $l_z$ , the equations for conservation of mass and momentum in the mushy zone are

$$\nabla \cdot \mathbf{u}_m = 0, \quad (4.3a)$$

$$\begin{aligned} \phi \frac{\partial}{\partial t} \left( \frac{\mathbf{u}_m}{\phi} \right) - V_l \phi \frac{\partial}{\partial z} \left( \frac{\mathbf{u}_m}{\phi} \right) + \mathbf{u}_m \cdot \nabla \left( \frac{\mathbf{u}_m}{\phi} \right) + 2 \Omega \times \mathbf{u}_m + \phi \Omega \times (\Omega \times \mathbf{r}) = \\ - \phi \frac{\nabla p_m}{\rho_0} - \phi \frac{\rho_l g}{\rho_0} l_z - v \phi \underline{P}(\phi) \cdot \mathbf{u}_m + v \nabla^2 \mathbf{u}_m, \end{aligned} \quad (4.3b)$$

where  $\mathbf{u}_m$  and  $p_m$  are the superficial velocity and pressure in the mushy zone,  $\phi$  is the volume fraction of liquid (henceforth referred to as the volume fraction), and  $\underline{P}(\phi)$  is an orthotropic tensor with horizontal isotropy whose horizontal and vertical components are  $P_h(\phi) = 1/K_h(\phi)$  and  $P_v(\phi) = 1/K_v(\phi)$ , respectively, with  $K_h(\phi)$  and  $K_v(\phi)$  the components of the orthotropic permeability tensor in the mushy zone. The functional dependence of  $K_h$  and  $K_v$  on  $\phi$  is discussed in Appendix D.

The mushy zone is considered to be a continuum, in which the porosity variation is continuous. The thermophysical properties of the mushy zone (specific heat, thermal conductivity, permeability, and solute diffusivity) are taken to be functions of the temporally and spatially varying volume fraction  $\phi$ . The models we use for conservation of energy and solute in the mushy zone have been employed by several investigators (Worster 1986; Nandapurkar *et al.* 1989). These conservation equations are also formulated on a scale large compared to the spacing between primary dendrite arms but small compared to the thickness of the mushy zone. The temperature and interdendritic solute concentration are assumed to be uniform in the representative volume. Transport of heat and solute in the mushy zone is by diffusion and convection. Moreover, as interdendritic fluid solidifies, latent heat is released

within the mushy zone and solute is rejected into the interdendritic fluid. Therefore, the conservation equations for energy and species must include terms proportional to the rate of change of volume fraction. They can be written as

$$c_{p,m} \frac{\partial T_m}{\partial t} - V_I c_{p,m} \frac{\partial T_m}{\partial z} + c_{p,L} u_m \cdot \nabla T_m = \nabla \cdot k_m \nabla T_m - L \frac{\partial \phi}{\partial t} + V_I L \frac{\partial \phi}{\partial z}, \quad (4.3c)$$

$$\phi \frac{\partial C_m}{\partial t} - V_I \phi \frac{\partial C_m}{\partial z} + u_m \cdot \nabla C_m = \nabla \cdot D_m \nabla C_m - (1-k) C_m \frac{\partial \phi}{\partial t} + V_I (1-k) C_m \frac{\partial \phi}{\partial z}, \quad (4.3d)$$

where  $T_m$  is the local temperature in the mushy zone,  $C_m$  is the solute concentration in the interdendritic fluid,  $c_{p,m}$  and  $c_{p,L}$  are the specific heats of the mushy zone and liquid, respectively,  $k_m$  and  $D_m$  are the thermal conductivity and solute diffusivity in the mushy zone,  $k$  is the segregation coefficient, and  $L$  is the latent heat of fusion per unit volume. The thermophysical properties of the mushy zone are taken as volume-fraction-weighted averages of the fluid and solid phases within the mushy zone

$$c_{p,m} = \phi c_{p,L} + (1 - \phi) c_{p,S}, \quad (4.3e)$$

$$k_m = \phi k_L + (1 - \phi) k_S, \quad (4.3f)$$

$$D_m = \phi D_L, \quad (4.3g)$$

where  $c_{p,S}$  and  $k_S$  are the specific heat and thermal conductivity of the solid. In the mushy zone, mass diffusion in the solid phase is orders of magnitude slower than in the interdendritic fluid, and so is neglected. The solidification kinetics in the mushy zone are taken to be sufficiently fast that nucleation and other nonequilibrium effects can be neglected. Hence, the temperature and composition within the mushy zone are related by the liquidus relationship, a linear approximation to which is given by

$$T_m = T_M + m_L C_m, \quad (4.3h)$$

where  $m_L$  is the slope of the liquidus. Equations 4.3(c,d) are written as two evolution equations for the algebraically related temperature and interdendritic solute concentration in the mushy zone. Thus 4.3(c,d) should be interpreted as evolution equations for  $\phi$  (time derivatives of which appear on the right-hand sides), and either  $T_m$  or  $C_m$ . The equation of state of the interdendritic fluid in the mushy zone is

$$\rho_f = \rho_0 \left[ 1 - \alpha_T (T_m - T_M) - \alpha_C C_m \right]. \quad (4.31)$$

In the solid the energy equation is taken as

$$\frac{\partial T_S}{\partial t} - V_I \frac{\partial T_S}{\partial z} = \kappa_S \nabla^2 T_S, \quad (4.4)$$

where  $T_S$  and  $\kappa_S$  are the temperature and thermal diffusivity of the solid, respectively.

#### 4.2.2. Boundary conditions

The boundary condition applied far from the liquid/mushy-zone interface as  $z \rightarrow \infty$  is

$$C_L \rightarrow C_\infty, \quad (4.5)$$

where  $C_\infty$  is the bulk mass fraction of solute. At the liquid/mushy-zone interface,  $\eta_L(x,y,t) - z = 0$ , the volume fraction, velocity, normal stress, and shear stress are continuous

$$\phi = 1, \quad (4.6a)$$

$$u_L = u_m, \quad (4.6b)$$

$$\frac{1}{\rho_0} (p_m - p_L) - v n \cdot \left\{ \left[ \nabla u_m + (\nabla u_m)^T \right] \cdot n - \left[ \nabla u_L + (\nabla u_L)^T \right] \cdot n \right\} = 0, \quad (4.6c)$$

$$t \cdot \left\{ \left[ \nabla u_m + (\nabla u_m)^T \right] \cdot n - \left[ \nabla u_L + (\nabla u_L)^T \right] \cdot n \right\} = 0, \quad (4.6d)$$



where  $\mathbf{n}$  and  $\mathbf{t}$  are normal and tangential unit vectors, respectively. We also require temperature and composition to be continuous

$$T_L = T_m, \quad (4.6e)$$

$$C_L = C_m, \quad (4.6f)$$

at the liquid/mushy-zone interface, and that the energy and solute balances across that interface

$$\nabla T_L \cdot \mathbf{n} = \nabla T_m \cdot \mathbf{n}, \quad (4.6g)$$

$$\nabla C_L \cdot \mathbf{n} = \nabla C_m \cdot \mathbf{n}, \quad (4.6h)$$

be satisfied.

On  $\eta_S(x,y,t) - z = 0$ , the general frame-invariant mass balance

$$(\rho_2 - \rho_1) \frac{\partial \eta}{\partial t} = (\rho_1 \mathbf{u}_1 - \rho_2 \mathbf{u}_2) \cdot \mathbf{n} \quad (4.7a)$$

across the interface between two regions reduces to

$$\mathbf{u}_m \cdot \mathbf{n} = 0, \quad (4.7b)$$

because we have assumed that the solid and fluid densities are equal. The no-slip condition is

$$\mathbf{u}_m \cdot \mathbf{t} = 0. \quad (4.7c)$$

The composition and temperature at the mushy-zone/solid interface satisfy the thermodynamic conditions

$$C_m = \min(C_E, C_\infty/k), \quad (4.7d)$$

$$T_m = T_S, \quad (4.7e)$$

where  $C_E$  is the solute concentration on the eutectic isotherm. Conservation of energy across the mushy-zone/solid interface requires

$$-L\phi V_S \cdot n = k_m \nabla T_m \cdot n - k_S \nabla T_S \cdot n, \quad (4.7f)$$

where  $V_S$  is the velocity of the mushy-zone/solid interface referred to the laboratory frame.

### 4.3. Nondimensionalization

#### 4.3.1. Dimensionless Governing Equations

We scale the length, time, temperature in the liquid and solid, and the velocity, vorticity, pressure, and solute mass fraction in the liquid with  $H_L$ ,  $H_L/V_I$ ,  $G_L H_L$ ,  $V_I$ ,  $V_I/H_L$ ,  $\rho_0 V_I v/H_L$ , and  $C_\infty$ , respectively, where  $H_L = D_L/V_I$  is the characteristic length associated with the solute gradient at the liquid/mushy-zone interface. The length, time, temperature, velocity, vorticity, pressure, and solute mass fraction in the mushy zone are scaled with  $H_m$ ,  $H_m/V_I$ ,  $G_L H_m$ ,  $V_I$ ,  $V_I/H_m$ ,  $\rho_0 V_I v/H_m$ , and  $C_\infty$ , respectively, where  $H_m$  is the mushy-zone thickness. The dimensionless governing equations in the liquid are

$$\nabla \cdot \hat{u}_L = 0, \quad (4.8a)$$

$$\begin{aligned} \frac{1}{Sc} \left[ \frac{\partial \hat{u}_L}{\partial \tau_L} - \frac{\partial \hat{u}_L}{\partial z} + \hat{u}_L \cdot \nabla \hat{u}_L + 2 \Omega^* \times \hat{u}_L + \Omega^* \times (\Omega^* \times r) \right] = \\ - \nabla \hat{p}_L - \frac{\rho_l}{\rho_0 \gamma^3 Sc} l_z + \nabla^2 \hat{u}_L, \end{aligned} \quad (4.8b)$$

$$Le \left( \frac{\partial \hat{T}_L}{\partial \tau_L} - \frac{\partial \hat{T}_L}{\partial z} + \hat{u}_L \cdot \nabla \hat{T}_L \right) = \nabla^2 \hat{T}_L, \quad (4.8c)$$

$$\frac{\partial \hat{C}_L}{\partial \tau_L} - \frac{\partial \hat{C}_L}{\partial z} + \hat{u}_L \cdot \nabla \hat{C}_L = \nabla^2 \hat{C}_L, \quad (4.8d)$$

where the dimensionless variables  $\hat{u}_L$ ,  $\hat{p}_L$ ,  $\hat{T}_L$ , and  $\hat{C}_L$  are, respectively, velocity, pressure, temperature, and solute mass fraction in the liquid,  $Sc = v/D_L$  and  $Le = D_L/\kappa_L$  are the Schmidt and Lewis numbers, respectively,  $\gamma = V_I/(g D_L)^{1/3}$  is the dimensionless solidification rate, and  $\Omega^* = \Omega H_L/V_I = \Omega (D_L/g^2)^{1/3}/\gamma^2$  is the dimensionless angular velocity.

The dimensionless equations in the mushy zone are

$$\nabla_m \cdot \hat{u}_m = 0, \quad (4.9a)$$

$$\begin{aligned} \frac{\xi}{Sc} \left[ \phi \frac{\partial}{\partial \tau_m} \left( \frac{\hat{u}_m}{\phi} \right) - \phi \frac{\partial}{\partial z_m} \left( \frac{\hat{u}_m}{\phi} \right) + \hat{u}_m \cdot \nabla_m \left( \frac{\hat{u}_m}{\phi} \right) + 2\xi \Omega^* \times \hat{u}_m + \xi^2 \phi \Omega^* \times (\Omega^* \times r) \right] = \\ - \phi \nabla_m \hat{p}_m - \frac{\xi^2 \rho_f}{\rho_0 \gamma^3 Sc} \phi I_z - \phi \underline{P}^* \hat{u}_m + \nabla_m^2 \hat{u}_m, \end{aligned} \quad (4.9b)$$

$$\xi Le \left[ c_{pm}^* \frac{\partial \hat{T}_m}{\partial \tau_m} - c_{pm}^* \frac{\partial \hat{T}_m}{\partial z_m} + \hat{u}_m \cdot \nabla_m \hat{T}_m \right] = \nabla_m \cdot k_m^* \nabla_m \hat{T}_m - \frac{\gamma}{\Gamma} \left( \frac{\partial \phi}{\partial \tau_m} - \frac{\partial \phi}{\partial z_m} \right), \quad (4.9c)$$

$$\xi \left[ \phi \frac{\partial \hat{C}_m}{\partial \tau_m} - \phi \frac{\partial \hat{C}_m}{\partial z_m} + \hat{u}_m \cdot \nabla_m \hat{C}_m \right] = \nabla_m \cdot \phi \nabla_m \hat{C}_m - \xi(1-k) \hat{C}_m \left( \frac{\partial \phi}{\partial \tau_m} - \frac{\partial \phi}{\partial z_m} \right), \quad (4.9d)$$

$$\hat{T}_m = \frac{T_M^*}{\Gamma} + \frac{m^*}{\Gamma} \hat{C}_m, \quad (4.9e)$$

where  $\nabla_m = (\partial/\partial x_m, \partial/\partial y_m, \partial/\partial z_m)$ , the dimensionless variables  $\hat{u}_m$ ,  $\hat{p}_m$ ,  $\hat{T}_m$ , and  $\hat{C}_m$  are, respectively, the velocity, pressure, temperature, and solute mass fraction in the mushy zone,  $\Gamma = G_L k_L / [L(g D_L)^{1/3}]$  is the dimensionless liquid-side temperature gradient at the liquid/mushy-zone interface,  $\xi = \gamma g^{1/3} H_m / D_L^{2/3}$  is the ratio of the mushy-zone thickness to the characteristic length associated with the solute gradient in the liquid,  $k_m^* = \phi + (1 - \phi)k^*$  is the thermal conductivity of the mushy zone scaled by the thermal conductivity of the liquid,  $k^* = k_S/k_L$  is the ratio of the thermal conductivity in the solid to that in the fluid,  $c_{p,m}^* = \phi + (1 - \phi)c_p^*$  is the specific heat in the mushy zone scaled by the specific heat of the fluid,  $c_p^* = c_{p,S}/c_{p,L}$  is the ratio of the specific heat in the solid to that in the fluid,  $\underline{P}^* = H_m^2 \underline{P}$ ,  $m^* = m_L C_\infty k_L / [L H_m (g D_L)^{1/3}]$ , and  $T_M^* = T_M k_L / [L H_m (g D_L)^{1/3}]$ .

The dimensionless energy equation in the solid is

$$Le \left( \frac{\partial \hat{T}_S}{\partial \tau} - \frac{\partial \hat{T}_S}{\partial z} \right) = \kappa^* \nabla^2 \hat{T}_S, \quad (4.10)$$

where  $\hat{T}_S$  is the dimensionless temperature in the solid, and  $\kappa^* = \kappa_S/\kappa_L$  is the thermal diffusivity ratio.

#### 4.3.2. Dimensionless Boundary Conditions

The dimensionless boundary condition applied far from the liquid/mushy-zone interface as  $z \rightarrow \infty$  is

$$\hat{C}_L \rightarrow 1. \quad (4.11)$$

At the liquid/mushy-zone interface  $\hat{\eta}_L(x_m, y_m, \tau_m) - z_m = 0$ , the dimensionless boundary conditions are

$$\phi = 1, \quad (4.12a)$$

$$\hat{u}_L = \hat{u}_m, \quad (4.12b)$$

$$(\hat{p}_m - \xi \hat{p}_L) = \mathbf{n} \cdot \left\{ \left[ \nabla_m \hat{u}_m + (\nabla_m \hat{u}_m)^T \right] \cdot \mathbf{n} - \xi \left[ \nabla \hat{u}_L + (\nabla \hat{u}_L)^T \right] \cdot \mathbf{n} \right\}, \quad (4.12c)$$

$$\mathbf{t} \cdot \left\{ \left[ \nabla_m \hat{u}_m + (\nabla_m \hat{u}_m)^T \right] \cdot \mathbf{n} - \xi \left[ \nabla \hat{u}_L + (\nabla \hat{u}_L)^T \right] \cdot \mathbf{n} \right\} = 0, \quad (4.12d)$$

$$\hat{T}_L = \xi \hat{T}_m, \quad (4.12e)$$

$$\hat{C}_L = \hat{C}_m, \quad (4.12f)$$

$$\nabla \hat{T}_L \cdot \mathbf{n} = \nabla_m \hat{T}_m \cdot \mathbf{n}, \quad (4.12g)$$

$$\xi \nabla \hat{C}_L \cdot \mathbf{n} = \nabla_m \hat{C}_m \cdot \mathbf{n}. \quad (4.12h)$$

The boundary conditions at the mushy-zone/solid interface  $\hat{\eta}_S(x_m, y_m, \tau_m) - z_m = 0$  are

$$\hat{u}_m \cdot \mathbf{n} = 0, \quad (4.13a)$$

$$\hat{u}_m \cdot \mathbf{t} = 0, \quad (4.13b)$$

$$\hat{C}_m = \min(C_E/C_\infty, 1/k) , \quad (4.13c)$$

$$\xi \hat{T}_m = \hat{T}_S , \quad (4.13d)$$

$$-\frac{\gamma}{\Gamma} \phi V_S^* \cdot n = k_m^* \nabla_m \hat{T}_m \cdot n - k^* \nabla \hat{T}_S \cdot n , \quad (4.13e)$$

where  $V_S^*$  is the velocity of the mushy-zone/solid interface scaled by  $V_I$ .

## 4.4. Basic State and Linear Disturbance Equations

### 4.4.1. Basic State

The governing equations and boundary conditions (4.8)-(4.13) in the reference frame translating upward with the nominal interface velocity  $V_I$  and rotating at constant angular velocity  $\Omega$  about the vertical axis admit a one-dimensional steady basic state solution. The temperature and composition in each region, along with the porosity of the mushy zone, depend only on the vertical coordinate  $z$ . The motionless basic state in the laboratory frame corresponds to a nonuniform superficial velocity distribution in the mushy zone in the moving frame. The mushy-zone/solid and liquid/mushy-zone interfaces are horizontal, stationary, and located at  $z = 0$  and  $H_m$ , respectively, with the thickness  $H_m$  being determined as part of the solution. The dimensionless equations governing the steady temperature, composition, and volume fraction distributions in this motionless basic state are

$$\frac{d^2 \bar{T}_L}{dz^2} + Le \frac{d \bar{T}_L}{dz} = 0 , \quad (4.14a)$$

$$\frac{d^2 \bar{C}_L}{dz^2} + \frac{d \bar{C}_L}{dz} = 0 , \quad (4.14b)$$

In the liquid,

$$\frac{d}{dz_m} \left( k_m^*(\bar{\phi}) \frac{d \bar{T}_m}{dz_m} \right) + Le \xi c_{p,m}^*(\bar{\phi}) \frac{d \bar{T}_m}{dz_m} + \frac{\gamma}{\Gamma} \frac{d \bar{\phi}}{dz_m} = 0 , \quad (4.14c)$$

$$\frac{d}{dz_m} \left( \bar{\phi} \frac{d\bar{C}_m}{dz_m} \right) + \xi \bar{\phi} \frac{d\bar{C}_m}{dz_m} + \xi(1-k)\bar{C}_m \frac{d\bar{\phi}}{dz_m} = 0, \quad (4.14d)$$

$$\bar{T}_m = \frac{T_M^*}{\Gamma} + \frac{m^*}{\Gamma} \bar{C}_m, \quad (4.14e)$$

in the mushy zone, and

$$\kappa^* \frac{d^2 \bar{T}_s}{dz^2} + Le \frac{d\bar{T}_s}{dz} = 0, \quad (4.14f)$$

in the solid. Here  $\bar{T}_L$ ,  $\bar{C}_L$ ,  $\bar{T}_m$ ,  $\bar{C}_m$ ,  $\bar{\phi}$ , and  $\bar{T}_s$  are the dimensionless basic state distributions of temperature and concentration in the liquid, temperature, concentration, and volume fraction in the mushy zone, and temperature in the solid, respectively.

The dimensionless boundary conditions applicable to the basic state are

$$\bar{C}_L \rightarrow 1 \quad (4.15a)$$

as  $z \rightarrow \infty$ ,

$$\bar{\phi}(1) = 1, \quad (4.15b)$$

$$\bar{T}_L(\xi) = \xi \bar{T}_m(1), \quad (4.15c)$$

$$\bar{C}_L(\xi) = \bar{C}_m(1), \quad (4.15d)$$

$$1 = \frac{d\bar{T}_L(\xi)}{dz} = \frac{d\bar{T}_m(1)}{dz_m}, \quad (4.15e-f)$$

$$\xi \frac{d\bar{C}_L(\xi)}{dz} = \frac{d\bar{C}_m(1)}{dz_m}, \quad (4.15g)$$

at the liquid/mushy-zone interface, and

$$\xi \bar{T}_m(0) = \bar{T}_s(0), \quad (4.15h)$$

$$\bar{C}_m(0) = \min(C_E/C_\infty, 1/k), \quad (4.15i)$$

$$-\frac{\gamma}{\Gamma} \bar{\phi}(0) = k_m^*(\bar{\phi}) \frac{d\bar{T}_m(0)}{dz_m} - k^* \frac{d\bar{T}_s(0)}{dz}, \quad (4.15j)$$

at the mushy-zone/solid interface. We note that (4.15a-j) constitute ten boundary conditions for a ninth-order differential equation system. However, the mushy-zone thickness  $H_m$  is unknown, so that the problem is not overdetermined. Dimensionless basic state temperature and concentration distributions in the liquid and the temperature distribution in the solid can be determined by integrating (4.14a,b,f) subject to (4.15a), (4.15e), and a linear combination of (4.15f,g) to get

$$\bar{T}_L(z) = \frac{\xi T_M^*}{\Gamma} + \frac{\xi m^*}{\Gamma} - 1 + \frac{1}{Le} \left\{ 1 - \exp[-Le(z - \xi)] \right\}, \quad (4.16a)$$

$$\bar{C}_L(z) = 1 - \frac{\Gamma}{\xi m^*} \exp[-(z - \xi)], \quad (4.16b)$$

$$\bar{T}_S(z) = A_1 + A_2 \exp\left(-\frac{Le z}{\kappa^*}\right), \quad (4.16c)$$

where  $A_1$  and  $A_2$  are integration constants. The remaining nonlinear ordinary differential equations (4.14c,d) subject to the thermodynamic constraint (4.14e) are integrated subject to (4.15b,d,g,i) using a shooting technique to obtain  $\bar{T}_m$ ,  $\bar{C}_m$ , and  $\bar{\phi}$  along with the mushy-zone height  $H_m$ . The integration constants  $A_1$  and  $A_2$  in (4.16c) can be found using (4.15h,j). Our basic state composition and volume fraction distributions in the mushy zone are in excellent agreement with those of Flemings (1974).

#### 4.4.2. Disturbance Equations and Boundary Conditions

To determine the conditions under which disturbances grow or decay, we write the liquid velocity, temperature, composition, and pressure as

$$\hat{u}_L(x, y, z, \tau) = 0 + u_L'(x, y, z, \tau), \quad (4.17a)$$

$$\hat{T}_L(x, y, z, \tau) = \bar{T}_L(z) + T'_L(x, y, z, \tau) , \quad (4.17b)$$

$$\hat{C}_L(x, y, z, \tau) = \bar{C}_L(z) + C'_L(x, y, z, \tau) , \quad (4.17c)$$

$$\hat{p}_L(x, y, z, \tau) = \bar{p}_L(z) + p'_L(x, y, z, \tau) , \quad (4.17d)$$

the velocity, temperature, composition, pressure, and volume fraction in the mushy zone as

$$\hat{u}_m(x_m, y_m, z_m, \tau_m) = 0 + u'_m(x_m, y_m, z_m, \tau_m) , \quad (4.17e)$$

$$\hat{T}_m(x_m, y_m, z_m, \tau_m) = \bar{T}_m(z_m) + T'_m(x_m, y_m, z_m, \tau_m) , \quad (4.17f)$$

$$\hat{C}_m(x_m, y_m, z_m, \tau_m) = \bar{C}_m(z_m) + C'_m(x_m, y_m, z_m, \tau_m) , \quad (4.17g)$$

$$\hat{p}_m(x_m, y_m, z_m, \tau_m) = \bar{p}_m(z_m) + p'_m(x_m, y_m, z_m, \tau_m) , \quad (4.17h)$$

$$\phi(x_m, y_m, z_m, \tau_m) = \bar{\phi}(z_m) + \phi'(x_m, y_m, z_m, \tau_m) , \quad (4.17i)$$

the solid temperature as

$$\hat{T}_S(x, y, z, \tau) = \bar{T}_S(z) + T'_S(x, y, z, \tau) , \quad (4.17j)$$

the locations of the liquid/mushy-zone and mushy-zone/solid interfaces as

$$\hat{\eta}_L(x_m, y_m, \tau_m) = H_m + \eta'_L(x_m, y_m, \tau_m) , \quad (4.17k)$$

$$\hat{\eta}_S(x_m, y_m, \tau_m) = 0 + \eta'_S(x_m, y_m, \tau_m) , \quad (4.17l)$$

and the local velocity of the mushy-zone/solid interface as

$$V_S(x, y, \tau) = 0 + V'_S(x, y, \tau) , \quad (4.17m)$$

where  $u'_L$ ,  $T'_L$ ,  $C'_L$ ,  $p'_L$ , and  $u'_m$ ,  $T'_m$ ,  $C'_m$ ,  $p'_m$ , are the dimensionless velocity, temperature, concentration, and pressure disturbances in the liquid and mushy zone,  $T'_S$  is the dimensionless temperature disturbance in the solid,  $\phi'$  is the disturbance volume fraction,



$\eta_L'$  and  $\eta_S'$  are the dimensionless disturbances to the liquid/mushy-zone and mushy-zone/solid interface positions, and  $V_S'(x, y, \tau) = (\partial \eta_S' / \partial \tau_m) / \xi$  is the dimensionless disturbance to the mushy-zone/solid interface velocity.

Substituting (4.17a-m) into (4.8)-(4.13), subtracting the basic state equations, and retaining only linear terms, we obtain dimensionless linear disturbance equations and boundary conditions. The equations governing small disturbances in the liquid are

$$\nabla \cdot \mathbf{u}_L' = 0, \quad (4.18a)$$

$$\frac{1}{Sc} \left[ \frac{\partial \mathbf{u}_L'}{\partial \tau} - \frac{\partial \mathbf{u}_L'}{\partial z} + 2 \Omega^* \times \mathbf{u}_L' \right] = -\nabla p_L' + \frac{\Gamma F_T}{\gamma^4 Sc} T_L' \mathbf{i}_z + \frac{F_C}{\gamma^3 Sc} C_L' \mathbf{i}_z + \nabla^2 \mathbf{u}_L', \quad (4.18b)$$

$$Le \left( \frac{\partial T_L'}{\partial \tau} - \frac{\partial T_L'}{\partial z} + \frac{dT_L'}{dz} w_L' \right) = \nabla^2 T_L', \quad (4.18c)$$

$$\frac{\partial C_L'}{\partial \tau} - \frac{\partial C_L'}{\partial z} + \frac{dC_L'}{dz} w_L' = \nabla^2 C_L', \quad (4.18d)$$

where  $w_L'$  is the disturbance to the z-component of the liquid velocity,  $F_T = \alpha_T L D_L / \rho_0 k_L$ ,  $F_C = \alpha_C C_\infty / \rho_0$ ,  $\Omega^* = \Omega_0^* \mathbf{i}_z$  is the angular velocity, and  $\Omega_0^* = \Omega_0 (D_L / g^2)^{1/3} / \gamma^2$  is the dimensionless rotation rate. Taking the curl of (4.18b) and the dot product of the result with  $\mathbf{i}_z$ , we obtain an equation

$$\frac{1}{Sc} \left( \frac{\partial \omega_L'}{\partial \tau} - \frac{\partial \omega_L'}{\partial z} - 2 \Omega_0^* \frac{\partial w_L'}{\partial z} \right) = \nabla^2 \omega_L' \quad (4.19)$$

for the z-component of the disturbance vorticity in the liquid,  $\omega_L'$ . After twice taking the curl of (4.18b), the vertical component of the resulting equation is

$$\frac{1}{Sc} \left( \frac{\partial}{\partial \tau} \nabla^2 w_L' - \frac{\partial}{\partial z} \nabla^2 w_L' + 2 \Omega_0^* \frac{\partial \omega_L'}{\partial z} \right) = \frac{\Gamma F_T}{\gamma^4 Sc} \nabla^2 T_L' + \frac{F_C}{\gamma^3 Sc} \nabla^2 C_L' + \nabla^4 w_L'. \quad (4.20)$$

where  $\nabla_{\perp}^2 = \partial^2/\partial x^2 + \partial^2/\partial y^2$  is the horizontal portion of the Laplacian operator. The equations governing small disturbances in the mushy zone are

$$\nabla_m \cdot \mathbf{u}_m' = 0, \quad (4.21a)$$

$$\begin{aligned} \frac{\xi}{Sc} \left[ \frac{1}{\bar{\phi}} \frac{\partial \mathbf{u}_m'}{\partial \tau_m} - \frac{\partial}{\partial z_m} \left( \frac{\mathbf{u}_m'}{\bar{\phi}} \right) + \frac{2\xi}{\bar{\phi}} \Omega \times \mathbf{u}_m' \right] = -\nabla_m p_m' \\ + \frac{\xi^3 \Gamma F_I}{\gamma^4 Sc} T_m' I_z + \frac{\xi^2 F_C}{\gamma^3 Sc} C_m' I_z - P^*(\bar{\phi}) \mathbf{u}_m' + \frac{1}{\bar{\phi}} \nabla_m^2 \mathbf{u}_m', \end{aligned} \quad (4.21b)$$

$$\begin{aligned} Le \xi \left[ c_{pm}^*(\bar{\phi}) \frac{\partial T_m'}{\partial \tau_m} - c_{pm}^*(\bar{\phi}) \frac{\partial T_m'}{\partial z_m} - (1-c_p^*) \frac{dT_m}{dz_m} \phi' + \frac{dT_m}{dz_m} w_m' \right] = \\ \nabla_m \cdot k_m^*(\bar{\phi}) \nabla_m T_m' + (1-k^*) \frac{\partial}{\partial z_m} \left( \frac{dT_m}{dz_m} \phi' \right) - \frac{\gamma}{\Gamma} \left( \frac{\partial \phi'}{\partial \tau_m} - \frac{\partial \phi'}{\partial z_m} \right), \end{aligned} \quad (4.21c)$$

$$\begin{aligned} \xi \left( \bar{\phi} \frac{\partial C_m'}{\partial \tau_m} - \bar{\phi} \frac{\partial C_m'}{\partial z_m} - \frac{d\bar{C}_m}{dz_m} \phi' + \frac{d\bar{C}_m}{dz_m} w_m' \right) = \nabla_m \cdot \bar{\phi} \nabla_m C_m' + \frac{\partial}{\partial z_m} \left( \frac{d\bar{C}_m}{dz_m} \phi' \right) \\ - \xi(1-k) \bar{C}_m \frac{\partial \phi'}{\partial \tau_m} + \xi(1-k) \bar{C}_m \frac{\partial \phi'}{\partial z_m} + \xi(1-k) \frac{d\bar{C}_m}{dz_m} C_m', \end{aligned} \quad (4.21d)$$

$$T_m' = \frac{m}{\Gamma} C_m', \quad (4.21e)$$

where  $w_m'$  is the disturbance to the z-component of the fluid velocity in the mushy zone.

Taking the curl of (4.21b) and the dot product of the result with  $I_z$ , we obtain an equation

$$\frac{\xi}{Sc} \left[ \frac{\partial \omega_m'}{\partial \tau_m} - \bar{\phi} \frac{\partial}{\partial z_m} \left( \frac{\omega_m'}{\bar{\phi}} \right) - 2\xi \Omega_0^* \frac{\partial w_m'}{\partial z_m} \right] = \nabla_m^2 \omega_m' - P_h(\bar{\phi}) \omega_m' \quad (4.22)$$

for the z-component of the vorticity in the mushy zone,  $\omega_m'$ . After twice taking the curl of (4.21b), the vertical component of the resulting equation is

$$\begin{aligned} \frac{\xi}{Sc} \left[ \frac{\partial}{\partial \tau_m} \nabla_m^2 \left( \frac{w'_m}{\bar{\phi}} \right) - \frac{\partial}{\partial z_m} \nabla_m^2 \left( \frac{w'_m}{\bar{\phi}} \right) + 2 \xi \Omega_0^* \frac{\partial w'_m}{\partial z_m} \right] &= \frac{\xi^3 \Gamma F_I}{\gamma^4 Sc} \nabla_{\perp m}^2 T'_m \\ &+ \frac{\xi^2 F_C}{\gamma^3 Sc} \nabla_{\perp m}^2 C'_m + P_v(\bar{\phi}) \nabla_{\perp m}^2 w'_m + \frac{\partial}{\partial z_m} \left[ P_h(\bar{\phi}) \frac{\partial w'_m}{\partial z_m} \right] + \nabla_m^2 \left( \frac{\nabla_m^2 w'_m}{\bar{\phi}} \right). \end{aligned} \quad (4.23)$$

The disturbance energy equation in the solid is

$$Le \left( \frac{\partial T'_S}{\partial \tau} - \frac{\partial T'_S}{\partial z} \right) = \kappa^* \nabla^2 T'_S. \quad (4.24)$$

The far-field disturbance boundary conditions are

$$w'_L = \frac{\partial w'_L}{\partial z} = \omega'_L = C'_L = T'_L \rightarrow 0, \quad (4.25a-e)$$

as  $z \rightarrow \infty$ , and

$$\frac{\partial T'_S}{\partial z} \rightarrow 0 \quad (4.26)$$

as  $z \rightarrow -\infty$ . The disturbance boundary conditions linearized about the nominal liquid/mushy-zone interface position ( $z_m = 1$ ) are

$$\phi'(x_m, y_m, 1, \tau_m) + \frac{d\bar{\phi}(1)}{dz_m} \eta'_L(x_m, y_m, \tau_m) = 0, \quad (4.27a)$$

$$w'_L(x, y, \xi, \tau) = w'_m(x_m, y_m, 1, \tau_m), \quad (4.27b)$$

$$\xi \frac{\partial w'_L(x, y, \xi, \tau)}{\partial z} = \frac{\partial w'_m(x_m, y_m, 1, \tau_m)}{\partial z_m}, \quad (4.27c)$$

$$\xi^2 \frac{\partial^2 w'_L(x, y, \xi, \tau)}{\partial z^2} = \frac{\partial^2 w'_m(x_m, y_m, 1, \tau_m)}{\partial z_m^2}, \quad (4.27d)$$

$$\xi^3 \frac{\partial^3 w'_L(x, y, \xi, \tau)}{\partial z^3} = \frac{\partial^3 w'_m(x_m, y_m, 1, \tau_m)}{\partial z_m^3} + \frac{\xi}{Sc} \frac{d\bar{\phi}(1)}{dz_m} \frac{\partial w'_m(x_m, y_m, 1, \tau_m)}{\partial z_m}, \quad (4.27e)$$

$$\xi \omega'_L(x, y, \xi, \tau) = \omega'_m(x_m, y_m, 1, \tau_m), \quad (4.27f)$$

$$\xi^2 \frac{\partial \omega'_L(x, y, \xi, \tau)}{\partial z} = \frac{\partial \omega'_m(x_m, y_m, 1, \tau_m)}{\partial z_m}, \quad (4.27g)$$

$$T'_L(x, y, \xi, \tau) = \xi T'_m(x_m, y_m, 1, \tau_m), \quad (4.27h)$$

$$C'_L(x, y, \xi, \tau) = C'_m(x_m, y_m, 1, \tau_m), \quad (4.27i)$$

$$\begin{aligned} \frac{\partial T'_L(x, y, \xi, \tau)}{\partial z} + \xi \frac{d^2 \bar{T}_L(\xi)}{dz^2} \eta'_L(x_m, y_m, \tau_m) = \\ \frac{\partial T'_m(x_m, y_m, 1, \tau_m)}{\partial z_m} + \frac{d^2 \bar{T}_m(1)}{dz_m^2} \eta'_L(x_m, y_m, \tau_m), \end{aligned} \quad (4.27j)$$

$$\begin{aligned} \xi \frac{\partial C'_L(x, y, \xi, \tau)}{\partial z} + \xi^2 \frac{d^2 \bar{C}_L(\xi)}{dz^2} \eta'_L(x_m, y_m, \tau_m) = \\ \frac{\partial C'_m(x_m, y_m, 1, \tau_m)}{\partial z_m} + \frac{d^2 \bar{C}_m(1)}{dz_m^2} \eta'_L(x_m, y_m, \tau_m), \end{aligned} \quad (4.27k)$$

and those at the mushy-zone/solid interface are

$$w'_m(x_m, y_m, 0, \tau_m) = \frac{\partial w'_m(x_m, y_m, 0, \tau_m)}{\partial z_m} = \omega'_m(x_m, y_m, 0, \tau_m) = 0, \quad (4.28a-c)$$

$$T'_S(x, y, 0, \tau) + \xi \frac{d\bar{T}_S(0)}{dz} \eta'_S(x_m, y_m, \tau_m) = \xi T'_m(x_m, y_m, 0, \tau_m) + \xi \frac{d\bar{T}_m(0)}{dz_m} \eta'_S(x_m, y_m, \tau_m), \quad (4.28d)$$

$$C'_m(x, y, 0, \tau) + \frac{d\bar{C}_m(0)}{dz} \eta'_S(x_m, y_m, \tau_m) = 0, \quad (4.28e)$$

$$\begin{aligned} -\frac{\gamma}{\Gamma} \phi'(x_m, y_m, 0, \tau_m) - \frac{\gamma}{\Gamma} \bar{\phi}(0) \frac{\partial \eta'_S(x_m, y_m, \tau_m)}{\tau_m} = k_m^*(\bar{\phi}) \frac{\partial T'_m(x_m, y_m, 0, \tau_m)}{\partial z_m} \\ - k^* \frac{\partial T'_S(x, y, 0, \tau)}{\partial z} + k_m^*(\bar{\phi}) \frac{d^2 \bar{T}_m(0)}{dz_m^2} \eta'_S(x_m, y_m, \tau_m) - k^* \frac{d^2 \bar{T}_S(0)}{dz^2} \eta'_S(x_m, y_m, \tau_m) \\ + (1-k^*) \frac{d\bar{T}_m(0)}{dz_m} \phi'(x_m, y_m, 0, \tau_m) + (1-k^*) \frac{d\bar{T}_m(0)}{dz_m} \frac{d\bar{\phi}(0)}{dz_m} \eta'_S(x_m, y_m, \tau_m). \end{aligned} \quad (4.28f)$$

#### 4.4.3. Fourier Decomposition

We write the horizontal and temporal dependence of the dimensionless disturbance quantities in the liquid and solid as  $\exp(\sigma\tau + ia_x x + ia_y y)$ , where  $a_x$  and  $a_y$  are the  $x$ - and  $y$ -components of the horizontal wavevector, and  $\sigma$  is the temporal eigenvalue. The dimensionless disturbance quantities in the mushy zone are similarly decomposed as  $z$ -dependent amplitudes multiplied by  $\exp(\sigma_m \tau + ia_{m,x} x + ia_{m,y} y)$ . Substitution into (4.18c-d), (4.19), (4.20), (4.21c-e), and (4.22)-(4.24) yields

$$L_2 \left( L_2 + \frac{1}{Sc} \frac{d}{dz} - \frac{1}{Sc} \sigma \right) W_L - 2 \frac{\Omega_0^*}{Sc} \frac{d\Omega_L}{dz} - \frac{\Gamma F_T}{\gamma^4 Sc} a^2 \Theta_L - \frac{F_C}{\gamma^3 Sc} a^2 \chi_L = 0, \quad (4.29a)$$

$$\left( L_2 + \frac{1}{Sc} \frac{d}{dz} - \frac{1}{Sc} \sigma \right) \Omega_L + 2 \frac{\Omega_0^*}{Sc} \frac{dW_L}{dz} = 0, \quad (4.29b)$$

$$\left( L_2 + Le \frac{d}{dz} - \sigma Le \right) \Theta_L - Le \frac{d\bar{T}_L}{dz} W_L = 0, \quad (4.29c)$$

$$\left( L_2 + \frac{d}{dz} - \sigma \right) \chi_L - \frac{d\bar{\chi}_L}{dz} W_L = 0, \quad (4.29d)$$

in the liquid,

$$\left\{ L_{2m} \frac{1}{\bar{\phi}} L_{2m} + \frac{\xi}{Sc} \left( \frac{d}{dz_m} - \sigma_m \right) L_{2m} \frac{1}{\bar{\phi}} - P_v(\bar{\phi}) a_m^2 + \frac{d}{dz_m} \left[ P_h(\bar{\phi}) \frac{d}{dz_m} \right] \right\} W_m - \frac{2\xi\Omega_0^*}{Sc} \frac{d\Omega_m}{dz_m} - \frac{\xi^3 \Gamma F_T}{\gamma^4 Sc} a_m^2 \Theta_m - \frac{\xi^2 F_C}{\gamma^3 Sc} a_m^2 \chi_m = 0, \quad (4.29e)$$

$$\left[ L_{2m} + \frac{1}{Sc} \bar{\phi} \frac{d}{dz_m} \frac{1}{\bar{\phi}} - P_h(\bar{\phi}) - \frac{1}{Sc} \sigma_m \right] \Omega_m + \frac{2\xi\Omega_0^*}{Sc} \frac{dW_m}{dz_m} = 0, \quad (4.29f)$$

$$\left[ k_m^*(\bar{\phi}) L_{2m} + \frac{dk_m^*(\bar{\phi})}{dz_m} \frac{d}{dz_m} + (1-k^*) \frac{d}{dz_m} \frac{d\bar{\phi}}{dz_m} + Le \xi c_{pm}^*(\bar{\phi}) \frac{d}{dz_m} - Le \xi c_{pm}^*(\bar{\phi}) \sigma_m \right] \Theta_m$$

$$+ \left[ Le \xi (1-c_p^*) \frac{d\bar{T}_m}{dz_m} + \frac{\gamma}{\Gamma} \frac{d}{dz_m} + (1-k^*) \frac{d}{dz_m} \frac{d\bar{T}_m}{dz_m} - \frac{\gamma}{\Gamma} \sigma_m \right] \Phi - Le \frac{d\bar{T}_m}{dz_m} W_m = 0, \quad (4.29g)$$

$$\left[ \bar{\phi} L_{2m} + \frac{d\bar{\phi}}{dz_m} \frac{d}{dz_m} + \xi \bar{\phi} \frac{d}{dz_m} + \xi (1-k) \frac{d\bar{\phi}}{dz_m} - \xi \bar{\phi} \sigma_m \right] \chi_m - \xi \frac{d\bar{C}_m}{dz_m} W_m$$

$$+ \left[ \frac{d}{dz_m} \frac{d\bar{C}_m}{dz_m} + \xi (1-k) \bar{C}_m \frac{d}{dz_m} + \frac{d\bar{C}_m}{dz_m} - \xi (1-k) \bar{C}_m \sigma_m \right] \Phi = 0, \quad (4.29h)$$

$$\Theta_m = \frac{m^*}{\Gamma} \chi_m, \quad (4.29i)$$

In the mushy zone, and

$$\left( \kappa^* L_2 + Le \frac{d}{dz} - Le \sigma \right) \Theta_s = 0 \quad (4.29j)$$

in the solid, where  $W_L$ ,  $\Omega_L$ ,  $\chi_L$ , and  $\Theta_L$  are, respectively, amplitudes of disturbances to the vertical velocity, vorticity, solute distribution, and temperature in the liquid,  $W_m$ ,  $\Omega_m$ ,  $\chi_m$ ,  $\Theta_m$ , and  $\Phi$  are, respectively, amplitudes of disturbances to the vertical velocity, vorticity, solute distribution, temperature, and volume fraction in the mushy zone,  $\Theta_s$  is the amplitude of the disturbance temperature in the solid, and  $L_2 = d^2/dz^2 - a^2$  and  $L_{2m} = d^2/dz_m^2 - a_m^2$  are linear operators. Here  $a$  and  $a_m$  are the dimensionless horizontal wavenumbers in the liquid and solid, and mushy zone, respectively. Matching the solutions at the two interfaces requires that the dimensional horizontal wavenumbers be the same. This gives the ratio of the dimensionless wavenumbers as  $a_m/a = \xi = H_m/H_L$ . A similar matching procedure for the temporal dependence gives the relationship  $\sigma/\sigma_m = \xi = H_m/H_L$ .

The dimensionless disturbance quantities satisfy the boundary conditions

$$\Phi(1) + \frac{d\Phi(1)}{dz_m} \beta_L = 0, \quad (4.30a)$$

$$W_L(\xi) = W_m(1), \quad (4.30b)$$

$$\xi \frac{dW_L(\xi)}{dz} = \frac{dW_m(1)}{dz_m}, \quad (4.30c)$$

$$\xi^2 \frac{d^2W_L(\xi)}{dz^2} = \frac{d^2W_m(1)}{dz_m^2}, \quad (4.30d)$$

$$\xi^3 \frac{d^3W_L(\xi)}{dz^3} = \frac{d^3W_m(1)}{dz_m^3} + \frac{\xi}{Sc} \frac{d\phi(1)}{dz_m} \frac{dW_m(1)}{dz_m}, \quad (4.30e)$$

$$\xi \Omega_L(\xi) = \Omega_m(1), \quad (4.30f)$$

$$\xi^2 \frac{d\Omega_L(\xi)}{dz} = \frac{d\Omega_m(1)}{dz_m}, \quad (4.30g)$$

$$\Theta_L(\xi) = \xi \Theta_m(1), \quad (4.30h)$$

$$\chi_L(\xi) = \chi_m(1), \quad (4.30i)$$

$$\frac{d\Theta_L(\xi)}{dz} + \xi \frac{d^2\bar{T}_L(\xi)}{dz^2} \beta_L = \frac{d\Theta_m(1)}{dz_m} + \frac{d^2\bar{T}_m(1)}{dz_m^2} \beta_L, \quad (4.30j)$$

$$\xi \frac{d\chi_L(\xi)}{dz} + \xi^2 \frac{d^2\bar{C}_L(\xi)}{dz^2} \beta_L = \frac{d\chi_m(1)}{dz_m} + \frac{d^2\bar{C}_m(1)}{dz_m^2} \beta_L, \quad (4.30k)$$

at the liquid/mushy-zone interface, and

$$W_m(0) = \frac{dW_m(0)}{dz_m} = \Omega_m(0) = 0, \quad (4.31a-c)$$

$$\Theta_S(0) + \xi \frac{d\bar{T}_S(0)}{dz} \beta_S = \xi \Theta_m(0) + \xi \frac{d\bar{T}_m(0)}{dz_m} \beta_S, \quad (4.31d)$$

$$\chi_m(0) + \frac{d\bar{C}_m(0)}{dz_m} \beta_S = 0, \quad (4.31e)$$

$$\left[ \bar{k}_m \frac{d^2 \bar{T}_m(0)}{dz_m^2} - k^* \frac{d^2 \bar{T}_s(0)}{dz^2} + (1 - k^*) \frac{d\bar{T}_m(0)}{dz_m} \frac{d\bar{\phi}(0)}{dz_m} + \frac{\gamma}{\Gamma} \bar{\phi}(0) \sigma_m \right] \beta_s$$

$$+ k_m^*(\bar{\phi}) \frac{d\Theta_m(0)}{dz_m} - k^* \frac{d\Theta_s(0)}{dz} + \left[ (1 - k^*) \frac{d\bar{T}_m(0)}{dz_m} + \frac{\gamma}{\Gamma} \right] \Phi(0) = 0, \quad (4.31f)$$

where the constants  $\beta_s$  and  $\beta_L$  are the amplitudes of the disturbed mushy-zone/solid and liquid/mushy-zone interface positions, respectively. For the boundary conditions far from the interface, we set all disturbances to zero

$$W_L = \frac{dW_L}{dz} = \chi_L = \Theta_L = \Omega_L = 0 \quad \text{as } z \rightarrow \infty, \quad (4.32a-f)$$

$$\frac{d\Theta_s}{dz} = 0 \quad \text{as } z \rightarrow -\infty. \quad (4.32g)$$

#### 4.5. Numerical Solution

Our objective is to find conditions for which infinitesimally small disturbances decay ( $\text{Re}(\sigma) < 0$ ) for all but a finite number of critical wavenumbers (typically one), and are neutral ( $\text{Re}(\sigma) = 0$ ) for the critical wavenumber(s). These conditions separate basic states that are linearly stable from those that are not.

In the previous section, we formulated an eigenvalue problem for systems of ordinary differential equations on two semi-infinite intervals (in the liquid and solid) and a finite interval (in the mushy zone), coupled by boundary conditions at the deformable liquid/mushy-zone and mushy-zone/solid interfaces. For convenience, we truncate the domain and solve the problem on a finite computational domain. With regard to the far-field boundary conditions at  $z = \pm \infty$ , we set all disturbances to zero at  $z = \xi + h$

$$W = DW = \chi_L = \Theta_L = \Omega_L = 0 \quad \text{at } z = \xi + h, \quad (4.33a-e)$$

in the liquid and at  $z = -h$

$$\Theta_s = 0 \quad \text{at } z = -h. \quad (4.33f)$$



in the solid. In this work, we have taken  $h$  to be 10. (We have checked a number of our results using larger values of  $h$ , and have found that eigenvalues do not change sensibly for  $h$  larger than 10.) Since we use Chebyshev polynomials in our numerical solution, we scale the liquid, mushy-zone, and solid coordinates by  $z_1 = (2z - 2\xi - h)/h$ ,  $z_2 = 2z_m - h$ , and  $z_3 = (2z - h)/h$  respectively, so that each region lies between  $-1$  and  $+1$ . The resulting system is solved using a Galerkin technique developed by Zebib (1987).

We approximate the highest derivatives of the amplitudes of the disturbance velocity, vorticity, solute distribution, and temperature in the liquid, the velocity, vorticity, solute distribution, temperature, and porosity in the mushy zone, and the temperature in the solid, by truncated sums of Chebyshev polynomials of the form

$$W_L^{(4)}(z_1) = \sum_{j=0}^N A_j T_j(z_1), \quad (4.34a)$$

$$\Omega_L^{(2)}(z_1) = \sum_{j=0}^N B_j T_j(z_1), \quad (4.34b)$$

$$\chi_L^{(2)}(z_1) = \sum_{j=0}^N C_j T_j(z_1), \quad (4.34c)$$

$$\Theta_L^{(2)}(z_1) = \sum_{j=0}^N D_j T_j(z_1), \quad (4.34d)$$

$$W_m^{(4)}(z_2) = \sum_{j=0}^N E_j T_j(z_2), \quad (4.34e)$$

$$\Omega_m^{(2)}(z_2) = \sum_{j=0}^N F_j T_j(z_2), \quad (4.34f)$$

$$\chi_m^{(2)}(z_2) = \sum_{j=0}^N G_j T_j(z_2), \quad (4.34g)$$

$$\Theta_m^{(2)}(z_2) = \sum_{j=0}^N H_j T_j(z_2), \quad (4.34h)$$

$$\Phi^{(1)}(z_2) = \sum_{j=0}^N K_j T_j(z_2), \quad (4.34i)$$

$$\Theta_s^{(2)}(z_3) = \sum_{j=0}^N M_j T_j(z_3), \quad (4.34j)$$

where  $T_j$  is the  $j$ -th Chebyshev polynomial and the coefficients  $A_j, B_j, C_j, D_j, E_j, F_j, G_j, H_j, K_j$ , and  $M_j$  are to be found. Representations of lower order derivatives can be found by integrating (4.34a-j) and using standard properties of Chebyshev polynomials. The procedure described by Zebib (1987) reduces the problem to a matrix eigenvalue problem

$$\mathbf{A} \mathbf{s} + \sigma \mathbf{B} \mathbf{s} = 0, \quad (4.35)$$

where  $\sigma$  is the temporal eigenvalue, and the elements of the square matrices  $\mathbf{A}$  and  $\mathbf{B}$  depend on the square of the horizontal wavenumber  $a^2 = a_x^2 + a_y^2$ , the bulk mole fraction  $C_\infty$ , and the other dimensionless parameters.

In §4.6 we characterize the stability of the nominal one-dimensional basic state solution in terms of the bulk concentration  $C_\infty$  and dimensionless solidification rate  $\gamma$ , with all other parameters taken as fixed. For each value of  $C_\infty$ , we seek one or more critical values of  $\gamma$  (denoted by  $\gamma^*$ ) such that for  $\gamma > \gamma^*$ , disturbances decay for all wavenumbers, while for  $\gamma < \gamma^*$ , disturbances grow for all wavenumbers in some range. In order to determine the critical value(s) of  $\gamma$ , we first determine the neutral curve ( $\gamma$  versus the wavenumber  $a$ ) separating those combinations of  $\gamma$  and  $a$  for which all temporal eigenvalues  $\sigma$  lie in the left half-plane (a stable basic state) from those for which at least one eigenvalue lies in the right half-plane (an unstable basic state). To determine the bulk concentration on the neutral curve for an arbitrarily chosen wavenumber  $a$ , we first choose a value of  $\gamma$  and compute all eigenvalues  $\sigma$  using (4.35). If all eigenvalues have negative real parts,  $\gamma$  is decreased by half the previous value; otherwise the new value of  $\gamma$  is chosen as twice the previous value. This process is

continued until we determine two values of  $\gamma$  between which at least one sign change is obtained in the real part of the least stable temporal eigenvalue. The dimensionless solidification rate on the neutral curve is then determined using a bisection method.

To compute the critical dimensionless solidification rate  $\gamma^*$  at which instability first occurs (i.e., the maximum on the neutral curve), we arbitrarily choose a wavenumber and compute the corresponding  $\gamma$  on the neutral curve using the procedure described above. We then fix  $\gamma$  at the value computed at the previous step and compute the eigenvalues  $\sigma$  for a discrete set of wavenumbers in a chosen range. From this set we select the wavenumber corresponding to the  $\sigma$  with largest real part. If this wavenumber is at an endpoint of the chosen range, we extend the range to include the wavenumber corresponding to the largest  $\text{Re}(\sigma)$ . We then select this wavenumber and determine the corresponding  $\gamma$  on the neutral curve. We continue this process until the relative change in  $\gamma$  is less than  $10^{-6}$ . Spectral and domain convergence results are shown in Table 3.

#### 4.6. Results

The solutions of (4.29)-(4.33) depend on seventeen dimensionless parameters, as defined in §§4.2 and 4.3. (The approximate solutions on the finite interval also depend on  $h$ .) It is therefore not feasible to numerically explore the effects of more than a few combinations of these parameters on the onset of convection. In this work, we have thus restricted ourselves to the Pb-Sn system which, due to the low melting points of both components, has been the subject of several experimental studies. The thermophysical properties of the liquid and solid phases are as used by Coriell *et al.* (1980) at reference conditions corresponding to pure lead at its melting point. (The diffusivity of Sn in Pb used corresponds to an infinitely dilute solution.)

Figure 4.2(a,b) shows the dimensionless basic state solute mass fraction profiles in the liquid and mushy zone for  $C_\infty = 0.2$ ,  $\gamma = 2.59 \times 10^{-2}$ , and  $\Gamma = 7.12 \times 10^{-2}$ . (For Pb-Sn alloys, these values of the dimensionless solidification rate and liquid-side temperature

gradient correspond to  $V_I = 80 \mu \text{ sec}^{-1}$  and  $G_L = 50 \text{ K cm}^{-1}$ .) Note that the solute profile varies almost linearly with the vertical coordinate  $z_m$  in the mushy zone, within which almost all of the solute variation is confined. In the liquid region adjacent to the liquid/mushy-zone interface there is a compositional boundary layer, the thickness of which is very small compared to the mushy-zone thickness. (Note that we have used different length scales in the liquid and mushy zone. For the mushy zone the length scale is the thickness  $H_m$ , the dimensional value of which is 1.685 cm for this combination of  $G_L$ ,  $V_I$ , and  $C_\infty$ , and for the liquid the length scale is the diffusion length, which in this case is  $3.75 \times 10^{-3}$  cm.) For the same values of  $\gamma$ ,  $\Gamma$ , and  $C_\infty$ , figure 4.2(c) shows the basic state porosity profile. Figure 4.2(d-f) shows  $\phi(z_m)$  for three other values of  $C_\infty$ . The volume fraction is largest ( $\phi = 1$ ) at the liquid/mushy-zone interface, and decreases monotonically to a nonzero value at the mushy-zone/solid interface. These results show that as  $C_\infty$  increases, the porosity distribution becomes more linear and its value at the mushy-zone/solid interface increases monotonically. Figure 4.2(f) shows that the mushy-zone thickness ( $H_m = 0.527$  cm) for  $C_\infty = 0.5$  is much smaller (so that the liquid in the porous medium is more mobile) than for  $C_\infty = 0.1, 0.2$  or  $0.35$ .

The dependence of the dimensional mushy-zone thickness,  $H_m$ , on the bulk mass fraction and temperature gradient is shown in figure 4.3(a-c) for three solidification rates. The solid, dashed, and dotted curves in each figure show  $H_m$  for  $\gamma = 3.24 \times 10^{-2}$  ( $V_I = 100 \mu \text{ sec}^{-1}$ ),  $1.62 \times 10^{-3}$  ( $V_I = 50 \mu \text{ sec}^{-1}$ ),  $9.72 \times 10^{-3}$  ( $V_I = 30 \mu \text{ sec}^{-1}$ ), respectively. We see that  $H_m$  is a strong function of  $\Gamma$  (note that three different logarithmic scales have been used for  $H_m$ ) and  $C_\infty$ , depends relatively weakly on  $\gamma$ , and assumes a maximum near  $C_\infty = 0.2$  for each combination of solidification rate and temperature gradient. This maximum occurs because the composition difference  $\Delta C_m = C_m(1) - C_m(0)$  between the top and bottom of the mushy zone reaches a maximum near  $C_\infty = 0.2$ , and the mushy-zone composition varies almost linearly with  $z$ , as shown in figure 4.2. As  $\Delta C_m$  decreases to zero as  $C_\infty$  approaches  $C_E$ ,  $H_m$  asymptotically decreases to zero. The decrease of  $H_m$  as  $C_\infty$  decreases

to the left of the maximum  $H_m$  is again due to the fact that  $\Delta C_m$  decreases with decreasing  $C_\infty$ . For  $\Gamma = 7.12 \times 10^{-3}$  ( $G_L = 5 \text{ K cm}^{-1}$ ), figure 4.3(a) shows that  $H_m$  is a decreasing function of  $\gamma$ . For  $\Gamma = 7.12 \times 10^{-2}$  ( $G_L = 50 \text{ K cm}^{-1}$ ), the variation of  $H_m$  with  $\gamma$  is much weaker (figure 4.3b), and for  $\Gamma = 0.285$  ( $G_L = 200 \text{ K cm}^{-1}$ ) is nearly independent of  $\gamma$  (figure 4.3c). We also note that the mushy-zone thickness decreases strongly with increasing temperature gradient.

For three values of  $C_\infty$ , figures 4.4(a-c) show neutral curves ( $\gamma$  versus  $a$ ) for  $\Gamma = 7.12 \times 10^{-2}$  ( $G_L = 50 \text{ K cm}^{-1}$ ) and rotation rates  $\Omega_0 = 0 \text{ rpm}$  (solid curve), 300 rpm (dashed-dot curve), and 500 rpm (dashed curve). These neutral curves correspond to steady onset of buoyancy-driven convection; we have found no evidence for the oscillatory onset of instability in the dendritic solidification of Pb-Sn alloys. For given values of  $C_\infty$  and  $\Gamma$ , the critical solidification rate (denoted by  $\gamma^*$ ) is the maximum point on each neutral curve and determines one point on the stability boundary. For  $\gamma > \gamma^*$ , the one-dimensional dendritic basic state solution is stable for all wavenumbers  $a$ , whereas for  $\gamma < \gamma^*$  it is unstable for some range of  $a$ .

Figure 4.4(a) shows neutral curves ( $\gamma$  versus  $a$ ) for  $C_\infty = 0.1$ . At the extremum, the critical solidification rate is  $\gamma = 2.20 \times 10^{-2}$  ( $V_I = 68 \mu \text{ sec}^{-1}$ ) and the critical wavenumber is  $a = 0.32$  for the nonrotating case (solid curve). For  $\Omega_0 = 300 \text{ rpm}$  the neutral curve (dashed-dot curve) is displaced downward for all wavenumbers, indicating the stabilization associated with rotation. Although the reduction in  $\gamma^*$  (to  $\gamma = 1.82 \times 10^{-2}$ , corresponding to  $V_I = 56 \mu \text{ sec}^{-1}$ ) is significant (note the logarithmic  $\gamma$ -scale), the effect is particularly strong at smaller wavenumbers (higher wavelengths). We also note that the critical wavenumber has been shifted to a higher value. These effects will be discussed in §4.7. For  $\Omega_0 = 500 \text{ rpm}$ , the critical solidification rate is reduced to  $\gamma^* = 1.571 \times 10^{-2}$  ( $V_I = 48.5 \mu \text{ sec}^{-1}$ ) and the critical wavenumber has nearly doubled to  $a = 0.65$ . For  $C_\infty = 0.2$ , figure 4.4(b) shows neutral curves ( $\gamma$  versus  $a$ ) analogous to those for  $C_\infty = 0.1$ . The critical solidification rate assumes a maximum for this value of  $C_\infty$  (nearly independent

of  $\Omega_0$ ) [ $\gamma^* = 2.59 \times 10^{-2}$  ( $V_I = 80.0 \mu \text{ sec}^{-1}$ ),  $2.30 \times 10^{-2}$  ( $V_I = 71 \mu \text{ sec}^{-1}$ ), and  $1.86 \times 10^{-2}$  ( $V_I = 57.5 \mu \text{ sec}^{-1}$ ) for  $\Omega_0 = 0, 300$ , and  $500$  rpm, respectively) and the critical wavenumber increases ( $a = 0.27, 0.41$ , and  $0.55$  for  $\Omega_0 = 0, 300$ , and  $500$  rpm, respectively). The Coriolis acceleration again suppresses the onset of buoyancy-driven convection with large wavelength as illustrated in figure 4.4(b). From the neutral curves for  $C_\infty = 0.55$  in figure 4.4(c) we see that aside from a slight shift downward to smaller solidification rates [ $\gamma^* = 1.98 \times 10^{-2}$  ( $V_I = 61.3 \mu \text{ sec}^{-1}$ ),  $1.75 \times 10^{-2}$  ( $V_I = 54 \mu \text{ sec}^{-1}$ ), and  $1.42 \times 10^{-2}$  ( $V_I = 43.9 \mu \text{ sec}^{-1}$ ) for  $\Omega_0 = 0, 300$ , and  $500$  rpm, respectively], the results are qualitatively similar to those for  $C_\infty = 0.1$  and  $0.2$ . We note that the smallest stable range of solidification rates is obtained for  $C_\infty = 0.2$ , which will be discussed below in connection with the stability boundaries.

The vertical structure of the disturbance amplitudes of vertical velocity, temperature, and vorticity in the liquid and mushy zone, solute mass fraction in the liquid, and volume fraction in the mushy zone are shown in figures 4.5 and 4.6 for  $\Omega_0 = 0$  and  $500$  rpm, respectively. The disturbances shown correspond to the least stable mode (i.e., that with least positive or most negative  $\text{Re}(\sigma)$ ). For graphical clarity, the same length scale (based on mushy-zone thickness) is used in both layers. In these two figures, the mushy zone extends from  $z = -1$  to  $0$ , and the liquid lies above. Since temperature and composition in the mushy zone are linearly related, only the structure of the temperature disturbance is shown.

For  $C_\infty = 0.55$  and  $\Gamma = 7.12 \times 10^{-2}$ , figure 4.5 shows the disturbance amplitudes for the nonrotating case at the critical conditions  $\gamma = 1.976 \times 10^{-2}$  ( $V_I = 61 \mu \text{ sec}^{-1}$ ) and  $a = 0.32$  (as determined from the neutral curve in figure 4.4c). Figure 4.5(a) shows that the vertical velocity disturbance assumes a maximum just above the liquid/mushy-zone interface and decays strongly in both layers. We also note that the depth of penetration of the convective disturbance in each layer is of the same order. Figure 4.5(b) shows that the structure of the temperature disturbance is similar, except near the mushy-zone/solid interface where the temperature disturbance does not approach zero. This is due to the fact that the boundary

condition (4.31e) (derived from the dimensional condition (4.7d)) requires that the solute mass fraction in the interdendritic fluid be equal to the eutectic mass fraction on the deformed mushy-zone/solid interface. Thus, the relationship (4.29j) between the temperature and solute mass fraction disturbances in the mushy zone requires that the disturbance temperature be nonzero whenever that interface is deformed. Figure 4.5(c,d) shows that disturbances to the liquid composition and mushy-zone volume fraction are largely confined to very thin layers adjacent to the liquid/mushy-zone interface

For the same bulk mass fraction and temperature gradient as in figure 4.5, the vertical structure of the same disturbance amplitudes, along with the vertical vorticity in the liquid and mushy zone, are shown in figure 4.6 for the  $\Omega_0 = 500$  rpm for the corresponding critical conditions [ $\gamma = 1.458 \times 10^{-2}$  ( $V_I = 45 \mu \text{ sec}^{-1}$ ) and  $a = 0.66$ ]. Aside from the considerable increase in the critical wavenumber, only quantitative differences are apparent in the velocity, temperature, composition, and volume fraction disturbances compared to the nonrotating case. The vertical component of the vorticity in the liquid and mushy zone is shown in figure 4.6(e) to be highly localized near the liquid/mushy-zone interface and to decay strongly within each layer.

For  $\Omega_0 = 0$  and 500 rpm, we present our principal results in terms of a division of the  $\gamma$ - $C_\infty$  plane in figures 4.7-4.10 for four values of  $\Gamma$ . These figures show the region (bounded by the dashed curve) in which the one-dimensional dendritic solution exists along with information regarding its stability and the stability of the one-dimensional plane-front solution (which exists for all combinations of  $C_\infty$ ,  $\gamma$ ,  $\Gamma$ , and  $\Omega_0$ ). Each region is characterized according to whether the one-dimensional dendritic solution exists (and if so, whether it is stable), and whether the plane-front solution is stable with respect to morphological and convective disturbances (Chapter 2; cf. Coriell *et al.* 1980).

Figure 4.7(a) shows the division of the  $\gamma$ - $C_\infty$  plane for  $\Gamma = 0.285$  ( $G_L = 200 \text{ K cm}^{-1}$ ) and  $\Omega_0 = 0$  rpm. The one-dimensional dendritic solution exists in regions 1 and 2, and is stable at sufficiently high solidification rates (region 1) and unstable for lower values of  $\gamma$  (region

2). (The turning point on the dendritic stability boundary (curve D) near  $C_\infty = 0.2$  is discussed in §4.7.) In regions 3-5, no one-dimensional steady solution of (4.8)-(4.13) exists. The plane-front solution exists in regions 1-5, but is unstable with respect to the morphological instability (curve M) in regions 1-3. The plane-front convective stability boundary (curve C) separates region 4, in which the plane-front solution is morphologically stable but convectively unstable, from region 5, in which the plane-front solution is stable with respect to both morphological and convective disturbances. In summary, the one-dimensional dendritic solution is stable in region 1 and the one-dimensional plane-front solution is stable in region 5; elsewhere the plane-front solution is unstable and the dendritic solution either does not exist or is unstable.

For the same value of  $\Gamma$  (0.285), figure 4.7(b) shows a similar division of the  $\gamma$ - $C_\infty$  plane for  $\Omega_0 = 500$  rpm. The dendritic stability boundary is shifted to slightly smaller values of  $\gamma$  relative to the nonrotating case, constituting a small enlargement of region 1, in which the dendritic solution is stable. As for disturbances to the plane-front solution, the morphological branch is not sensibly changed, but the plane-front convective stability boundary has shifted upward (Chapter 2), and so the range of bulk mass fraction and solidification rate for which plane-front solidification is stable is significantly enlarged relative to the nonrotating case. The greater degree of suppression of buoyancy-driven convection that is achieved for the plane-front solution relative to the dendritic case is discussed in §4.7.

Figures 4.8-4.10 show that the topology of the division of the  $\gamma$ - $C_\infty$  plane becomes more complex as the temperature gradient decreases. For  $\Gamma = 7.12 \times 10^{-2}$  ( $G_L = 50 \text{ K cm}^{-1}$ ), figure 4.8(a-b) shows that for  $\Omega_0 = 0$  and 500 rpm, a new region (6) exists in which both the plane-front and dendritic solutions are stable. For  $\Omega_0 = 0$  rpm, figure 4.8(a) shows that for the plane-front solution, the morphological and convective stability boundaries have shifted downward, and stable plane-front solidification is confined to a smaller part of the  $\gamma$ - $C_\infty$  plane than for  $\Gamma = 0.285$ . However, for this smaller temperature gradient, dendritic



solidification is stable for a larger range of  $\gamma$  and  $C_{\infty}$  relative to the  $\Gamma = 0.285$  case. For  $\Gamma = 7.12 \times 10^{-2}$ , the dendritic stability boundary intersects the dendritic existence curve just above the latter's intersection with the plane-front morphological stability boundary. Note also that the turning point on the dendritic stability boundary is more pronounced. For  $\Omega_0 = 500$  rpm, figure 4.8(b) shows that the regions in which only one one-dimensional solution is stable (regions 1 and 5 for dendritic and plane-front solidification, respectively) are considerably enlarged relative to the nonrotating case, whereas the size of the region in which both one-dimensional solutions are stable (region 6) is relatively unchanged, since its boundaries (the existence curve for dendritic solidification and the plane-front morphological stability boundary) are unaltered by rotation. The effect of rotation on the dendritic stability boundary is considerably stronger than for  $\Gamma = 0.285$ .

For  $\Gamma = 3.56 \times 10^{-2}$  ( $G_L = 25 \text{ K cm}^{-1}$ ) and  $\Omega_0 = 0$  rpm, figure 4.9(a) shows that the dendritic stability boundary intersects the dendritic existence curve well below the plane-front morphological stability boundary, so that the part of the  $\gamma$ - $C_{\infty}$  plane in which the plane-front solution is stable and the dendritic solution exists (region 6 in figure 4.8) has been divided according to the stability of the dendritic solution. In region 6, the dendritic and plane-front solutions are both stable, as for  $\Gamma = 7.12 \times 10^{-2}$ , while in region 7, the dendritic solution is unstable. We note that the mushy-zone thickness predicted in the lower part of region 6 is exceedingly small; one can conceive of more sophisticated solidification models (e.g., specifically predicting cellular solidification and imposing a threshold criterion on mushy-zone thickness for dendritic solidification) that would not predict the existence of dendritic solution in the lower part of region 6. For  $\Omega_0 = 500$  rpm, figure 4.9(b) shows that region 7 disappears at the expense of region 6, consistent with the stabilizing influence of rotation on dendritic solution manifested in the significant displacement of the dendritic stability boundary.

For  $\Gamma = 7.12 \times 10^{-3}$  ( $G_L = 5 \text{ K cm}^{-1}$ ) figure 4.10(a) shows for the nonrotating case that the dendritic solution exists in a part of the  $\gamma$ - $C_{\infty}$  plane (region 8) in which the plane-front

solution is morphologically stable and convectively unstable. Here, as in region 2, both the dendritic and plane-front solutions exist, but neither is stable. The characteristics of the other regions are unchanged. (We have not computed the boundary separating regions 6 and 7 for  $C_\infty < 1 \times 10^{-5}$  because, as discussed above, the basic state mushy-zone thickness predicted by our model becomes exceedingly small as the bulk mass fraction decreases further.) Note that the stable region of dendritic solidification becomes larger with decreasing temperature gradient. For  $\Omega_0 = 500$  rpm, figure 4.10(b) shows that region 8 has disappeared at the expense of regions 6 and 7, owing to the intersection of the dendritic existence curve and the plane-front morphological stability boundary at a larger value of  $\gamma$  than the latter's intersection with the plane-front convective stability boundary. We also note that the dendritic stability boundary intersects the dendritic existence curve at a value of  $C_\infty$  in excess of  $1 \times 10^{-5}$ . We also note that the degree of rotational stabilization for both the plane-front and dendritic solutions is considerably greater than shown in figures 4.7-4.9 for larger dimensionless temperature gradients.

#### 4.7. Discussion

Our analysis of the conditions under which the governing equations (4.8-13) admit a steady one-dimensional dendritic solution for Pb-Sn alloys, and the conditions under which that solution and the one-dimensional plane-front solution are stable, allows for a more complete discussion of the solidification regimes for binary alloys than has heretofore been possible.

That a one-dimensional steady dendritic solution exists for only some combinations of the temperature gradient, solidification rate, and bulk mass fraction is not surprising since this basic state is determined as the solution of a nonlinear ordinary differential equation system, for which a solution need not exist. The boundary in the parameter space within which the dendritic solution exists is determined by two constraints. One is that the liquid volume fraction at the liquid/mushy-zone interface is unity and cannot exceed that value within the

mushy zone. Hence, the vertical derivative of the volume fraction at the liquid/mushy-zone interface should be nonnegative. This condition is satisfied in the region above the lower branch of the dendritic existence curve. The other constraint is that the solute mass fraction in the interdendritic fluid cannot exceed the eutectic composition,  $C_E$ . The interdendritic solute mass fraction in the basic state depends monotonically on the vertical coordinate  $z$ . Therefore, if the solute mass fraction at the liquid/mushy-zone interface is less than  $C_E$ , this constraint can be satisfied everywhere in the mushy zone. Below the upper branch of the dendritic existence curve, the latter constraint is satisfied, and the mushy-zone thickness asymptotically approaches zero as this branch of the curve is approached from below. Hence, a one-dimensional dendritic solution exists only in the region between the two branches of the dendritic existence curve.

When the plane-front morphological stability boundary is crossed, a cellular interface develops. As the solidification rate increases past the critical value, the cells become deformed and deepen. The formation and evolution of the cells have been studied theoretically by Ungar & Brown (1984) and Ungar *et al.* (1984). For still larger solidification rates, dendritic solidification occurs, with dendrites typically consisting of long vertical stems with secondary and tertiary branches. The development of the cellular interface and transition to dendritic solidification were observed experimentally by Trivedi (1984) and Venugopalan & Kirkaldy (1984). We thus conclude that the part of region 3 (cf. figures 4.7-4.10) below the lower branch of the dendritic existence curve is a region of cellular solidification, in which the plane-front solution is morphologically unstable and the dendritic solution does not exist. The experimental evidence showing that dendritic solidification occurs when either the bulk mass fraction or solidification rate is increased for fixed temperature gradient is consistent with the location and character of the dendritic regions 1 and 2 in our results.

For a given value of the bulk solute mass fraction, there exists a critical solidification rate above which the one-dimensional dendritic solution is stable with respect to infinitesimal disturbances. For all values of  $\Gamma$ , and  $\Omega_0^*$  dendritic solidification is least stable

with respect to buoyancy-driven convection for solute mass fractions near 0.2 (the value at which the dendritic stability boundary has a turning point). This occurs because for this value of  $C_\infty$  the mushy-zone thickness  $H_m$  and the composition difference  $\Delta C_m$  attain their maximum values independent of temperature gradient and solidification rate (cf. figure 4.3 and accompanying description). If the Rayleigh number  $R_m$  we define for the mushy zone is proportional to  $\Delta C_m H_m$  (Worster 1992), maximum destabilization for the Pb-Sn system occurs for  $C_\infty$  near 0.2. Fowler (1985) defined a Rayleigh number  $R = (\alpha_C - \alpha_T) m_L \rho_0 g \tilde{K} / V_1$ , where  $\tilde{K}$  is a monotonically increasing function of the permeability, and showed that there is a critical value  $R_c \propto 1/(C_E - C_\infty)$  such that if  $R < R_c$ , then dendritic solidification is stable with respect to small disturbances. Note that for Pb-Sn,  $R_c$  assumes a minimum near  $C_\infty = 0.2$ . Thus, there is a critical solidification rate above which the condition  $R < R_c$  is satisfied, and dendritic solidification is convectively stable. Our numerical results are thus consistent with the approximate analytical results of Fowler (1985) and Worster (1992).

We also note that the stable range of  $\gamma$  and  $C_\infty$  grows as  $\Gamma$  decreases. This is due to the fact that liquid volume fraction (and hence permeability) decreases with decreasing temperature gradient, so that the mushy zone becomes more immobile and the onset of convection is suppressed. That is also consistent with Fowler's result, since the Rayleigh number decreases as permeability decreases.

The amplitudes of the disturbance to the vertical velocity assume a maximum in the liquid ahead of the liquid/mushy-zone interface, and decay strongly in each region. Buoyancy-driven convection is largely confined to the liquid ahead of the interface and to the part of the mushy zone where the fluid is most mobile (near the liquid/mushy-zone interface). The interdendritic fluid farther from the liquid/mushy-zone interface is essentially stagnant. For  $\Gamma = 7.12 \times 10^{-2}$  ( $G_L = 50 \text{ K cm}^{-1}$ ), the critical wavenumber range is approximately  $0.25 < a < 0.35$  (depending on  $C_\infty$ ) for the nonrotating case (figures 4.4a-c). The corresponding convective wavelength of 0.06 cm is small compared to the mushy-zone thickness ( $H_m = 0.311 \text{ cm}$  for  $C_\infty = 0.55$ ), but large compared to the diffusion length for

a typical solidification rate ( $4.92 \times 10^{-3}$  cm for  $V_I = 61 \mu \text{ sec}^{-1}$  at the critical value of  $\gamma$ ). We believe that this convection corresponds to the mushy layer mode described by Worster (1992). Rotating the system at  $\Omega_0 = 500$  rpm suppresses the convective instability at relatively small wavenumbers and nearly doubles the critical wavenumber, so that the wavelength of the buoyancy-driven convection is reduced by almost half relative to the nonrotating case.

That a one-dimensional dendritic solution exists under conditions for which plane-front solidification is linearly stable with respect to morphological disturbances might at first seem inconsistent. However, our result implies no such inconsistency, because the plane-front stability analysis (Coriell *et al.* 1980) is restricted to infinitesimal disturbances. In fact, in part of the region where the plane-front solution is linearly stable, it is known (Wollkind & Segel 1970; Alexander *et al.* 1986; Ungar & Brown 1984) to be unstable with respect to a subcritical ("finite amplitude") instability. Thus, in the region in which the plane-front solution is linearly stable, it is not surprising that we also find a one-dimensional dendritic solution.

The remarkable suppression at modest rotation rates of plane-front convective instability in Pb-Sn binary alloys was discussed in Chapter 2 in terms of the well known Taylor-Proudman mechanism, described by Chandrasekhar (1961). The Coriolis acceleration also inhibits the onset of buoyancy-driven convection in the dendritic case, but to a lesser extent than for plane-front solidification. This is because the effective Taylor number (a dimensionless measure of the Coriolis acceleration) is smaller in the dendritic case, due to the larger "effective viscosity" of the interdendritic fluid in the porous medium. The far greater suppression of dendritic solidification at smaller wavenumbers than at larger wavenumbers, and the shift of the critical wavenumber to a higher value (both shown in figure 4.4) are expected on the basis of the character of the Taylor-Proudman mechanism.

## CHAPTER 5

### Conclusion

For liquid Pb-Sn undergoing plane-front solidification, a remarkable suppression of the onset of buoyancy-driven convection is obtained at low solidification rates (more than a hundredfold increase in the critical value of  $C_{\infty}$  at  $V_1 = 1 \mu \text{ sec}^{-1}$  by rotating the layers at 500 rpm for the two values of  $G_L$  considered). The mechanism of this stabilization is discussed in terms of the Taylor-Proudman theorem, in Chapter 2. It is not surprising that the morphological instability is unaffected by rotation. The morphological instability occurs at very short wavelengths, so the motion is almost perpendicular to the solidification front (i.e., aligned with the axis of rotation). Hence, the Coriolis acceleration does not sensibly affect the morphological instability. The predicted inhibitory effects of rotation on convection are discussed in terms of previous experimental and theoretical studies of the effect of rotation on the onset of buoyancy-driven convection in single-component fluids heated from below and in binary fluids subject to thermal and solutal stratification.

For mercury cadmium telluride  $\text{Hg}_{1-x}\text{Cd}_x\text{Te}$ , the liquid density does not depend monotonically on temperature for some range of the bulk solute composition. For certain combinations of the operating parameters (solidification rate, nominal liquid-side vertical temperature gradient, and bulk solute concentration) a density maximum occurs at a temperature greater than the liquidus temperature and there exists a sublayer adjacent to the solid-liquid interface in which temperature gradient is destabilizing. This has profound effects on the nature of neutral curves, eigenfunctions, and the stability boundaries.

The morphological instability is completely insensitive to the net density stratification in the liquid, and is relatively insensitive to the variations of temperature and composition outside a relatively thin layer adjacent to the interface. This is evident from a comparison of the neutral curves and stability boundaries for  $\text{Hg}_{1-x}\text{Cd}_x\text{Te}$  to those for Pb-Sn. On the other hand, the onset of buoyancy-driven convection depends strongly on the nature of the

stabilizing or destabilizing temperature and solute gradients in the liquid, as well as on the diffusivities of the stratifying agencies. For Pb-Sn, the onset of buoyancy-driven convection is monotonic in time (corresponding to the fingering regime of doubly-diffusive convection), while for  $\text{Hg}_{1-x}\text{Cd}_x\text{Te}$  the motion is overstable or oscillatory in time (the diffusive regime). This is discussed in terms of the standard "parcel" argument for a linearly stratified doubly-diffusive fluid (Turner 1973, page 251) in Chapter 3.

In contrast to the case where the density depends monotonically on temperature and composition (e.g., the lead-tin alloys considered by Coriell *et al.* (1980)), for  $\text{Hg}_{1-x}\text{Cd}_x\text{Te}$  there exists a critical value of the bulk mole fraction below which plane-front solidification is unstable at all solidification rates. This differs from the Pb-Sn case in that for Pb-Sn, plane-front solidification at any  $C_\infty$  is linearly stable for all sufficiently small solidification rates. Moreover, when the density varies nonmonotonically, there can exist a critical value of the dimensionless solidification rate  $\gamma$  (denoted by  $\gamma^*$ ) such that for  $\gamma > \gamma^*$ , plane-front solidification is unstable for all values of the bulk mole fraction  $C_\infty$ . In this case, for  $\gamma < \gamma^*$ , there is a finite range of  $C_\infty$  for which the plane-front solution is stable. This latter result differs from the Pb-Sn case, for which at all dimensionless solidification rates, plane-front solidification is stable for all values of  $C_\infty$  lying below some critical value.

For  $\text{Hg}_{1-x}\text{Cd}_x\text{Te}$ , the disturbances associated with the oscillatory onset of buoyancy-driven convection are largely confined to that thermally unstably stratified sublayer. The results should be expected to apply to the solidification of other binary or multicomponent liquids in which  $(\partial\rho_L/\partial T_L)(\partial T_L/\partial z)$  changes sign within the layer.

The effect of rotation on the stability of plane-front solidification of  $\text{Hg}_{1-x}\text{Cd}_x\text{Te}$  pseudobinary liquid has also been investigated. Similar to the case for Pb-Sn alloys, the onset of buoyancy-driven convection is inhibited significantly by modest rotation rates, but the morphological instability is not sensibly altered.

In Chapter 4, we show that a one-dimensional steady mushy-zone solution exists for only some combinations of the temperature gradient, solidification rate, and bulk mass fraction.

This is not surprising since this basic state is computed from a nonlinear ordinary differential equation system for which a solution need to exist. The one-dimensional mushy-zone solution is stable for sufficiently large solidification rates for all wavenumbers. At lower solidification rates, it is unstable with respect to disturbances which grow monotonically in time. We also found that the dendritic basic state solution exists in part of the region where plane-front solidification is linearly stable with respect to morphological instability. This does not imply any inconsistency between our models of plane-front and dendritic solidification, since the plane-front stability analysis is restricted to infinitesimal disturbances. In part of the region where the plane-front solution is linearly stable, previous studies have shown that it is unstable with respect to subcritical instabilities. Hence, it is not surprising that we find a one-dimensional dendritic basic state solution in the region where the plane-front solidification is linearly stable.

We have also found that the Coriolis acceleration suppresses the onset of buoyancy-driven convection during dendritic solidification of Pb-Sn binary liquids. The relative degree of stabilization is less than for plane-front solidification. This is due to the fact that the effective Taylor number (a dimensionless measure of the Coriolis acceleration) is smaller in the dendritic case, due to the larger effective viscosity of the fluid in the porous medium.

Even though the analysis in this dissertation is restricted to horizontally unbounded fluid layers, the predictions will be qualitatively correct for finite aspect ratios (ratio of mold radius to height) if the parameter  $\Omega_0^2 R_0/g$  (a Froude number, where  $R_0$  is the mold radius) is sufficiently small, as discussed in detail in Chapter 2. For the onset of thermal convection in rotating water or mercury layers heated from below, the excellent quantitative agreement between classical linear stability analysis for a horizontally unbounded layer and experimental work for finite aspect ratios provides a clear demonstration of the potential of the Coriolis acceleration to suppress buoyancy-driven convection in a rotating fluid.

The relatively modest rotation rates required to significantly inhibit the onset of convection in the Pb-Sn and  $\text{Hg}_{1-x}\text{Cd}_x\text{Te}$  systems make the proposed method an interesting



candidate for a program of laboratory experiments. Experiments might be conducted using a completely filled cylindrical mold, thermally insulated on the vertical surface, and mounted axisymmetrically on a rotating horizontal turntable. If the liquid at the top of the rotating mold is in contact with a gas or vacuum, it will have a nearly paraboloidal free surface, on which the elevation above the point on the axis of rotation is  $\Delta z = \Omega_0^2 r^2 / (2g)$ . Although this configuration is consistent with rigid-body rotation, it also leads to a nearly paraboloidal solid-melt interface. For high rotation rates or large mold radius, this will in turn lead to significant radial variations in the solidified alloy. Also, cooling at the radial boundary leads to a radial temperature gradient, which in turn leads to significant centrifugal effects. Therefore, the present results can not be compared to the experimental works in which strong radial variations in macrosegregation are observed in the solid.

In our models for both plane-front and dendritic solidification, the domain considered is horizontally unbounded and, the liquid and solid extend vertically to  $z = \infty$  and  $z = -\infty$ , respectively. The interfaces in the basic state are assumed to be nominally planar. We also assume that solidification occurs sufficiently fast at the growing interface or in the mushy-zone so that the solid-liquid interface for plane-front solidification, or the entire mushy-zone for dendritic solidification can be considered to be in thermodynamic equilibrium. Thus nucleation and other kinetic effects are neglected in our models.

We have also assumed that the solid is thermally isotropic, and that for plane-front solidification, the liquid-solid interface is isotropic. The effects of boundary thermal anisotropy have been dealt with in Rayleigh-Bénard problem by Pearlstein & Öztekin (1989), while anisotropic surface tension has been considered for plane-front solidification by Voorhees *et al.* (1984). Both of these effects can be incorporated easily into the present work.

## Appendix A

The numerical solution of (2.17)-(2.19) can be obtained using a spectral Galerkin technique developed by Zebib (1987). We approximate the highest derivatives of the amplitudes of the disturbance velocity, vorticity, solute distribution, and temperature in the liquid, and temperature in the solid, by truncated sums of Chebyshev polynomials of the form

$$W^{(4)}(z_2) = \sum_{j=0}^J K_j T_j(z_2), \quad (\text{A1a})$$

$$\omega^{(2)}(z_2) = \sum_{j=0}^J M_j T_j(z_2), \quad (\text{A1b})$$

$$\chi_L^{(2)}(z_2) = \sum_{j=0}^J P_j T_j(z_2), \quad (\text{A1c})$$

$$\Theta_L^{(2)}(z_2) = \sum_{j=0}^J Q_j T_j(z_2), \quad (\text{A1d})$$

$$\Theta_S^{(2)}(z_1) = \sum_{j=0}^J Z_j T_j(z_1), \quad (\text{A1e})$$

where the coefficients  $K_j$ ,  $M_j$ ,  $P_j$ ,  $Q_j$ , and  $Z_j$  are to be found. Representations of lower order derivatives can be found by integrating (A1a-e) and using the following standard properties of Chebyshev polynomials

$$2 T_n(z) = \frac{\alpha_n}{n+1} \frac{dT_{n+1}(z)}{dz} - \frac{\lambda_{n-2}}{n-1} \frac{dT_{n-1}(z)}{dz}, \quad (\text{A2a})$$

and

$$2z T_n(z) = \alpha_n T_{n+1}(z) - \lambda_{n-1} T_{n-1}(z), \quad (\text{A2b})$$

where  $\alpha_n = \lambda_n = 0$  if  $n < 0$ ,  $\alpha_0 = 2$ ,  $\lambda_0 = 1$ , and  $\alpha_n = \lambda_n = 1$  if  $n > 0$ . The integration constants in the lower-order derivatives can be determined as functions of  $K_j$ ,  $M_j$ ,  $P_j$ ,  $Q_j$ , and  $Z_j$  using the boundary conditions (2.19), leading to

$$W^{(m)}(z_2) = \sum_{j=0}^J \sum_{l=0}^{J+4-m} [W_{jl}^{(m)} K_j + y_{12jl}^{(m)} M_j + y_{13jl}^{(m)} P_j + y_{14jl}^{(m)} Q_j + y_{15jl}^{(m)} Z_j] T_j(z_2) + \sum_{j=0}^{J+3-m} g_{1j}^{(m)} \beta T_j(z_2), \quad (A3a)$$

$$\omega^{(n)}(z_2) = \sum_{j=0}^J \sum_{l=0}^{J+2-n} [\omega_{jl}^{(n)} M_j + y_{21jl}^{(n)} K_j + y_{23jl}^{(n)} P_j + y_{24jl}^{(n)} Q_j + y_{25jl}^{(n)} Z_j] T_j(z_2) + \sum_{j=0}^{J+1-n} g_{2j}^{(n)} \beta T_j(z_2), \quad (A3b)$$

$$\chi_L^{(n)}(z_2) = \sum_{j=0}^J \sum_{l=0}^{J+2-n} [\chi_{Ljl}^{(n)} P_j + y_{31jl}^{(n)} K_j + y_{32jl}^{(n)} M_j + y_{34jl}^{(n)} Q_j + y_{35jl}^{(n)} Z_j] T_j(z_2) + \sum_{j=0}^{J+1-n} g_{3j}^{(n)} \beta T_j(z_2), \quad (A3c)$$

$$\theta_L^{(n)}(z_2) = \sum_{j=0}^J \sum_{l=0}^{J+2-n} [\theta_{Ljl}^{(n)} Q_j + y_{41jl}^{(n)} K_j + y_{42jl}^{(n)} M_j + y_{43jl}^{(n)} P_j + y_{45jl}^{(n)} Z_j] T_j(z_2) + \sum_{j=0}^{J+1-n} g_{4j}^{(n)} \beta T_j(z_2), \quad (A3d)$$

$$\theta_S^{(n)}(z_2) = \sum_{j=0}^J \sum_{l=0}^{J+2-n} [\theta_{Sjl}^{(n)} Z_j + y_{51jl}^{(n)} K_j + y_{52jl}^{(n)} M_j + y_{53jl}^{(n)} P_j + y_{54jl}^{(n)} Q_j] T_j(z_2) + \sum_{j=0}^{J+1-n} g_{5j}^{(n)} \beta T_j(z_2), \quad (A3e)$$

for  $m = 0, 1, 2, 3$  and  $n = 0, 1$ . Substituting (A3a-e) into the governing equations and taking inner products with

$$\sum_{j=0}^{J+4} W_{jl}^{(0)} T_j, \quad \sum_{j=0}^{J+2} \omega_{jl}^{(0)} T_j, \quad \sum_{j=0}^{J+2} \chi_{Ljl}^{(0)} T_j, \quad \sum_{j=0}^{J+2} \theta_{Ljl}^{(0)} T_j, \quad \text{and} \quad \sum_{j=0}^{J+2} \theta_{Sjl}^{(0)} T_j, \quad (A4)$$

respectively, we reduce the solution of (2.17)-(2.19) to a matrix eigenvalue problem

$$\mathbf{A} \mathbf{s} + \sigma \mathbf{B} \mathbf{s} = \mathbf{0}, \quad (\text{A5})$$

where  $\sigma$  is the temporal eigenvalue,  $\mathbf{A}$  and  $\mathbf{B}$  are square matrices, and  $\mathbf{s} = [K_j, M_j, P_j, Q_j, Z_j, \beta]^T$  is the eigenvector. The choice (A4) eliminates the spurious eigenvalues frequently encountered in the solution of eigenvalue problems for ordinary differential equations when using basis functions not satisfying the boundary conditions.

## Appendix B

To the best of our knowledge, the only data available for the density of liquid  $\text{Hg}_{1-x}\text{Cd}_x\text{Te}$  are those of Mokrovskii & Regel (1952) for pure HgTe, and Chandra & Holland (1983) for CdTe mole fractions in the range  $0 \leq C \leq 0.2$ . On the basis of the latter, three equations of state (Chandra 1985; Antar 1987, 1988, 1991; Apanovich & Ljumkis 1991) have been proposed for liquid  $\text{Hg}_{1-x}\text{Cd}_x\text{Te}$ . Unfortunately, for  $C = 0$ , Chandra & Holland's data differ systematically from those in Mokrovskii & Regel's well-known paper from Ioffe's Physico-Technical Institute in St. Petersburg. Chandra & Holland refer to two other papers by Regel, but make no reference to his work with Mokrovskii on the density of HgTe.

Although the relative difference between the  $C = 0$  data of Chandra & Holland and Mokrovskii & Regel is only about 0.65%, the average difference amounts to about 60% of the density variation reported by Mokrovskii & Regel over  $963 \text{ K} \leq T \leq 1173 \text{ K}$  and to about 75% of the variation reported by Chandra & Holland over  $953 \text{ K} \leq T \leq 1073 \text{ K}$ . Moreover, the  $C = 0.1$  data of Chandra & Holland show density extrema at three temperatures, whereas all other data vary either unimodally (for  $C \leq 0.05$ ) or monotonically (for  $C > 0.1$ ) with temperature. Finally, Chandra & Holland reported data only for the  $\text{Hg}_{1-x}\text{Cd}_x\text{Te}$  system, whereas Mokrovskii & Regel's (1952) density measurements for other liquids are in good agreement with those of Lucas & Urbain (1962) and Lucas (1964) for germanium, and of Glazov, Chizhevskaya & Evgen'ev (1969) for germanium, gallium antimonide, and indium antimonide, thus allowing an independent assessment of accuracy.

We have thus chosen to regard the  $C = 0$  data of Mokrovskii & Regel as accurate, and have undertaken to recalculate the data of Chandra & Holland on that basis. Chandra & Holland measured the liquid height  $\Delta$  in a capillary tube, from which their reported liquid volumes  $V_{\text{CH}}$  were inferred using a linear equation of the form  $V_{\text{CH}} = \delta_1 \Delta + \delta_2$ . Based on discussion with Chandra (private communication), we hypothesize that the primary source of error is in either the determination of  $\Delta$  or the determination of  $V$  from  $\Delta$ . Thus, we have recalculated

Chandra & Holland's data (excluding their measurements for  $C = 0.1$  at the two artifactual extremal temperatures of 1053 K and 1083 K) by using

$$V_{rc} = s_1 V_{CH} + s_2, \quad (B1)$$

and regarding  $s_1$  and  $s_2$  as unknowns, which we determine by minimizing the sum of the squared differences of the specific volumes

$$E_p = \sum_i \left[ \frac{1}{\rho_{MR}(T_i)} - \frac{1}{\rho_{rc}(T_i)} \right]^2, \quad (B2)$$

at  $C = 0$ , where  $\rho_{MR}$  refers to the experimental HgTe density data of Mokrovskii & Regel,  $\rho_{rc} = m_{HgTe} / (s_1 V_{CH} + s_2)$  is the recalculated density of Chandra & Holland for  $C = 0$ , the mass of pure HgTe used by Chandra & Holland for  $C = 0$  is  $m_{HgTe} = 62.6457$  g, and  $V_{CH}$  is the HgTe volume reported by Chandra & Holland at each temperature  $T_i$  at which they measured the density for  $C = 0$ . The sum  $E_p$  is minimized by  $s_1 = 0.9935$  and  $s_2 = 4.553 \times 10^{-10} \text{ cm}^3$ . Noting that the volumes reported by Chandra & Holland are on the order of  $10 \text{ cm}^3$ , we see that (B1) is nearly equivalent to multiplying the data of Chandra & Holland by a constant.

This allows recalculation of Chandra & Holland's reported volumes (for all but the two data points cited above) according to (B1). Recalculated values of Chandra & Holland's data at all mole fractions are used to fit by least-squares a bivariate polynomial of the form (3.7a) in the temperature range of their density data. The coefficients  $b_{ij}$  are

$b_{00} = 8.108$	$\text{g cm}^{-3}$	$b_{01} = -1.578 \times 10^{-4}$	$\text{g cm}^{-3} \text{K}^{-1}$
$b_{02} = -1.046 \times 10^{-5}$	$\text{g cm}^{-3} \text{K}^{-2}$	$b_{03} = 4.268 \times 10^{-8}$	$\text{g cm}^{-3} \text{K}^{-3}$
$b_{04} = 1.983 \times 10^{-10}$	$\text{g cm}^{-3} \text{K}^{-4}$	$b_{10} = -2.419$	$\text{g cm}^{-3}$
$b_{11} = 1.757 \times 10^{-3}$	$\text{g cm}^{-3} \text{K}^{-1}$	$b_{12} = 1.145 \times 10^{-5}$	$\text{g cm}^{-3} \text{K}^{-2}$
$b_{13} = 4.687 \times 10^{-8}$	$\text{g cm}^{-3} \text{K}^{-3}$	$b_{20} = -2.181$	$\text{g cm}^{-3}$
$b_{21} = 5.885 \times 10^{-4}$	$\text{g cm}^{-3} \text{K}^{-1}$	$b_{22} = -2.049 \times 10^{-4}$	$\text{g cm}^{-3} \text{K}^{-2}$
$b_{30} = 8.892$	$\text{g cm}^{-3}$	$b_{31} = 4.436 \times 10^{-2}$	$\text{g cm}^{-3} \text{K}^{-1}$

Far from the liquid-solid interface, however, the liquid temperature exceeds the maximum temperature ( $T_{\max}(C)$ ) at which  $\rho_L$  data are available. For  $T > T_{\max}(C)$ , the liquid density is approximated by a linear function of temperature (3.7b). The coefficients  $d_{ij}$  in (3.7b) are computed by matching the density and its temperature derivative at  $T = T_{\max}(C)$  and are found to be

$$\begin{array}{llll} d_{00} = 8.119 & \text{g cm}^{-3} & d_{10} = -2.435 & \text{g cm}^{-3} \\ d_{20} = -1.985 & \text{g cm}^{-3} & d_{30} = 10.48 & \text{g cm}^{-3} \\ d_{01} = -7.703 \times 10^{-4} & \text{g cm}^{-3}\text{K}^{-1} & d_{11} = 2.753 \times 10^{-3} & \text{g cm}^{-3}\text{K}^{-1} \\ d_{21} = -1.358 \times 10^{-2} & \text{g cm}^{-3}\text{K}^{-1} & d_{31} = 1.302 \times 10^{-2} & \text{g cm}^{-3}\text{K}^{-1} \end{array}$$

The coefficients  $r_i$  in (3.8) are computed by a least-squares fit of the maximum temperatures at which Chandra & Holland reported the density for different CdTe mole fractions. The values of  $r_i$  are

$$r_0 = 1073 \text{ K} \quad r_1 = 291.7 \text{ K} \quad r_2 = -2250 \text{ K} \quad r_3 = 8333 \text{ K}.$$

The results are shown in figure B1. Solid curves represent liquid density determined from (3.7a,b) as functions of temperature for  $C = 0, 0.05, 0.1$ , and  $0.2$ . Filled circles denote the  $C = 0$  density data reported by Mokrovskii & Regel (1952). The other symbols denote density data reported by Chandra & Holland (1983). For  $0 \leq C \leq 0.16$ , we obtain a unimodal density variation with temperature. (At the value of  $C$  at which  $\rho$  becomes a monotonic function of  $T$ , the maximum occurs at the liquidus temperature.) Although the  $C = 0$  density data of Chandra & Holland are consistently lower than those of Mokrovskii & Regel, the density maxima occur at nearly the same temperature.

## Appendix C

The thermophysical properties of the liquid and solid (other than the density of the liquid) are taken as constants evaluated using the functional forms shown below at the bulk mole fraction and corresponding liquidus or solidus temperatures ( $T_{liq}$  and  $T_{sol}$ ).

We have taken the density of solid  $Hg_{1-x}Cd_xTe$  as

$$\frac{1}{\rho_s} = \frac{\zeta}{\rho_{CdTe}} + \frac{1-\zeta}{\rho_{HgTe}}, \quad (C1)$$

where  $\zeta = CM_{CdTe}/M$  is the CdTe mass fraction, the molecular weights of CdTe and HgTe are  $M_{CdTe} = 240$  g/mol and  $M_{HgTe} = 328.2$  g/mol,  $M = CM_{CdTe} + (1-C)M_{HgTe}$ , and  $\rho_{CdTe}$  and  $\rho_{HgTe}$  are the solid densities of pure CdTe and HgTe, respectively, represented by

$$\rho_{CdTe} = \lambda_0 + \lambda_1 T, \quad (C2a)$$

and

$$\rho_{HgTe} = \phi_0 + \phi_1 T, \quad (C2b)$$

where the coefficients  $\lambda_i$  and  $\phi_i$  are determined by least-squares fits to the experimental data of Glazov, Chizhevskaya & Evgen'ev (1969) and Mokrovskii & Regel (1952), respectively.

The values of  $\lambda_i$  and  $\phi_i$  are

$$\lambda_0 = 5.820 \text{ g cm}^{-3}$$

$$\lambda_1 = -8.095 \times 10^{-5} \text{ g cm}^{-3} \text{ K}^{-1}$$

$$\phi_0 = 8.201 \text{ g cm}^{-3}$$

$$\phi_1 = -1.230 \times 10^{-4} \text{ g cm}^{-3} \text{ K}^{-1}.$$

The viscosity is represented over the entire range by

$$\nu = 1 \times 10^{-2} \exp(\Phi_0 + \Phi_1/T) \text{ cm}^2/\text{sec}, \quad (C3)$$

where the coefficients  $\Phi_0 = -3.401$  and  $\Phi_1 = 3445$  K are computed by least-squares fit to the experimental data of Glazov, Chizhevskaya & Glagoleva (1969) for pure CdTe. Due to the lack



of experimental viscosity data for HgTe, we use (C3) for the viscosity of  $\text{Hg}_{1-x}\text{Cd}_x\text{Te}$ , independent of composition.

The thermal diffusivity of liquid and solid  $\text{Hg}_{1-x}\text{Cd}_x\text{Te}$  are approximated by functions of the form

$$\kappa_L = (\omega_0 + \omega_1 C^{1/2} + \omega_2 C) \ln(T/K) - (\Omega_0 + \Omega_1 C^{1/2} + \Omega_2 C), \quad (\text{C4a})$$

$$\kappa_S = \sum_{j=0}^2 T^j (S_{0j} + S_{1j} C^{1/2} + S_{2j} C) \quad (\text{C4b})$$

where the coefficients

$\omega_0 = 0.104$	$\text{cm}^2\text{sec}^{-1}$	$\omega_1 = -0.146$	$\text{cm}^2\text{sec}^{-1}$
$\omega_2 = 0.118$	$\text{cm}^2\text{sec}^{-1}$	$\Omega_0 = 0.668$	$\text{cm}^2\text{sec}^{-1}$
$\Omega_1 = -0.941$	$\text{cm}^2\text{sec}^{-1}$	$\Omega_2 = 0.783$	$\text{cm}^2\text{sec}^{-1}$
$S_{00} = -5.945 \times 10^{-3}$	$\text{cm}^2\text{sec}^{-1}$	$S_{10} = 1.698 \times 10^{-2}$	$\text{cm}^2\text{sec}^{-1}$
$S_{20} = -0.114$	$\text{cm}^2\text{sec}^{-1}$	$S_{01} = 7.148 \times 10^{-5}$	$\text{cm}^2\text{sec}^{-1}\text{K}^{-1}$
$S_{11} = 1.646 \times 10^{-4}$	$\text{cm}^2\text{sec}^{-1}\text{K}^{-1}$	$S_{21} = 4.475 \times 10^{-4}$	$\text{cm}^2\text{sec}^{-1}\text{K}^{-1}$
$S_{02} = -7.829 \times 10^{-8}$	$\text{cm}^2\text{sec}^{-1}\text{K}^{-2}$	$S_{12} = 1.969 \times 10^{-7}$	$\text{cm}^2\text{sec}^{-1}\text{K}^{-2}$
$S_{22} = -4.120 \times 10^{-7}$	$\text{cm}^2\text{sec}^{-1}\text{K}^{-2}$		

are determined by least-squares fit to the experimental data of Holland & Taylor (1983).

The specific heat of liquid  $\text{Hg}_{1-x}\text{Cd}_x\text{Te}$  is represented by

$$c_{p,L}(T,C) = \sum_{l=0}^2 \sum_{j=0}^{2-l} q_{lj} C^j (T-943 \text{ K})^l. \quad (\text{C5})$$

The coefficients  $q_{ij}$  are found by least-squares fit to the calculated specific heat of Su (1986).

The values are

$q_{00} = 65.08$	$\text{J K}^{-1} \text{mol}^{-1}$	$q_{01} = -0.101$	$\text{J K}^{-2} \text{mol}^{-1}$
$q_{02} = 3.961 \times 10^{-4}$	$\text{J K}^{-3} \text{mol}^{-1}$	$q_{10} = 1.648$	$\text{J K}^{-1} \text{mol}^{-1}$
$q_{11} = 7.004 \times 10^{-3}$	$\text{J K}^{-2} \text{mol}^{-1}$	$q_{20} = -5.044 \times 10^{-3}$	$\text{J K}^{-1} \text{mol}^{-1}$

where we have used the relation 1 mol = 2 g-atom for the pseudobinary system  $\text{Hg}_{1-x}\text{Cd}_x\text{Te}$  to convert Su's data (in  $\text{cal K}^{-1} \text{g-atom}^{-1}$ ) to  $\text{J K}^{-1} \text{mol}^{-1}$ .

The specific heat of solid  $\text{Hg}_{1-x}\text{Cd}_x\text{Te}$  is taken as

$$C_{p,S} = C_{p,S,\text{HgTe}} (1-C) + C_{p,S,\text{CdTe}} C, \quad (\text{C6})$$

where the temperature-dependence of the specific heats of pure HgTe and CdTe is found from Mills (1974) to be

$$C_{p,S,\text{HgTe}} = [52.09 + 9.08 \times 10^{-3} (T/K)] \text{ J K}^{-1} \text{mol}^{-1} \quad (\text{C7a})$$

and

$$C_{p,S,\text{CdTe}} = [40.0 + 3.3 \times 10^{-2} (T/K)] \text{ J K}^{-1} \text{mol}^{-1}. \quad (\text{C7b})$$

The latent heat of fusion is approximated by

$$L(C) = (1-C)L_{\text{HgTe}} + CL_{\text{CdTe}}, \quad (\text{C8})$$

where data for the pure components are given by Mills (1974) as  $L_{\text{HgTe}} = 3.6 \times 10^4 \text{ J mol}^{-1}$  and  $L_{\text{CdTe}} = 4.48 \times 10^4 \text{ J mol}^{-1}$ . The interfacial energy is estimated by comparing  $\text{Hg}_{1-x}\text{Cd}_x\text{Te}$  and InSb (Seidensticker & Hamilton (1963) compared Ge and InSb to estimate the interfacial energy of InSb)

$$\sigma_{\text{Hg}_{1-x}\text{Cd}_x\text{Te}} = \sigma_{\text{InSb}} \left( \frac{L}{a_0^2} \right)_{\text{Hg}_{1-x}\text{Cd}_x\text{Te}} \left( \frac{a_0^2}{L} \right)_{\text{InSb}}, \quad (\text{C9})$$

where the latent heat of fusion per unit volume for  $\text{Hg}_{1-x}\text{Cd}_x\text{Te}$  is taken to vary linearly with solute mole fraction (see (C8)),  $a_0 = 6.4797 \text{ \AA}$  for InSb, and  $a_0 = 6.465 \text{ \AA}$  is used for  $\text{Hg}_{1-x}\text{Cd}_x\text{Te}$  independent of composition (Glazov, Chizhevskaya & Glagoleva 1969). Here the surface tension is taken as  $\sigma_{\text{InSb}} = 8.5 \times 10^{-6} \text{ J cm}^{-2}$ , and the latent heat of fusion per unit volume of InSb is  $L = 1.20 \times 10^3 \text{ J cm}^{-3}$ . The capillary coefficient is then computed from

$$\Psi = \sigma_{\text{Hg}_{1-x}\text{Cd}_x\text{Te}} \frac{T_{\text{liq}}}{L}, \quad (\text{C10})$$

where  $T_{\text{liq}}$  is the liquidus temperature for a given bulk mole fraction of CdTe in the liquid.

The liquidus and solidus temperatures

$$T_{\text{liq}} = (943 + 681 C - 372 C^2) \text{ K} \quad (\text{C11a})$$

and

$$T_{\text{sol}} = (943 + 202 C - 150 C^2 + 324 C^3) \text{ K}, \quad (\text{C11b})$$

liquidus slope

$$m_L = (681 - 745 C) \text{ K}, \quad (\text{C12})$$

and segregation coefficient

$$k = C (0.30 - 2.24 \times 10^{-3} \text{ K}^{-1} T_{\text{sol}} + 2.67 \times 10^{-6} \text{ K}^{-2} T_{\text{sol}}^2)^{-1} \quad \text{for } C > 0.1, \quad (\text{C13a})$$

$$k = 3.74 \quad \text{for } C < 0.1, \quad (\text{C13b})$$

as functions of CdTe mole fraction were determined by least-squares fits to the experimental data of Szofran & Lehoczky (1981).

Finally, the solute diffusion coefficient is taken as  $D_L = 5.5 \times 10^{-5} \text{ cm}^2/\text{sec}$ , the value most commonly used in the literature (see e.g., Kim & Brown 1989).

## Appendix D

Our model of flow in the mushy zone is based on the observation that the primary dendrites formed during dendritic solidification of binary alloys are columnar and oriented parallel to the nominal solidification direction. We treat the dendritic region, saturated by interdendritic fluid to be a porous medium the permeability of which is taken to be orthotropic with horizontal isotropy. The functional dependence of the components  $K_h$  and  $K_v$  of the permeability is determined from the calculated drag coefficients of Sangani & Acrivos (1982a) and Drummond & Tahir (1984) for flows normal and parallel to the axes of cylinders in hexagonal and triangular arrays, respectively. The asymptotic solutions for concentrated and dilute arrays (solid curves in figure D1)

$$\frac{K_h}{\lambda^2} = \frac{1-\phi}{4\pi} (\ln \phi^{-1/2} - 0.745 + \phi - 0.25 \phi^2) \quad \text{for } \phi < 0.3, \quad (D1)$$

$$\frac{K_h}{\lambda^2} = \frac{(1-\phi)4\sqrt{2}}{27\pi} \left[ 1 - \left( \frac{\phi}{\phi_{\max}} \right)^{1/2} \right]^{5/2} \quad \text{for } \phi > 0.7, \quad (D2)$$

are derived by Sangani & Acrivos (1982a), where  $\phi = 1 - \phi$  is the solid volume fraction,  $\phi_{\max}$  is the maximum value of the solid volume fraction when the cylinders touch, and  $\lambda$  is the primary dendrite arm spacing. The open circles are permeability values calculated by Sangani & Acrivos (1982a) for flow through a hexagonal array of cylinders, and match the asymptotes (D1) and (D2) for sufficiently large and small  $\phi$ . Hence, for  $0.3 < \phi < 0.7$ , we use a functional form

$$\frac{K_h}{\lambda^2} = \frac{1-\phi}{4\pi} (\ln \phi^{-1/2} - b + \phi - 0.25 \phi^2) \quad \text{for } \phi < 0.3, \quad (D3)$$

similar to (D1), and determine  $b = 0.7508$  by least-squares fit to the calculated drag coefficients of Sangani & Acrivos (1982a). Our fit is shown for  $0.25 < \phi < 0.725$  by the

dashed curve in figure D1. The dotted curve of figure D1 shows the permeability calculated by Sangani & Acrivos (1982b) for simple cubic arrays of spheres.

For the normal component of permeability, we use the results of Drummond & Tahir (1984) for flows parallel to the axes of cylinders in triangular arrays

$$\frac{K_v}{\lambda^2} = \frac{(1-\phi)^2 \sqrt{2}}{16\pi} \left( -\ln \phi - 1.4975 + 2\phi - 0.5\phi^2 - 0.002514\phi^6 \right) \quad \text{for } \phi < 0.7, \quad (D4)$$

$$\frac{K_v}{\lambda^2} = \frac{(1-\phi)^2}{10} \left\{ 1 + 1.5 \left[ \left( \frac{2\pi}{\phi 3\sqrt{3}} \right)^{1/2} - 1 \right] + \dots \right\} \quad \text{for } \phi > 0.7. \quad (D5)$$

The primary dendrite arm spacing  $\lambda$  for Pb-Sn systems was determined by Mason *et al.* (1982) using experimental data over a wide range of temperature gradient  $G_L$  and solidification rate  $V_I$  by the relationship

$$\lambda = A G_L^{-B}, \quad (D6)$$

where the coefficients A and B given by Mason *et al.* (in their table 2) are functions of solidification rate. In our calculations, we have determined A and B by interpolation.

## References

- Alexander, J.I.D., Ouazzani, J. & Rosenberger, F. 1989 Analysis of the low gravity tolerance of Bridgman-Stockbarger crystal growth. I. Steady and impulse accelerations. *J. Crystal Growth*, **97**, 285-302.
- Alexander, J.I.D., Wollkind, D.J. & Sekerka, R.F. 1986 The effect of latent heat on weakly non-linear morphological stability. *J. Crystal Growth*, **79**, 849-865.
- Antar, B.N. 1987 Penetrative double-diffusive convection. *Phys. Fluids*, **30**, 322-330.
- Antar, B.N. 1988 Penetrative double diffusive convection: effects of the Lewis and Prandtl numbers. *Int. J. Heat Mass Transfer*, **31**, 895-898.
- Antar, B.N. 1991 Convective instabilities in the melt for solidifying mercury cadmium telluride. *J. Crystal Growth*, **113**, 92-102.
- Antoranz, J.C. & Velarde, M.G. 1979 Thermal diffusion and convective stability: The role of uniform rotation of the container. *Phys. Fluids*, **22**, 1038-1043.
- Antoranz, J.C. & Velarde, M.G. 1978 Soret-driven convective instability with rotation. *Phys. Lett. A*, **65**, 377-379.
- Apanovich, Yu.V. & Ljumkis, E.D. 1991 The numerical simulation of heat and mass transfer during growth of a binary system by the travelling heater method. *J. Crystal Growth*, **110**, 839-854.
- Baines, P.G. & Gill, A.E. 1969 On thermohaline convection with linear gradients. *J. Fluid Mech.* **37**, 289-306.
- Bhattacharjee, J.K. 1988a Convection in rotating binary mixtures. I. Thresholds. *Phys. Fluids*, **31**, 2456-2461.
- Bhattacharjee, J.K. 1988b Convection in rotating binary mixtures. II. Küppers-Lortz instability. *Phys. Fluids*, **31**, 2462-2466.
- Bhattacharjee, J.K. 1988c Preferred patterns in convection in rotating binary mixtures. *Phys. Rev. A*, **37**, 1368-1370.

- Bourret, E.D., Derby, J.J. & Brown, R.A. 1985 Dynamics of Bridgman-Stockbarger growth of non-dilute binary alloys. *J. Crystal Growth*, **71**, 587-596.
- Bühler, K. & Oertel, H. 1982 Thermal cellular convection in rotating rectangular boxes. *J. Fluid Mech.* **114**, 261-282.
- Capper, P. 1989 Bridgman growth of  $\text{Cd}_x\text{Hg}_{1-x}\text{Te}$  - A review. *Prog. Crystal Growth and Charact.* **19**, 259-293.
- Capper, P., Gosney, J.J., Jones, C.L. & Kenworthy, I. 1986 Bridgman growth of  $\text{Cd}_x\text{Hg}_{1-x}\text{Te}$  using ACRT. *J. Electron. Mater.* **15**, 371-376.
- Chandra, D. & Holland, L.R. 1983 Density of liquid  $\text{Hg}_{1-x}\text{Cd}_x\text{Te}$ . *J. Vac. Sci. Tech. A*, **1**, 1620-1624.
- Chandrasekhar, S. 1953 The instability of a layer of fluid heated below and subject to Coriolis forces. *Proc. Roy. Soc. London A*, **217**, 306-327.
- Chandrasekhar, S. 1961 *Hydrodynamic and Hydromagnetic Stability*. Clarendon, Oxford, pp. 76-85.
- Chandrasekhar, S. & Elbert, D.D. 1955 The instability of a layer of fluid heated below and subject to Coriolis forces. II. *Proc. Roy. Soc. London A*, **231**, 198-210.
- Chen, C.F. & Chen, F. 1991 Experimental study of directional solidification of aqueous ammonium chloride solution. *J. Fluid Mech.* **227**, 567-586.
- Chen, F. & Chen, C.F. 1988 Onset of finger convection in a horizontal porous layer underlying a fluid layer. *J. Heat Transfer*, **110**, 403-409.
- Copley, S.M. 1976 private communication to A.J. Pearlstein.
- Copley, S.M., Giamei, A.F., Johnson, S.M. & Hornbecker, M.F. 1970 The origin of freckles in unidirectionally solidified castings. *Metall. Trans.* **1**, 2193-2204.
- Coriell, S.R., Cordes, M.R., Boettinger, W.J. & Sekerka, R.F. 1980 Convective and interfacial instabilities during unidirectional solidification of a binary alloy. *J. Crystal Growth*, **49**, 13-28.

- Davis, S.H. 1990 Hydrodynamic interactions in directional solidification. *J. Fluid Mech.* **212**, 241-262.
- Drummond, J.E. & Tahir, M.I. 1984 Laminar viscous flow through regular arrays of parallel solid cylinders. *Int. J. Multiphase Flow*, **10**, 515-540.
- Flemings, M.C. 1974 *Solidification Processing*. McGraw-Hill, New York.
- Foster, T.D. 1972 An analysis of the cabbeling instability in sea water. *J. Phys. Oceanogr.* **2**, 294-301.
- Fowler, A.C. 1985 The formation of freckles in binary alloys. *IMA J. Appl. Maths.* **35**, 159-174.
- Fultz, D. & Nakagawa, Y. 1955 Experiments on over-stable thermal convection in mercury. *Proc. Roy. Soc. London A*, **231**, 211-225.
- Galazka, R.R., Warminski, T., Bak, J., Auleytner, J., Dietl, T., Okhotin, A.S., Borovikova, R.P. & Zubritskij, I.A. 1981 Directional crystallization of CdHgTe in microgravity conditions. *J. Crystal Growth*, **53**, 397-408.
- Ganesan, S. & Poirier, D.R. 1990 Conservation of mass and momentum for the flow of interdendritic liquid during solidification. *Metall. Trans. B*, **21**, 173-181.
- Gebhart, B. & Mollendorf, J.C. 1978 Buoyancy-induced flows in water under conditions in which density extrema may arise. *J. Fluid Mech.* **89**, 673-707.
- Giamei, A.F. & Kear, B.H. 1970 On the nature of freckles in nickel base superalloys. *Metall. Trans.* **1**, 2185-2192.
- Glazov, V.M., Chizhevskaya, S.N. & Evgen'ev, S.B. 1969 Thermal expansion of substances having a diamondlike structure and the volume changes accompanying their melting. *Russ. J. Phys. Chem.* **43**, 201-205.
- Glazov, V.M., Chizhevskaya, S.N. & Glagoleva, N.N. 1969 *Liquid Semiconductors*. Plenum, New York.
- Glicksman, M.E., Coriell, S.R. & McFadden, G.B. 1986 Interaction of flows with the crystal-melt interface. *Ann. Rev. Fluid Mech.* **18**, 307-335.



- Goroff, I.R. 1960 An experiment on heat transfer by overstable and ordinary convection. *Proc. Roy. Soc. London A*, **254**, 537-541.
- Greenspan, H.P. 1968 *The Theory of Rotating Fluids*. Cambridge University Press, Cambridge.
- Heinrich, J.C., Felicelli, S., Nandapurkar, P. & Poirier, D.R. 1989a Thermosolutal convection during dendritic solidification of alloys: Part II. Nonlinear convection. *Metall. Trans. B*, **20**, 883-891.
- Heinrich, J.C., Felicelli, S., Nandapurkar, P. & Poirier, D.R. 1989b Thermosolutal convection during dendritic solidification. AIAA Paper 89-0626. 27th AIAA Aerospace Science Meeting, Reno, Nev., Jan. 8-12.
- Holland, L.R. & Taylor, R.E. 1983 Measured thermal diffusivity of  $\text{Hg}_{1-x}\text{Cd}_x\text{Te}$  solids and melts. *J. Vac. Sci. Tech. A*, **1**, 1615-1619.
- Homsy, G.M. & Hudson, J.L. 1969 Centrifugally driven thermal convection in a rotating cylinder. *J. Fluid Mech.* **35**, 33-52.
- Homsy, G.M. & Hudson, J.L. 1971a The asymptotic stability of a bounded rotating fluid heated from below: conductive basic state. *J. Fluid Mech.* **45**, 353-373.
- Homsy, G.M. & Hudson, J.L. 1971b Centrifugal convection and its effect on the asymptotic stability of a bounded rotating fluid heated from below. *J. Fluid Mech.*, **48**, 605-624.
- Homsy, G.M. & Hudson, J.L. 1972 Stability of a radially bounded rotating fluid heated from below. *Appl. Sci. Res.* **26**, 53-67.
- Huppert, H.E. 1990 The fluid mechanics of solidification. *J. Fluid Mech.*, **212**, 209-240.
- Huppert, H.E. & Worster, M.G. 1985 Dynamic solidification of a binary melt. *Nature*, **314**, 703-707.
- Keller, H.B. 1976 *Numerical Solution of Two Point Boundary Value Problems*. SIAM, Philadelphia, pp. 49-58.
- Kim, D.H. & Brown, R.A. 1989 Models for convection and segregation in the growth of  $\text{HgCdTe}$  by the vertical Bridgman method. *J. Crystal Growth*, **96**, 609-627.

- Kou, S. 1978 *Macrosegregation in Electroslag Remelted Ingots*. Ph.D. Thesis, Massachusetts Institute of Technology.
- Kou, S., Poirier, D.R., & Flemings, M.C. 1978 Macrosegregation in rotated remelted ingots. *Metall. Trans. B*, **9**, 711-719.
- Lucas, L.-D. & Urbain, G. 1962 Densité du silicium, du germanium, de l'antimoine et du bismuth à l'état liquide. *Comptes Rend. Acad. Sci.* **255**, 2414-2416.
- Lucas, L.-D. 1964 Volume spécifique de métaux et alliages liquides à hautes températures. *Mém. Scient. Rev. Métallurgie*. **61**, 1-24.
- Maples, A.L. & Poirier, D.R. 1984 Convection in the two-phase zone of solidifying alloys. *Metall. Trans. B*, **15**, 163-172.
- Mason, J.T., Verhoeven, J.D. & Trivedi, R. 1982 Primary dendrite spacing. I. Experimental studies. *J. Crystal Growth*, **59**, 516-524.
- Masuda, A. 1978 Double diffusive convection in a rotating system *J. Oceanogr. Soc. Japan*, **34**, 8-16.
- Merker, G.P., Waas, P. & Grigull, U. 1979 Onset of convection in a horizontal water layer with maximum density effects. *Int. J. Heat Mass Transfer*, **22**, 505-515.
- Micklethwaite, W.F.H. 1981 The crystal growth of cadmium mercury telluride. In Mercury Cadmium Telluride, Volume 18 in *Semiconductors and Semimetals*. Academic Press, New York, pp. 47-119.
- Mills, K.C. 1974 *Thermodynamic Data for Inorganic Sulphides, Selenides, and Tellurides*. Butterworths, London.
- Mokrovskii, N.P. & Regel, A.R. 1952 Correlation between variations of density and electronic conductivity during the melting of substances with diamond or zinc blende structure. *Zh. Tekh. Fiz.* **22**, 1281-1289.
- Müller, G. 1988 Convection and inhomogeneities in crystal growth from the melt. In *Crystals*, vol. 12, Springer-Verlag, Berlin.

- Müller, G. 1990 A comparative study of crystal growth phenomena under reduced and enhanced gravity. *J. Crystal Growth*, **99**, 1242-1257.
- Mullins, W.W. & Sekerka, R. F. 1964 Stability of a planar interface during solidification of a dilute binary alloy. *J. Appl. Phys.* **35**, 444-451.
- Nakagawa, Y. & Frenzen, P. 1955 A theoretical and experimental study of cellular convection in rotating fluids. *Tellus*, **7**, 1-21.
- Nandapurkar, P., Poirier, D.R., Heinrich, J.C. & Felicelli, S. 1989 Thermosolutal convection during dendritic solidification of alloys: Part 1. Linear stability analysis. *Metall. Trans. B*, **20**, 711-721.
- Niiler, P.P. & Bisshopp, F.E. 1965 On the influence of Coriolis force on onset of thermal convection. *J. Fluid Mech.*, **22**, 753-761.
- Normand, C. & Azouni, A. 1992 Penetrative convection in an internally heated layer of water near the maximum density point. *Phys. Fluids A*, **4**, 243-253.
- Öztekin, A. & Pearlstein, A. J. 1992 Coriolis effects on the stability of plane-front solidification of dilute Pb-Sn binary alloys. *Metall. Trans. B*, **23**, 73-80.
- Pearlstein, A.J. 1981 Effect of rotation on the stability of a doubly diffusive fluid layer. *J. Fluid Mech.* **103**, 389-412.
- Pearlstein, A.J. & Oztekin A. 1989 Selection of convective planform orientation by boundary anisotropy. *J. Fluid Mech.* **207**, 267-294.
- Poirier, D.R., Flemings, M.C., Mehrabian, R. & Klein, H.J. 1981 Modelling macrosegregation in Electrosag Remelted Ingots, in *Advances in Metal Processing*, J.J. Burke, R. Mehrabian, and V. Weiss, eds., Plenum, New York, 1981, pp. 277-317.
- Polezhaev, V.I. 1984 Hydrodynamics, heat and mass transfer during crystal growth. In *Growth and Defect Structures, Crystals*, vol. 10, Springer-Verlag, Berlin.
- Qureshi, Z.H. & Gebhart, B. 1986 The stability of vertical thermal buoyancy induced flows in cold pure and saline water. *Int. J. Heat Mass Transfer*, **29**, 1383-1392.

- Riahi, N. 1983 Double diffusive convection in a rotating fluid. *J. Phys. Soc. Japan*, **52**, 2620-2621.
- Ridder, S.D., Kou, S. & Mehrabian, R. 1981 Effect of fluid flow on macrosegregation in axisymmetric ingots. *Metall. Trans. B*, **12**, 435-447.
- Sample, A.K. & Hellawell, A. 1984 The mechanisms of formation and prevention of channel segregation during alloy solidification. *Metall. Trans. A*, **15**, 2163-2173.
- Sangani, A.S. & Acrivos, A. 1982a Slow flow past periodic arrays of cylinders with application to heat transfer. *Int. J. Multiphase Flow*, **8**, 193-206.
- Sangani, A.S. & Acrivos, A. 1982b Slow flow through a periodic array of spheres. *Int. J. Multiphase Flow*, **8**, 343-360.
- Sarazin, J.R. & Hellawell, A. 1988 Channel formation in Pb-Sn, Pb-Sb, and Pb-Sn-Sb alloy ingots and comparison with the system  $\text{NH}_4\text{Cl-H}_2\text{O}$ . *Metall. Trans. A*, **19**, 1861-1871.
- Schmitt, R.W. & Lambert, R.B. 1979 The effects of rotation on salt fingers. *J. Fluid Mech.* **90**, 449-463.
- Schulz-DuBols, E.O. 1972 Accelerated crucible rotation: Hydrodynamics and stirring effect. *J. Crystal Growth*, **12**, 81-87.
- Seidensticker, R.G. & Hamilton, D. R. 1963 The dendritic growth of InSb. *J. Phys. Chem. Solids*, **24**, 1585-1591.
- Sekerka, R.F. & Coriell, S.R. 1987 Coupled morphological and convective instabilities in a microgravity environment. In *Proc. Sixth European Symp. on Material Sciences under Microgravity Conditions*, Bordeaux, December 2-5, ESA-SP-256, 3-11.
- Sengupta, S. & Gupta, A.S. 1971 Thermohaline convection with finite amplitude in a rotating fluid. *Z. Angew. Math. Phys.* **22**, 906-914.
- Stern, M.E. 1960 The "salt-fountain" and thermohaline convection. *Tellus*, **12**, 172-175.
- Su, C.-H. 1978 Heat capacity, enthalpy of mixing, and thermal conductivity of  $\text{Hg}_{1-x}\text{Cd}_x\text{Te}$  pseudobinary melts. *J. Crystal Growth*, **78**, 51-57.

- Szofran, F.R. & Lehoczy, S. L. 1981 The pseudobinary HgTe-CdTe phase diagram. *J. Electron. Mater.* **10**, 1131-1150.
- Trivedi, R. 1984 Interdendritic spacing: Part II. A comparison of theory and experiment. *Metall. Trans. A*, **15**, 977-982.
- Turner, J.S. 1973 *Buoyancy Effects in Fluids*. Cambridge University Press, Cambridge.
- Ungar, L.H., Bennett, M.J. & Brown, R.A. 1984 Cellular interface morphologies in directional solidification. III. The effects of heat transfer and solid diffusivity. *Phys. Rev. B*, **31**, 5923-5930.
- Ungar, L.H. & Brown, R.A. 1984 Cellular interface morphologies in directional solidification. The one-sided model. *Phys. Rev. B*, **29**, 1367-1380.
- Venugopalan, D. & Kirkaldy, J.S. 1984 Theory of cellular solidification of binary alloys with applications to succinonitrile-salol. *Acta. Metall.* **32**, 893-906.
- Veronis, G. 1959 Cellular convection with finite amplitude in a rotating fluid. *J. Fluid Mech.* **5**, 401-435.
- Veronis, G. 1963 Penetrative convection. *Astrophys. J.* **137**, 641-663.
- Veronis, G. 1966 Motions at subcritical values of the Rayleigh number in a rotating fluid. *J. Fluid Mech.* **24**, 545-554.
- Veronis, G. 1968 Large-amplitude Bénard convection in a rotating fluid. *J. Fluid Mech.* **31**, 113-139.
- Voorhees, P.W., Coriell, S.R., McFadden, G.B. & Sekerka, R.F. 1984 The effect of anisotropic crystal-melt surface tension on grain boundary groove morphology. *J. Crystal Growth*, **67**, 425-440.
- Walton, I.C. 1982 Double-diffusive convection with large variable gradients. *J. Fluid Mech.* **125**, 123-135.
- Weber, W., Neumann, G. & Müller, G. 1990 Stabilizing influence of the Coriolis force during melt growth on a centrifuge. *J. Crystal Growth*, **100**, 145-158.

- Wollkind, D.J. & Segel, L.A. 1970 A nonlinear stability analysis of the freezing of a dilute binary alloy. *Phil. Trans. Roy. Soc. London, A* **268**, 351-380.
- Worster, M.G. 1986 Solidification of an alloy from a cooled boundary. *J. Fluid Mech.* **167**, 481-501.
- Worster, M. G. 1991 Natural convection in a mushy layer. *J. Fluid Mech.* **224**, 335-359.
- Worster, M.G. 1992 Onset of compositional convection during solidification of a mushy layer from a binary alloy cooled from below. *J. Fluid Mech.*, to appear.
- Worthern, S., Mollo-Christensen, E. & Ostapoff, F. 1983 Effects of rotation and shear on doubly diffusive instability. *J. Fluid Mech.* **133**, 297-319.
- Young, G.W. & Davis, S. H. 1989 Morphological instabilities in directional solidification of a binary alloy: end effects. *SIAM J. Appl. Math.* **49**, 152-164.
- Zangrando, F & Bertram, L. A. 1985 The effect of variable stratification on linear doubly diffusive stability. *J. Fluid Mech.* **151**, 55-79.
- Zebib, A. 1987 Removal of spurious modes encountered in solving stability problems by spectral methods. *J. Comput. Phys.* **70**, 521-525.

## Tables

N	15	20	25	30
$a_c$	2.855	2.860	2.862	2.863
$c_{\infty}^*$	$3.6879 \times 10^{-2}$	$3.6893 \times 10^{-2}$	$3.6896 \times 10^{-2}$	$3.6898 \times 10^{-2}$

Table 1. Convergence test for  $Hg_{1-x}Cd_xTe$  for  $\Gamma = 1.64 \times 10^{-3}$  ( $G_L = 50$  K/cm) and  $\gamma = 2.64 \times 10^{-4}$  ( $V_1 = 1 \mu\text{sec}$ ),  $h = 10$ .  $a_c$  is the critical wavenumber, corresponding to the extremal points on the oscillatory convective neutral curve.

	N	15	20	25
$h = 10$	$a_c$	1.480	1.489	1.483
	$c_{\infty}^*$	$3.8525 \times 10^{-2}$	$3.8581 \times 10^{-2}$	$3.8601 \times 10^{-2}$
$h = 20$	$a_c$	1.403	1.479	1.481
	$c_{\infty}^*$	$3.7654 \times 10^{-2}$	$3.8575 \times 10^{-2}$	$3.8590 \times 10^{-2}$
$h = 30$	$a_c$	1.385	1.445	1.481
	$c_{\infty}^*$	$3.5901 \times 10^{-2}$	$3.8103 \times 10^{-2}$	$3.8604 \times 10^{-2}$

Table 2. Convergence test for  $Hg_{1-x}Cd_xTe$  for  $\Gamma = 1.64 \times 10^{-3}$  ( $G_L = 50$  K/cm) and  $\gamma = 3.96 \times 10^{-4}$  ( $V_1 = 1.5 \mu\text{sec}$ ).



	$V_I$	$h$	$N = 15$		$N = 20$		$N = 25$	
			$a_L$	$a_R$	$a_L$	$a_R$	$a_L$	$a_R$
$C_\infty = 0.2$	$75 \mu/\text{sec}$	$h = 10$	0.1852		0.1828		0.1816	
		$h = 20$	$a_R$	0.4024	0.4043		0.4052	
			$a_L$	0.1837	0.1812		0.1809	
			$a_R$	0.4003	0.4027		0.4043	
	$50 \mu/\text{sec}$	$h = 10$	$a_L$	$8.9357 \times 10^{-2}$	$8.6241 \times 10^{-2}$		$8.5782 \times 10^{-2}$	
		$h = 20$	$a_R$	0.8893	0.9164		0.9243	
$C_\infty = 0.1$	$65 \mu/\text{sec}$	$h = 10$	$a_L$	$8.7361 \times 10^{-2}$	$8.5877 \times 10^{-2}$		$8.5801 \times 10^{-2}$	
			$a_R$	0.8596	0.9065		0.9157	
		$h = 20$	$a_L$	0.2302	0.2253		0.2237	
			$a_R$	0.4539	0.4588		0.4612	
		$h = 10$	$a_L$	0.2114	0.2226		0.2231	
			$a_R$	0.4500	0.4558		0.4596	
	$50 \mu/\text{sec}$	$h = 10$	$a_L$	0.1213	0.1235		0.1247	
			$a_R$	0.8315	0.8408		0.8446	
		$h = 20$	$a_L$	0.1154	0.1216		0.1242	
			$a_R$	0.8043	0.8379		0.8420	

Table 3. Convergence test for dendritic solidification of PbSn for  $G_L = 50 \text{ K/cm}$ .  $a_L$  and  $a_R$  determine the lower (left) and upper (right) limits of the wavenumber range in which the one-dimensional dendritic solution is unstable.

## Figures

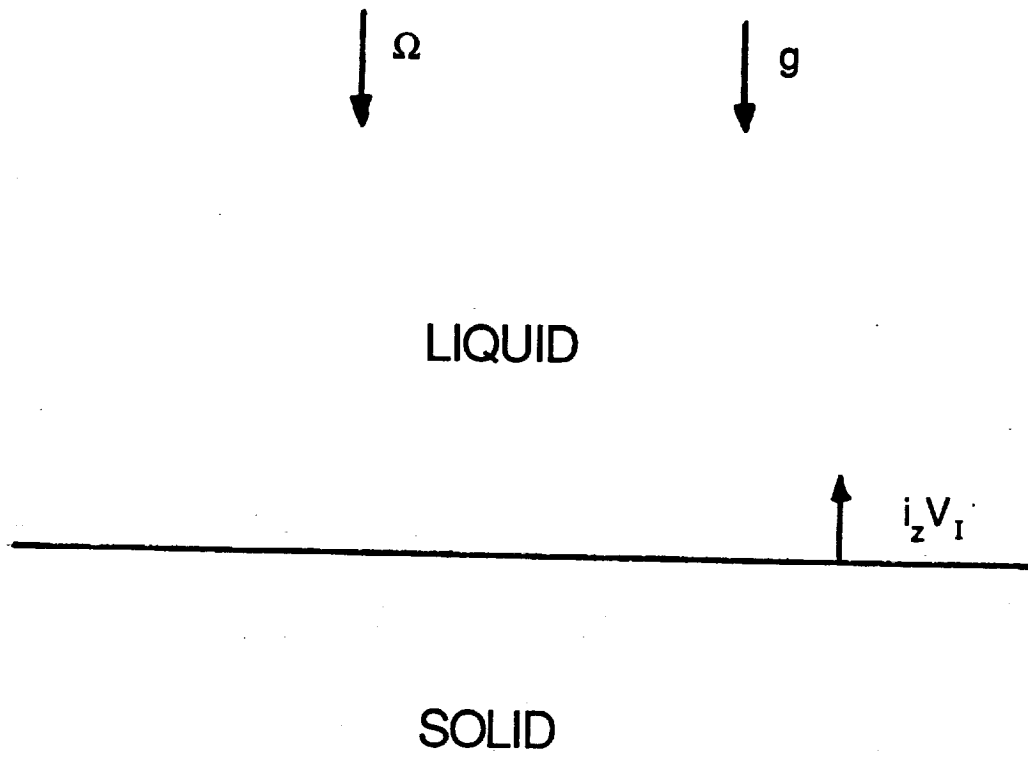


Figure 2.1. Schematic depiction of plane-front solidification

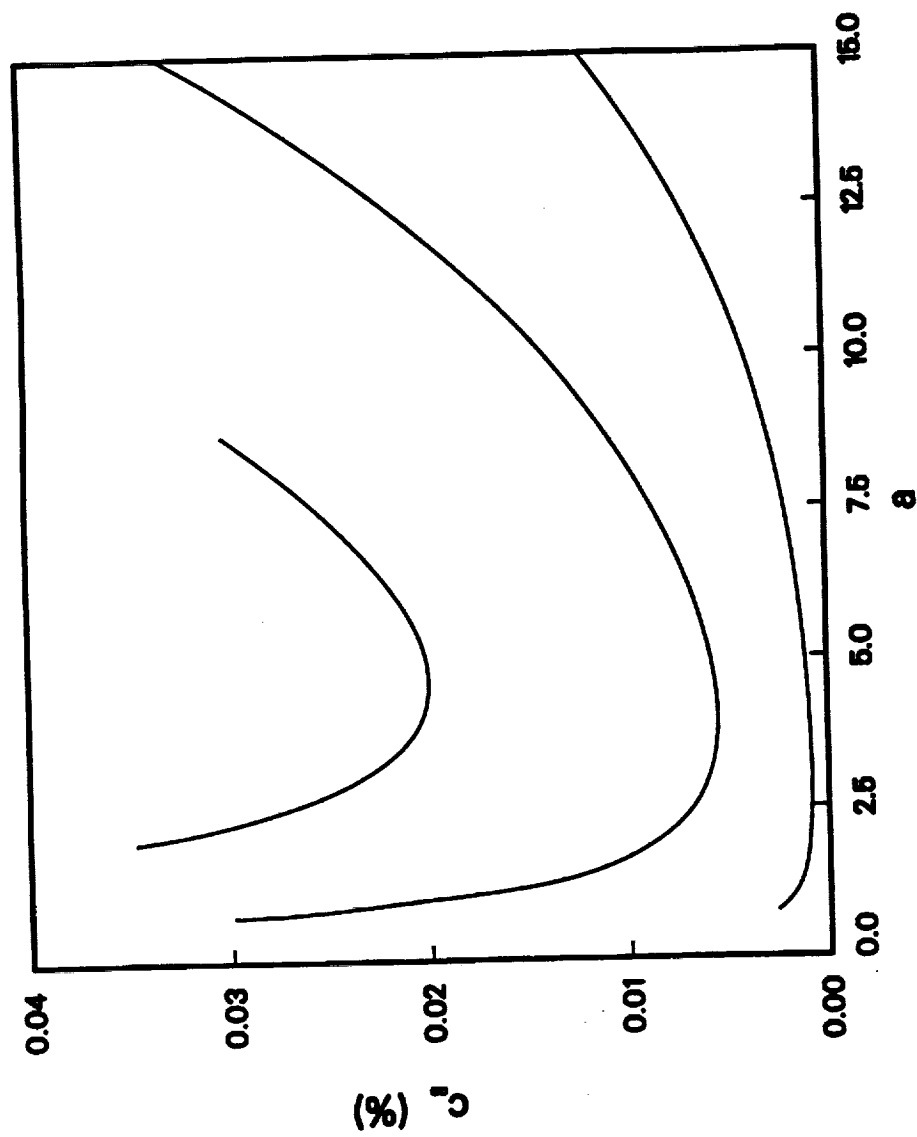


Figure 2.2a.  $C_0$ -a neutral curves for plane-front solidification of Pb-Sn with  $G_L = 200 \text{ K cm}^{-1}$  and  $\Omega_0 = 0 \text{ rpm}$  for  $V_I = 5 \mu \text{ sec}^{-1}$ .

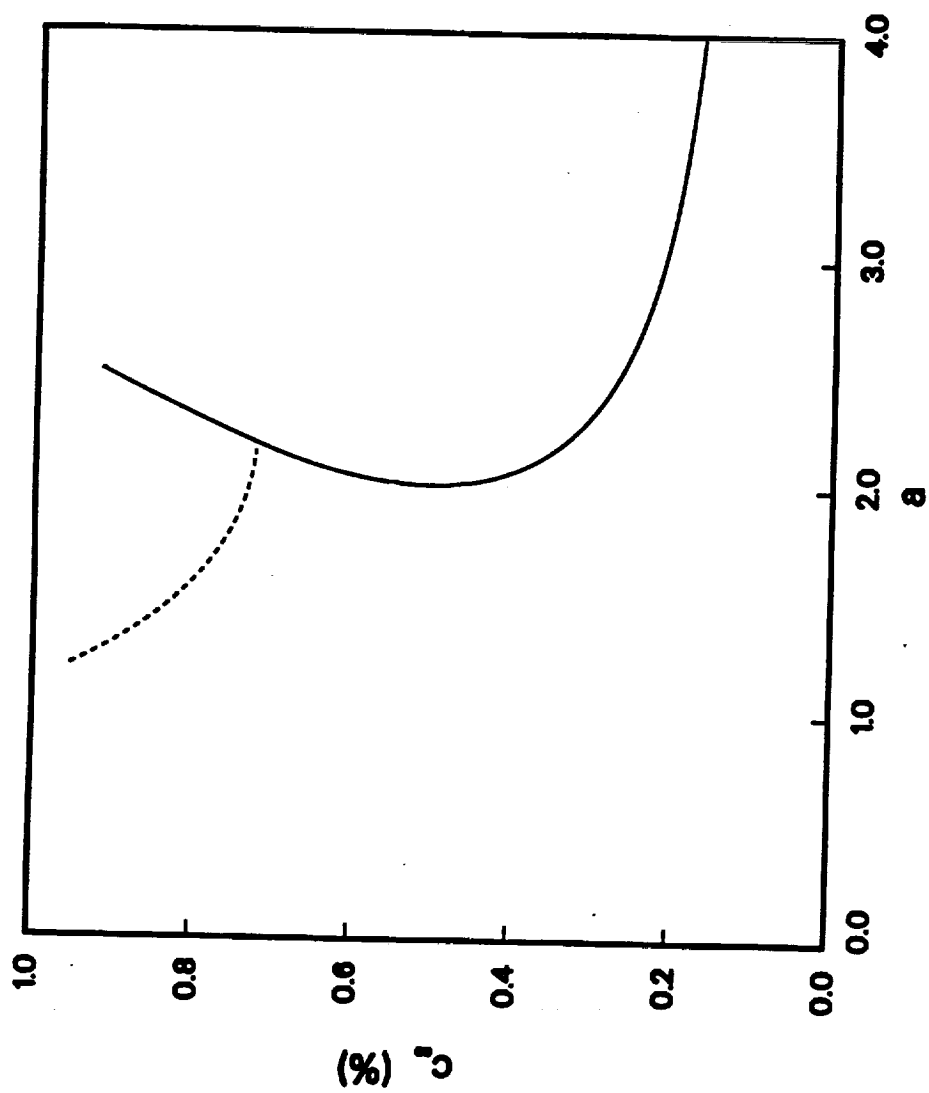


Figure 2.2b.  $C_{\infty}$ - $a$  neutral curves for plane-front solidification of Pb-Sn with  $G_L = 200 \text{ K cm}^{-1}$  and  $\Omega_0 = 0 \text{ rpm}$  for  $V_1 = 80 \mu \text{ sec}^{-1}$ .

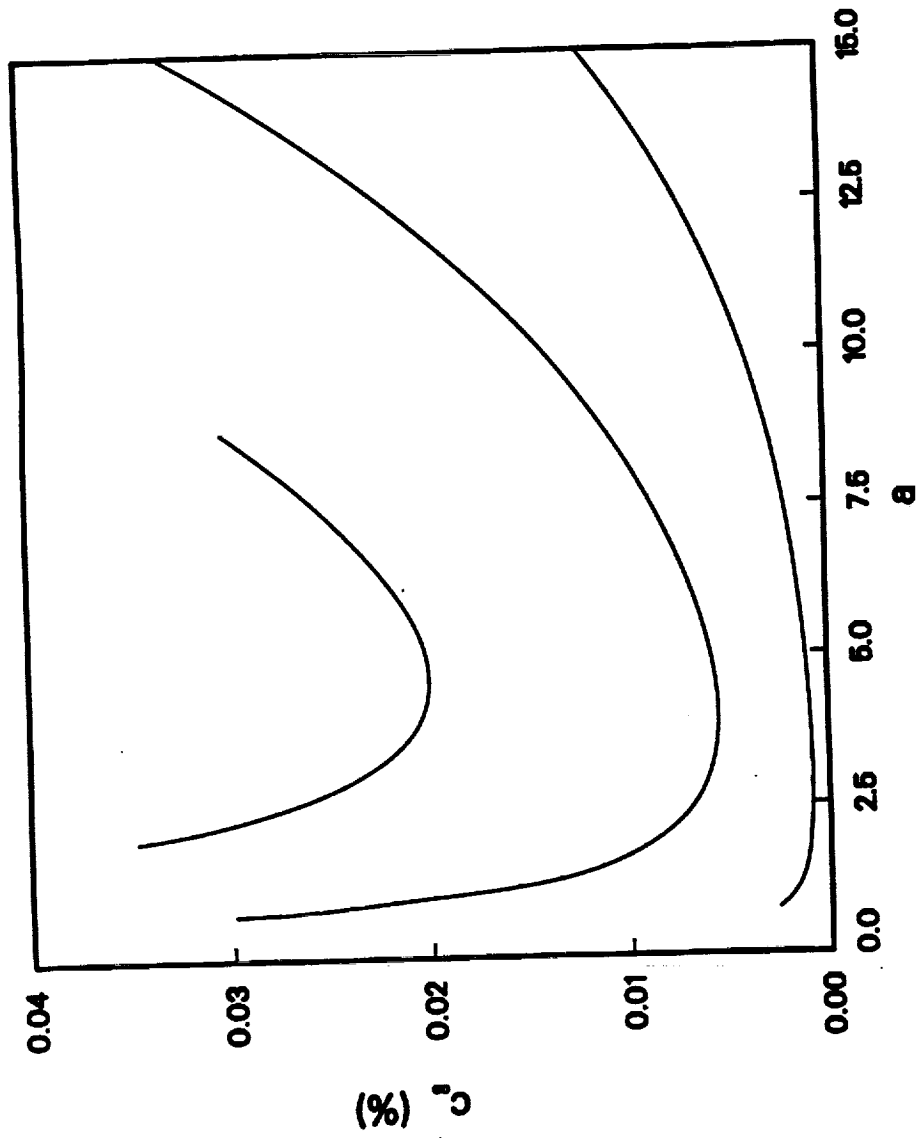


Figure 2.3a.  $C_{\infty}$ -a neutral curves for plane-front solidification of Pb-Sn with  $G_L = 200 \text{ K cm}^{-1}$  and  $\Omega_0 = 0 \text{ rpm}$  for  $V_1 = 5 \mu \text{ sec}^{-1}$ .

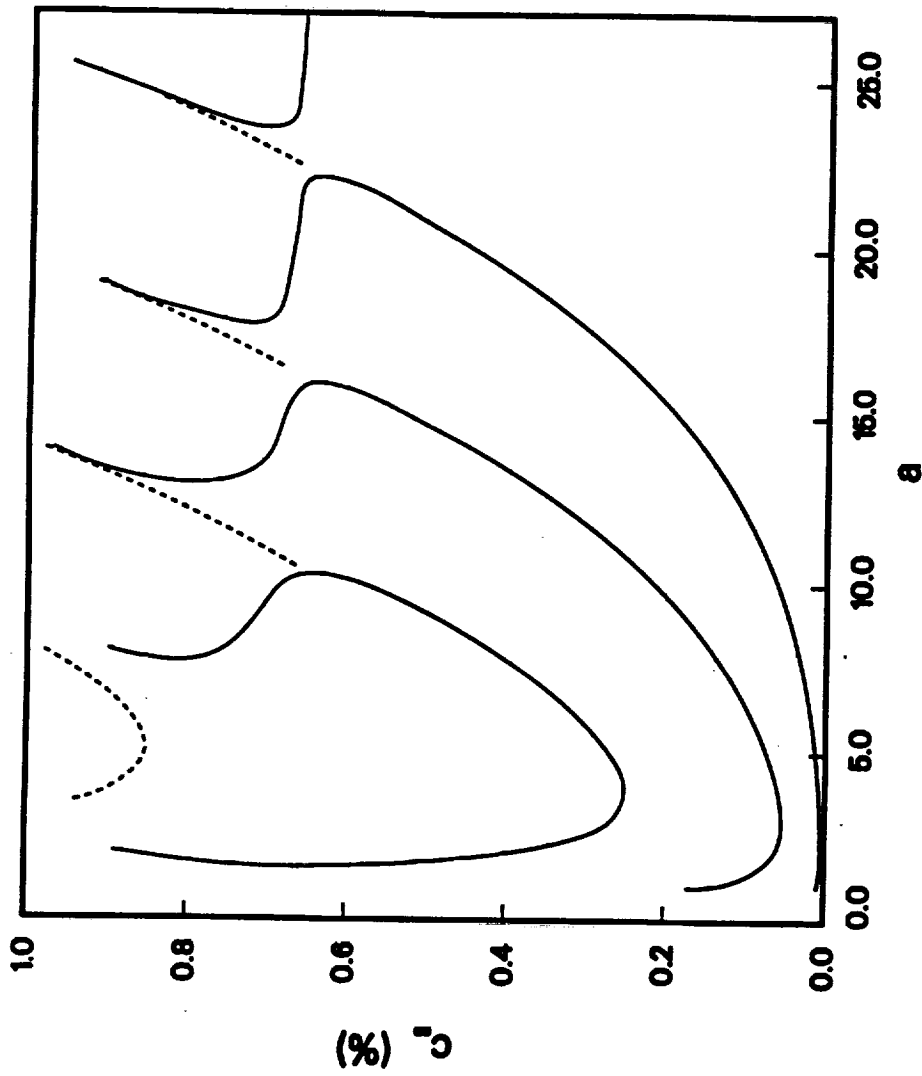


Figure 2.3b.  $C_a$ -a neutral curves for plane-front solidification of Pb-Sn with  $G_L = 200 \text{ K cm}^{-1}$  and  $\Omega_0 = 0 \text{ rpm}$  for  $V_1 = 12.5 \mu \text{ sec}^{-1}$ .

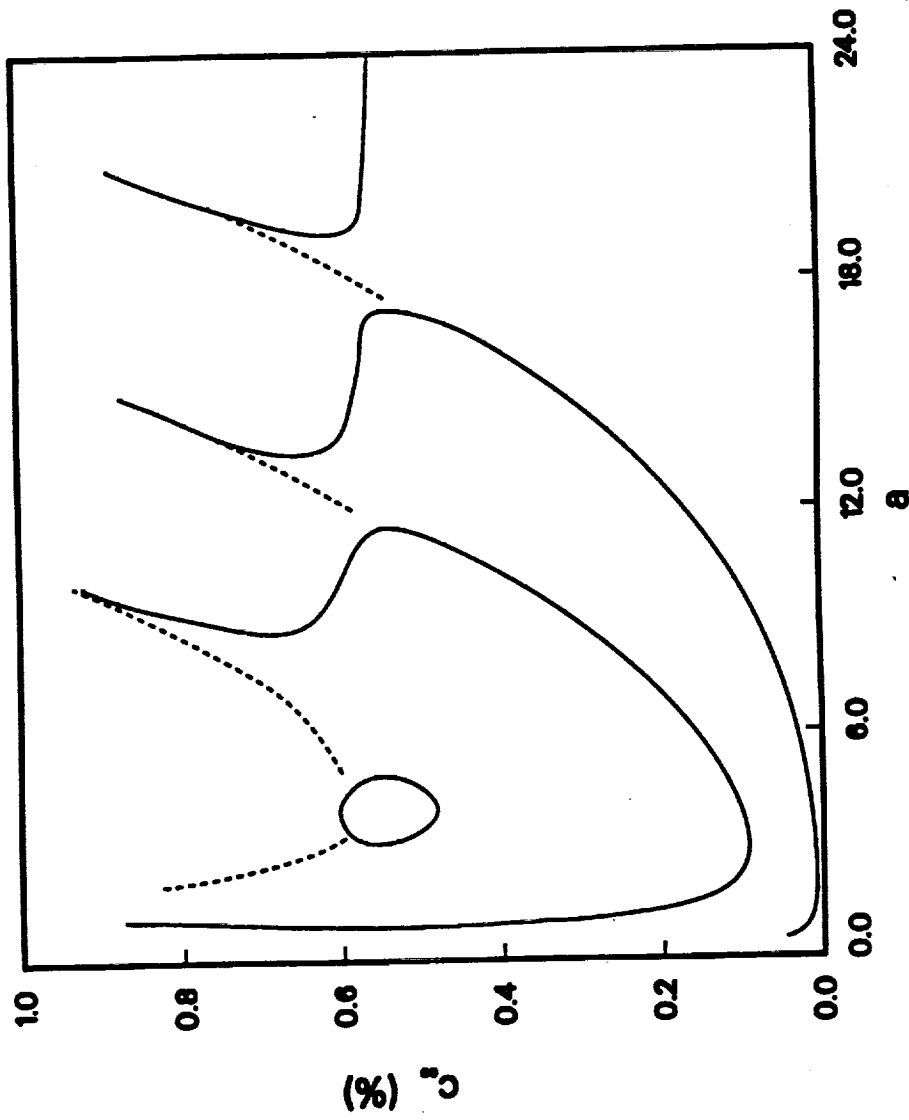


Figure 2.3c.  $C_{\infty}$ -a neutral curves for plane-front solidification of Pb-Sn with  $G_L = 200 \text{ K cm}^{-1}$  and  $\Omega_0 = 0 \text{ rpm}$  for  $V_1 = 15 \mu \text{ sec}^{-1}$ .



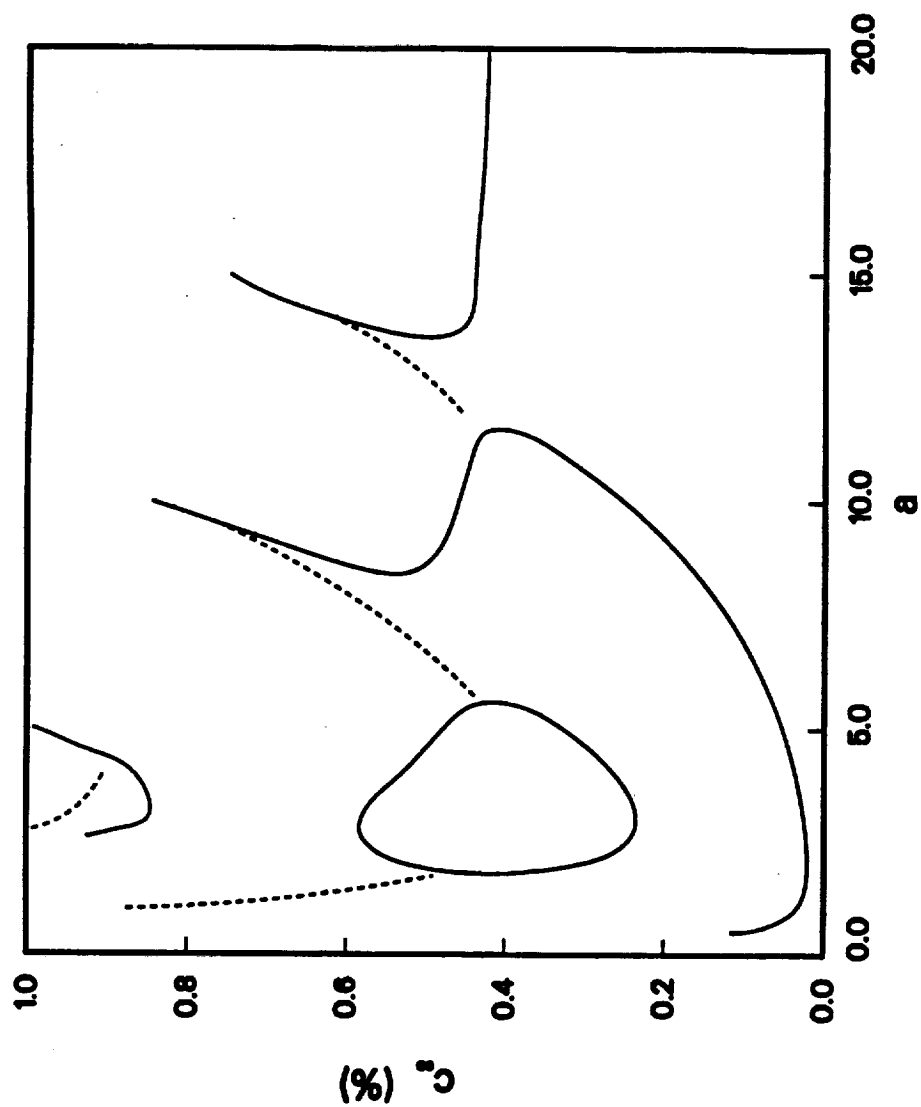


Figure 2.3d.  $C_{\infty}$ -a neutral curves for plane-front solidification of Pb-Sn with  $G_L = 200 \text{ K cm}^{-1}$  and  $\Omega_0 = 0 \text{ rpm}$  for  $V_1 = 20 \mu \text{ sec}^{-1}$ .

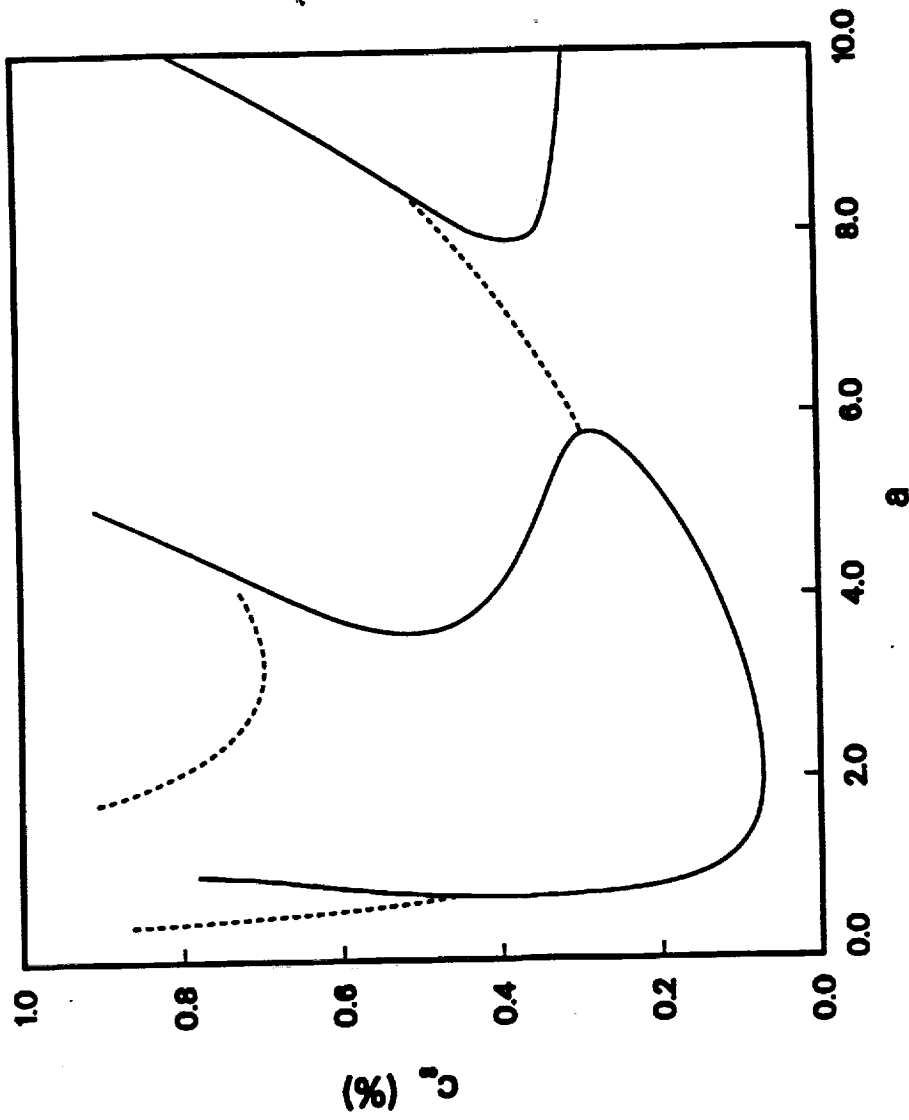


Figure 2.3e.  $C_0$ - $a$  neutral curves for plane-front solidification of Pb-Sn with  $G_L = 200 \text{ K cm}^{-1}$  and  $\Omega_0 = 0 \text{ rpm}$  for  $V_1 = 30 \mu \text{ sec}^{-1}$ .

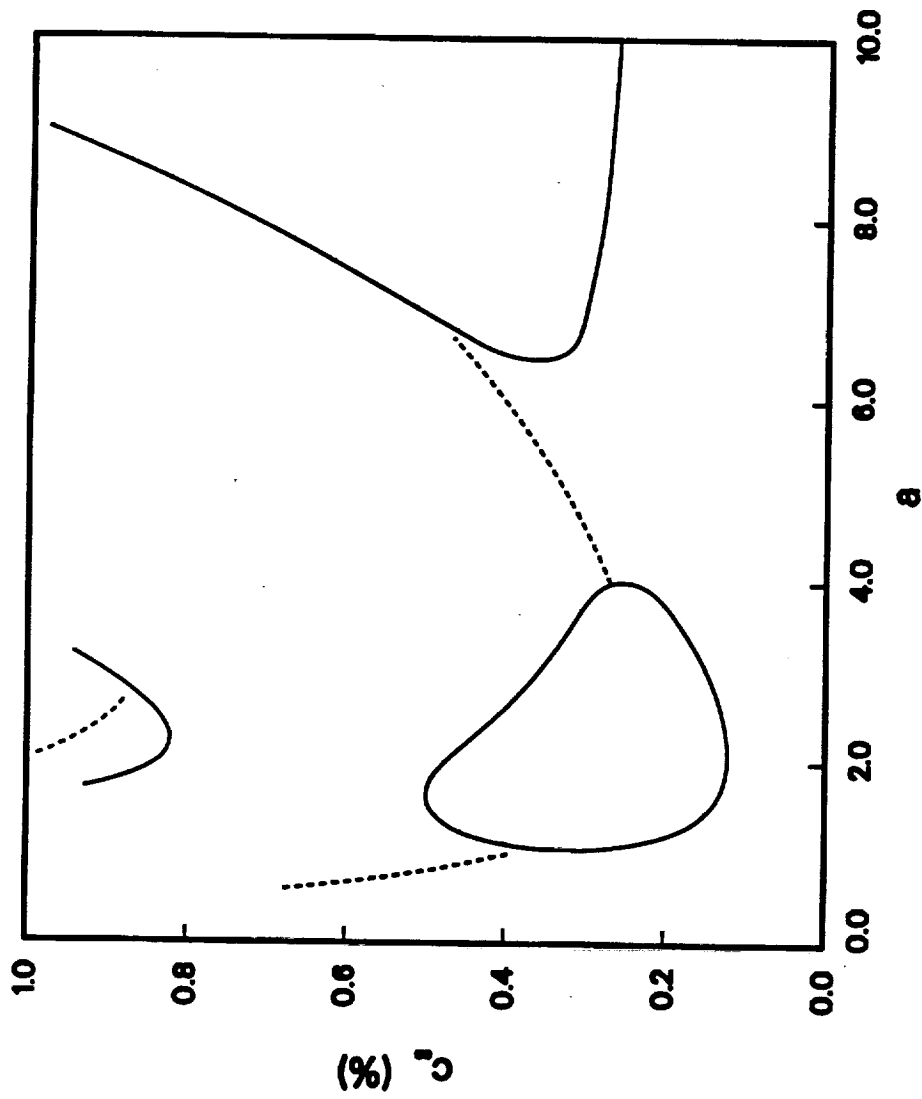


Figure 2.3f.  $C_{\infty}$ -a neutral curves for plane-front solidification of Pb-Sn with  $G_L = 200 \text{ K cm}^{-1}$  and  $\Omega_0 = 0 \text{ rpm}$  for  $V_f = 35 \mu \text{ sec}^{-1}$ .

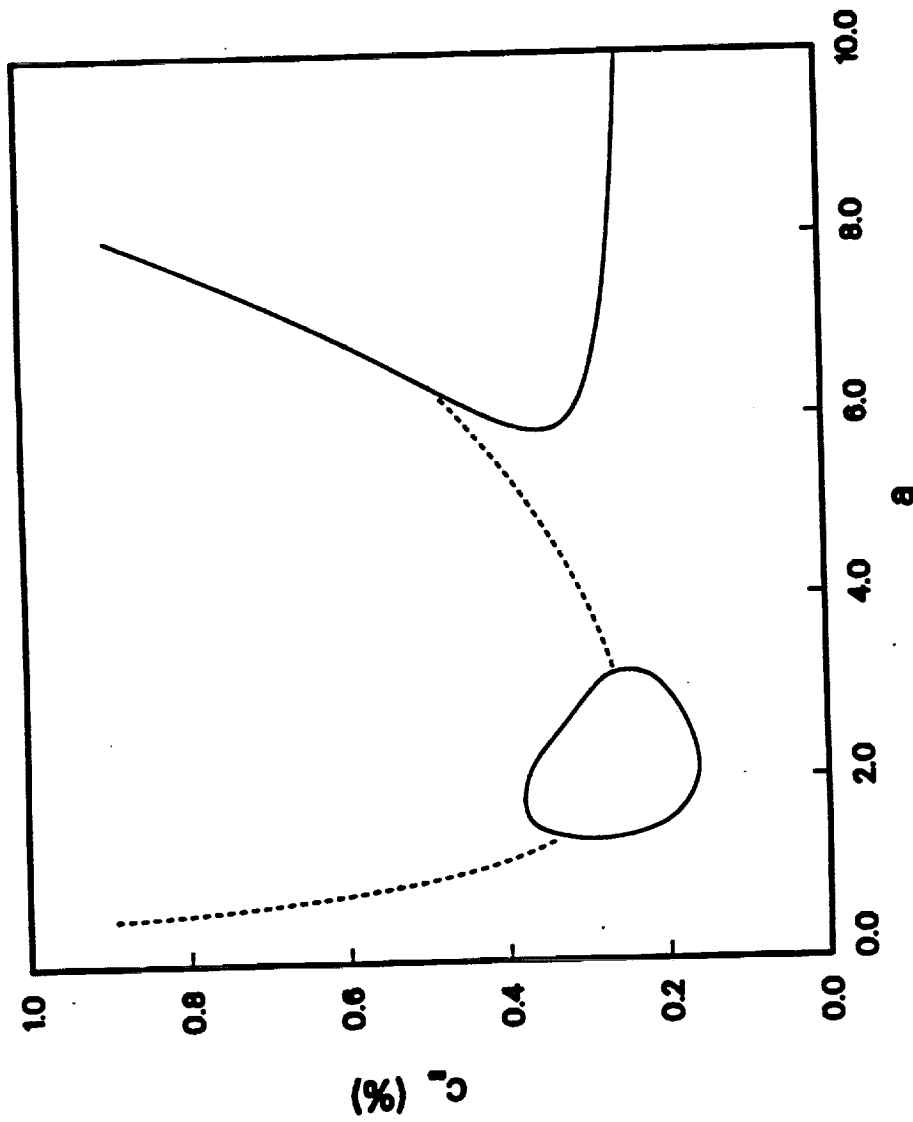


Figure 2.3g.  $C_{\infty}$ -a neutral curves for plane-front solidification of Pb-Sn with  $G_L = 200 \text{ K cm}^{-1}$  and  $\Omega_0 = 0 \text{ rpm}$  for  $V_1 = 37.5 \mu \text{ sec}^{-1}$ .

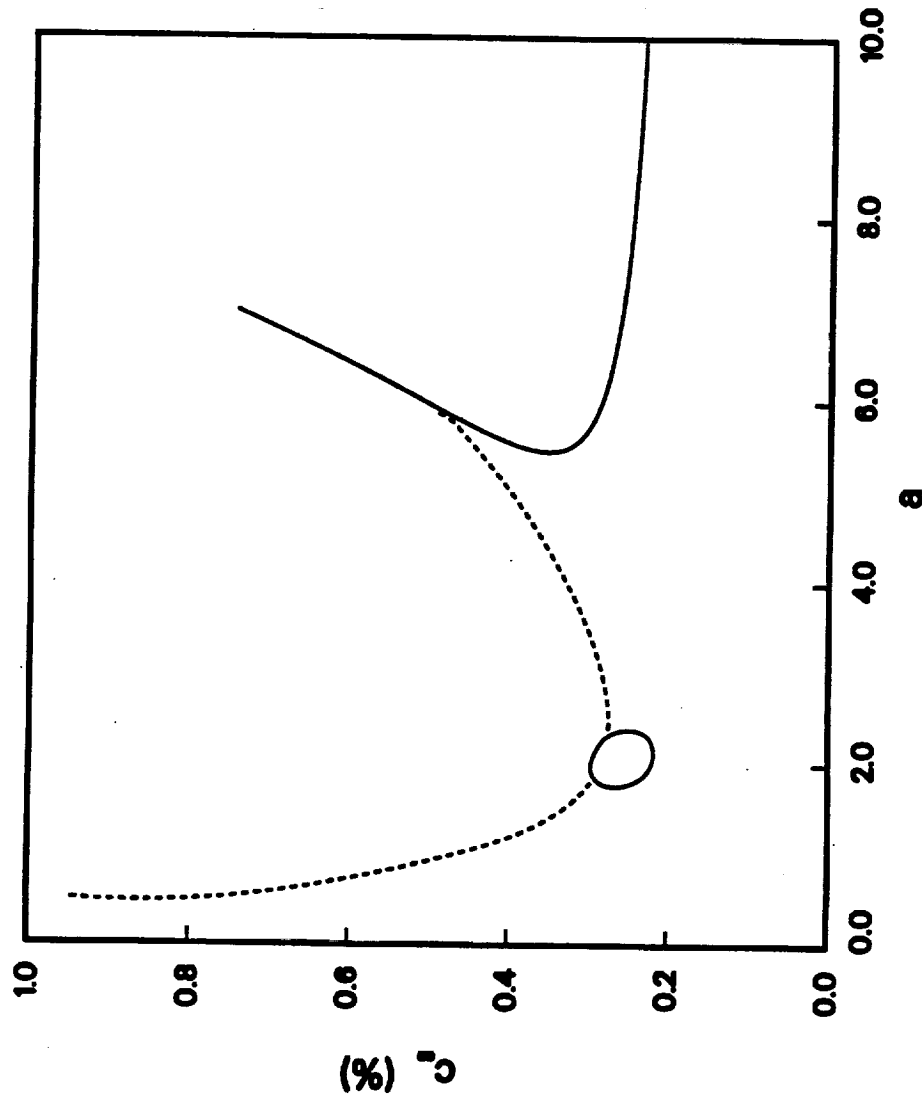


Figure 2.3h.  $C_0$ - $a$  neutral curves for plane-front solidification of Pb-Sn with  $G_L = 200 \text{ K cm}^{-1}$  and  $\Omega_0 = 0 \text{ rpm}$  for  $V_1 = 39.375 \text{ } \mu \text{ sec}^{-1}$ .

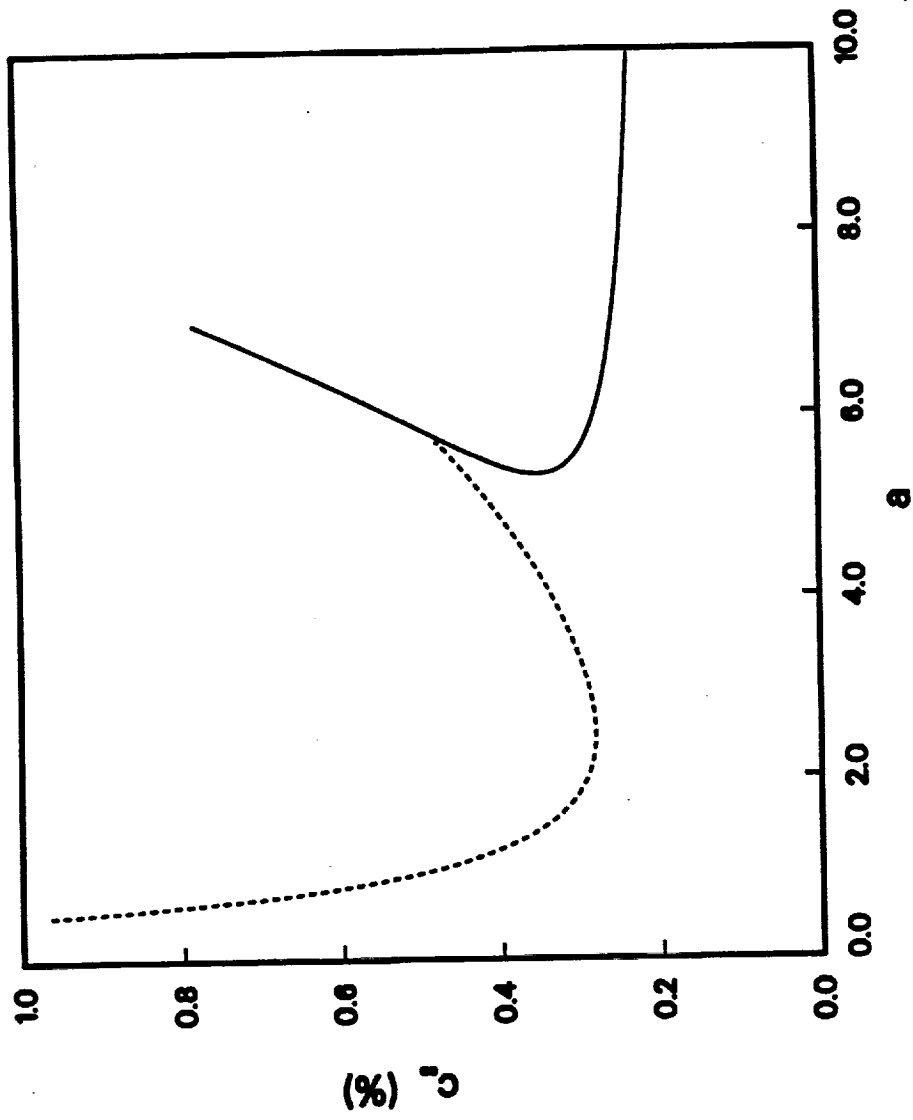


Figure 2.3i.  $C_{\infty}$ - $a$  neutral curves for plane-front solidification of Pb-Sn with  $G_L = 200 \text{ K cm}^{-1}$  and  $\Omega_0 = 0 \text{ rpm}$  for  $V_I = 40 \mu \text{ sec}^{-1}$ .

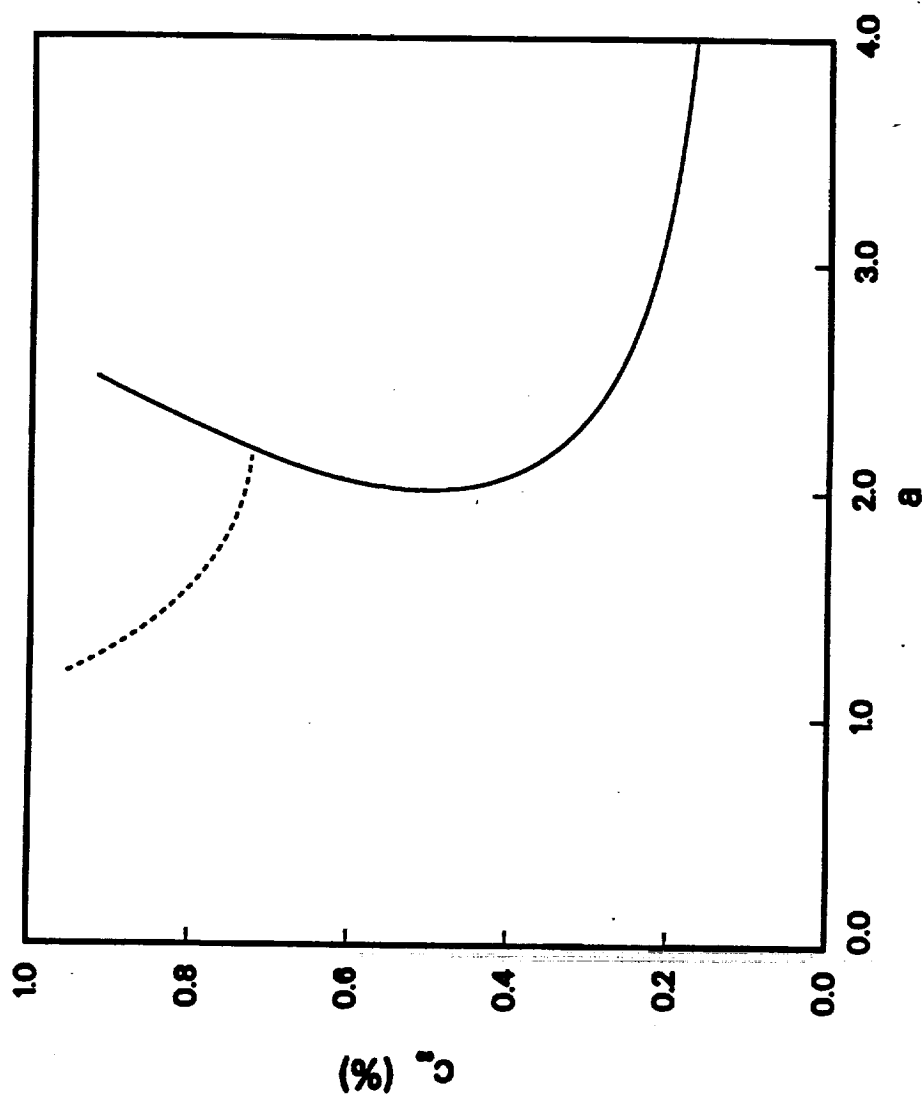


Figure 2.3j.  $C_o$ - $a$  neutral curves for plane-front solidification of Pb-Sn with  $G_L = 200 \text{ K cm}^{-1}$  and  $\Omega_0 = 0 \text{ rpm}$  for  $V_I = 80 \mu \text{ sec}^{-1}$ .

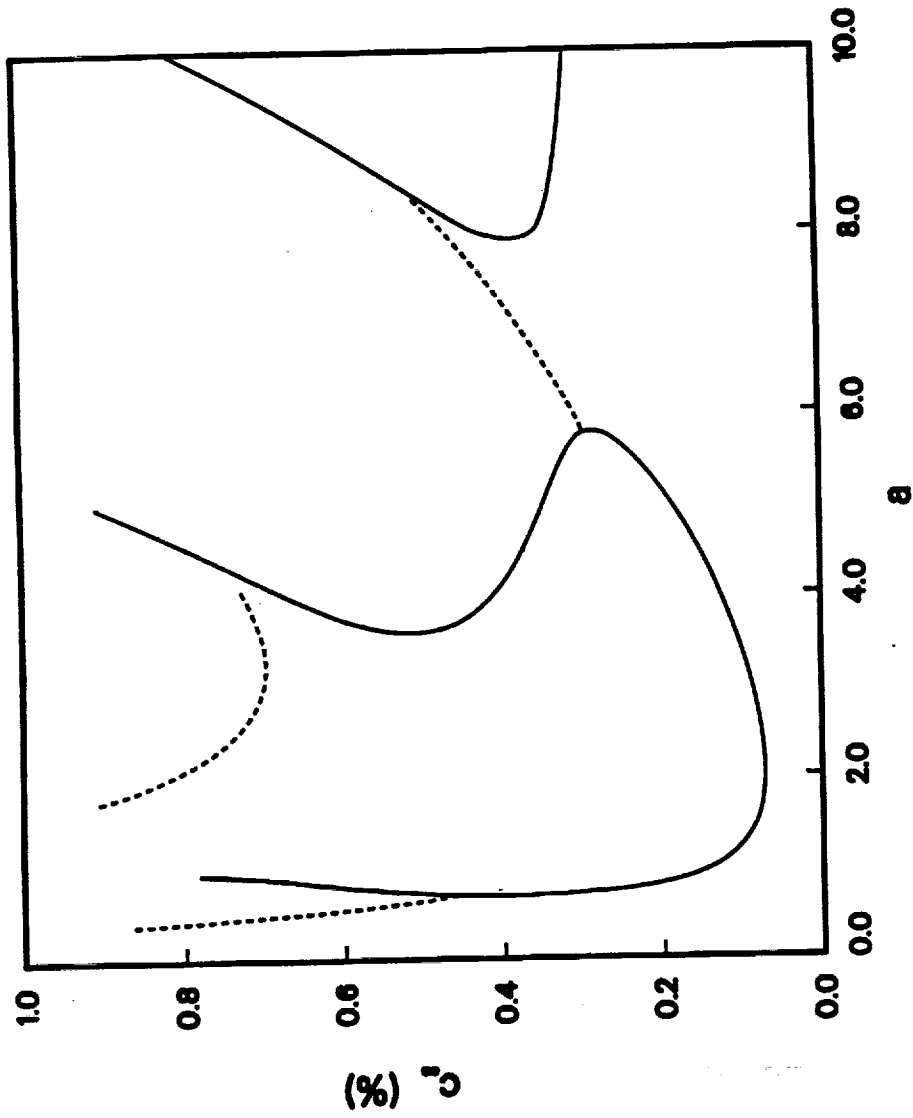


Figure 2.4a.  $C_0$ - $a$  neutral curves for plane-front solidification of Pb-Sn with  $G_L = 200 \text{ K cm}^{-1}$  and  $V_1 = 30 \mu \text{ sec}^{-1}$  for  $\Omega_0 = 0 \text{ rpm}$ .



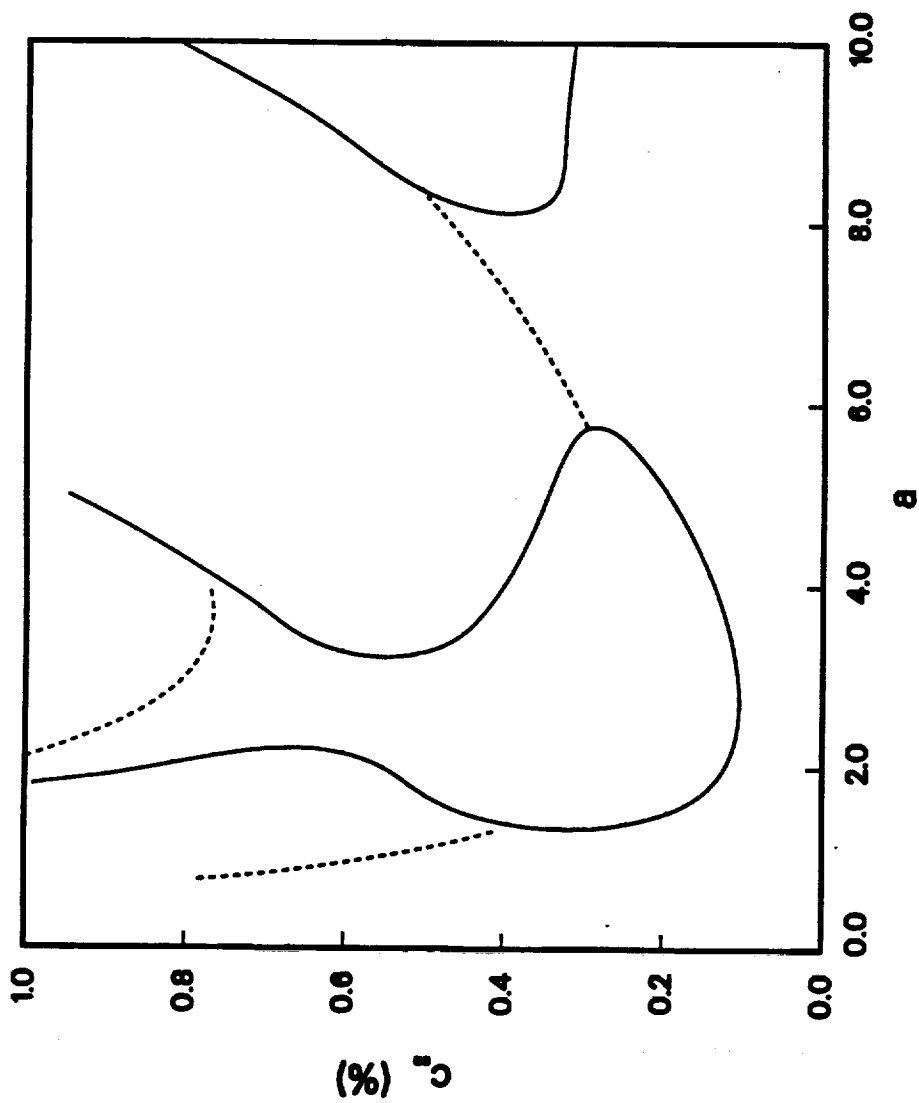


Figure 2.4b.  $C_{\infty}$ -a neutral curves for plane-front solidification of Pb-Sn with  $G_L = 200 \text{ K cm}^{-1}$  and  $V_I = 30 \mu \text{ sec}^{-1}$  for  $\Omega_0 = 90 \text{ rpm}$ .

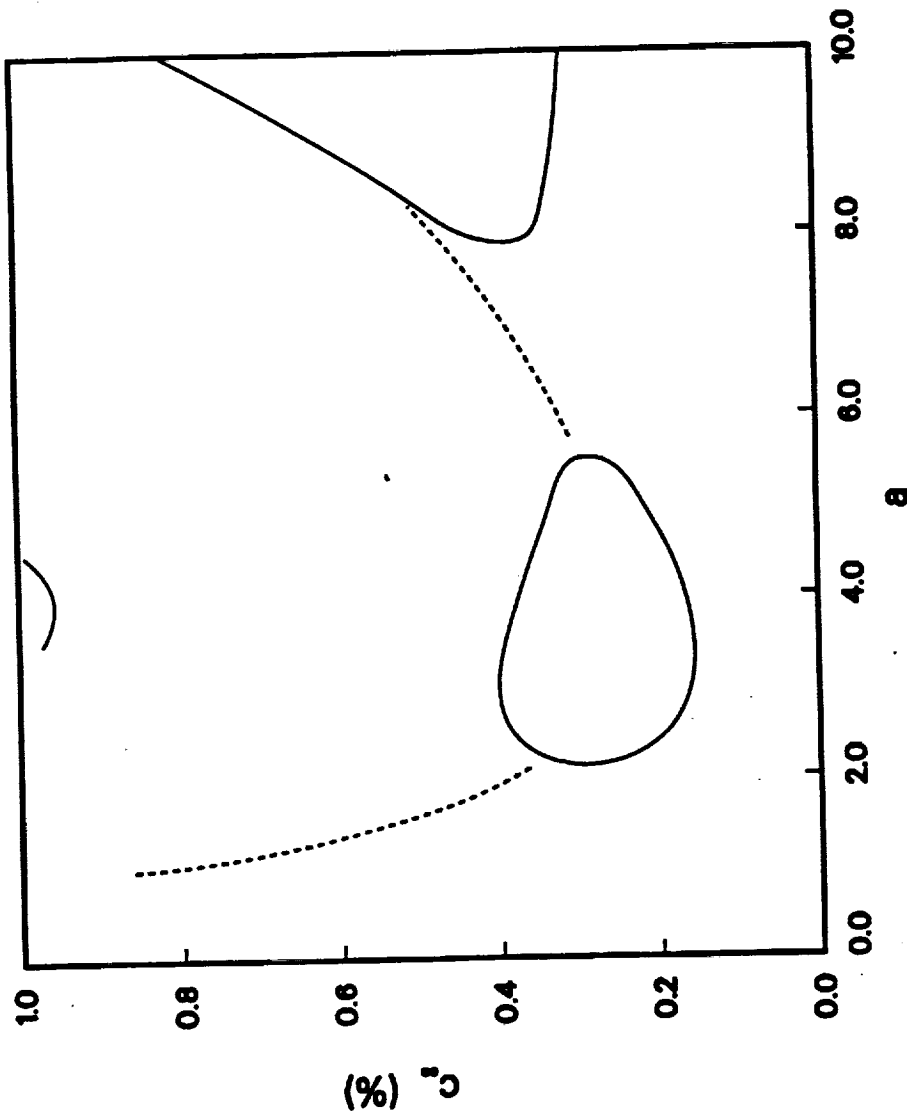


Figure 2.4c.  $C$ - $a$  neutral curves for plane-front solidification of Pb-Sn with  $G_L = 200 \text{ K cm}^{-1}$  and  $V_I = 30 \mu \text{ sec}^{-1}$  for  $\Omega_0 = 180 \text{ rpm}$ .

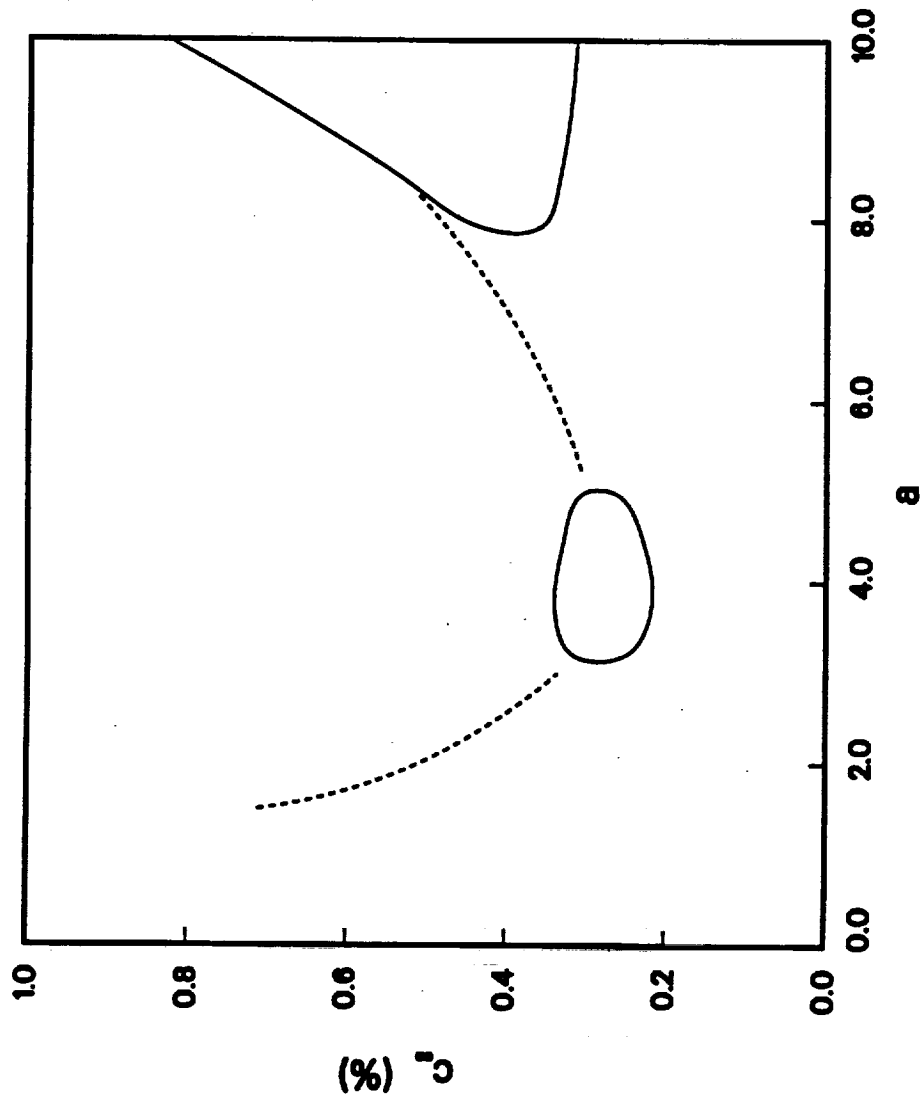


Figure 2.4d.  $C_0$ - $a$  neutral curves for plane-front solidification of Pb-Sn with  $G_L = 200 \text{ K cm}^{-1}$  and  $V_I = 30 \mu \text{ sec}^{-1}$  for  $\Omega_0 = 270 \text{ rpm}$ .

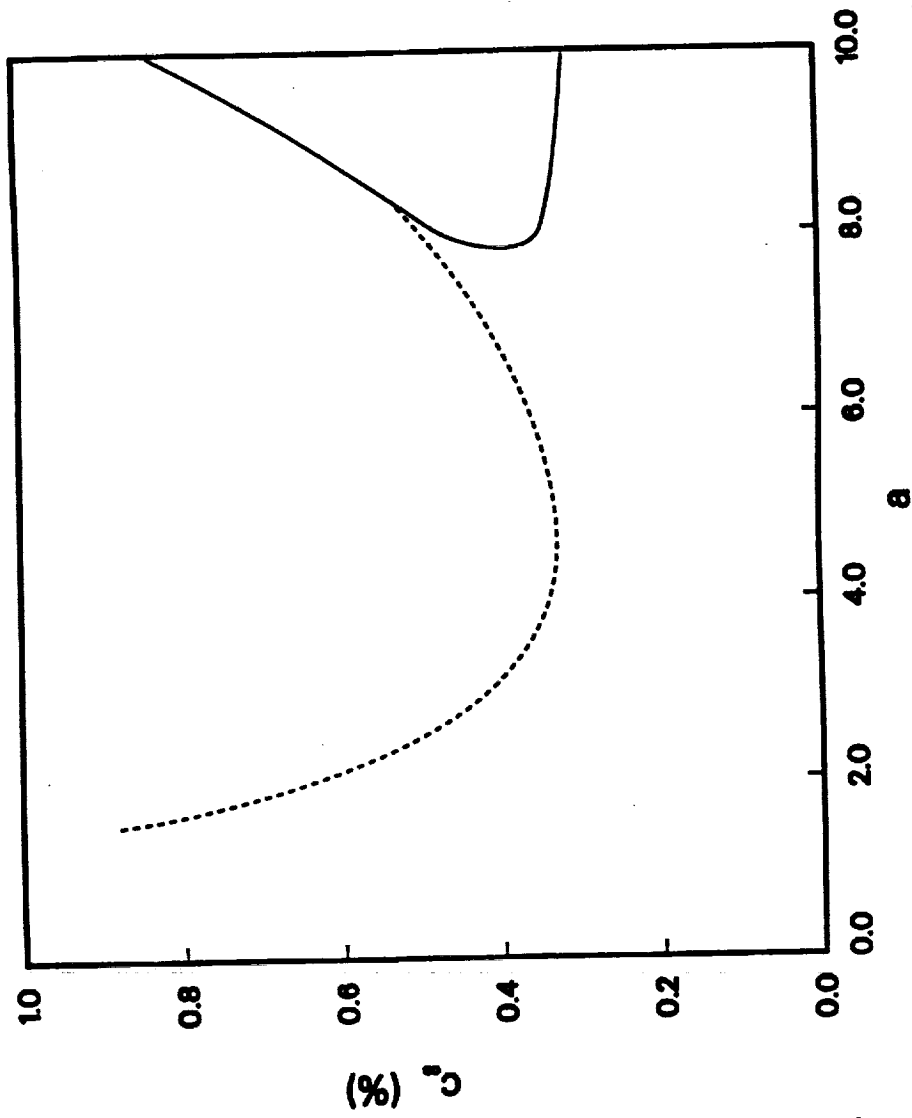


Figure 2.4e.  $C_{\infty}$ - $a$  neutral curves for plane-front solidification of Pb-Sn with  $G_L = 200 \text{ K cm}^{-1}$  and  $V_I = 30 \mu \text{ sec}^{-1}$  for  $\Omega_0 = 360 \text{ rpm}$ .

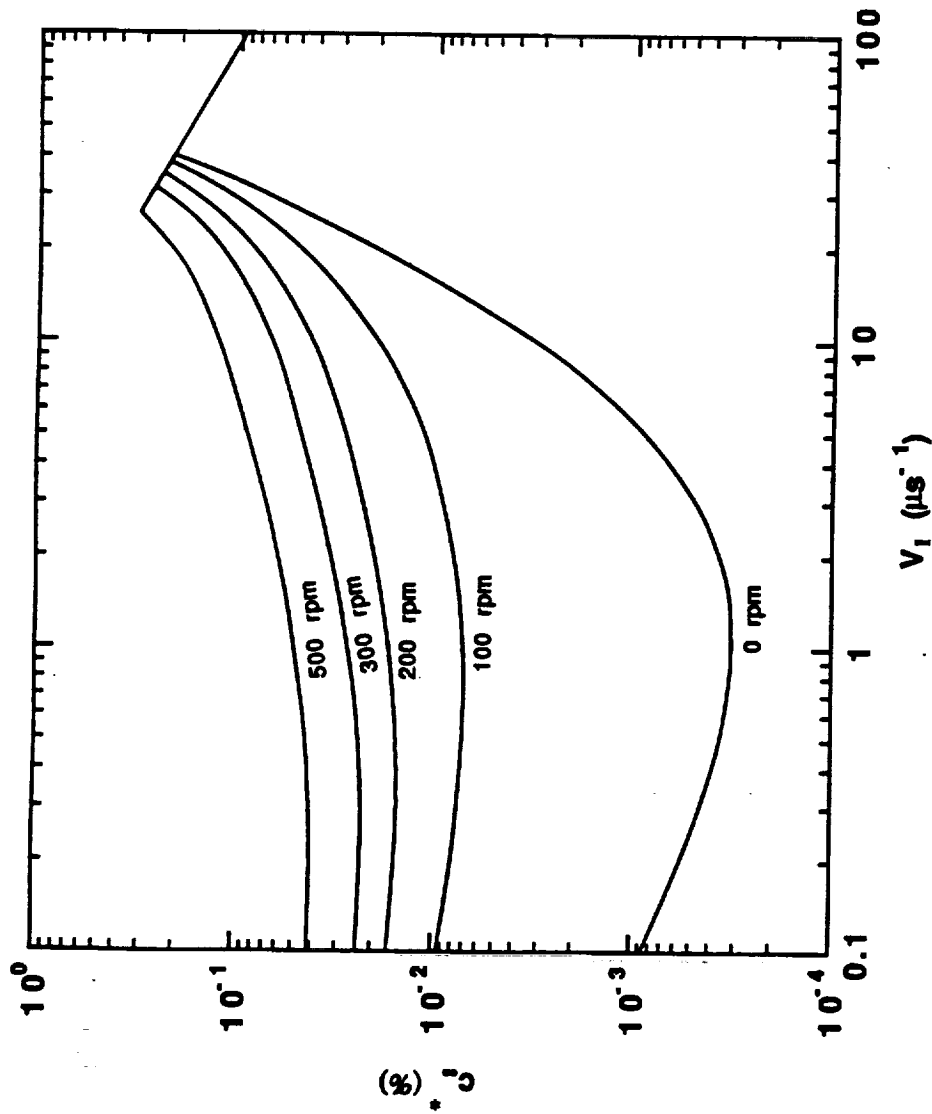


Figure 2.5.  $V_I$ - $c^*$  stability boundaries for plane-front solidification of Pb-Sn with  $G_L = 200 \text{ K cm}^{-1}$  at  $\Omega_0 = 0, 100, 200, 300$ , and  $500 \text{ rpm}$ .

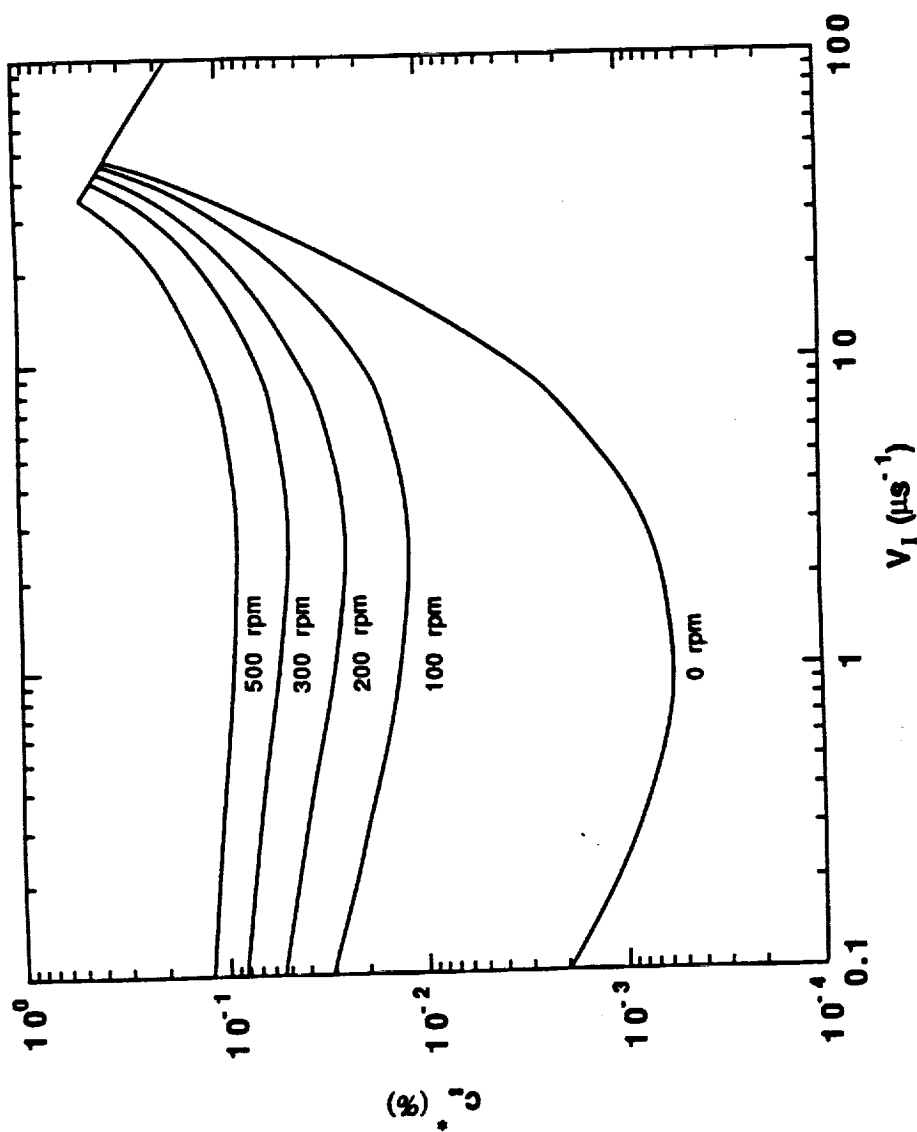


Figure 2.6.  $V_I$ - $C^*$  stability boundaries for plane-front solidification of Pb-Sn with  $G_L = 400 \text{ K cm}^{-1}$  at  $\Omega_0 = 0, 100, 200, 300$ , and 500 rpm.

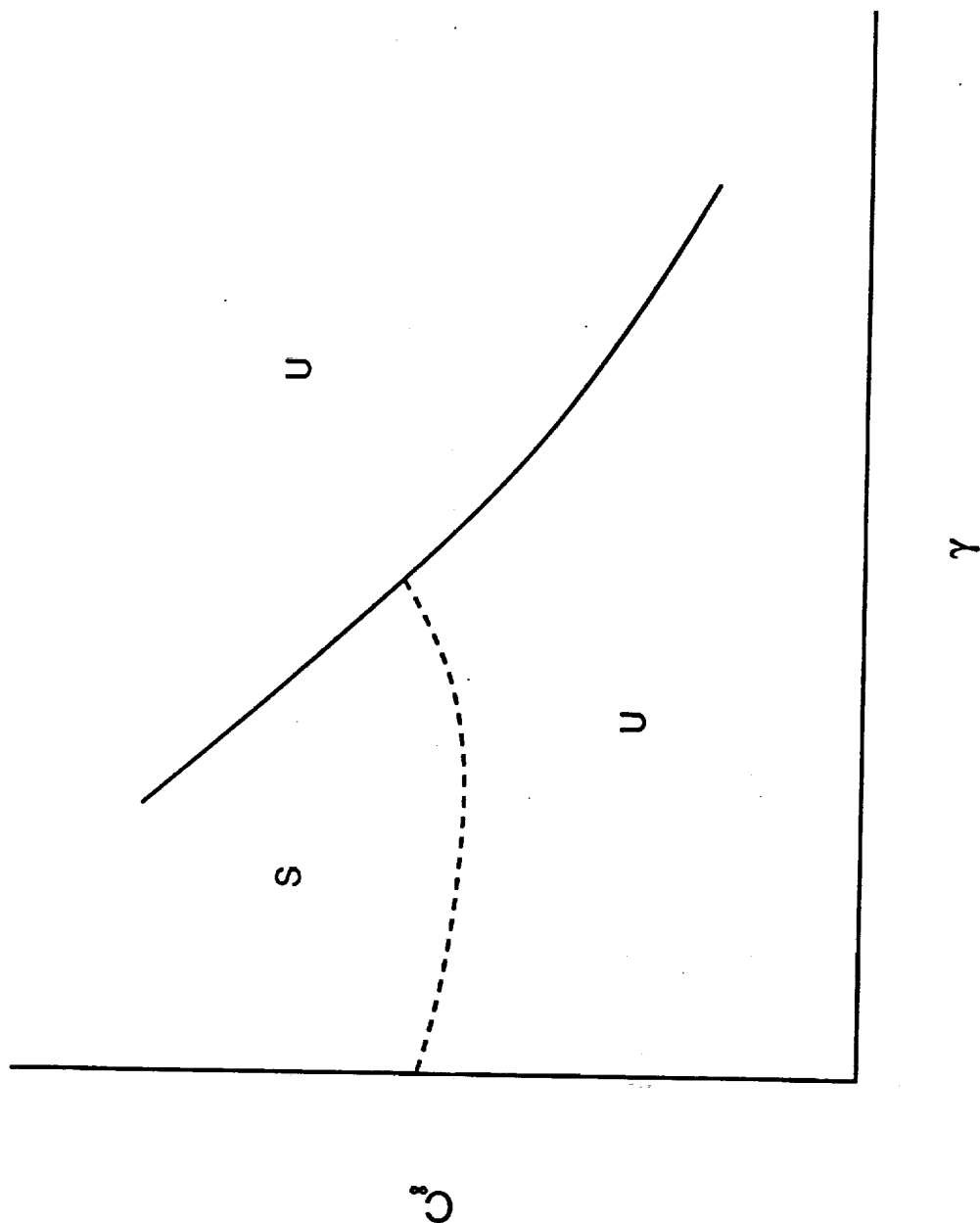


Figure 3.1. Schematic depiction of the stability boundary for plane-front solidification of  $\text{Hg}_{1-x}\text{Cd}_x\text{Te}$ .

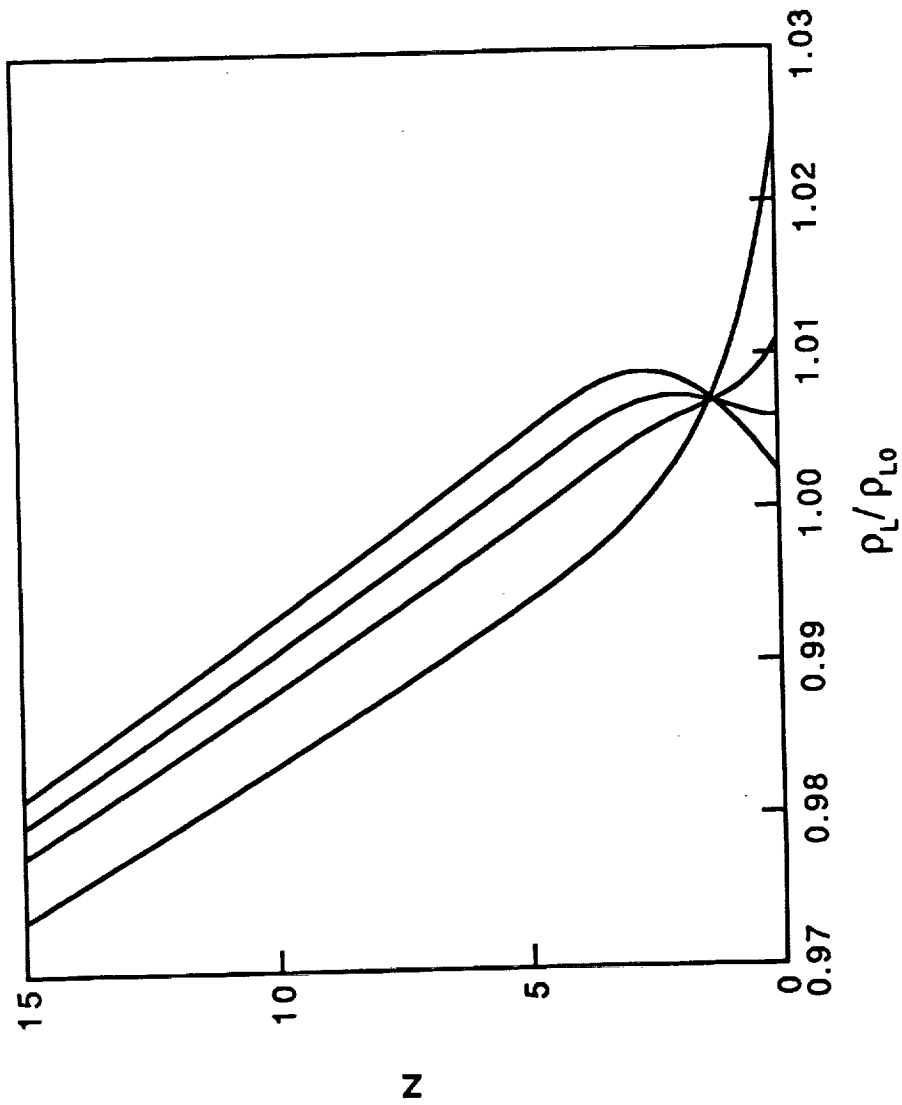


Figure 3.2a. Dimensionless liquid-phase basic state density profiles for  $\text{Hg}_{1-x}\text{Cd}_x\text{Te}$  for several values of  $C_{\infty}$  with  $\Gamma = 8.2 \times 10^{-4}$  ( $G_L = 25 \text{ K/cm}$ ) and  $\gamma = 1.32 \times 10^{-4}$  ( $V_1 = 0.5 \mu\text{sec}$ ).



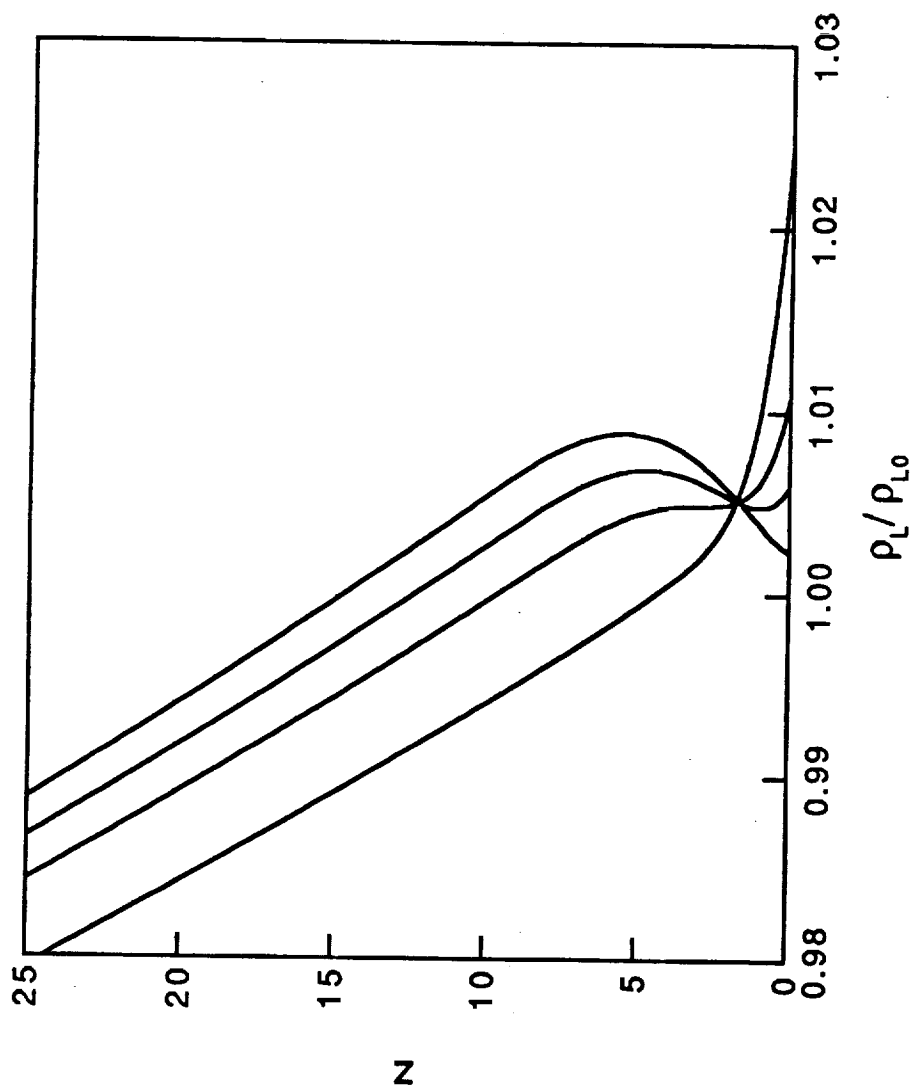


Figure 3.2b. Dimensionless liquid-phase basic state density profiles for  $\text{Hg}_{1-x}\text{Cd}_x\text{Te}$  for several values of  $C_\infty$  with  $\Gamma = 8.2 \times 10^{-4}$  ( $G_L = 25 \text{ K/cm}$ ) and  $\gamma = 2.64 \times 10^{-4}$  ( $V_I = 1 \text{ } \mu\text{/sec}$ ).

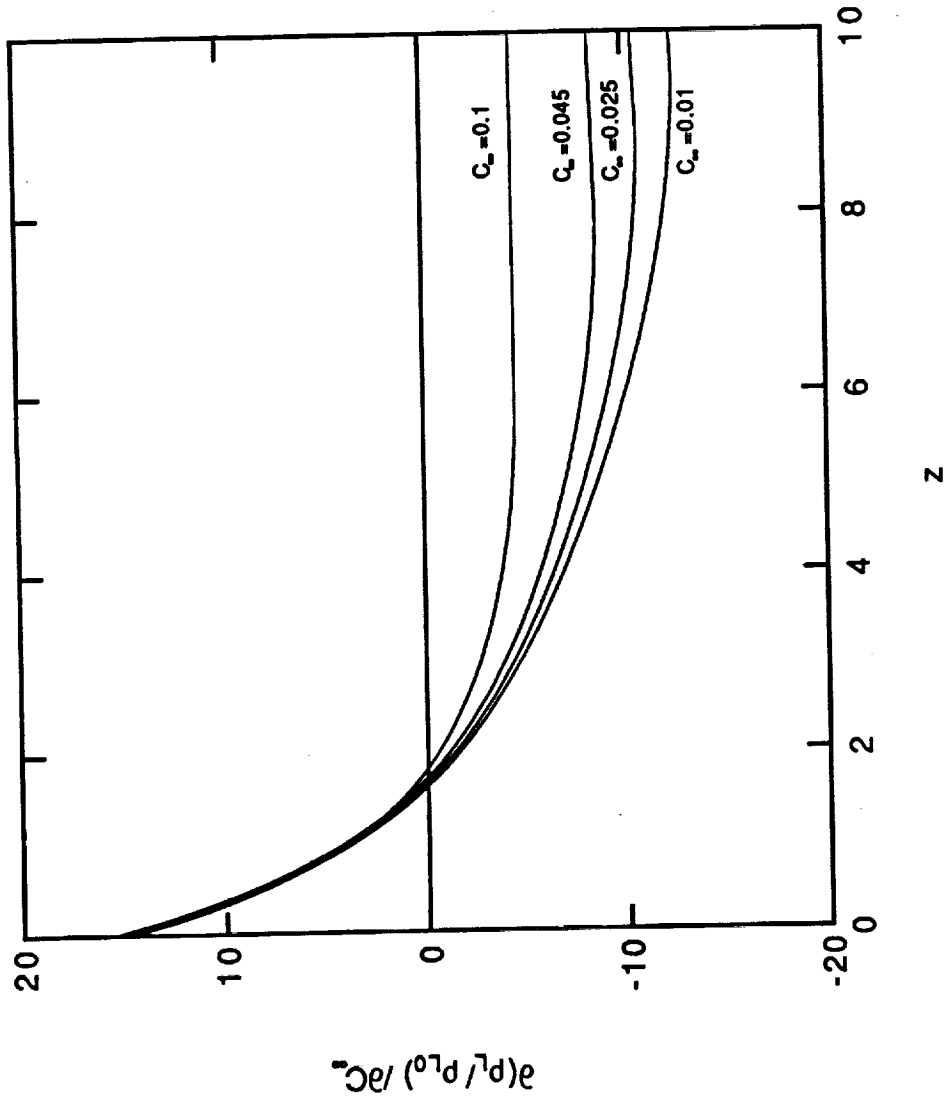


Figure 3.3.  $\partial(\rho_L/\rho_{L0})/\partial C_\infty$  versus  $z$  for several values of  $C_\infty$  with  $\gamma = 2.64 \times 10^{-4}$  and  $\Gamma = 8.2 \times 10^{-4}$  ( $V_1 = 1 \mu/\text{sec}$  and  $G_L = 25 \text{ K/cm}$ ).

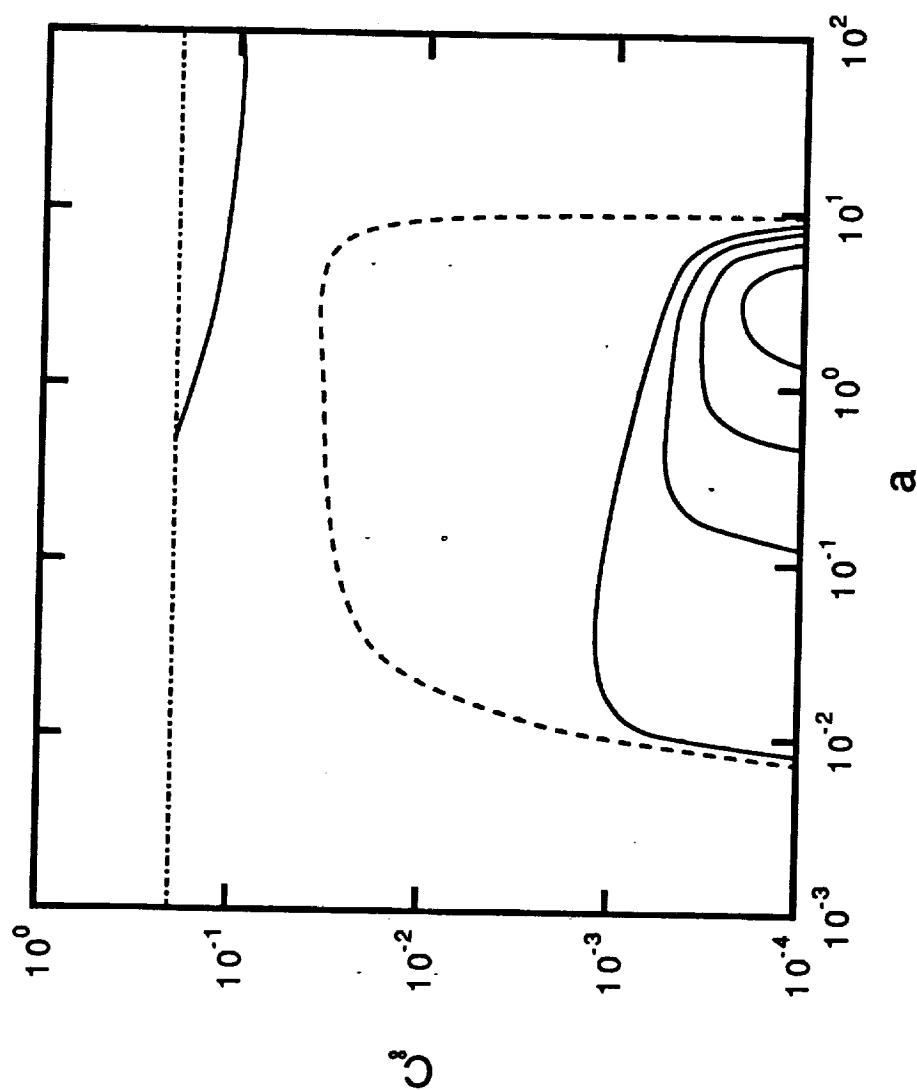


Figure 3.4a.  $C_\infty$ - $a$  neutral curves for  $\text{Hg}_{1-x}\text{Cd}_x\text{Te}$  for  $\Gamma = 1.64 \times 10^{-3}$  ( $G_L = 50 \text{ K/cm}$ ) and  $\gamma = 2.64 \times 10^{-4}$  ( $V_I = 1 \mu\text{sec}$ ).

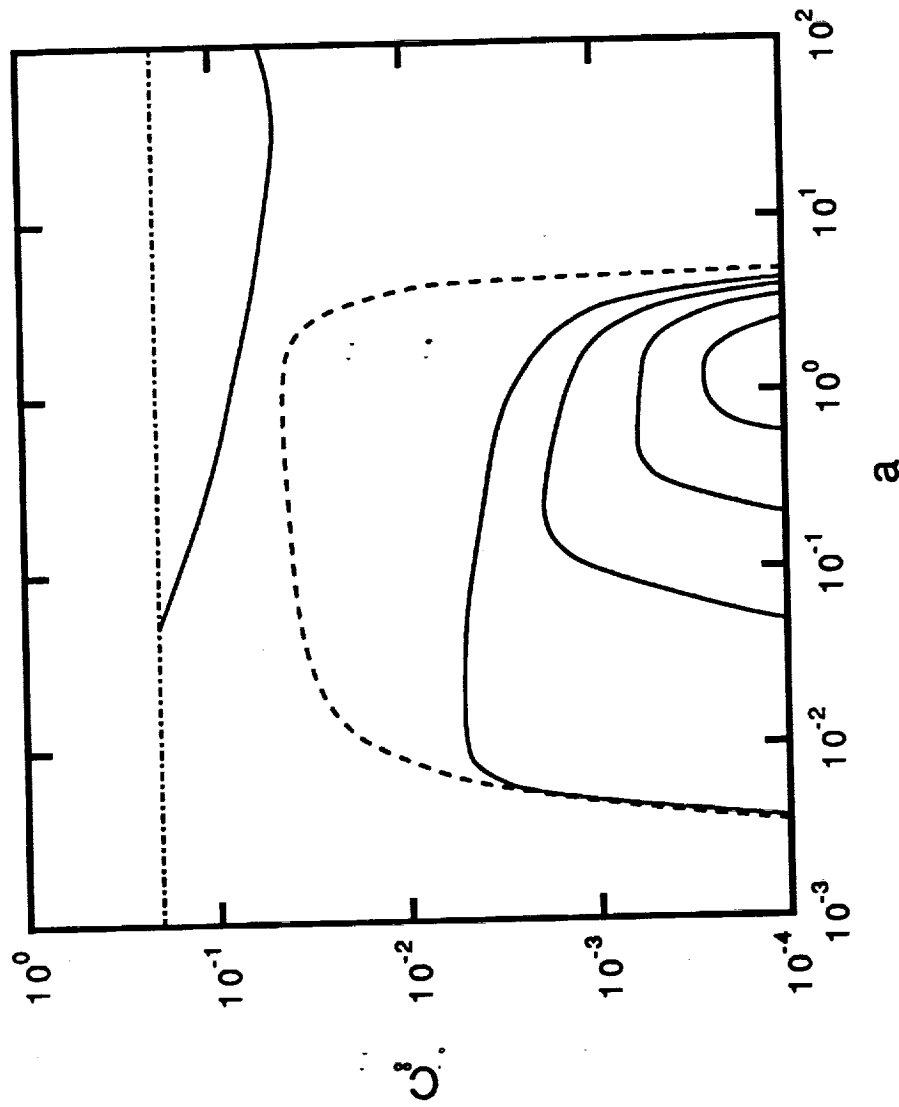


Figure 3.4b.  $C_{\infty}$ - $a$  neutral curves for  $\text{Hg}_{1-x}\text{Cd}_x\text{Te}$  for  $\Gamma = 1.64 \times 10^{-3}$  ( $G_L = 50 \text{ K/cm}$ ) and  $\gamma = 5.28 \times 10^{-4}$  ( $V_1 = 2 \mu\text{sec}$ ).

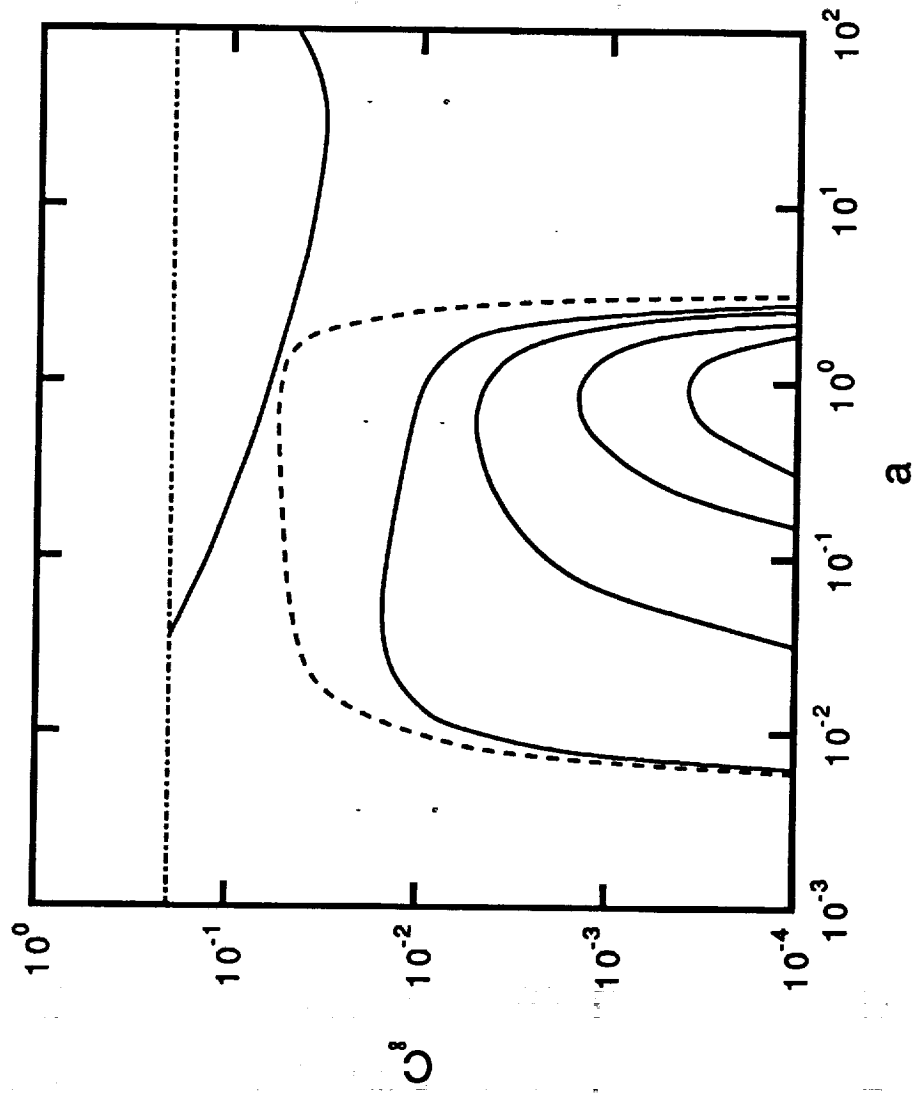


Figure 3.4c.  $C_{\infty}$ - $a$  neutral curves for  $\text{Hg}_{1-x}\text{Cd}_x\text{Te}$  for  $\Gamma = 1.64 \times 10^{-3}$  ( $G_L = 50 \text{ K/cm}$ ) and  $\gamma = 7.92 \times 10^{-4}$  ( $V_1 = 3 \mu\text{sec}$ ).

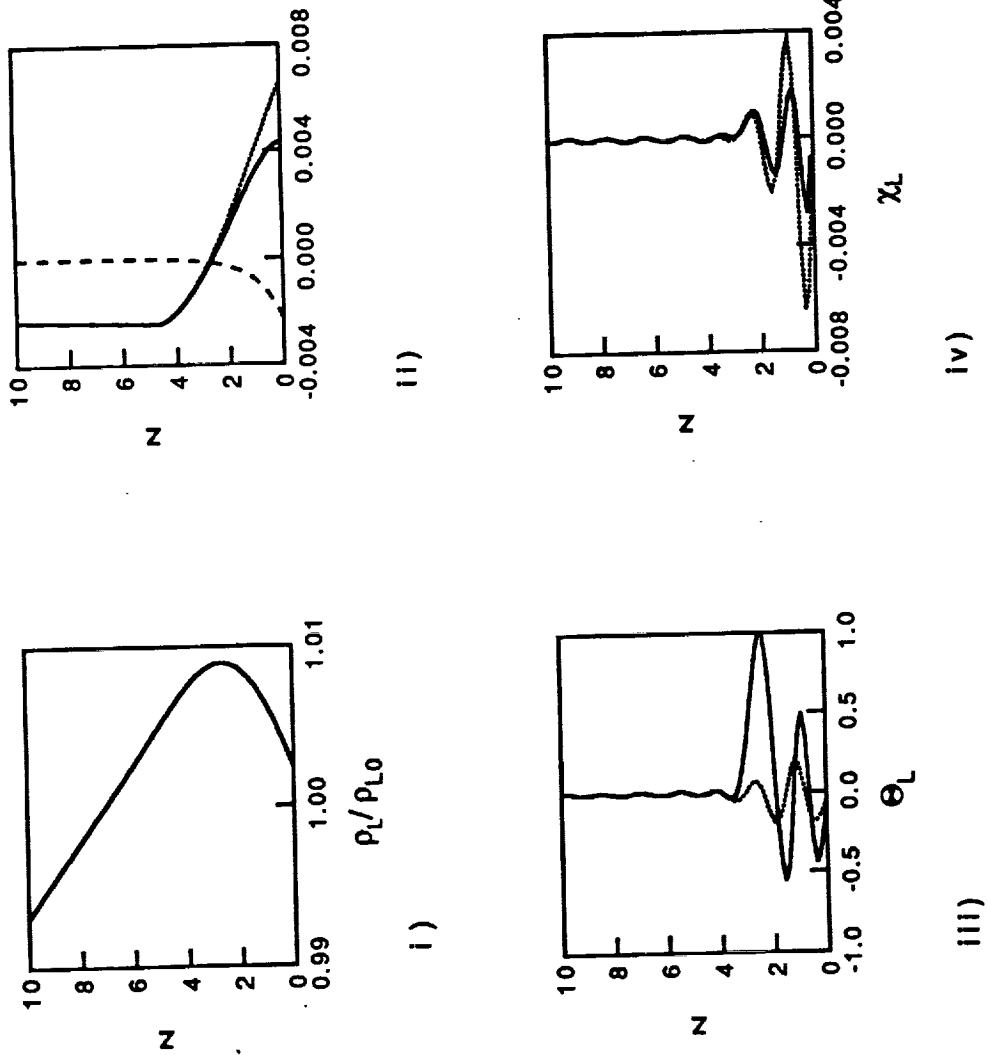


Figure 3.5a. For  $\text{Hg}_{1-x}\text{Cd}_x\text{Te}$  with  $C_{\infty} = 0.01$ ,  $\gamma = 2.64 \times 10^{-4}$ , and  $\Gamma = 1.64 \times 10^{-3}$  ( $V_1 = 1 \mu/\text{sec}$  and  $G_L = 50 \text{ K/cm}$ ), dimensionless basic state and disturbance profiles. i) Basic state density gradient  $(\partial \rho_L / \partial z) / \rho_{L0}$  (solid curve) and the additive contributions from thermal (dotted) and solutal (dashed) stratification,  $(\partial \rho_L / \partial T) (\partial T / \partial z) / \rho_{L0}$  and  $(\partial \rho_L / \partial C) (\partial C / \partial z) / \rho_{L0}$ , respectively; iii) amplitude of disturbance temperature; iv) amplitude of disturbance solute distribution; v) amplitude of disturbance vertical velocity. The disturbances shown are those which are the most unstable for  $a = 2.85$ , and real and imaginary parts are indicated by solid and dotted curves, respectively.

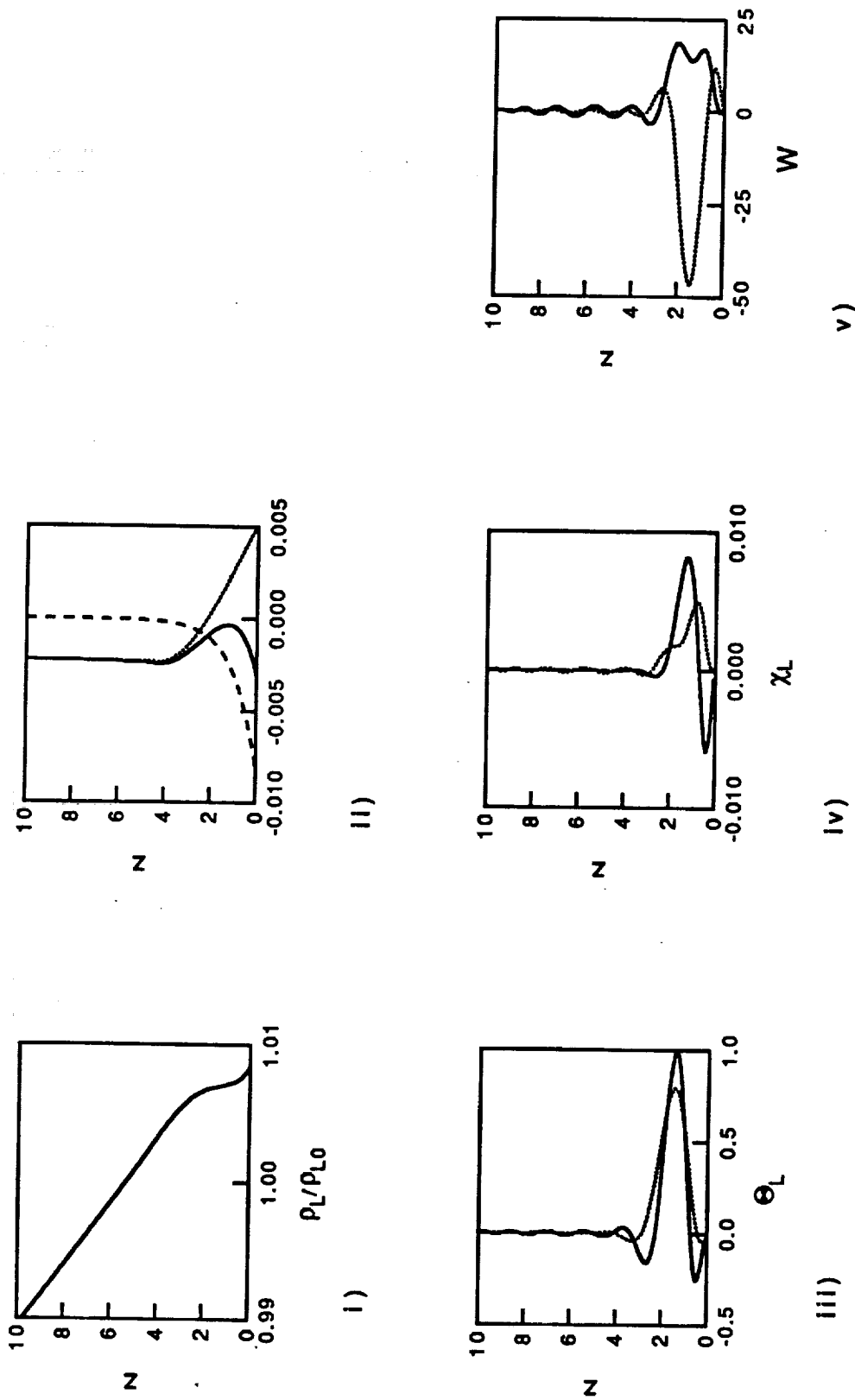


Figure 3.5b. For  $\text{Hg}_{1-x}\text{Cd}_x\text{Te}$  with  $C_{\infty} = 0.035$ ,  $\gamma = 2.64 \times 10^{-4}$ , and  $\Gamma = 1.64 \times 10^{-3}$  ( $V_1 = 1 \mu/\text{sec}$  and  $G_L = 50 \text{ K/cm}$ ), dimensionless basic state and disturbance profiles. i) Basic state density profile; ii) basic state density gradient  $(\partial \rho_L / \partial z) / \rho_{L0}$  (solid curve) and the additive contributions from thermal (dotted) and solutal (dashed) stratification,  $(\partial \rho_L / \partial T)(\partial T_L / \partial z) / \rho_{L0}$  and  $(\partial \rho_L / \partial C)(\partial C_L / \partial z) / \rho_{L0}$ , respectively; iii) amplitude of disturbance temperature; iv) amplitude of disturbance solute distribution; v) amplitude of disturbance vertical velocity. The disturbances shown are those which are the most unstable for  $a = 2.85$ , and real and imaginary parts are indicated by solid and dotted curves, respectively.

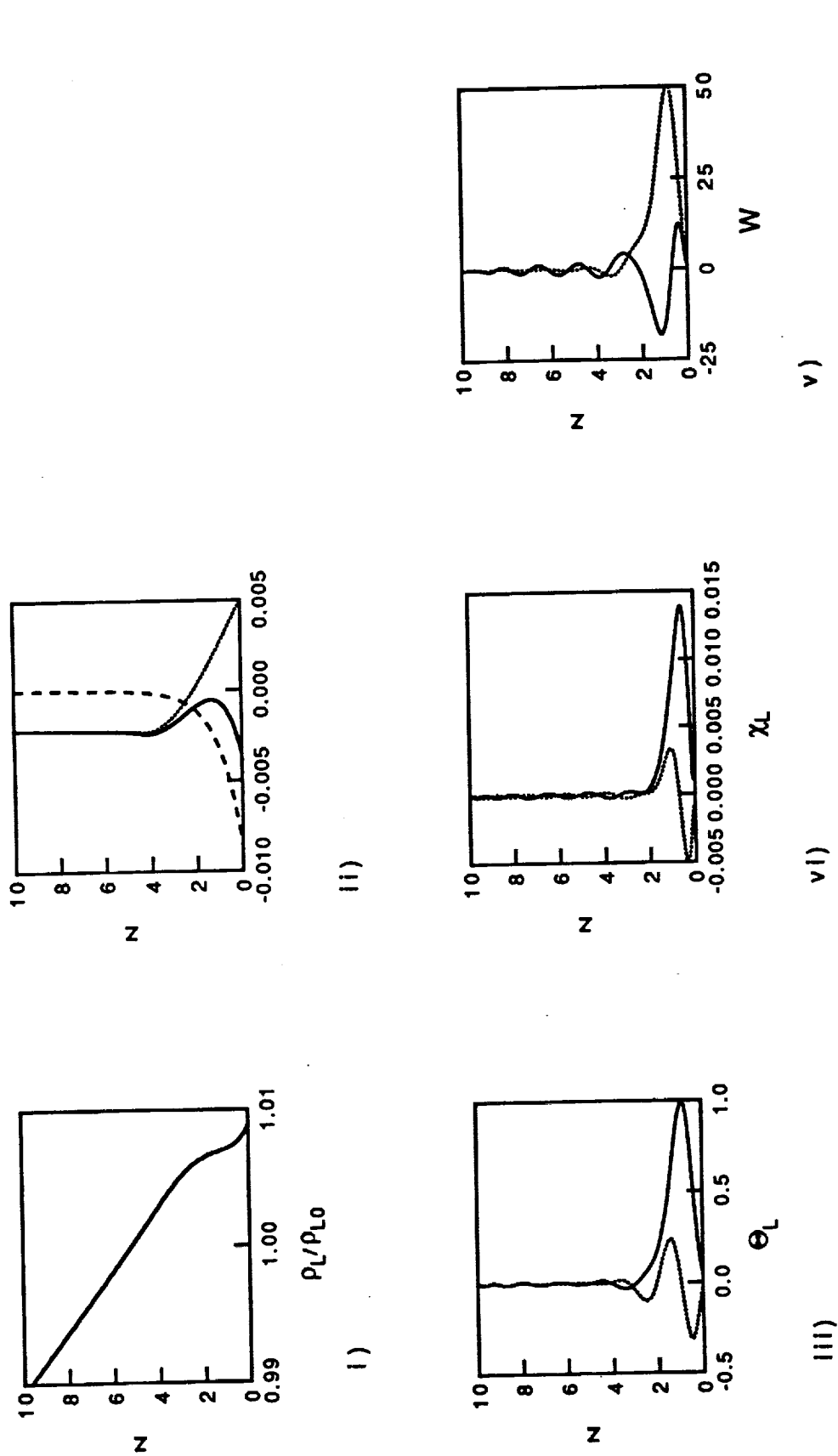


Figure 3.5c. For  $\text{Hg}_{1-x}\text{Cd}_x\text{Te}$  with  $C_\infty = 0.0369$ ,  $\gamma = 2.64 \times 10^{-4}$ , and  $\Gamma = 1.64 \times 10^{-3}$  ( $V_1 = 1 \mu/\text{sec}$  and  $G_L = 50 \text{ K/cm}$ ). dimensionless basic state and disturbance profiles. i) Basic state density profile; ii) basic state density gradient  $(\partial \rho_L / \partial z) / \rho_{L0}$  (solid curve) and the additive contributions from thermal (dotted) and solutal (dashed) stratification,  $(\partial \rho_L / \partial T) (\partial T_L / \partial z) / \rho_{L0}$  and  $(\partial \rho_L / \partial C) (\partial C_L / \partial z) / \rho_{L0}$ , respectively; iii) amplitude of disturbance temperature; iv) amplitude of disturbance solute distribution; v) amplitude of disturbance vertical velocity. The disturbances shown are those which are the most unstable for  $a = 2.85$ , and real and imaginary parts are indicated by solid and dotted curves, respectively.



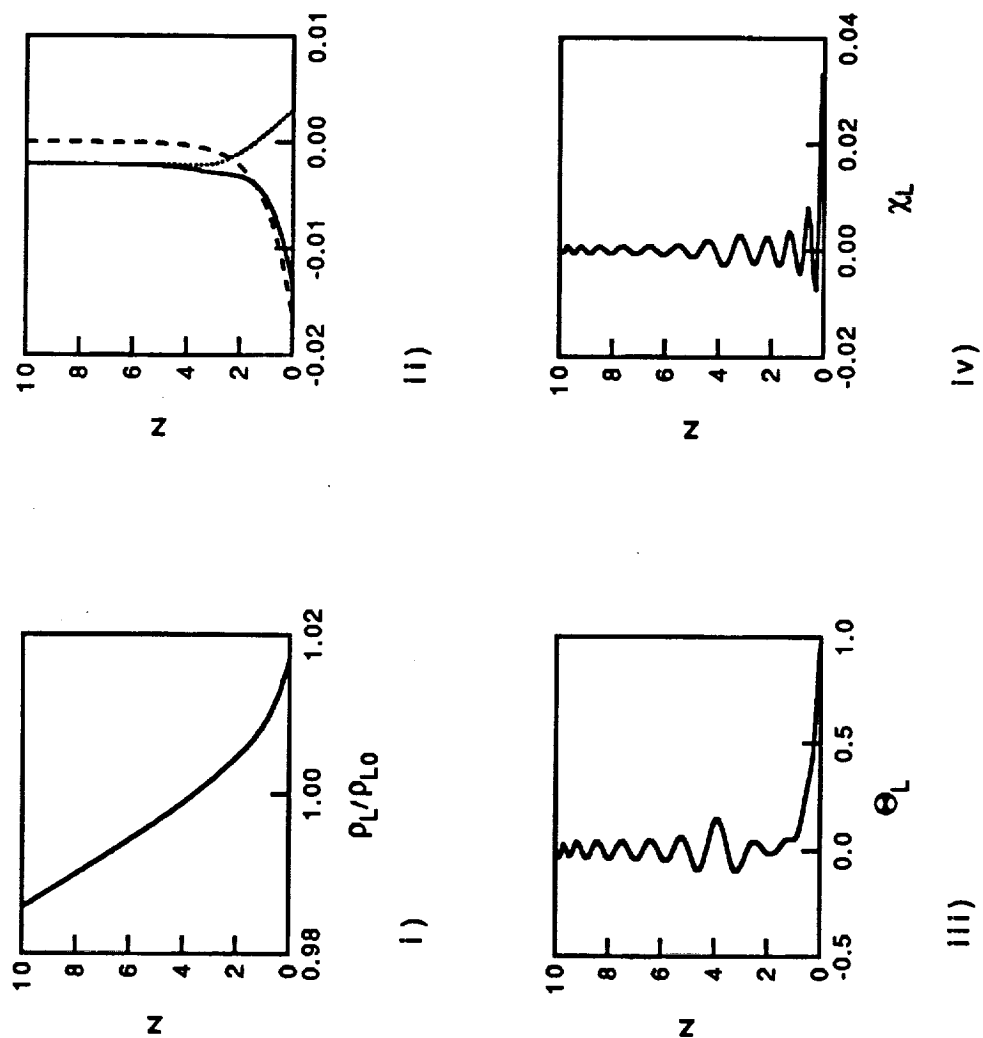


Figure 3.5d. For  $\text{Hg}_{1-x}\text{Cd}_x\text{Te}$  with  $C_\infty = 0.07$ ,  $\gamma = 2.64 \times 10^{-4}$ , and  $\Gamma = 1.64 \times 10^{-3}$  ( $V_1 = 1 \mu/\text{sec}$  and  $G_L = 50 \text{ K/cm}$ ), dimensionless basic state and disturbance profiles. i) Basic state density profile; ii) basic state density gradient  $(\partial \rho_L / \partial z) / \rho_{L0}$  (solid curve) and the additive contributions from thermal (dotted) and solutal (dashed) stratification,  $(\partial \rho_L / \partial T) (\partial T_L / \partial z) / \rho_{L0}$  and  $(\partial \rho_L / \partial C) (\partial C_L / \partial z) / \rho_{L0}$ , respectively; iii) amplitude of disturbance temperature; iv) amplitude of disturbance solute distribution; v) amplitude of disturbance vertical velocity. The disturbances shown are those which are the most unstable for  $a = 2.85$ .

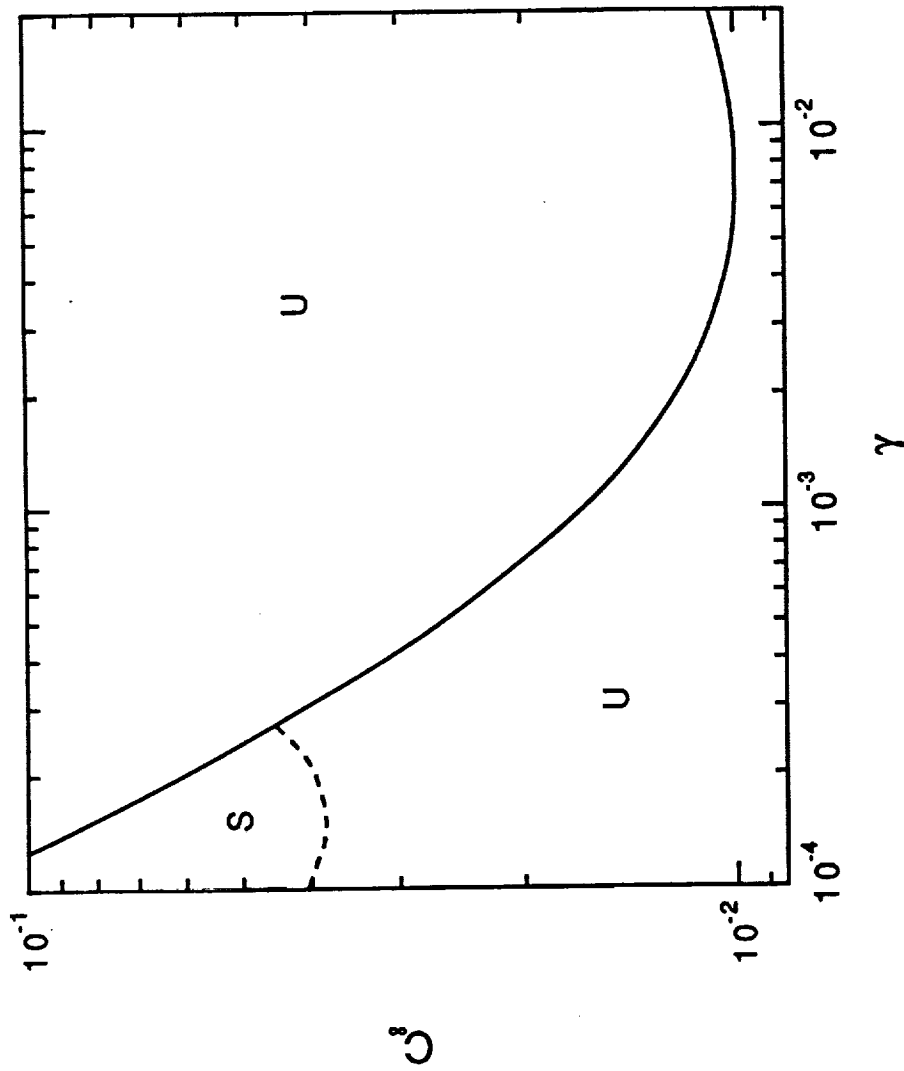


Figure 3.6a. Stable region in  $\gamma$ - $C_\infty$  plane for  $\text{Hg}_{1-x}\text{Cd}_x\text{Te}$  for  $\Gamma = 8.2 \times 10^{-4}$  ( $G_L = 25 \text{ K/cm}$ ). The solid and dashed curves are the morphological ( $C_\infty^*$ ) and buoyancy-driven convective ( $C_\infty^{**}$ ) stability boundaries, respectively, which intersect at  $\gamma_c = 2.70 \times 10^{-4}$ .

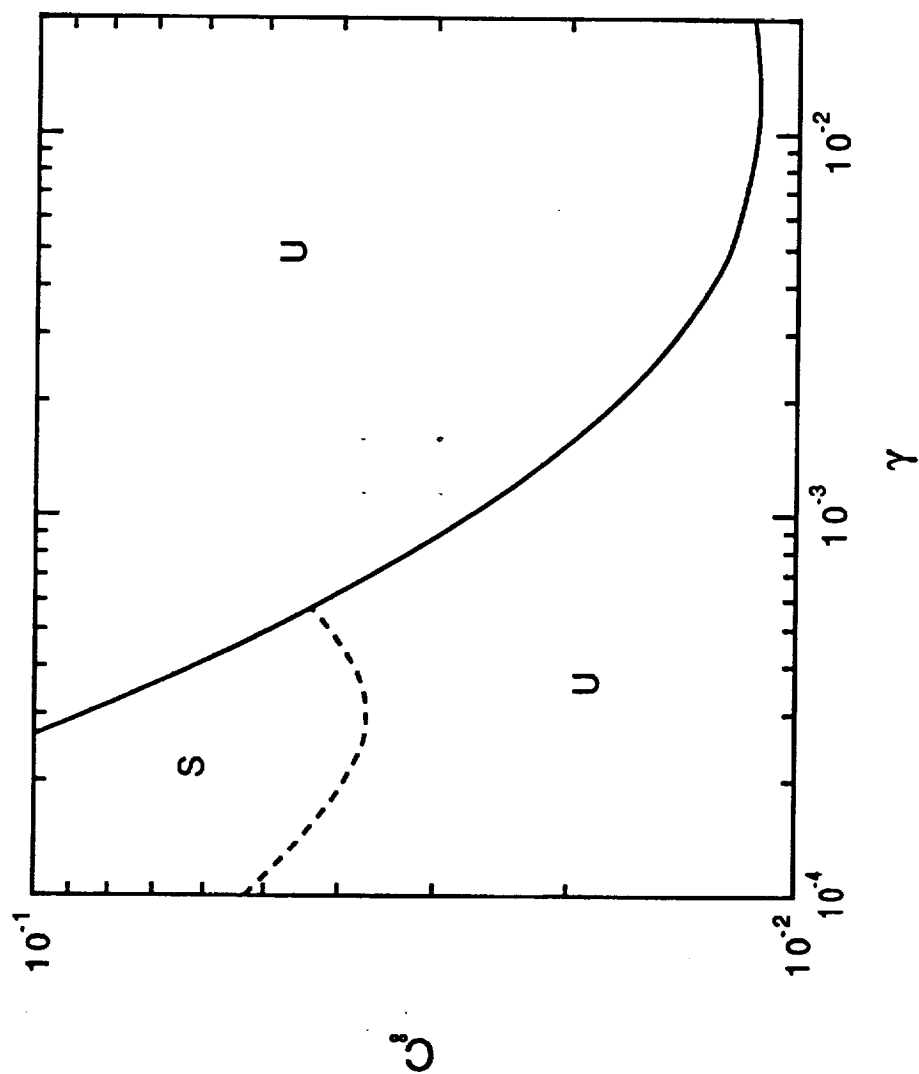


Figure 3.6b. Stable region in  $\gamma$ - $C_\infty$  plane for  $\text{Hg}_{1-x}\text{Cd}_x\text{Te}$  for  $\Gamma = 1.64 \times 10^{-3}$  ( $G_L = 50 \text{ K/cm}$ ). The solid and dashed curves are the morphological ( $C_\infty^*$ ) and buoyancy-driven convective ( $C_\infty^{**}$ ) stability boundaries, respectively, which intersect at  $\gamma_c = 5.62 \times 10^{-4}$ .

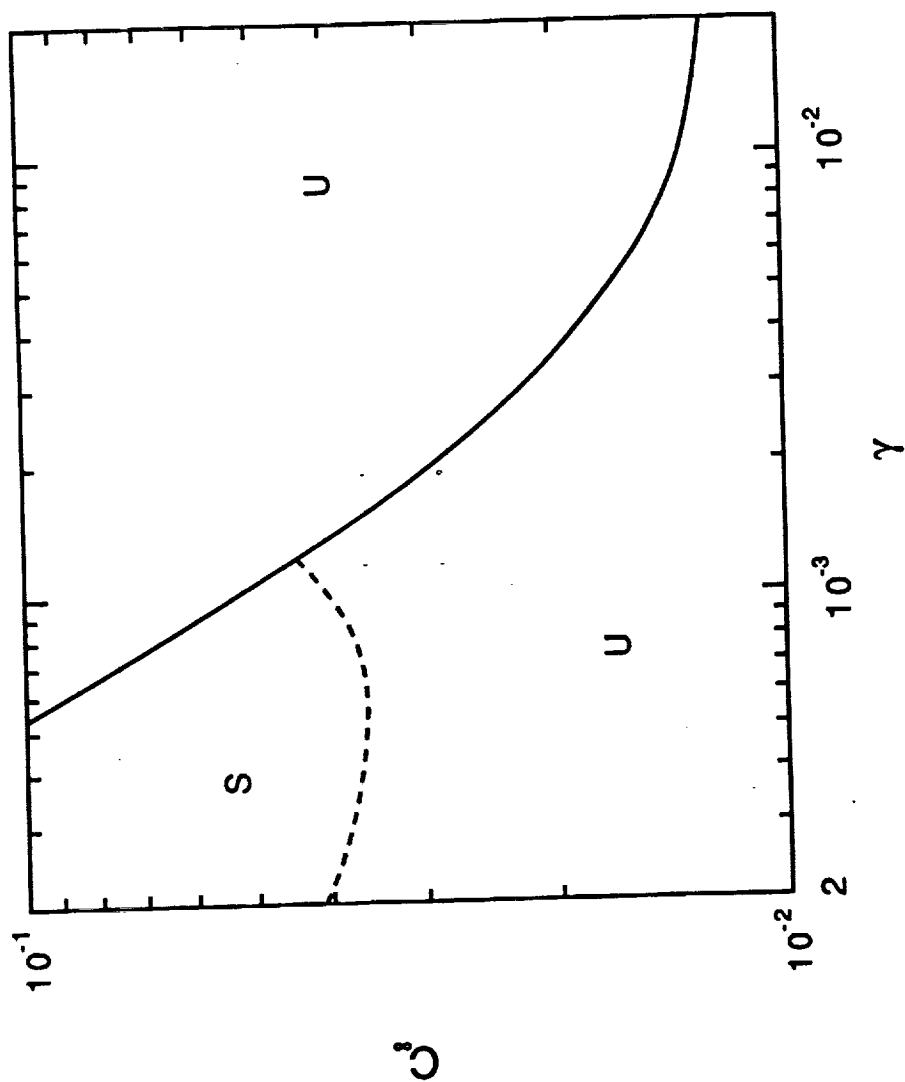


Figure 3.6c. Stable region in  $\gamma$ - $C_\infty$  plane for  $\text{Hg}_{1-x}\text{Cd}_x\text{Te}$  for  $\Gamma = 3.28 \times 10^{-3}$  ( $G_L = 100 \text{ K/cm}$ ). The solid and dashed curves are the morphological ( $C_\infty^*$ ) and buoyancy-driven convective ( $C_\infty^{**}$ ) stability boundaries, respectively, which intersect at  $\gamma_c = 1.22 \times 10^{-3}$ .

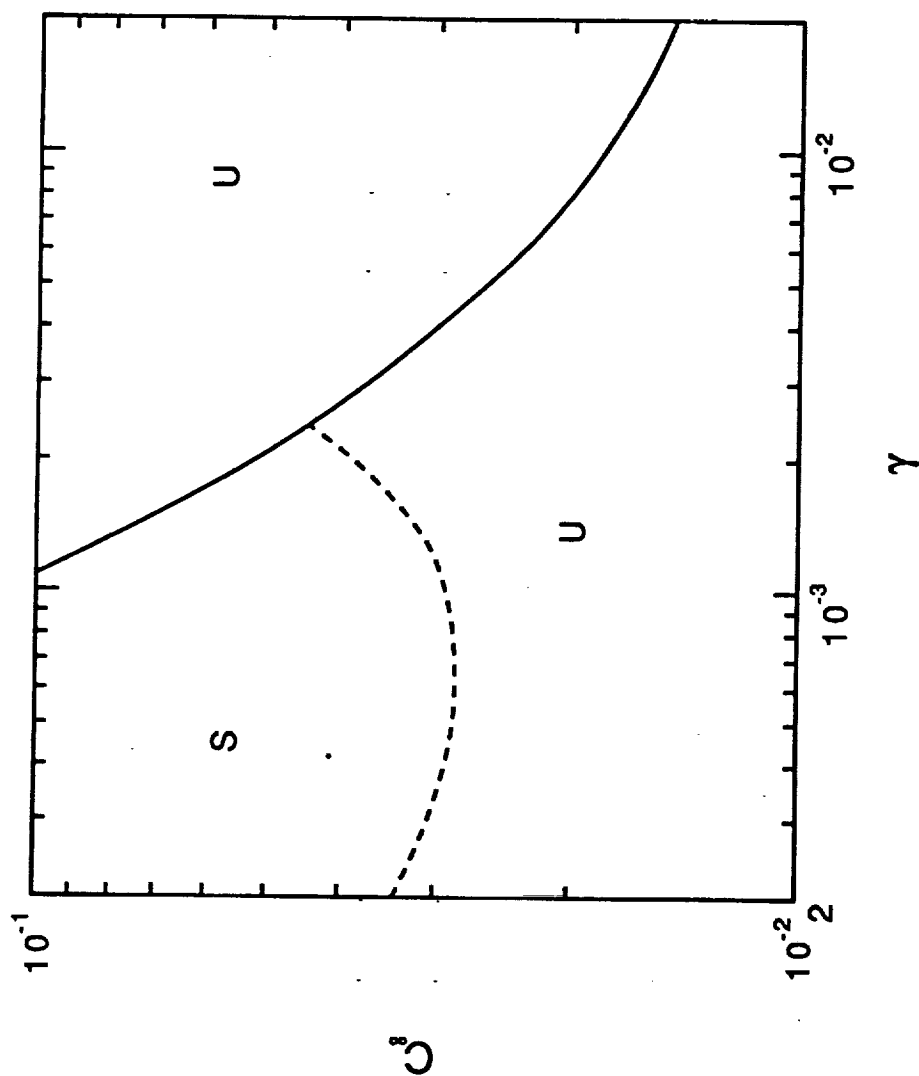


Figure 3.6d. Stable region in  $\gamma$ - $C_\infty$  plane for  $\text{Hg}_{1-x}\text{Cd}_x\text{Te}$  for  $\Gamma = 6.56 \times 10^{-3}$  ( $G_L = 200 \text{ K/cm}$ ). The solid and dashed curves are the morphological ( $C_\infty^*$ ) and buoyancy-driven convective ( $C_\infty^{**}$ ) stability boundaries, respectively, which intersect at  $\gamma_c = 2.37 \times 10^{-3}$ .

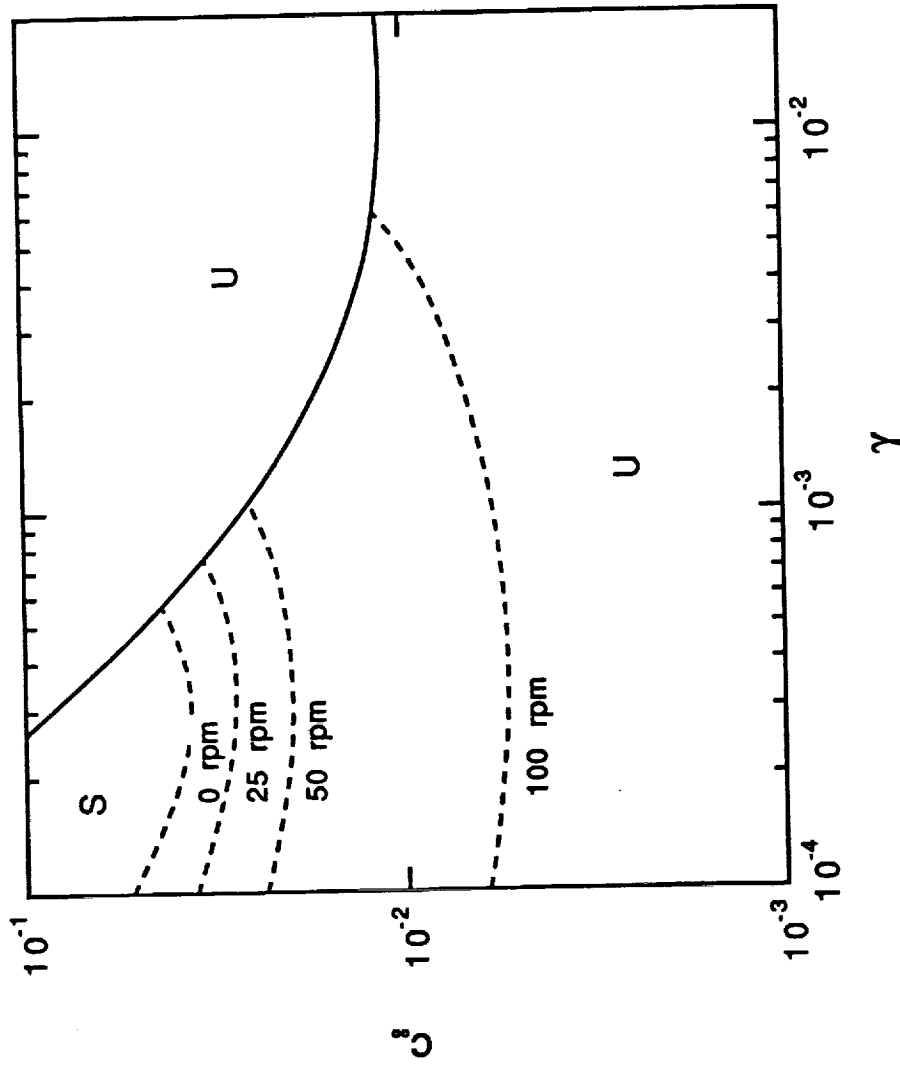


Figure 3.7. Stable region in  $\gamma$ - $C_{\infty}$  plane for  $\text{Hg}_{1-x}\text{Cd}_x\text{Te}$  for various values of  $\Omega_0$  with  $\Gamma = 1.64 \times 10^{-3}$  ( $G_L = 50 \text{ K cm}^{-1}$ ). The solid curve is the morphological ( $C_{\infty}^*$ ) stability boundary, and the dashed curves are the buoyancy-driven convective ( $C_{\infty}^*$ ) stability boundaries.

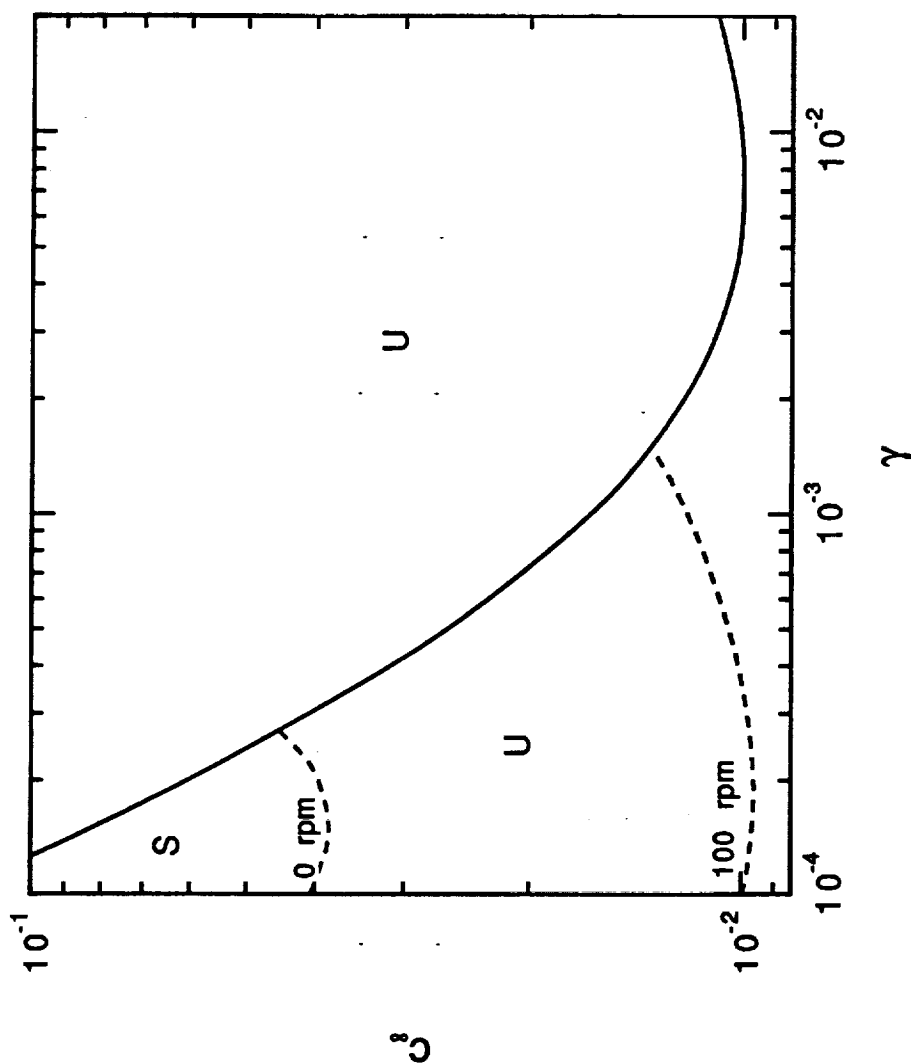


Figure 3.8. Stable region in  $\gamma$ - $C_\infty$  plane for  $\text{Hg}_{1-x}\text{Cd}_x\text{Te}$  for  $\Omega_0 = 100$  rpm and  $\Gamma = 8.2 \times 10^{-4}$  ( $G_L = 25 \text{ K cm}^{-1}$ ). The solid curve is the morphological ( $C_\infty^*$ ) stability boundary, and the dashed curves are the buoyancy-driven convective ( $C_\infty^{**}$ ) stability boundaries.

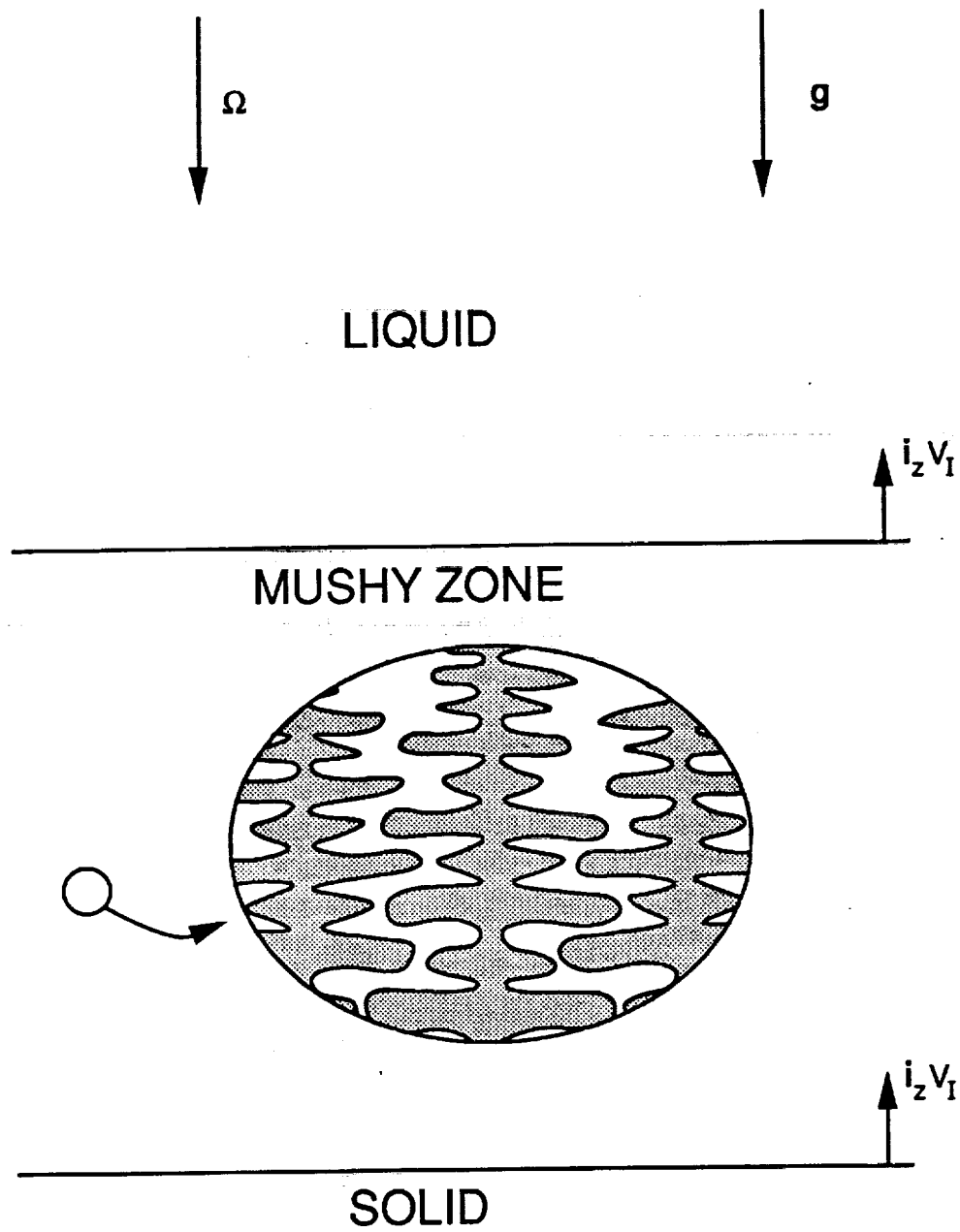


Figure 4.1. Schematic depiction of dendritic solidification



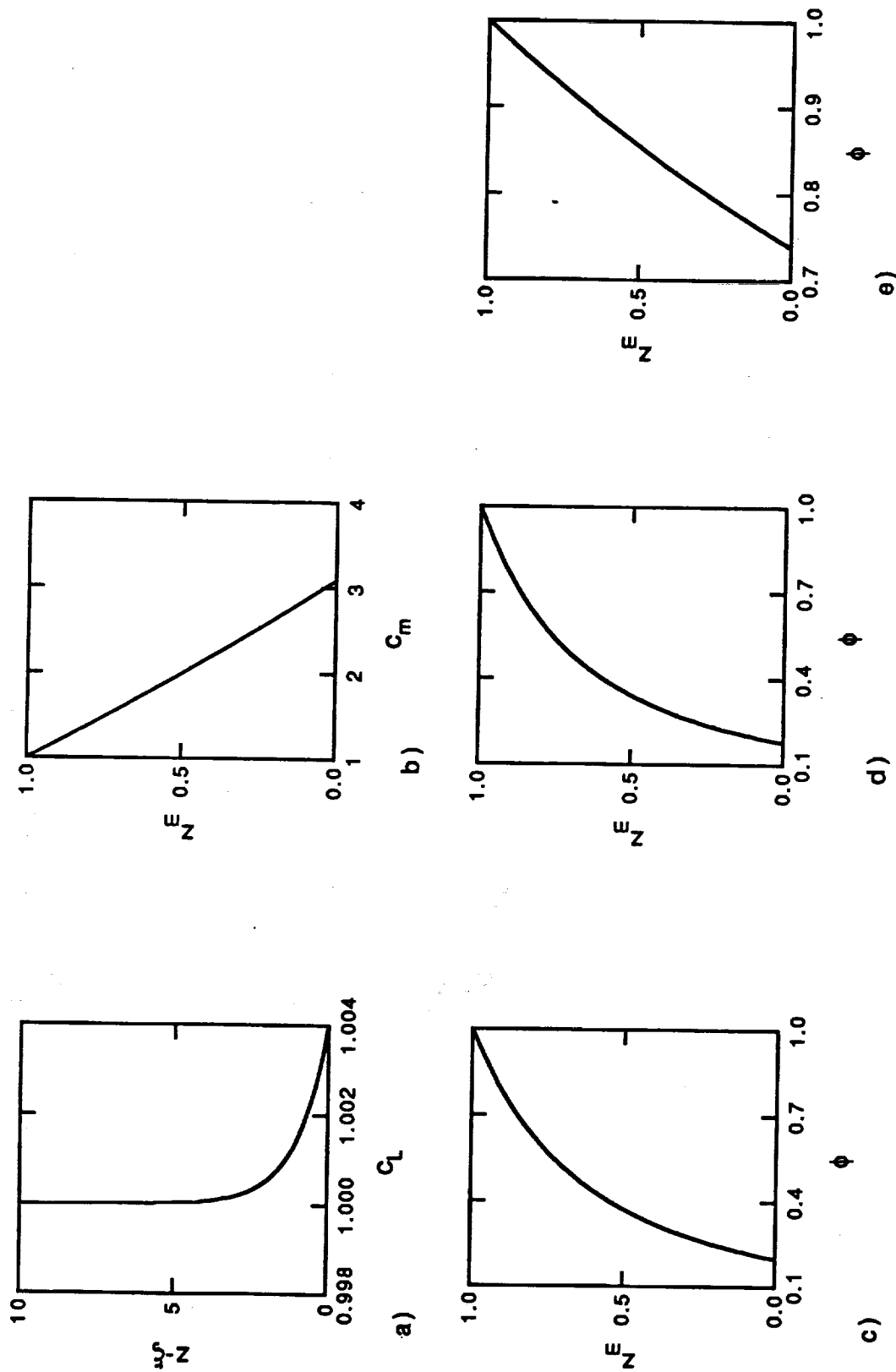


Figure 4.2. For dendritic solidification of Pb-Sn with  $\gamma = 2.59 \times 10^{-2}$  and  $\Gamma = 7.12 \times 10^{-2}$  ( $V_1 = 80 \mu \text{ sec}^{-1}$  and  $G_L = 50 \text{ K cm}^{-1}$ ), dimensionless basic state profiles of the composition a) in the liquid; b) in the mushy zone for  $C_\infty = 0.2$ ; e)  $C_\infty = 0.35$ ; f)  $C_\infty = 0.5$ . c)  $C_\infty = 0.1$ ; d)  $C_\infty = 0.2$ .

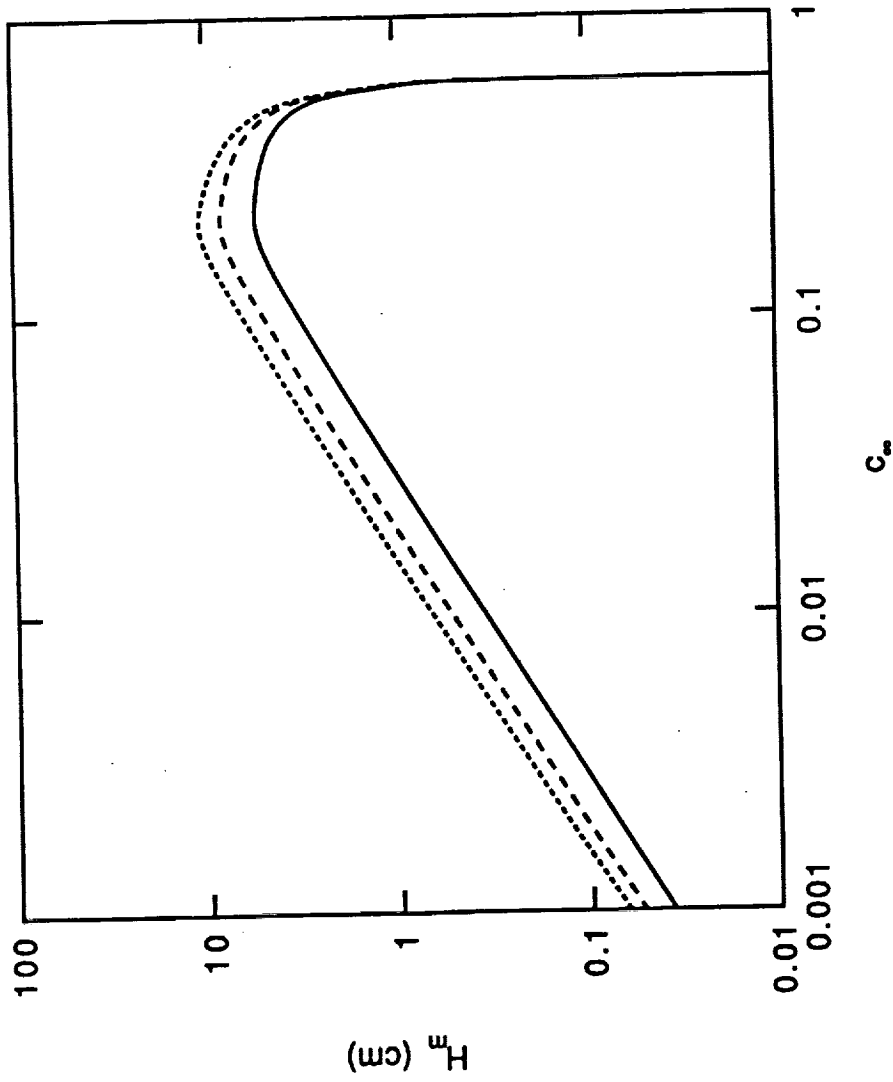


Figure 4.3a. For dendritic solidification of Pb-Sn, mushy-zone thickness  $H_m$  versus  $C_\infty$  for several values of  $\gamma$  with  $\Gamma = 7.12 \times 10^{-3}$  ( $G_L = 5 \text{ K cm}^{-1}$ ). The solid, dashed, and dotted curves in each figure are for  $\gamma = 3.24 \times 10^{-2}$  ( $V_1 = 100 \mu \text{ sec}^{-1}$ ),  $1.62 \times 10^{-2}$  ( $V_1 = 50 \mu \text{ sec}^{-1}$ ), and  $9.72 \times 10^{-3}$  ( $V_1 = 30 \mu \text{ sec}^{-1}$ ), respectively.

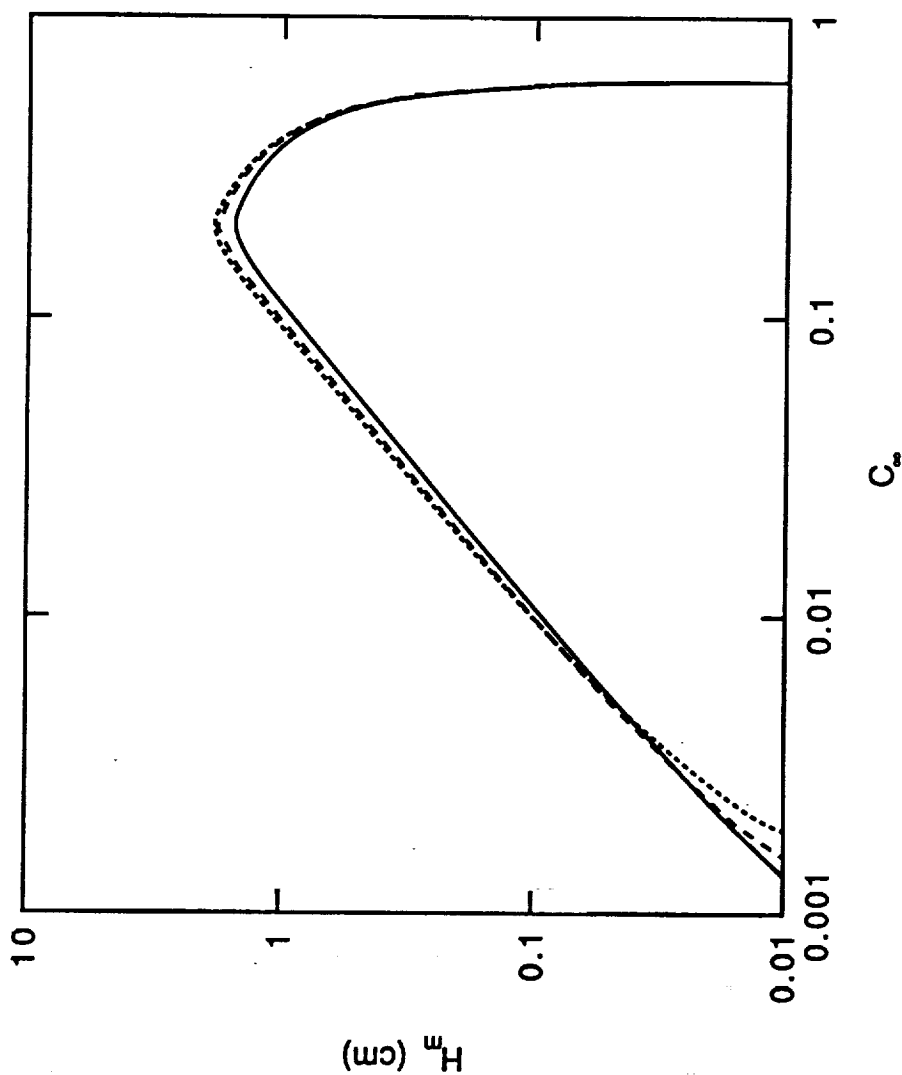


Figure 4.3b. For dendritic solidification of Pb-Sn, mushy-zone thickness  $H_m$  versus  $C_\infty$  for several values of  $\gamma$  with  $\Gamma = 7.12 \times 10^{-2}$  ( $G_L = 50 \text{ K cm}^{-1}$ ). The solid, dashed, and dotted curves in each figure are for  $\gamma = 3.24 \times 10^{-2}$  ( $V_1 = 100 \mu \text{ sec}^{-1}$ ),  $1.62 \times 10^{-2}$  ( $V_1 = 50 \mu \text{ sec}^{-1}$ ), and  $9.72 \times 10^{-3}$  ( $V_1 = 30 \mu \text{ sec}^{-1}$ ), respectively.

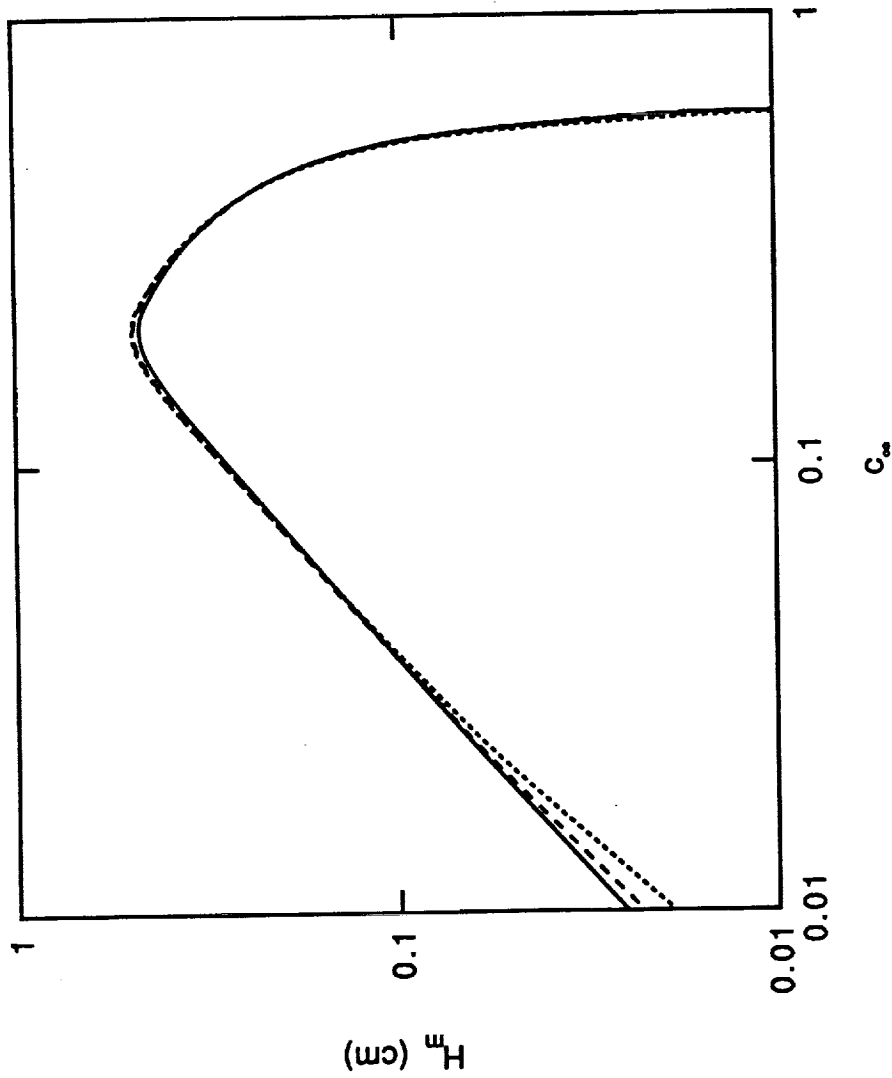


Figure 4.3c. For dendritic solidification of Pb-Sn, mushy-zone thickness  $H_m$  versus  $C_\infty$  for several values of  $\gamma$  with  $\Gamma = 0.285$  ( $G_L = 200 \text{ K cm}^{-1}$ ). The solid, dashed, and dotted curves in each figure are for  $\gamma = 3.24 \times 10^{-2}$  ( $V_1 = 100 \mu \text{ sec}^{-1}$ ),  $1.62 \times 10^{-2}$  ( $V_1 = 50 \mu \text{ sec}^{-1}$ ), and  $9.72 \times 10^{-3}$  ( $V_1 = 30 \mu \text{ sec}^{-1}$ ), respectively.

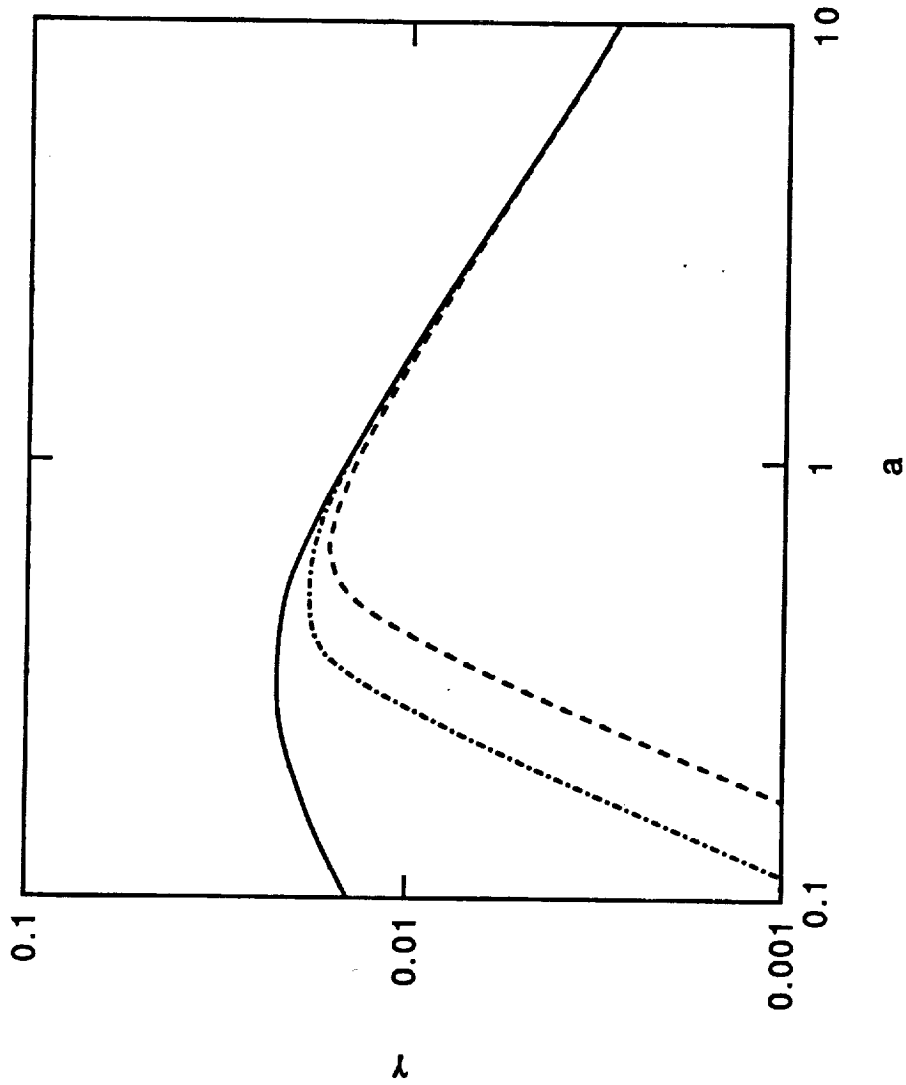


Figure 4.4a.  $\gamma$ - $a$  neutral curve for dendritic solidification of Pb-Sn with  $C_\infty = 0.1$ ,  $\Gamma = 7.12 \times 10^{-2}$  ( $G_L = 50 \text{ K cm}^{-1}$ ) for several values of  $\Omega_0$ . The solid, dashed-dot, and dashed curves in each figure are for  $\Omega_0 = 0, 300, 500 \text{ rpm}$ , respectively. The stable combinations of  $\gamma$  and  $a$  lie above the respective neutral curves.

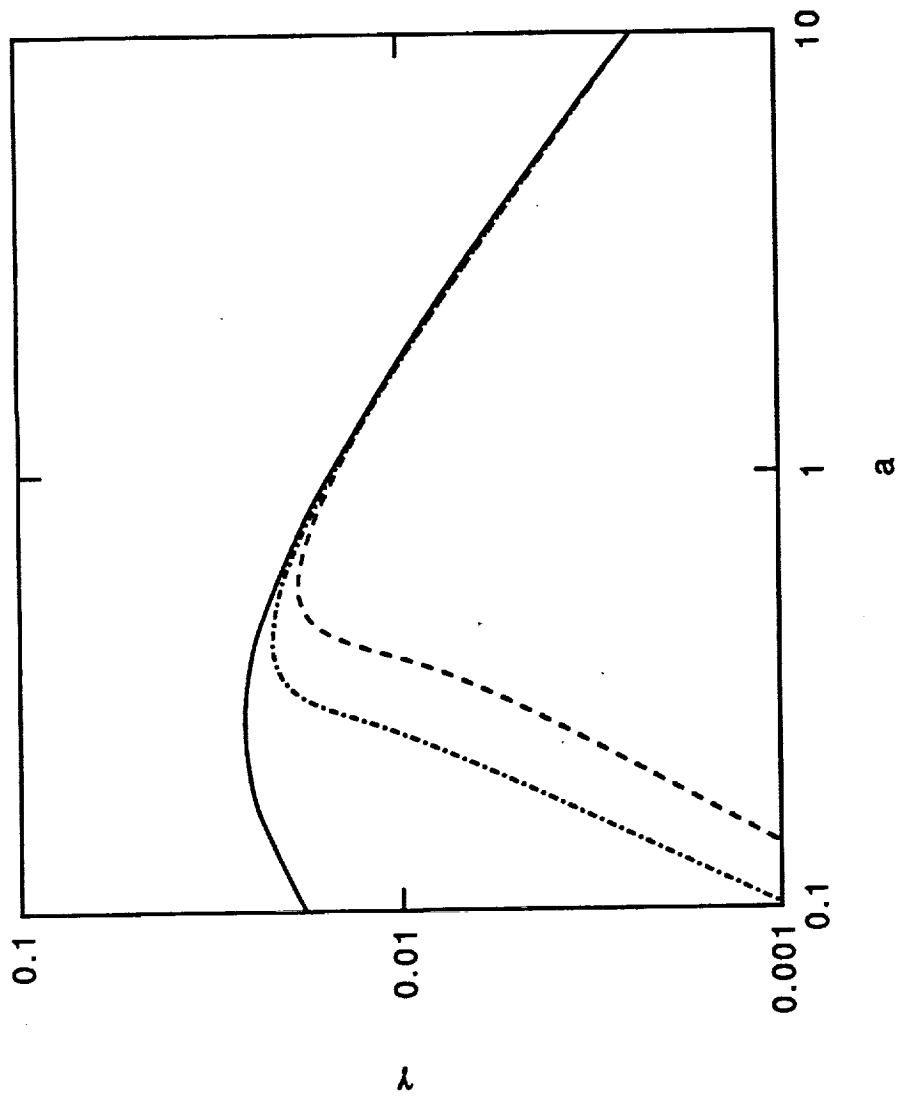


Figure 4.4b.  $\gamma$ - $a$  neutral curve for dendritic solidification of Pb-Sn with  $C_\infty = 0.2$ ,  $\Gamma = 7.12 \times 10^{-2}$  ( $G_L = 50 \text{ K cm}^{-1}$ ) for several values of  $\Omega_0$ . The solid, dashed-dot, and dashed curves in each figure are for  $\Omega_0 = 0$ , 300, 500 rpm, respectively. The stable combinations of  $\gamma$  and  $a$  lie above the respective neutral curves.

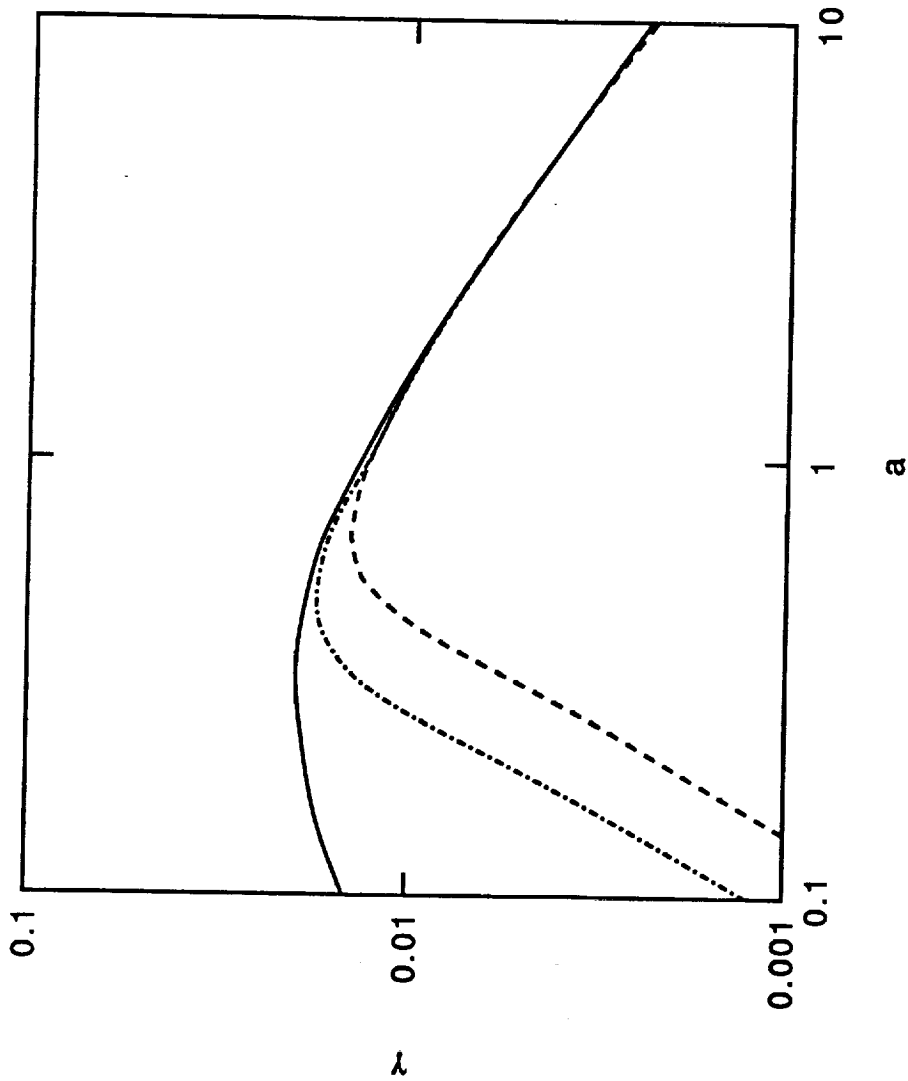


Figure 4.4c.  $\gamma$ - $a$  neutral curve for dendritic solidification of Pb-Sn with  $C_\infty = 0.55$ ,  $\Gamma = 7.12 \times 10^{-2}$  ( $G_L = 50 \text{ K cm}^{-1}$ ) for several values of  $\Omega_0$ . The solid, dashed-dot, and dashed curves in each figure are for  $\Omega_0 = 0$ , 300, 500 rpm, respectively. The stable combinations of  $\gamma$  and  $a$  lie above the respective neutral curves.

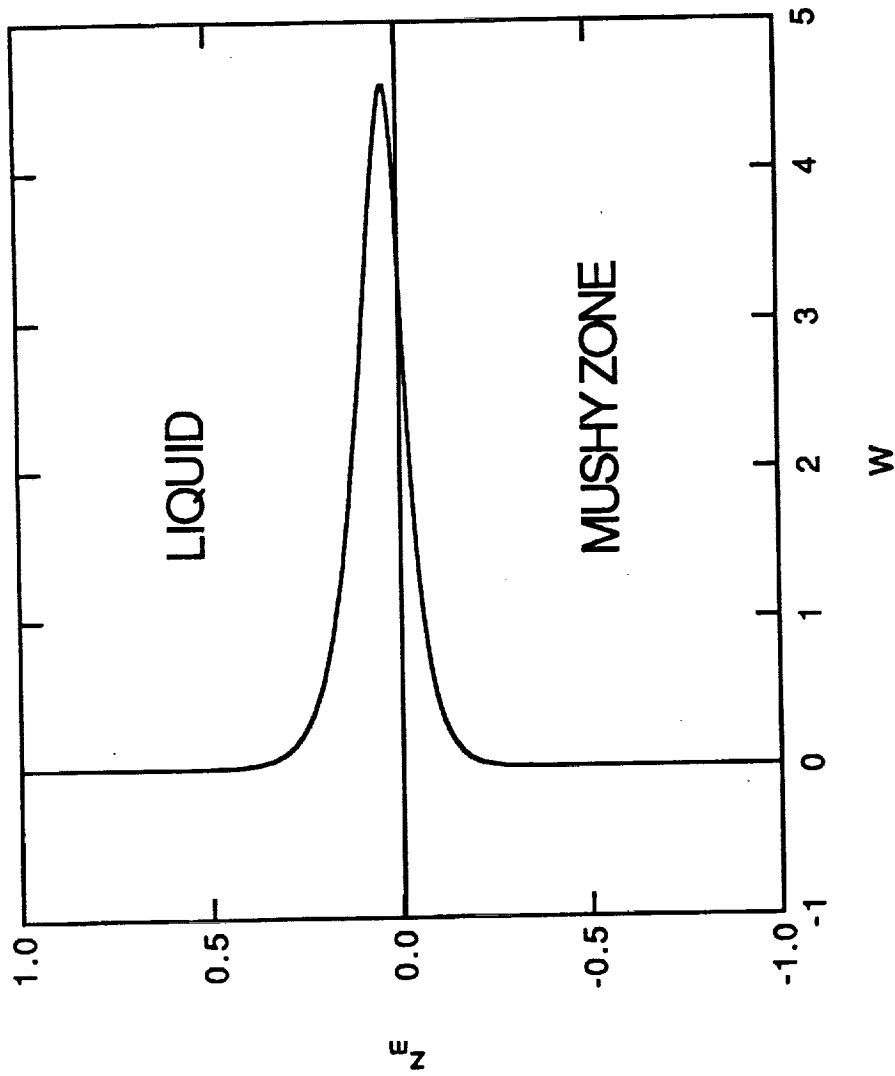


Figure 4.5a. For dendritic solidification of Pb-Sn with  $C_\infty = 0.55$ ,  $\Gamma = 7.12 \times 10^{-2}$  ( $G_L = 50 \text{ K cm}^{-1}$ ), and  $\Omega_0 = 0 \text{ rpm}$ , amplitude of dimensionless disturbances  $[y = 1.976 \times 10^{-2} (V_1 = 61 \mu \text{ sec}^{-1})$  and  $a = 0.32]$  to vertical velocity in the liquid and mushy zone.



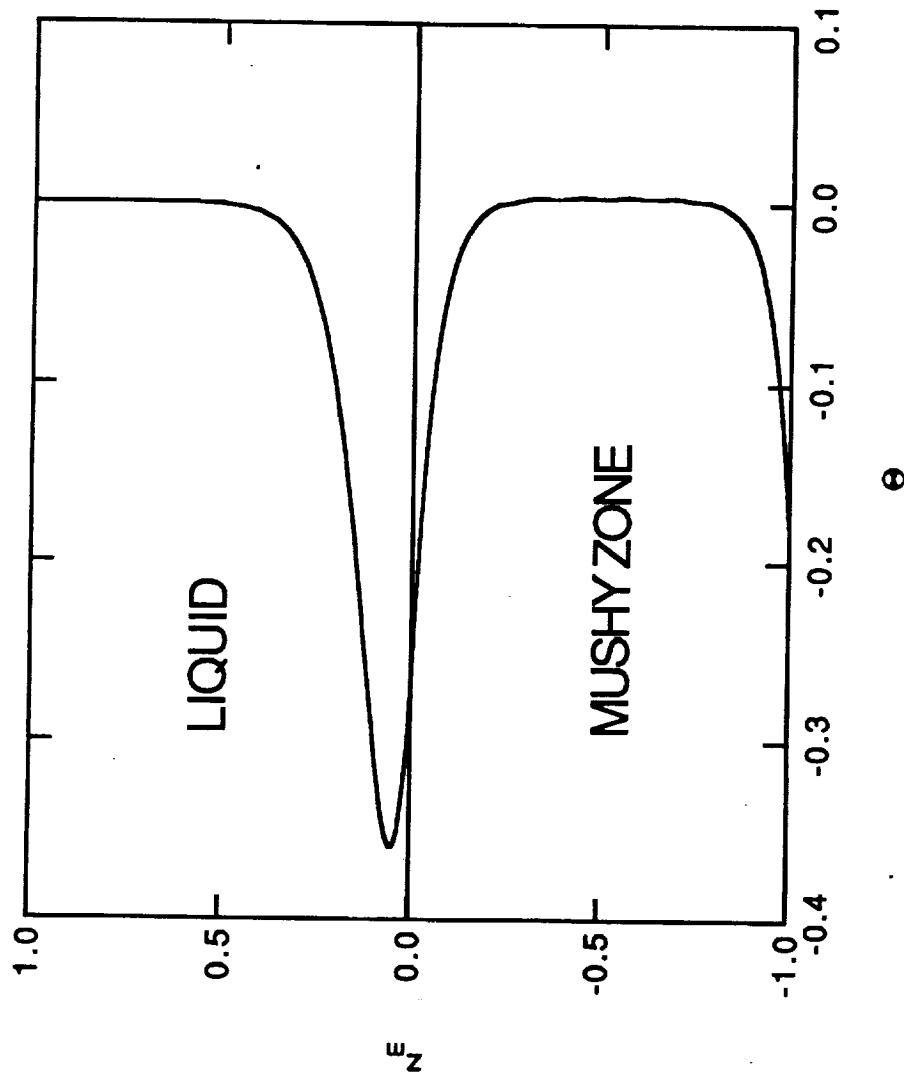


Figure 4.5b. For dendritic solidification of Pb-Sn with  $C_{\infty} = 0.55$ ,  $\Gamma = 7.12 \times 10^{-2}$  ( $G_L = 50 \text{ K cm}^{-1}$ ), and  $\Omega_0 = 0 \text{ rpm}$ , amplitude of dimensionless disturbances  $[\gamma = 1.976 \times 10^{-2}$  ( $V_I = 61 \mu \text{ sec}^{-1}$ ) and  $a = 0.32$ ] to temperature in the liquid and mushy zone.

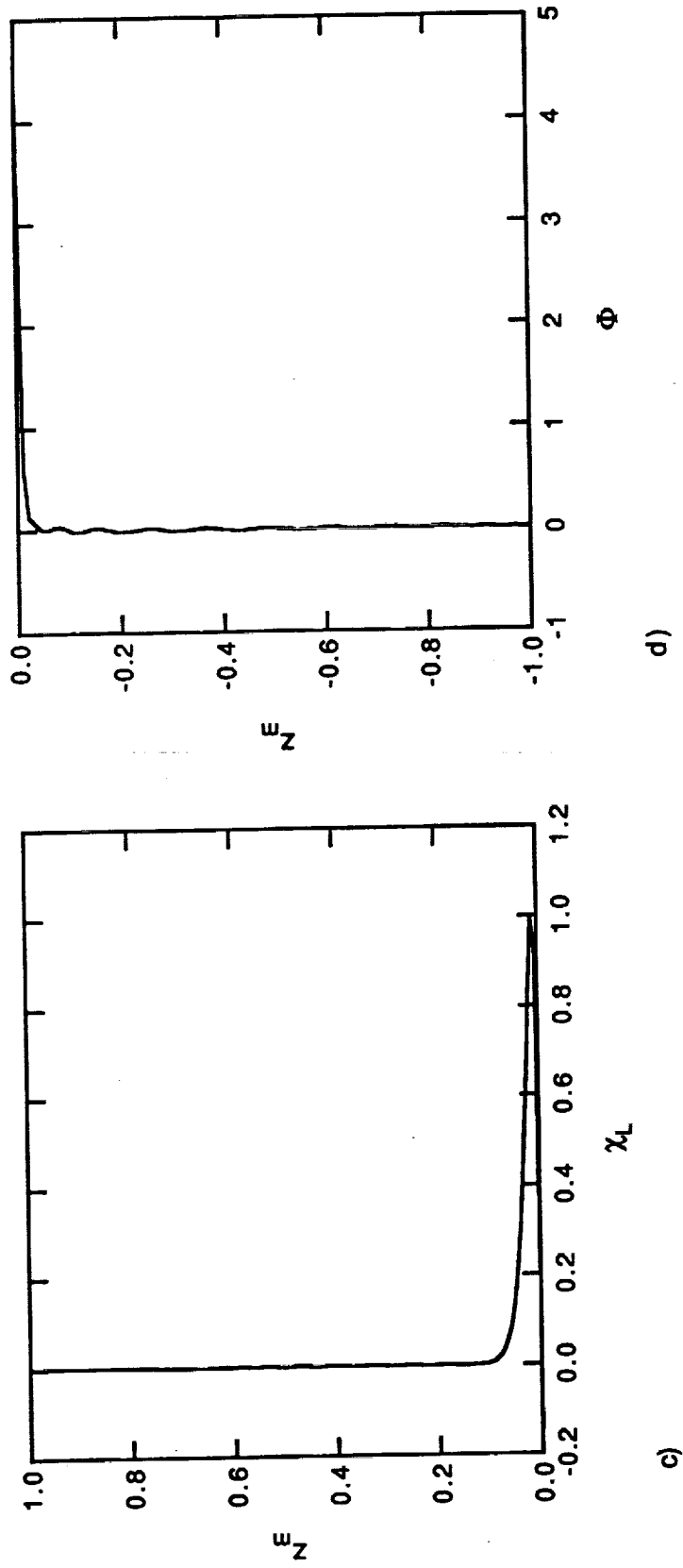


Figure 4.5. For dendritic solidification of Pb-Sn with  $C_\infty = 0.55$ ,  $\Gamma = 7.12 \times 10^{-2}$  ( $G_L = 50 \text{ K cm}^{-1}$ ), and  $\Omega_0 = 0 \text{ rpm}$ , amplitude of dimensionless disturbances at critical conditions [ $\gamma = 1.976 \times 10^{-2}$  ( $V_1 = 61 \mu \text{ sec}^{-1}$ ) and  $a = 0.32$ ] to c) composition in the liquid; d) volume fraction.

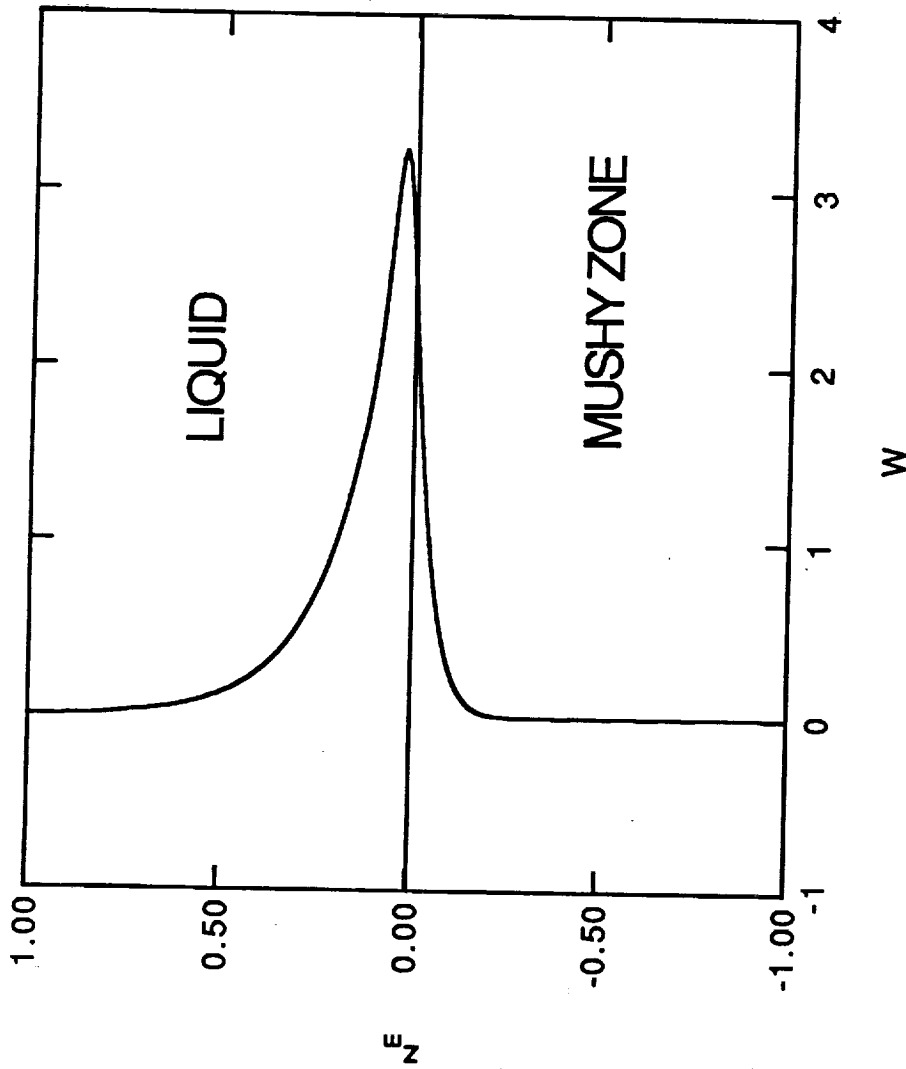


Figure 4.6a. For dendritic solidification of Pb-Sn with  $C_\infty = 0.55$ ,  $\Gamma = 7.12 \times 10^{-2}$  ( $G_L = 50 \text{ K cm}^{-1}$ ), and  $\Omega_0 = 500 \text{ rpm}$ , amplitude of dimensionless disturbances at critical conditions [ $\gamma = 1.976 \times 10^{-2}$  ( $V_1 = 61 \mu \text{ sec}^{-1}$ ) and  $a = 0.32$ ] to vertical velocity in the liquid and mushy zone.

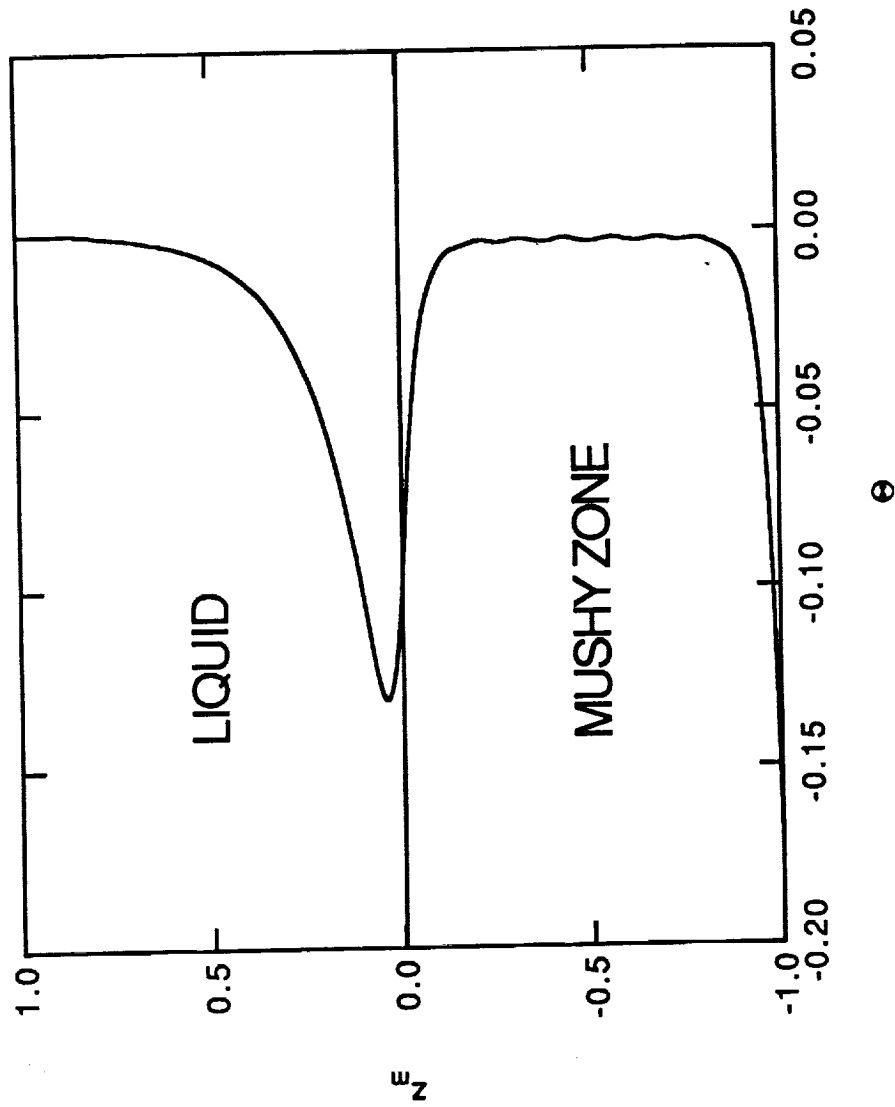


Figure 4.6b. For dendritic solidification of Pb-Sn with  $C_\infty = 0.55$ ,  $\Gamma = 7.12 \times 10^{-2}$  ( $G_L = 50 \text{ K cm}^{-1}$ ), and  $\Omega_0 = 500 \text{ rpm}$ , amplitude of dimensionless disturbances at critical conditions [ $\gamma = 1.976 \times 10^{-2}$  ( $V_f = 61 \mu \text{ sec}^{-1}$ ) and  $a = 0.32$ ] to temperature in the liquid and mushy zone.

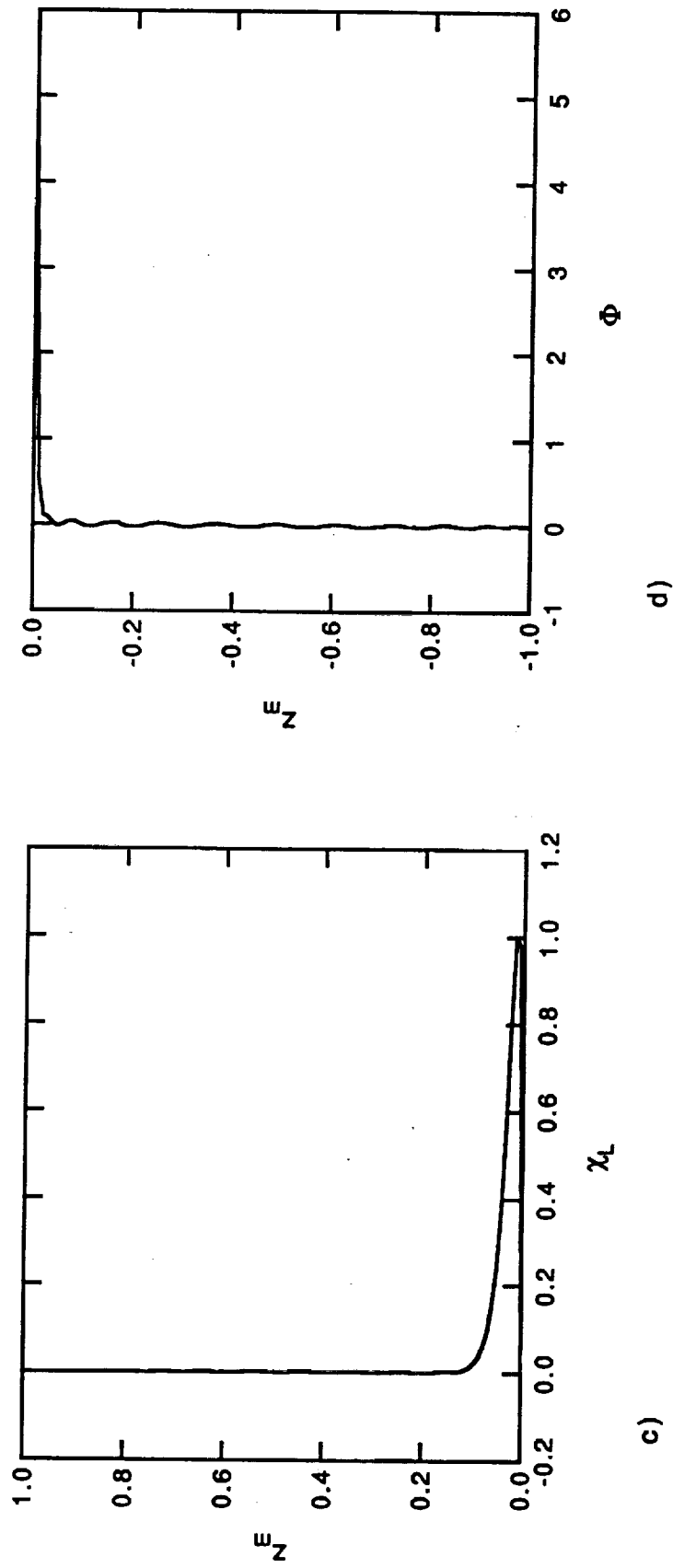


Figure 4.6. For dendritic solidification of Pb-Sn with  $C_\infty = 0.55$ ,  $\Gamma = 7.12 \times 10^{-2}$  ( $G_L = 50 \text{ K cm}^{-1}$ ), and  $\Omega_0 = 500 \text{ rpm}$ , amplitude of dimensionless disturbances at critical conditions [ $\gamma = 1.976 \times 10^{-2}$  ( $V_1 = 61 \mu \text{ sec}^{-1}$ ) and  $a = 0.32$ ] to c) composition in the liquid; d) volume fraction.

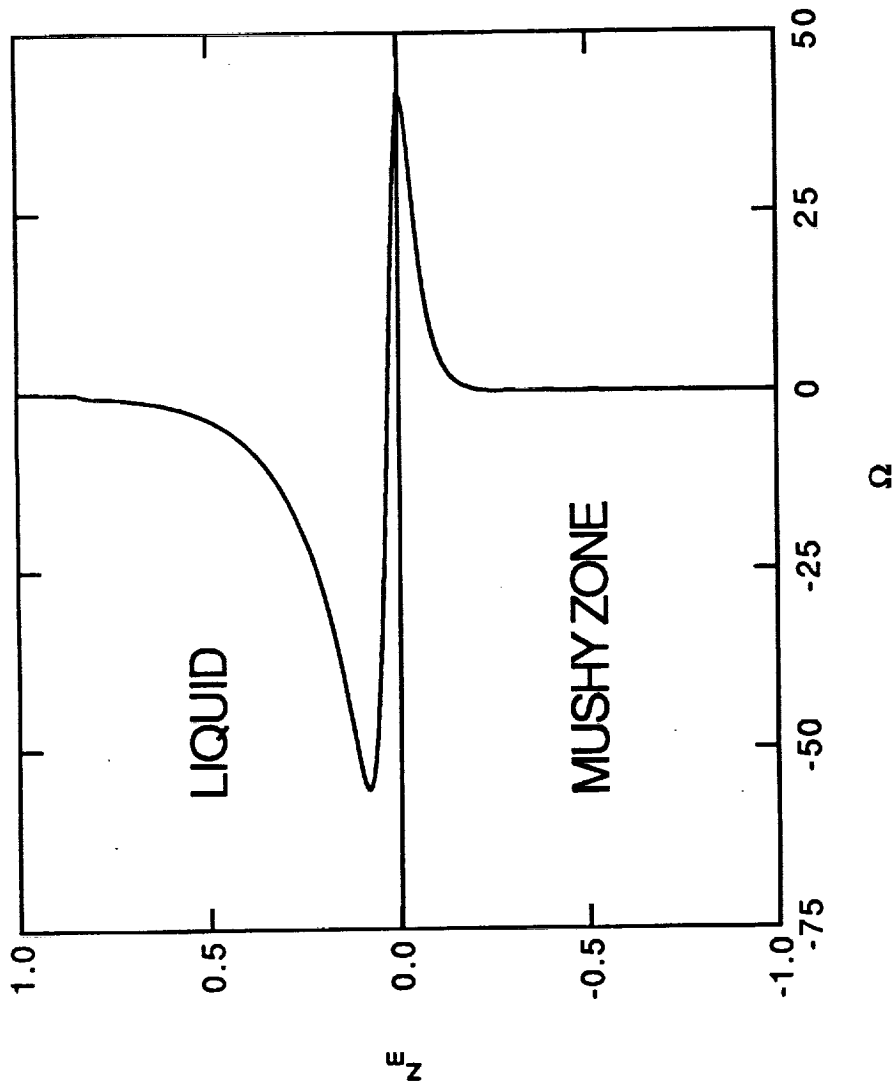


Figure 4.6e. For dendritic solidification of Pb-Sn with  $C_\infty = 0.55$ ,  $\Gamma = 7.12 \times 10^{-2}$  ( $G_L = 50 \text{ K cm}^{-1}$ ), and  $\Omega_0 = 500 \text{ rpm}$ , amplitude of dimensionless disturbances at critical conditions [ $\gamma = 1.976 \times 10^{-2}$  ( $V_I = 61 \mu \text{ sec}^{-1}$ ) and  $a = 0.32$ ] to vorticity in the liquid and mushy zone.

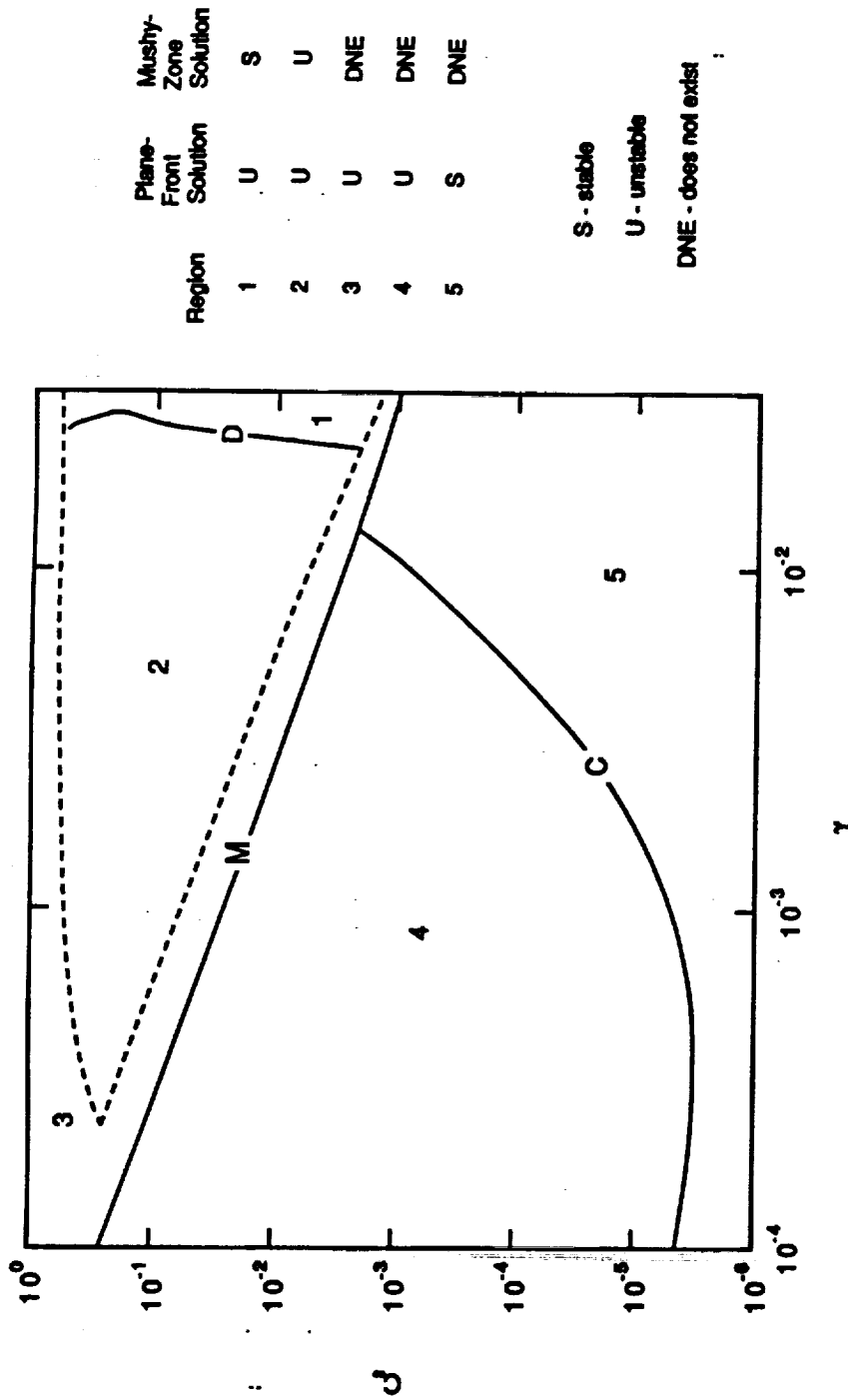


Figure 4.7a. Division of the  $\gamma$ - $C_m$  plane for solidification of Pb-Sn, according to existence and stability of one-dimensional solutions for  $\Gamma = 0.285$  ( $G_L = 200 \text{ K cm}^{-1}$ ) for  $\Omega_0 = 0 \text{ rpm}$ . The solid curves D, M, and C are the dendritic stability boundary, and the plane-front morphological and plane-front convective stability boundaries, respectively. The dashed curve bounds the region in which the one-dimensional dendritic solution exists. The numbering of the regions is described in the text.

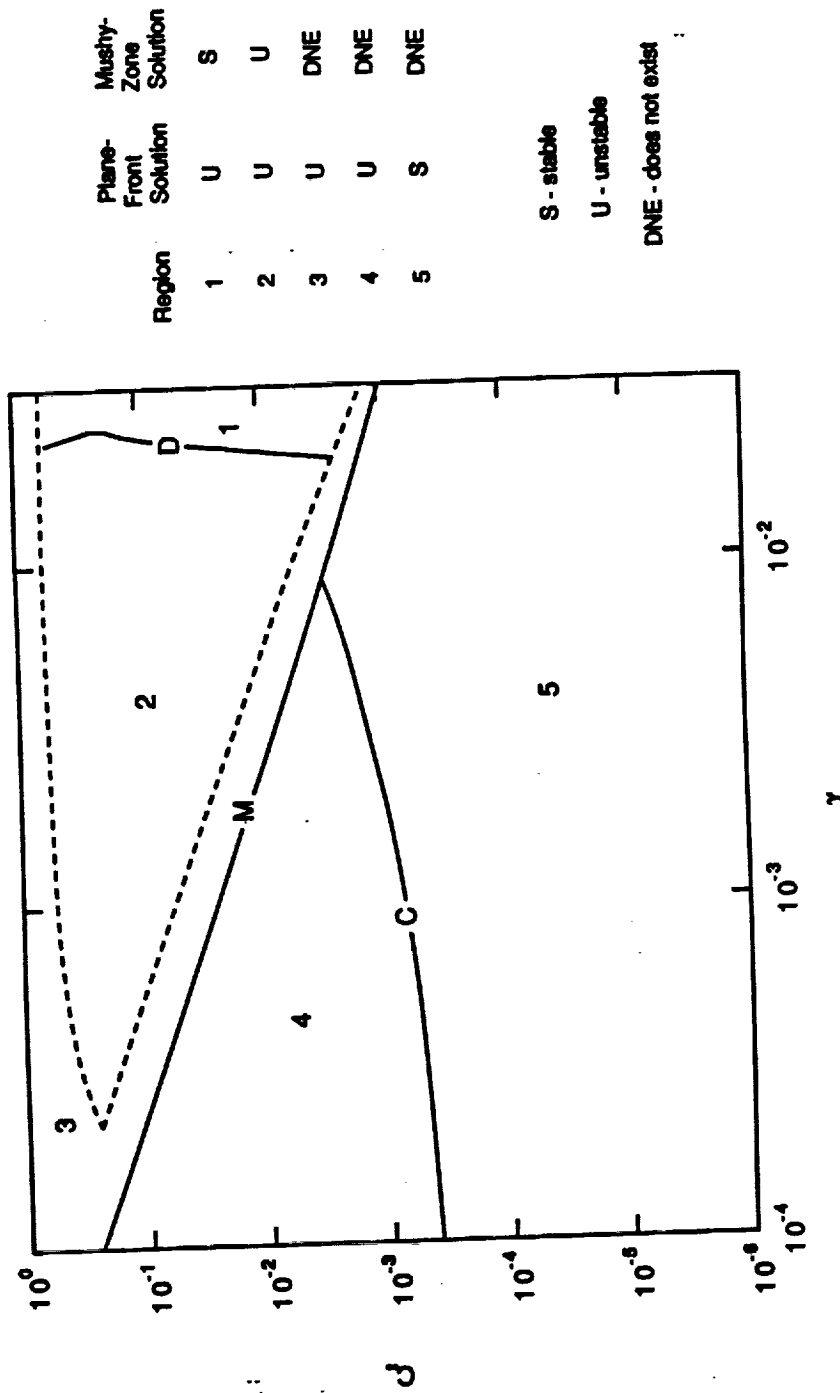


Figure 4.7b. Division of the  $\gamma$ - $C_{\infty}$  plane for solidification of Pb-Sn, according to existence and stability of one-dimensional solutions for  $\Gamma = 0.285$  ( $G_L = 200 \text{ K cm}^{-1}$ ) for  $\Omega_0 = 500 \text{ rpm}$ . The solid curves D, M, and C are the dendritic stability boundary, and the plane-front morphological and plane-front convective stability boundaries, respectively. The dashed curve bounds the region in which the one-dimensional dendritic solution exists. The numbering of the regions is described in the text.



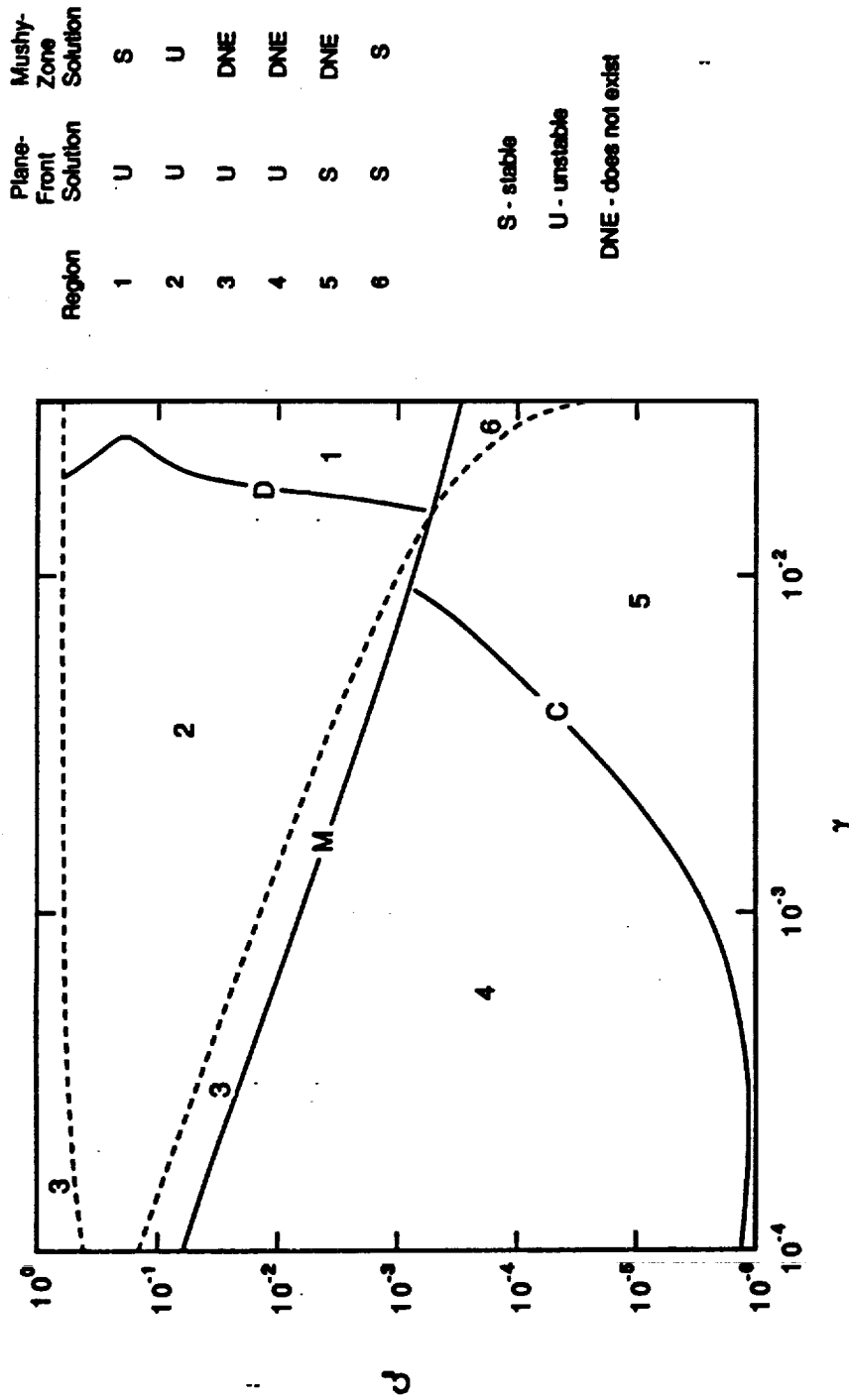


Figure 4.8a. Division of the  $\gamma$ - $C_\infty$  plane for solidification of Pb-Sn, according to existence and stability of one-dimensional solutions for  $\Gamma = 7.12 \times 10^{-2}$  ( $G_L = 50 \text{ K cm}^{-1}$ ) for  $\Omega_0 = 0 \text{ rpm}$ . The solid curves D, M, and C are the dendritic stability boundary, and the plane-front morphological and plane-front convective stability boundaries, respectively. The dashed curve bounds the region in which the one-dimensional dendritic solution exists. The numbering of the regions is described in the text.

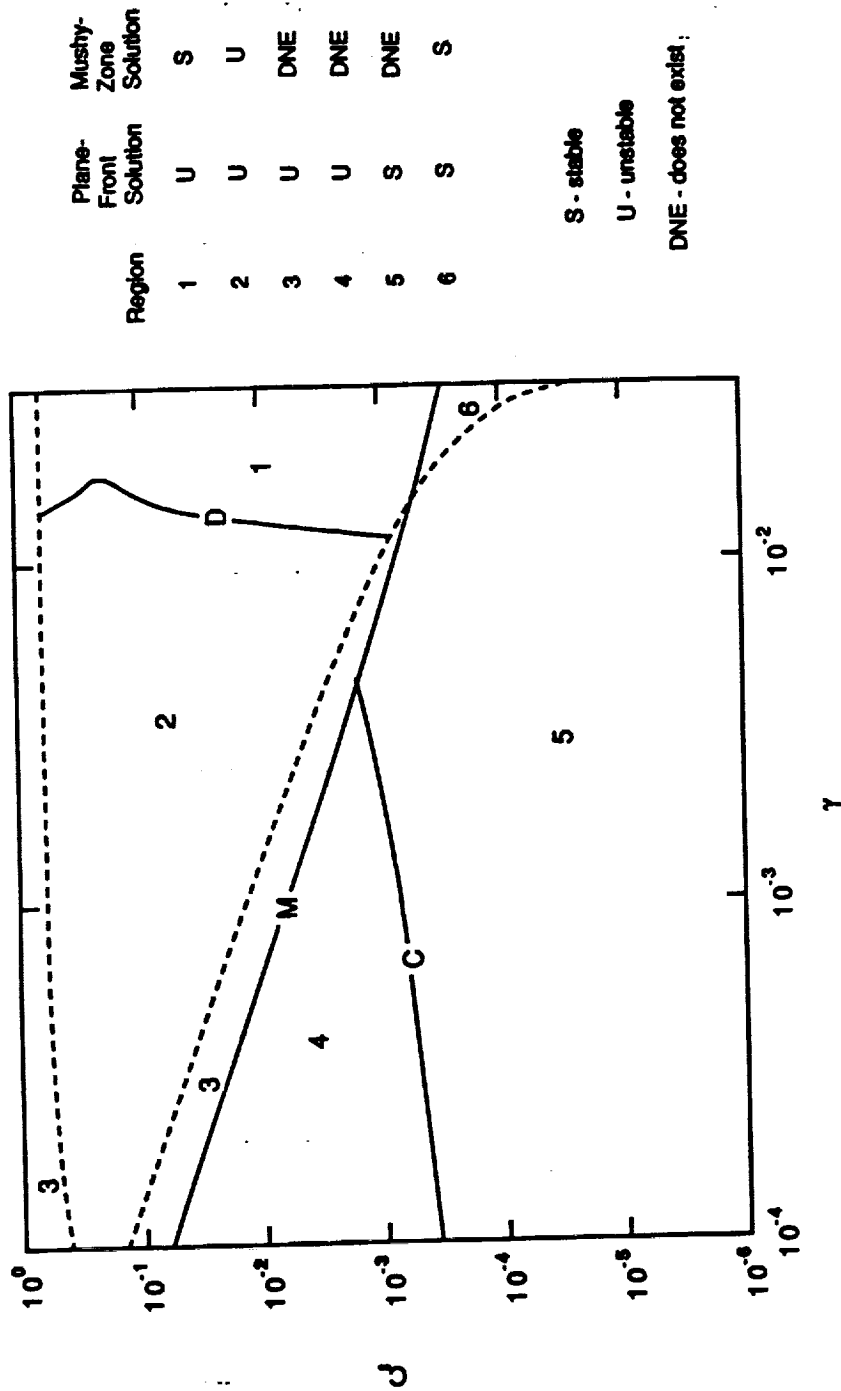


Figure 4.8b. Division of the  $\gamma$ - $C_m$  plane for solidification of Pb-Sn, according to existence and stability of one-dimensional solutions for  $\Gamma = 7.12 \times 10^{-2}$  ( $G_L = 50 \text{ K cm}^{-1}$ ) for  $\Omega_0 = 500 \text{ rpm}$ . The solid curves D, M, and C are the dendritic stability boundary, and the plane-front morphological and plane-front convective stability boundaries, respectively. The dashed curve bounds the region in which the one-dimensional dendritic solution exists. The numbering of the regions is described in the text.

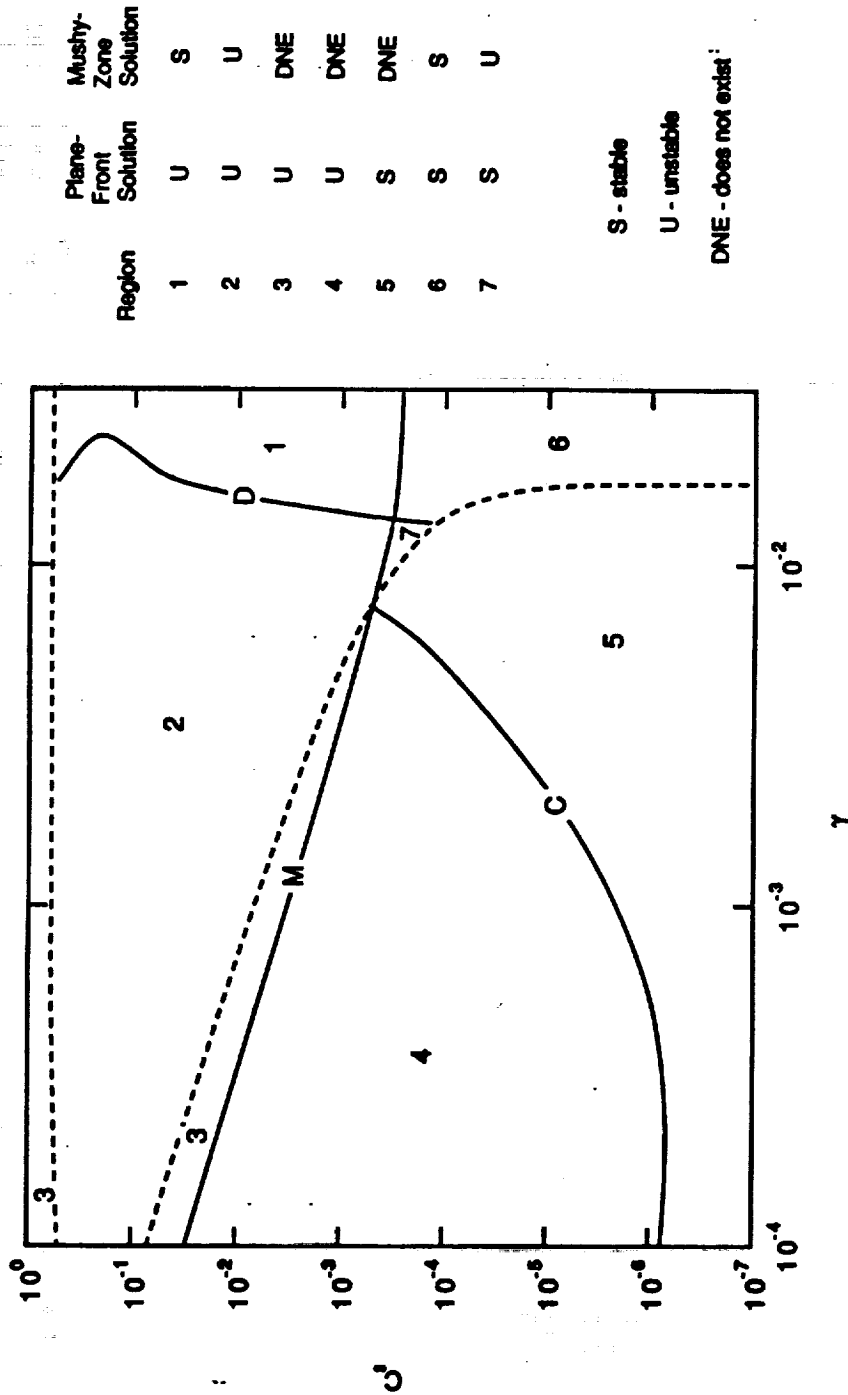


Figure 4.9a. Division of the  $\gamma$ - $C_{\infty}$  plane for solidification of Pb-Sn, according to existence and stability of one-dimensional solutions for  $\Gamma = 3.56 \times 10^{-2}$  ( $G_L = 25 \text{ K cm}^{-1}$ ) for  $\Omega_0 = 0 \text{ rpm}$ . The solid curves D, M, and C are the dendritic stability boundary, and the plane-front morphological and plane-front convective stability boundaries, respectively. The dashed curve bounds the region in which the one-dimensional dendritic solution exists. The numbering of the regions is described in the text.

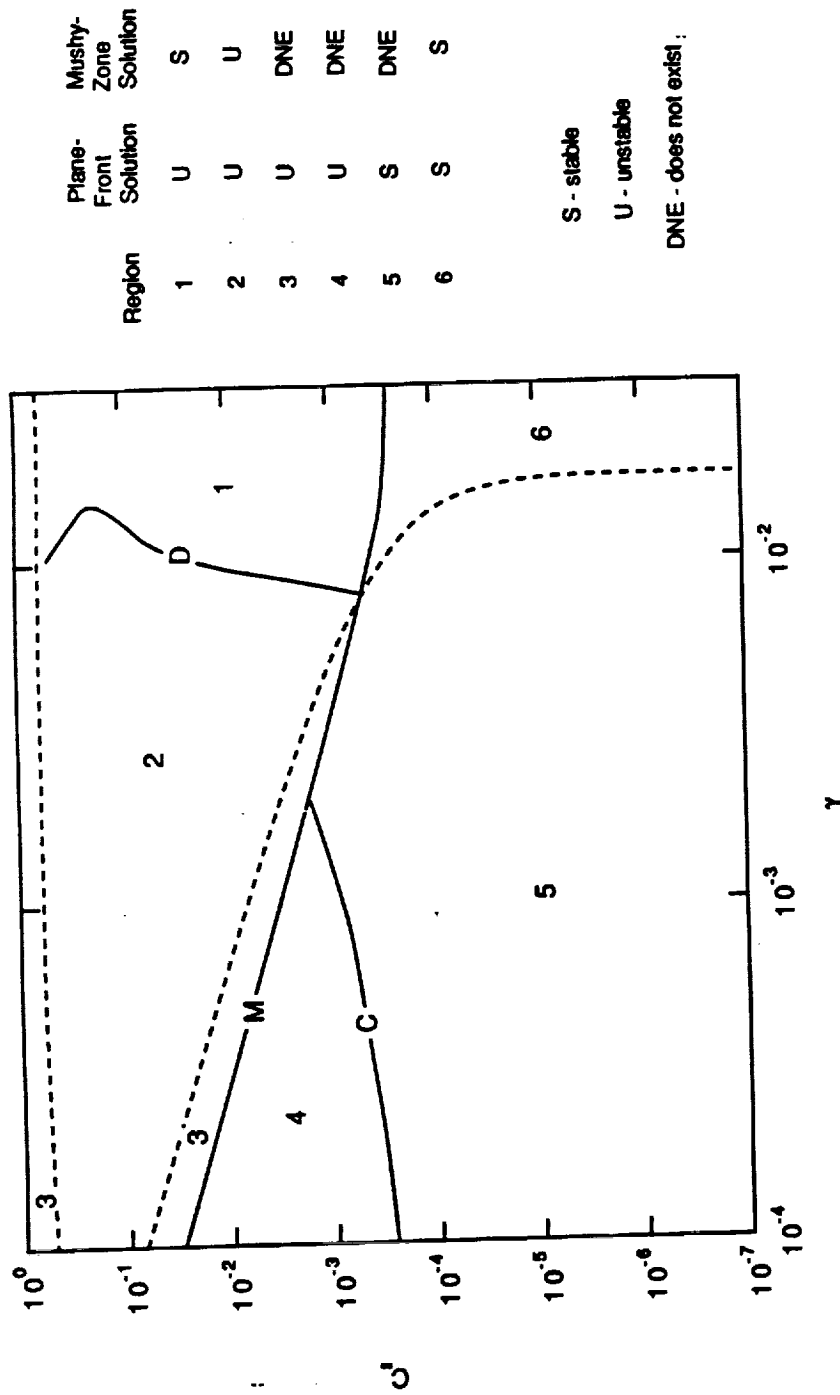


Figure 4.9b. Division of the  $\gamma$ - $C_{\infty}$  plane for solidification of Pb-Sn, according to existence and stability of one-dimensional solutions for  $\Gamma = 3.56 \times 10^{-2}$  ( $G_L = 25 \text{ K cm}^{-1}$ ) for  $\Omega_0 = 500 \text{ rpm}$ . The solid curves D, M, and C are the dendritic stability boundary, and the plane-front morphological and plane-front convective stability boundaries, respectively. The dashed curve bounds the region in which the one-dimensional dendritic solution exists. The numbering of the regions is described in the text.

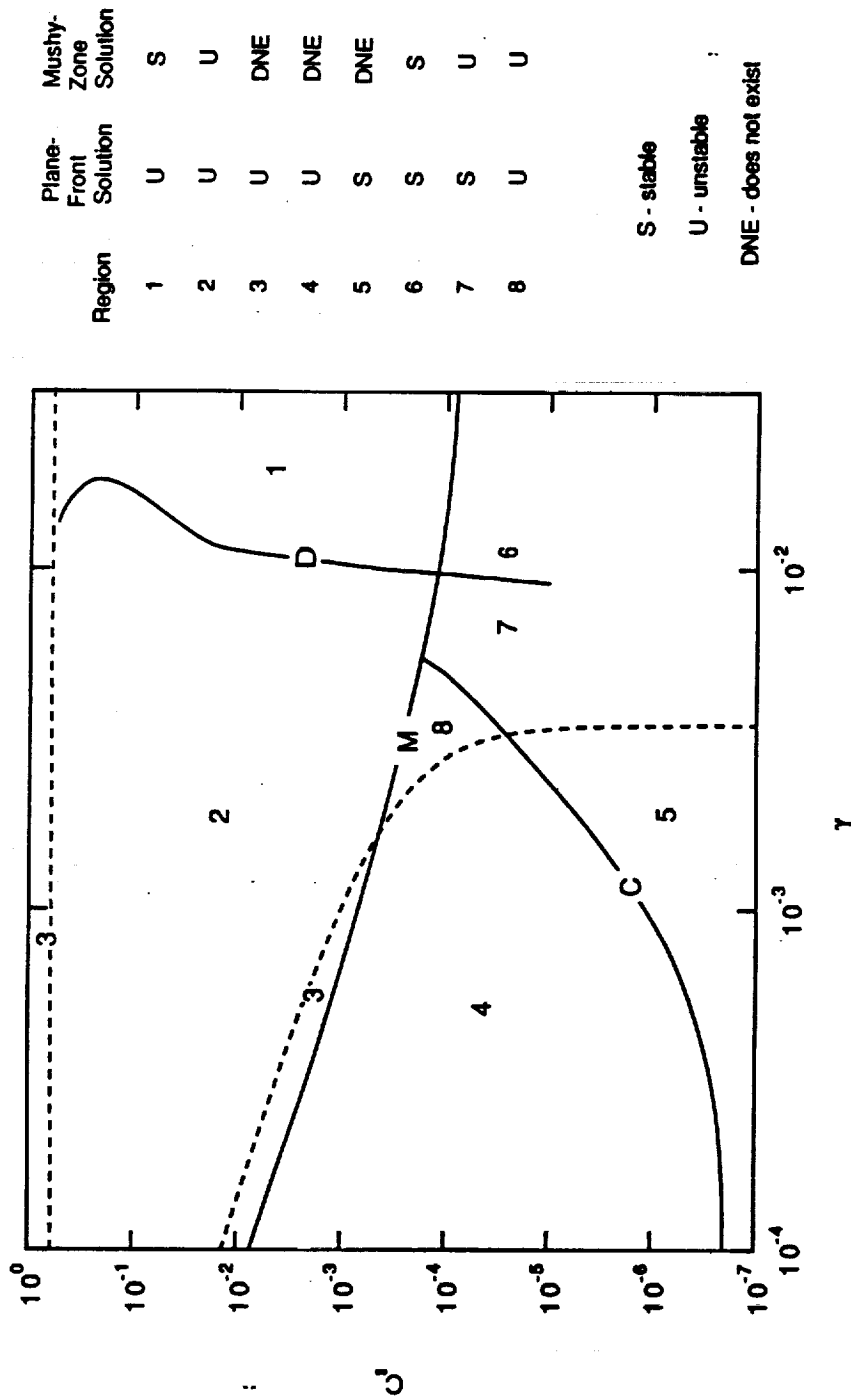


Figure 4.10a. Division of the  $\gamma$ - $C_{\infty}$  plane for solidification of Pb-Sn, according to existence and stability of one-dimensional solutions for  $\Gamma = 7.12 \times 10^{-3}$  ( $G_L = 5 \text{ K cm}^{-1}$ ) for  $\Omega_0 = 0 \text{ rpm}$ . The solid curves D, M, and C are the dendritic stability boundary, and the plane-front morphological and plane-front convective stability boundaries, respectively. The dashed curve bounds the region in which the one-dimensional dendritic solution exists. The numbering of the regions is described in the text.

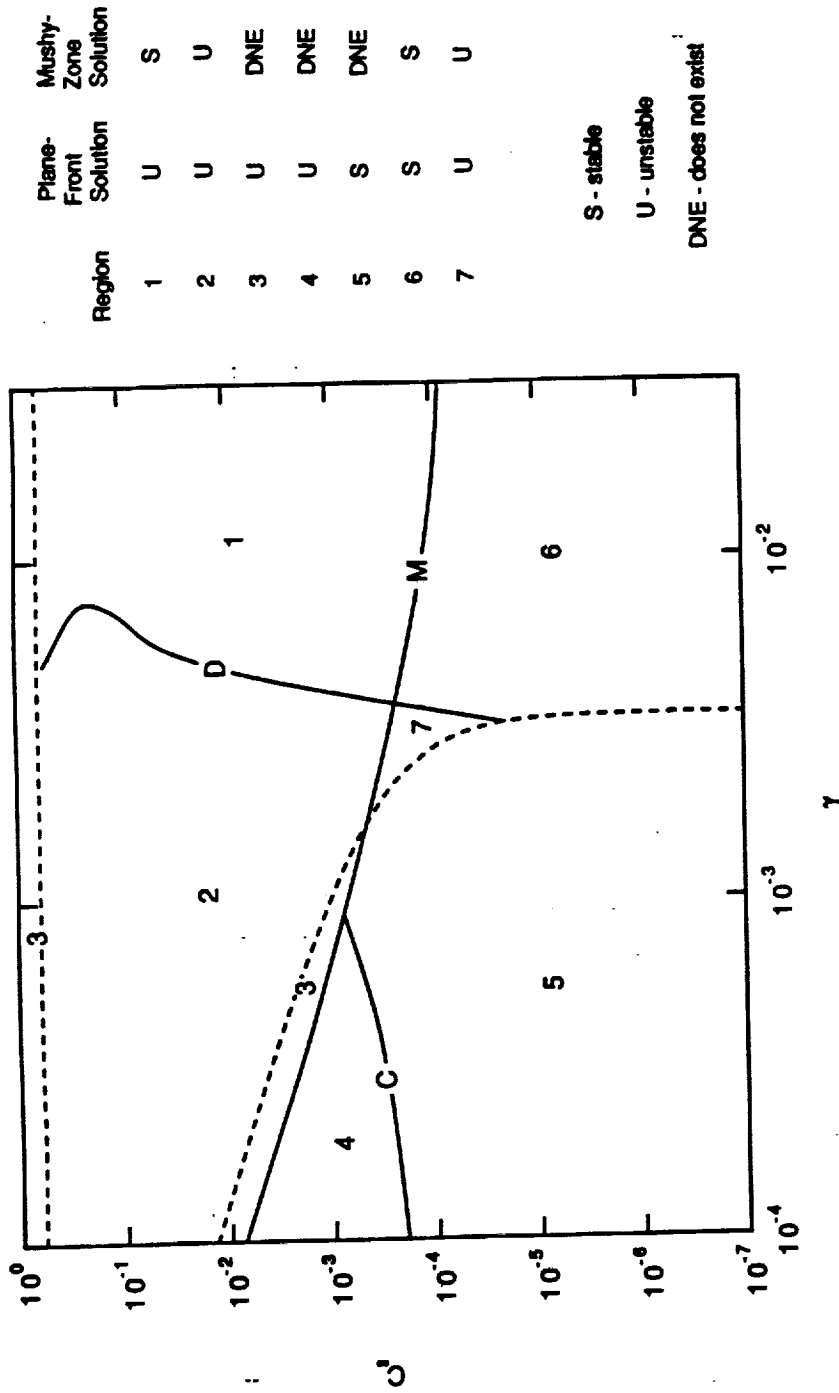


Figure 4.10b. Division of the  $\gamma$ - $C_\infty$  plane for solidification of Pb-Sn, according to existence and stability of one-dimensional solutions for  $\Gamma = 7.12 \times 10^{-3}$  ( $G_L = 5 \text{ K cm}^{-1}$ ) for  $\Omega_0 = 500 \text{ rpm}$ . The solid curves D, M, and C are the dendritic stability boundary, and the plane-front morphological and plane-front convective stability boundaries, respectively. The dashed curve bounds the region in which the one-dimensional dendritic solution exists. The numbering of the regions is described in the text.

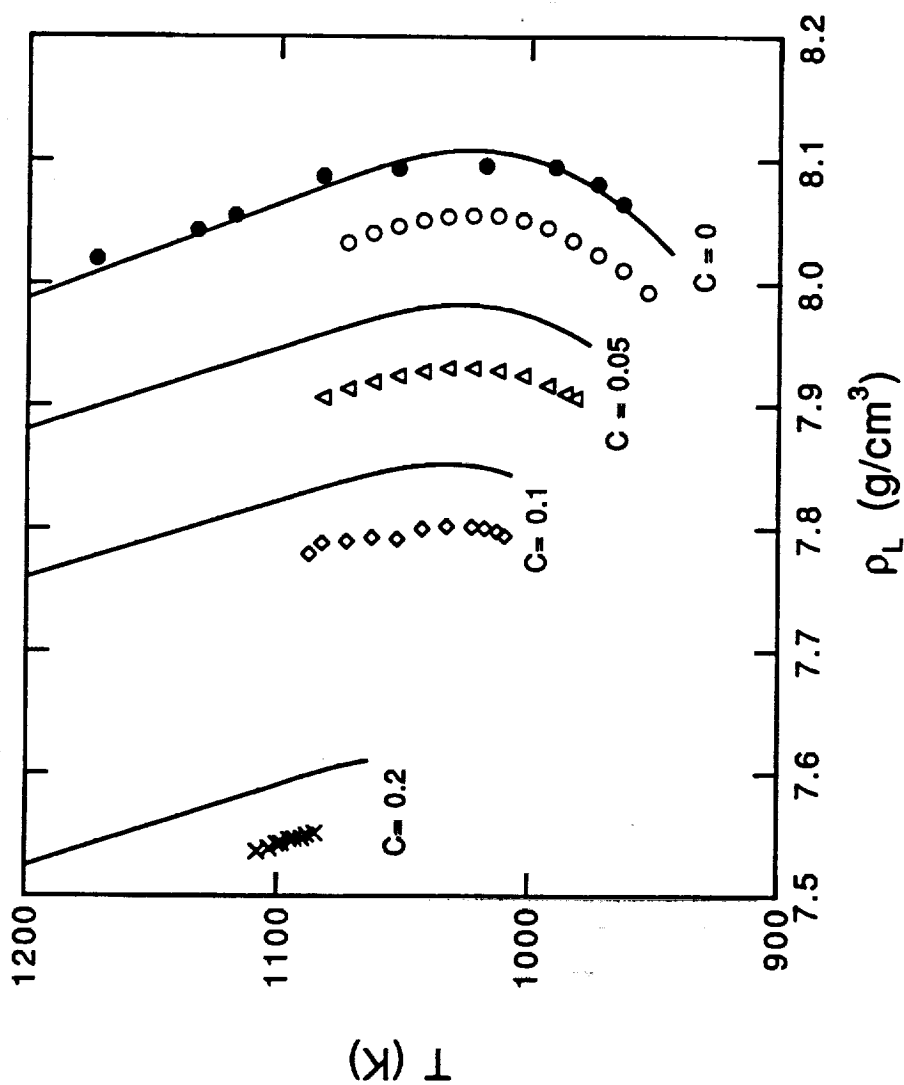


Figure B1. Liquid density versus  $T$  for  $C = 0$  and  $0.1$ .  $\circ$ : data of Mokrovskii & Regel (1952) for pure HgTe.  $\triangle$ : data of Chandra & Holland (1983) for pure HgTe.  $\diamond$ : data of Chandra & Holland for  $\text{Hg}_{0.9}\text{Cd}_{0.1}\text{Te}$ . —: least squares fit (3.7a,b) computed as per Appendix A. The low-temperature endpoint of each curve corresponds to the melting point determined from the phase diagram of Szofran & Lehoczky (1981).

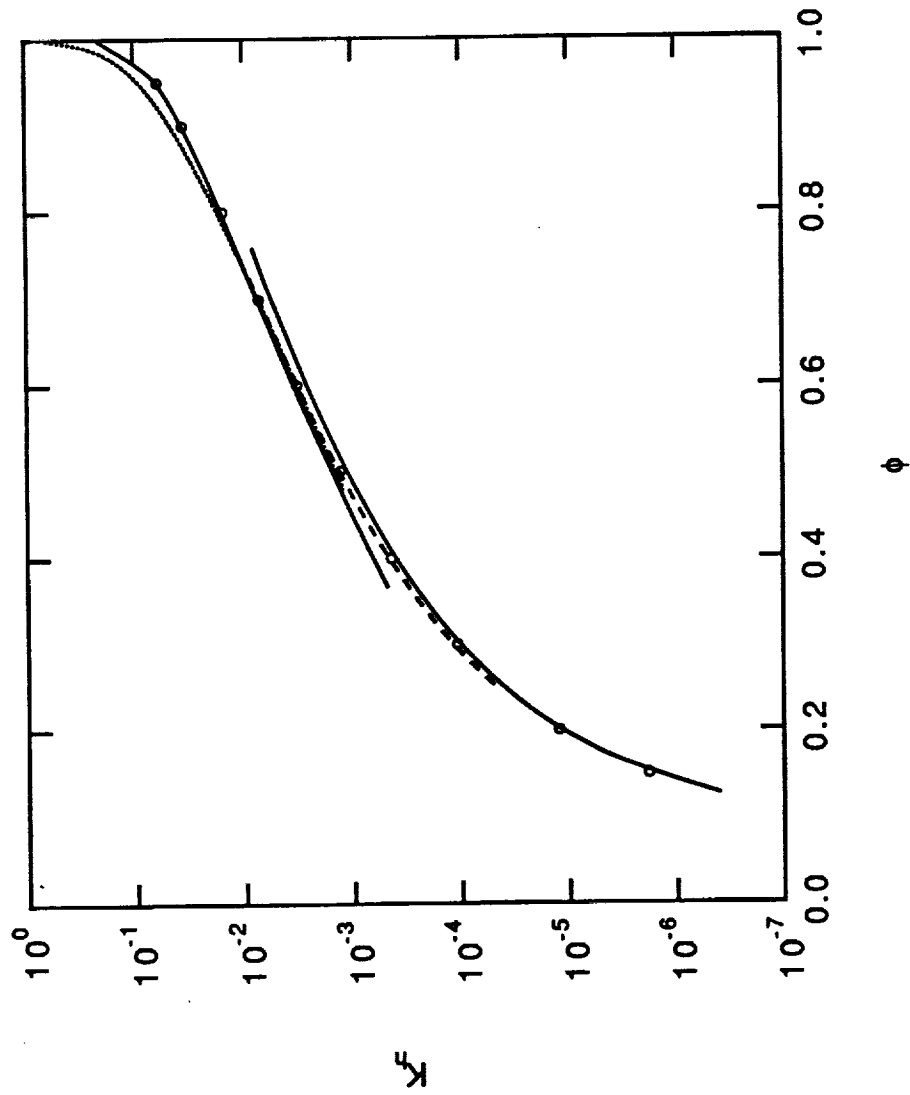


Figure D1. Horizontal component of permeability versus liquid volume fraction  $\phi$ . The solid curves are the asymptotes derived by Sangani & Acrivos (1982a) for flow normal to the axes of cylinders in dilute and concentrated hexagonal arrays. The open circles and dotted curve show the permeability calculations of Sangani & Acrivos (1982a-b) for hexagonal arrays of cylinders and simple cubic arrays of spheres, respectively. The dashed curve is our least-squares fit to the permeability calculations of Sangani & Acrivos (1982a) for hexagonal arrays of cylinders for  $0.25 < \phi < 0.725$ .



## Vita

Alparslan Öztekin was born on August 15, 1962 in Sivas, Turkey. He attended Bakirköy High School and entered the Technical University of Istanbul in 1978. In May, 1982, he received a Bachelor of Science in Mechanical Engineering. In January, 1984, he entered the Department of Aerospace and Mechanical Engineering at the University of Arizona. He was awarded the Master of Science degree in mechanical engineering in December, 1987. He was subsequently admitted to the Ph.D. program at the University of Arizona, and in August, 1989 transferred to the University of Illinois.

Alparslan has accepted a position as a Postdoctoral Research Associate in the Department of Chemical Engineering at the Massachusetts Institute of Technology.



1911

1912

1913

1914

1915

1916

1917

1918

1919

1920

1921

1922

1923

1924

1925

1926

1927

1928

1929

1930

1931

1932

1933

1934

1935

1936